LIÈGE université
Sciences Appliquées

Piezoelectric digital vibration absorbers for vibration mitigation of bladed structures

A thesis submitted in partial fulfillment of the requirements
for the degree of Doctor of Philosophy (Phd) in Engineering Science

by

Jennifer DIETRICH

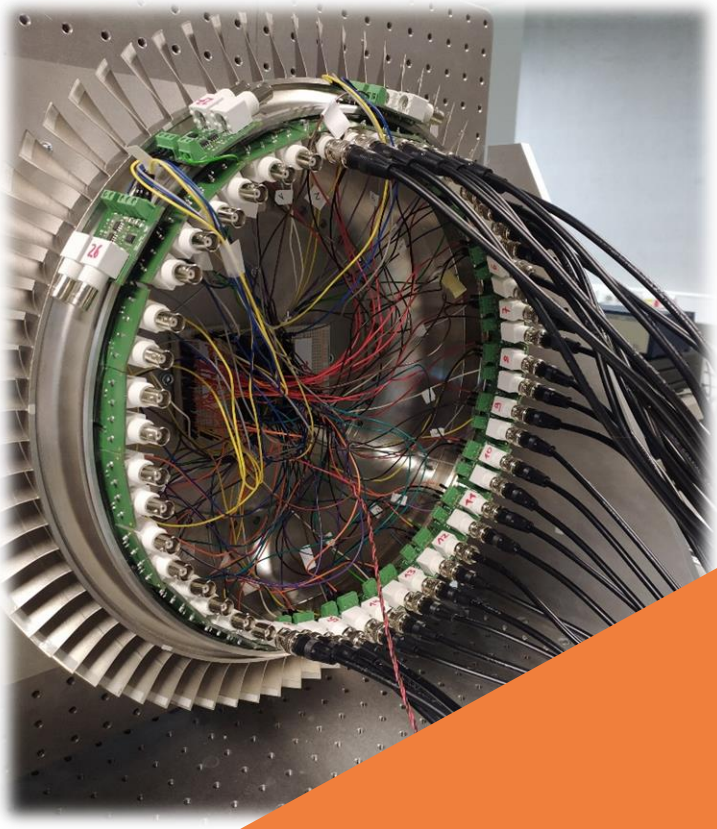

Supervisor: Gaëtan KERSCHEN

DOCTORAL COLLEGE IN AEROSPACE AND MECHANICS

AUGUST 2023

Members of the examination committee

Prof. Loïc Salles (President of the committee)
University of Liège (Liège, Belgium)

Prof. Gaëtan Kerschen (Supervisor)
University of Liège (Liège, Belgium)

Mr. Xavier Charles
Safran Aero Boosters (Herstal, Belgium)

Prof. Christophe Collette
University of Liège (Liège, Belgium), Université Libre de Bruxelles (Brussels, Belgium)

Prof. Vincent Denoël
University of Liège (Liège, Belgium)

Prof. Arnaud Deraemaeker
Université Libre de Bruxelles (Brussels, Belgium)

Prof. Fabrice Thouverez
École Centrale de Lyon (Lyon, France)

Abstract

Climate change and resource scarcity pose increasingly difficult challenges for the aviation industry requiring a reduction in fossil fuel consumption. To address these problems and increase the efficiency of aircraft engines, some of their parts are now manufactured in one piece. For example, a rotor of the compressor stage of an airplane engine consist of a drum with a large number of blades and is called BluM. These structures are lightweight and feature low structural damping and high modal density. Their particular dynamic characteristics require sophisticated solutions for vibration mitigation of these structures.

This is precisely the starting point of this thesis. Based on a digital realization of piezoelectric shunt circuits, we provide a damping concept that is able to tackle the complex dynamics of bladed structures and to mitigate their vibrations. To this end, multiple digital vibration absorbers (DVAs) are used simultaneously. Two new strategies to tune these DVAs are proposed in the thesis, namely the isolated mode and mean shunt strategies. These strategies not only take advantage of the fact that multiple absorbers act simultaneously on the structure, but they also address the problem of closely-spaced modes. In order to target multiple families of BluM modes, these strategies are incorporated in a multi-stage shunt circuit. The concepts are demonstrated experimentally using two bladed structures with increasing complexity, namely a bladed rail and a BluM. Both methods exhibit excellent damping performances on multiple groups of modes. In addition, they prove robust to changes in the host structure which could, e.g., be due to mistuning. Thanks to their digital realization, DVAs are also easily adjustable.

Finally, this thesis reveals the parallel that exists between resonant piezoelectric shunts with a negative capacitance and active positive position feedback (PPF) controllers. Based on this comparison, a new H_∞ norm-based tuning rule is found for a PPF controller. It is demonstrated using both numerical and experimental cantilever beams. To this end, a method that accounts for the influence of modes higher in frequency than the targeted one is developed.

Résumé

Le changement climatique et la raréfaction des ressources posent des défis de plus en plus complexes à relever pour l'industrie aéronautique. Un de ces défis est la réduction de la consommation en énergies fossiles. Pour accroître l'efficacité des moteurs d'avion, certains de leurs composants sont désormais fabriqués en une seule pièce. Dans le cas des compresseurs, ces pièces monoblocs sont appelées BluMs et sont constituées d'un tambour avec un grand nombre d'aubes. Ce type de structures bénéficie d'un allègement significatif, ce qui conduit à un faible amortissement structurel. De plus, ces pièces monoblocs présentent une densité modale élevée en raison du nombre important de diamètres nodaux. Ces caractéristiques dynamiques particulières nécessitent des solutions d'amortissement sophistiquées.

Cette thèse de doctorat aborde cette problématique. En exploitant le concept d'absorbeur de vibration digital (DVA), nous proposons une nouvelle technique d'amortissement des structures aubagées. Deux nouvelles stratégies d'accordage de ces DVA sont développées dans cette thèse, à savoir la stratégie du mode isolé et la stratégie du shunt moyen. Ces méthodes tirent non seulement parti du fait que plusieurs absorbeurs agissent simultanément sur la structure, mais elles s'attaquent aussi au problème des modes proches en fréquence. Afin de cibler plusieurs familles de modes, ces stratégies ont été incorporées dans un circuit de shunt à plusieurs étages. Les concepts sont testés expérimentalement sur deux structures aubagées de complexité croissante, à savoir un rail à aubes et un BluM comme application finale. Ces méthodes permettent d'obtenir d'excellentes performances d'amortissement sur plusieurs groupes de modes. Elles s'avèrent également robustes face à des variations de la structure, dues par exemple à un désaccordage de celle-ci. Il est à noter que, grâce à leur caractère digital, ces méthodes sont facilement adaptables.

Finalement, nous révélons le parallèle qui existe entre les shunts piézoélectriques résonants avec une capacitance négative et le contrôleur actif à rétroaction positive de position (PPF). Sur base de cette comparaison, de nouvelles règles d'accordage basées sur la norme H_∞ sont développées pour le contrôleur PPF. Leur efficacité est démontrée à la fois numériquement et expérimentalement sur une poutre encastrée-libre. Dans ce but, une méthode prenant en compte l'influence des modes dont la fréquence est supérieure au mode ciblé a été mise sur pied au moyen de facteurs de correction.

Acknowledgements

First of all, I want to thank the jury for accepting to read and evaluate this work. Christophe and Arnaud, thank you for also being part of my thesis committee and for enriching this work with your point of views, ideas and expertise. I appreciate all the discussions we had over these past years.

I feel particularly grateful to my advisor Gaëtan Kerschen who made this thesis possible on so many levels. Merci, Gaëtan, d'avoir toujours trouvé une solution pour le financement, pour ton avis professionnel, qui est toujours précieux. Tu étais constamment accessible pour moi et tu m'as toujours aidé à m'améliorer. Ton expertise est impressionnante et c'était un vrai plaisir de travailler avec toi et d'apprendre de toi.

Lab work can be fun but also hard and frustrating and having such a kind and genius colleague and mentor like Ghislain on your side makes life much more enjoyable – not only for all the chocolate moments that we shared. Thank your for all your patience, your constant availability and your willingness to share all your impressive expertise and ideas with me. I could learn so much from you and I feel extremely grateful for having had the opportunity to work with you. This work would clearly not be the same without you.

I could not have wished for a better office mate than Gaëtan A.. You have been a great support during all the difficulties that arise, not only during a PhD, but also during life, a wonderful companion for interesting discussions (technical or not) about various topics, and a qualified reference for my numerous questions about French language. Danke!

I was lucky to find myself surrounded by a very kind research group that integrated me quickly. Martin, Nico, Tong, Ghislain, Giancarlo, Sam, Gaëtan, Thibaut and Riccardo – thanks for all the progress meetings we shared together, all the lunch runs around the forest, the beer talks, the memories we could collect at conferences and after work, and all the laughs we had. I hope that we will find the opportunity to have some more of these moments in the future!

Many thanks to Christophe Brose and his team who realized the digital vibration absorbers used in this work on printed circuit boards. Ahmad and Rasa, thank you for the collaborations that we had and for all your kindness, expertise, and help in the field of active control.

Coming to the B52 would not be the same without this warm and welcoming group of the PML and all the people around. I appreciate all the moments we shared in and out of the department. It is great when things develop from small talk at the coffee machine to becoming friends. I would also like to thank Vinayak and Kevin for being my friends from the moment I joined the department. Being a foreigner is always more fun when you have people to share your experiences with. Jocelyn, un grand merci pour tout. Tu as toujours insisté à parler français avec moi et cela m'a beaucoup plus aidé que tous mes cours de français. J'apprécie vraiment tous les moments que nous avons partagés et je

suis très heureuse de notre amitié. Nayan, thank you for sharing all those precious moments together during this stressful phase of thesis writing, for all the climbing sessions, coffees and discussions. You've become an important person to me in no time, and I'm grateful to have had the chance to get to know you better than just crossing paths with you in the B52. Il y a plusieurs autres personnes que j'ai eu la chance de rencontrer en dehors du couloir de mon bureau. Vous m'avez permis de me sentir chez moi à Liège. Merci Tanguy et Salomé. Merci Javier et Cami, Pablo et Javi - pour tous les moments, les repas et les émotions partagés, pour être toujours là, pour tous vos conseils, et pour savoir que je peux toujours compter sur vous - vous faites maintenant partie de ma famille.

Clara, you have a huge place in my heart. Thank you so much for this very special friendship, for understanding me, for being there, for being open and honest, for being you. The PhD can be accompanied by doubts and insecurities. Having you by my side, Clara, Gab and Kutta, makes life so much easier and has allowed me on many occasions to see things from a different angle. I really appreciate all the moments we have shared and look forward to all the adventures to come. So many laughs, so many problem-solving moments, so many late-night discussions. Thank you for having become part of my family.

Sam, je suis tellement reconnaissante et heureuse que nos chemins se soient croisés ici à Liège. Merci pour ton soutien inconditionnel dans tant de domaines : tu étais là pour moi dans les moments de doute, tout au long du processus d'écriture, tu m'as aidé avec toute ton expertise mais aussi avec toute ta compassion. Merci d'être toi, une personne gentille, aimante et loyale. Merci d'être dans ma vie.

Ein unendlich grosses Dankeschön sende ich auch an meine Freunde aus Hannover, insbesondere Manu, Mareike, Lisa, Doro, Kathi, Carina, Marcus, Philipp, Jonas und Linda. Danke für all euren Support in Form von wunderschönen Telefongesprächen und zahlreichen Besuchen in Belgien. Und danke, dass ich mich trotz der Entfernung immer wieder direkt wie zu Hause fühle, wenn wir uns sehen - egal wo.

Ich kann all die Dankbarkeit, die ich für meine Eltern habe, gar nicht in Worte fassen. Dankbarkeit für all die Unterstützung und Form von Taten aber insbesondere für all die Fürsorge, Güte und bedingungslose Liebe. Danke für all eure Besuche und dafür, dass ihr immer mein Zuhause seid. Mama und Papa, ihr seid zwei ganz besondere Menschen und habt all meine Bewunderung und Liebe!

This work was supported by the Fonds de la Recherche scientifique - FNRS under Grant n° FRS-FNRS PDR T.0124.21, which we gratefully acknowledge together with the financial support from SPW (WALInnov grant 1610122) for the Maveric project.

Nomenclature

c_{kl}	Elastic stiffness constant [$\mathrm{N\,m^{-2}}$]
D_k	Electric displacement component [$\mathrm{C\,m^{-2}}$]
e_{kp}	Piezoelectric constant [$\mathrm{C\,m^{-2}}$]
$\bullet_E$	At constant electric field [$\mathrm{V\,m^{-1}}$]
$E_{p/l}$	Electric field component [$\mathrm{V\,m^{-1}}$]
$\bullet_S$	At constant strain
$S_{p/l}$	Strain component
$\bullet_T$	At constant stress
T_k	Stress vector component [$\mathrm{N\,m^{-2}}$]
ϵ_{kl}	Permittivity component [$\mathrm{F\,m^{-2}}$]
ω_{oc}	Open-circuit resonance frequency
ω_{sc}	Short-circuit resonance frequency
K_c^2	Electromechanical coupling factor (EMCF)
$\hat{K}_c^2$	Mean electromechanical coupling factor (MEMCF)
$\hat{\omega}_{oc}$	Mean open-circuit resonance frequency
C_p^{ε}	Capacitance of the piezoelectric patch p under constant strain
L	Shunt branch inductance
R	Shunt branch resistance
s	Laplace variable
$C_p(s)$	Dynamic capacitance
$E_p(s)$	Dynamic elastance
V_p	Voltage across the electrodes of a transducer p

q_p Charge of piezoelectric transducer p

$\dot{q}_p$ Current of piezoelectric transducer p

Z_{Shunt} Shunt impedance

Y_{Shunt} Shunt admittance

V_{ADC} Voltage input to a digital unit

V_{DAC} Voltage output of a digital unit

α Piezoelectric voltage division ratio

β Amplification gain

γ Attenuation gain

δ_c Factor representing the imperfections of the DVA

g_c Current source gain of the DVA

V_s Voltage across a shunt branch

q_s Charge of a shunt branch

$\tilde{C}_p^{\varepsilon}$ Equivalent capacitance seen from a specific shunt branch

$\tilde{\omega}_{oc}$ Equivalent open-circuit resonance frequency seen from a specific shunt branch

$\tilde{\omega}_{sc}$ Equivalent short-circuit resonance frequency seen from a specific shunt branch

$\tilde{L}$ Network inductance

$\tilde{R}$ Network resistance

R^* Optimal resistance of a fictitious shunt branch

L^* Optimal inductance of a fictitious shunt branch

List of Abbreviations

TMD	Tuned mass damper
IFF	Integral force feedback
PFF	Positive position feedback
NC	Negative capacitance
DVA	Digital vibration absorber
BluM	Bladed drum manufactured in one piece
BLISK	Bladed disk manufactured in one piece
SDOF	Single-degree-of-freedom
MDOF	Multiple-degree-of-freedom
EMCF	Electromechanical coupling factor
R	Resistive
L	Inductive
C	Capacitive
FRF	Frequency response function
OpAmp	Operational amplifier
ADC	Analog-to-digital-converter
DAC	Digital-to-analog-converter
I/O	Input-output
PCB	Printed circuit board
ZOH	Zero-order hold
LSE	Least square error
1B	First bending mode
2B	Second bending mode
1T	First torsional mode
FE	Finite element
DOF	Degree-of-freedom
MEMCF	Mean effective electromechanical coupling factor
MIMO	Multiple-input multiple-output
LSFD	Least-squares frequency-domain
RMS	Root mean square

Contents

Introduction

Motivation of this thesis

Our society is faced with a paradigm shift between its desire to travel and the need to reduce pollution and protect the environment [1]. With 9 % of the distribution of carbon dioxide emissions generated by the transportation sector worldwide (cf. Figure 1), there is not only considerable room, but also the need for improvement toward a greener way of air transport. There exist several directives and initiatives driving the aviation industry to progress further in the direction of more efficient and environment-friendly aircraft designs, e.g., ACARE, Clean Sky 2 or WINGS [3–8]. For example, by 2050, all flights departing from Europe must achieve carbon neutrality [6]. Additionally, due to wars and political conflicts, fossil resources are becoming more scarce or inaccessible. All these developments call for a reduction of the fuel consumption of aircraft or a shift to green alternatives. The growth in efficiency of the current fleet in the aviation sector is immense and aircraft designs can already be considered as being optimized to a great extent. However, the new generations of aircraft in the coming decade only are expected to save the significant amount of 25 % of fuel and CO_2 [9, 10]. In the mid-term, technical improvements in engine efficiency have a supporting role beside an adoption of sustainable aviation fuels. In the longer term, particularly after 2050, synthetic fuels are estimated to play the key role [10] to achieve the global requirements.

Global players of the aviation industry commit to progress toward carbon-friendly alternatives. In 2021, Safran and GE Aviation announced their RISE [11] project, aiming for an open fan rotor that drastically decreases fuel consumption thanks to a higher bypass ratio. With several future aircraft models in the pipeline, Airbus has launched the ZEROe project to develop the world's first hydrogen-powered commercial aircraft [12]. The HE-ART [13] project unites different sectors of the aviation industry, i.a. leading engine manufacturers like Rolls Royce and Safran, airframe producers such as ATR, Airbus and Leonardo, as well as important manufacturers and research institutions. It proposes a hybridization of the propulsion system by combining an electrical with an ultraefficient turboprop thermal engine. A demonstrator is expected to be available by early 2027. The aforementioned projects are only examples among others and their multitude shows that there is a great interest and initiative in politics and economy, proving the importance of CO_2 reduction for the future of aviation.

All these recent developments and requirements pose new challenges for the aviation industry. In the context of the mid-term perspective, the trend strongly goes toward more lightweight rotor designs. However, these lightweight structures come with several

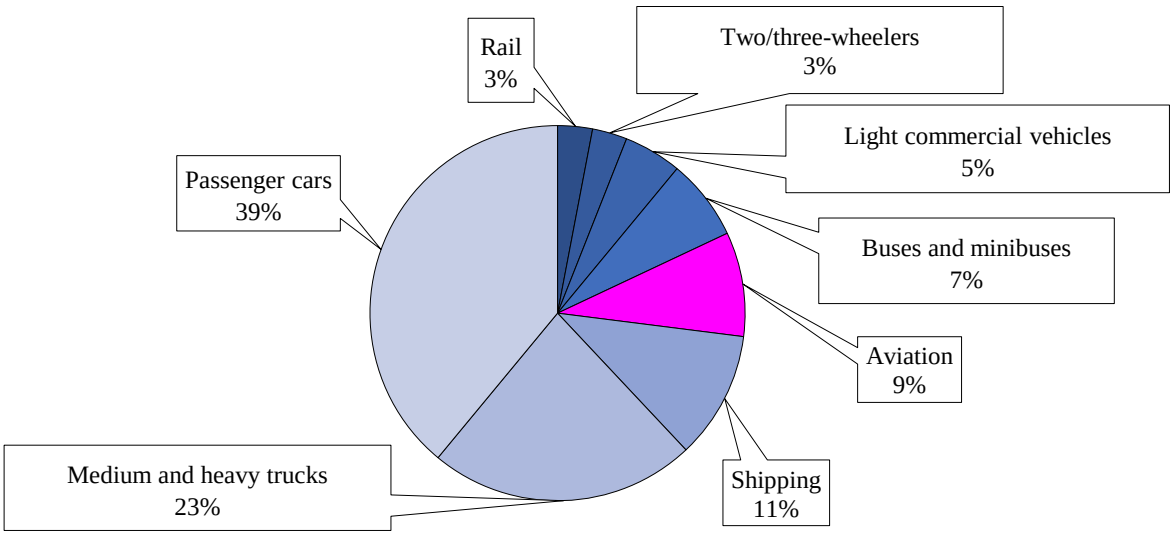

Figure 1: Worldwide distribution of carbon dioxide emissions produced by the transportation sector in 2021 [2].

challenges for engineers. Often, they feature a low structural damping so that larger vibrations occur, increasing the susceptibility to fatigue which can eventually lead to failure. Possibly, these large displacements can trigger strongly nonlinear behavior of the structural components. For all these reasons, it is desirable to avoid the excitation of the structure at its resonance frequencies, or, if this is not possible, attenuate the resonant vibrations. Since it is not always feasible to provide rotor designs according to the former solution, it is also important to address the latter. This problem forms the main thrust of this thesis. In the following section, the reader will be provided with an overview of different existing damping approaches.

Approaches to damp structural vibrations

Vibration mitigation is a well-known and ongoing challenge in engineering that can be tackled by introducing additional damping into the host system. There exist different vibration reduction approaches that can be classified as passive or active. Classical passive solutions consist, e.g., of damping layers and coatings, often made of viscoelastic material [14], dashpots or friction dampers [15]. Another popular passive damping solution is the tuned mass damper (TMD), where an additional mass is connected to the host structure via dampers and springs [16, 17]. The resonance frequency of the TMD is chosen to match the resonance frequency of the host structure so as to absorb its vibrations when it resonates. During the last decades, the use of piezoelectric vibration absorbers in which an electrical circuit resonates with the host structure has become increasingly popular [18, 19]. Traditionally, these applications operate according to a passive control law.

When active control techniques are used, energy is injected into the host system via a controller. In this way, the control authority over the structure can be enhanced, which comes at the risk of triggering instabilities of the controlled system. Typically, the struc-

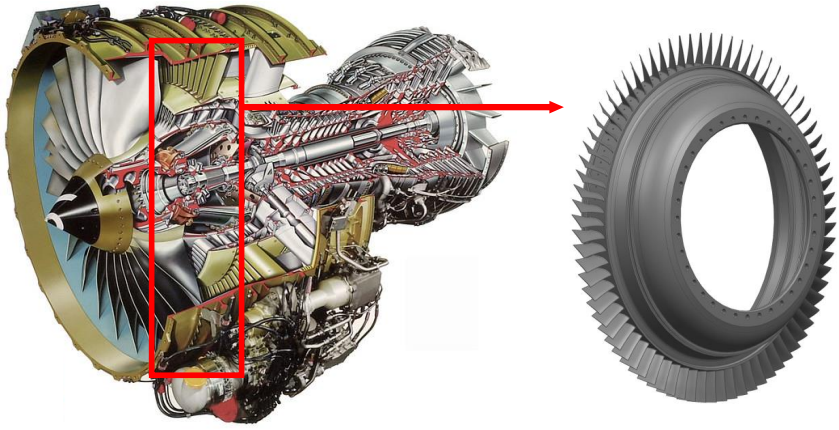

Figure 2: Schematic representation of an aircraft engine with indication of the position of the low-presssure compressor bladed drum (BluM). Left: CFM56 turbofan aircraft engine Cutaway Drawing [29]; right: BluM from Safran Aero Boosters. [30].

tural response is measured via one or more sensors, and, based on the measured signals, an appropriate control load provided by a controller is applied to the structure through actuators. Popular active control approaches are direct velocity feedback [20], integral force feedback (IFF) [21] or positive position feedback (PPF) [22]. Typically applied in the automotive industry, other candidates can be the skyhook damper [23], or, for high-precision mechanics, active isolation solutions [24]. As a counterpart to the passive TMD, there exist active TMDs where the feedback gain and the TMD parameters are subject to an online optimization process, enhancing the damping performance [25]. An interesting alternative to analog piezoelectric vibration absorbers is a digital implementation of the electrical circuit [26]. Additionally, the control authority of piezoelectric shunts can be enhanced by adding a negative capacitance (NC) [27, 28].

Two of the aforementioned damping solutions, namely the piezoelectric digital vibration absorber (DVA), with or without an additional NC component, and the PPF controller are considered in this thesis and will be described in more details later in the manuscript. Specifically, the problem of aircraft engine vibrations is addressed using a DVA. Indeed, a DVA offers a number of advantages, such as considerable versatility, compactness, and ease of adjustment, which makes it highly attractive for complex damping problems.

Vibration mitigation of aircraft engines

A popular aircraft engine is the turbofan CFM56 presented in Figure 2, comprising high- and low-pressure compressor stages. The compressors usually consist of bladed assemblies that operate at high rotational speeds. One way to reduce the weight of aircraft engines is to manufacture some of their parts in one piece. Figure 2 gives the example of a low-pressure compressor rotor called BluM. It consists of a drum to which a multitude of blades are attached. Realized as a single piece, they do not feature any interface between the blades and the drum support. There also exist examples of bladed disks manufactured in a single piece referred to as BLISK. Being part of an aircraft engine, these components are subject to two types of external forces that are of mechanical or aerodynamical na-

ture. The former results from a rotor imbalance or mechanical interactions (rotor/stator contact) whereas the latter is caused by the airflow entering the fan and going through the different stages of the engine [31]. In addition, small imperfections in the manufacturing process (the so-called mistuning) disturbing the cyclic symmetry of these structures can lead to vibration localizations and cause fatigue failures. All these factors justify the importance of damping these structures in order to guarantee safe operations. In this context, piezoelectric shunts begin to be considered as a promising damping solution [32].

Contributions of this thesis

Realized in the framework of the WALInnov Maveric project [33], this thesis can be seen as the continuation of Ghislain Raze's work [30]. The objective is to bring the DVA to the next level by applying it to real bladed structures. To this end, multiple DVAs are used simultaneously to mitigate the structural vibrations of bladed assemblies featuring complex multimodal dynamics. In order to address this challenge, different shunt tuning approaches are integrated into a new strategy with the aim to provide a solution for broadband vibration mitigation of industrial structures.

The manuscript is organized as follows. Chapter 1 presents the concept of a DVA and the practical realizations used in the experimental campaigns of this thesis. In its first part, Chapter 2 outlines the dynamical characteristics of bladed structures and the challenges they pose for shunt tuning. In the second part of this chapter, strategies that address these challenges are proposed. Chapters 3 and 4 present the results of the experimental application of these strategies, including detailed technical information on the implementation of a DVA. Chapter 3 is concerned with a bladed rail structure, which features a much smaller dimensionality than a BluM structure and serves as an intermediate demonstrator for a proof of concept. Chapter 4 studies an industrial BluM structure provided by Safran Aero Boosters. The BluM was already studied experimentally in Bilal Mokrani's work [32] where it was connected to analog shunt circuits. In this thesis, the emphasis is on a digital realization and takes advantage of the great versatility and adaptability of DVAs.

In the second part of this thesis, we provide new shunt tuning rules based on the H_∞ norm when a NC is connected in series in order to increase shunt performance. These tuning rules are derived in Chapter 5 based on a single-degree-of-freedom (SDOF) approximation. By comparing the resonant shunt controller with a NC to a PPF controller, the H_∞ tuning rules can be translated to the active control case in Chapter 6. To extend the applicability to the multimodal case, a procedure that accounts for the influence of higher-order modes during the tuning process is also developed.

The manuscript concludes with a discussion of the results obtained in the course of this work and an evaluation of them within the scientific context. Future directions and extensions of our research are finally outlined.

Chapter 1

A piezoelectric digital vibration absorber

1.1 Introduction

Piezoelectric vibration absorbers, first introduced by Forward [18] in 1979, have been an attractive damping solution for engineering structures over decades. They rely on the ability of piezoelectric materials to convert mechanical energy into electrical energy that is then dissipated in a suitably-designed circuit. Their working concept as well as practical realizations are the subject of this chapter. It is organized as follows. The first part is intended to serve as a reminder of the fundamentals of piezoelectric shunt damping and common circuit designs. Next, the concept of a digital realization of these absorbers is introduced and discussed. This digital implementation and application to complex engineering structures is one of the key elements of this thesis. A design of a DVA is presented and its working principle outlined. This design forms the basis for the practical applications presented in Chapters 3 and 4. Furthermore, advantages and disadvantages of digital implementations are discussed. In particular, the discretization process of a continuous measured signal that needs to be performed to make it comply with a digital unit is a potential source of instabilities, since it modifies the controller function. This chapter concludes by proposing a discretization method that accounts for these changes.

1.2 Piezoeletric structures

1.2.1 Linear piezoelectric materials

In 1880, Jacques and Pierre Curie discovered the property of piezoelectric materials to convert mechanical energy into electrical energy and vice versa. These materials have a crystalline structure with localized charge separations, also known as electric dipoles, which are normally balanced neutrally if not subjected to force. However, if the structure is mechanically loaded, these dipoles arrange themselves in such a way that an external electric field is created: the direct piezoelectric effect occurs. This effect is schematized in Figure 1.1. One can see that the polarization of the external electric field is inverted depending on whether a tension or a compression is applied to the material.

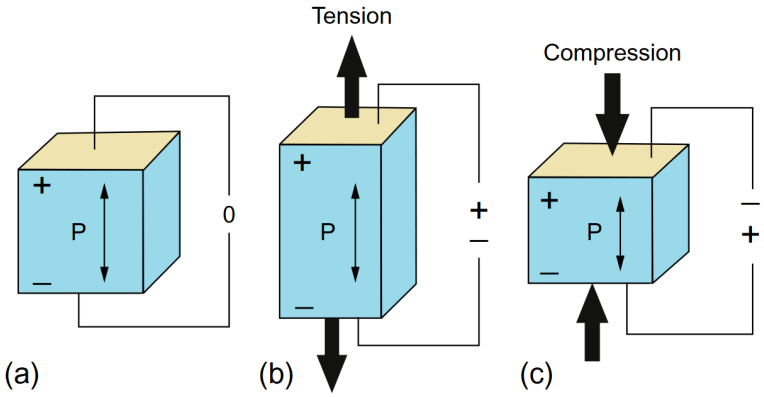

Figure 1.1: The direct piezoelectric effect: (a) piezoelectric material; electrical charge generation under (b) tension and (c) compression under the material polarization P [34].

The piezoelectric effect is a reversible process so that applying an electrical charge to the material, results in the creation of a mechanical strain [34].

In a first step, we recall the constitutive equations of linear piezoelectric materials. A complete derivation of these can, e.g., be found in [19, 35]. Based on the first law of thermodynamics, they read [35]

$$\begin{aligned} T_3 &= c_{33}^E S_3 - e_{33} E_3 \\ D_3 &= e_{33} S_3 + \epsilon_{33}^S E_3 \ . \end{aligned} \tag{1.1}$$

Here, for simplicity, the so-called '3' direction is considered directly. It corresponds to the poling direction, assuming isotropic material behavior in the other two directions [19]. T_3 and S_3 are components of the stress and strain vector, respectively, whereas D_3 is a component of the electric displacement field. E_3 corresponds to the electric field component and c_{33}^E is an elastic stiffness constant. ϵ_{33}^S represents the permittivity at constant strain. The piezoelectric constant e_{33} couples the mechanical and the electrical equations.

We consider the piezoelectric rod displayed in Figure 1.2 as an example for a piezoelectric material. The '3' direction corresponds to the x direction. In order to look at the electrical energy that is produced over the structure, we integrate Equation (1.1) over its volume Al (cf. Figure 1.2). Finally, to obtain an expression for the force f_p acting on the transducer, we divide by the distance l between the two electrodes. We introduce the following expressions

$$f_p = T_3 A, \qquad x = S_3 l, \qquad V_p = -E_3 l, \qquad q_p = D_3 A, \tag{1.2}$$

$$k_{p,sc} = \frac{A c_{33}^E}{l}, \qquad \gamma_p = \frac{A e_{33}}{l}, \qquad C_p^S = \frac{A \epsilon_{33}^S}{l} \ . \tag{1.3}$$

Here, V_p is the voltage across the transducer electrodes and q_p the charge flowing trough them. x can be interpreted as the stroke of the transducer. The constants $k_{p,sc}$, γ_p and C_p^S are characteristics of the piezoelectric material such as its stiffness (with short-circuited

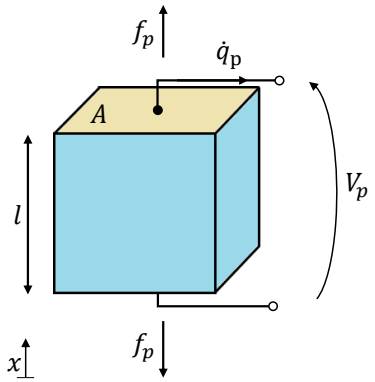

Figure 1.2: Presentation of a piezoelectric element.

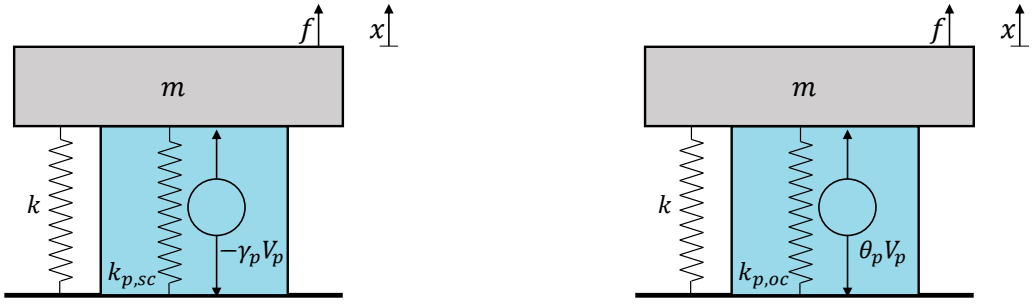

(a) The transducer acts as an ideal current source. **(b)** The transducer acts as an ideal voltage source.

Figure 1.3: SDOF piezoelectric system.

electrodes), the piezoelectric coupling coefficient and the piezoelectric capacitance at constant strain, respectively [30]. γ_p characterizes how much energy is transformed between the piezoelectric transducer and the mechanical system [19] so that an interaction between the electrical and mechanical dynamics takes place. In literature related to piezoelectric shunts, the piezoelectric capacitance C_p^S is also often referred to as C_p^ε. For convenience, this expression will be used in this thesis from now on. Inserting Equations (1.2) and (1.3) in Equation (1.1) yields

$$f_p = k_{p,sc} x + \gamma_p V_p \tag{1.4}$$

$$q_p = \gamma_p x - C_p^\varepsilon V_p \ . \tag{1.5}$$

1.2.2 The electro-mechanical system

In a next step, we regard the piezoelectric transducer bonded to a structure, here, an SDOF system consisting of a mass m and a spring of stiffness k and being excited by an external force f. The spring and the transducer are both in parallel connected to the ground (cf. Figure 1.3). We regard two ways of modeling the electromechanical system, also referred to as piezoelectric structure, in the following:

(i) The transducer acts as an ideal current source as displayed in Figure 1.3a;

(ii) the transducer acts as an ideal voltage source as displayed in Figure 1.3b.

(a) Norton's equivalent admittance. **(b)** Thévenin's equivalent impedance.

Figure 1.4: Electrical representations of the piezoelectric structures presented in Figure 1.3

Considering case (i), the governing equations for the electromechanical system in the Laplace domain read

$$\begin{cases} (ms^2 + k_{sc})x + \gamma_p V_p = f \\ \gamma_p x - C_p^\varepsilon V_p = q_p \ . \end{cases} \tag{1.6}$$

s is the Laplace variable and k_{sc} is the stiffness of the electromechanical structure when the electrodes of the transducer are in short-circuit ($V_p = 0$), so that $k_{sc} = k_{p,sc} + k$. One can see that the interaction between the electrical and the mechanical variables is represented by the coupling coefficient γ_p. Considering the second line of Equation (1.6) that represents the electrical part and building its derivative, we obtain

$$q_p s = \gamma_p x s - C_p^\varepsilon V_p s \ . \tag{1.7}$$

Recalling Kirchhoff's current law, we notice that the transducer is modeled like an ideal current source in parallel with the piezoelectric capacitance C_p^ε. This presentation of the electrical part of a piezoelectric structure is Norton's equivalent circuit [36] as illustrated in Figure 1.4a. We derive the short-circuit resonance frequency of the system

$$\omega_{sc} = \sqrt{\frac{k_{sc}}{m}} \ . \tag{1.8}$$

The open-circuit ($q_p = 0$) stiffness of the structure is

$$k_{oc} = k_{sc} + \frac{\gamma_p^2}{C_p^\varepsilon} \ . \tag{1.9}$$

Using Equations (1.6) and (1.9), the equations of motion for case (ii) are

$$\begin{cases} (ms^2 + k_{oc})x - \theta_p q_p = f \\ \theta_p x - C_p^\varepsilon q_p = V_p, \end{cases} \tag{1.10}$$

with

$$\theta_p = \frac{\gamma_p}{C_p^\varepsilon} \ . \tag{1.11}$$

In the same manner as Norton's admittance, the respective electrical representation of this system can be found as Thévenin's equivalent circuit [37] (see Figure 1.4b). The

open-circuit resonance frequency of this system is then defined as

$$\omega_{oc} = \sqrt{\frac{k_{oc}}{m}} \ . \tag{1.12}$$

The short- and open-circuit resonance frequencies can be used for the evaluation of the electromechanical coupling which is a key quantity for the control authority over the structure for piezoelectric shunt damping. It can be expressed by the dimensionless electromechanical coupling factor (EMCF) K_c, relating the modal strain energies when the transducer is in short- and in open-circuit [38]:

$$K_c^2 = \frac{\omega_{oc}^2 - \omega_{sc}^2}{\omega_{sc}^2} \ . \tag{1.13}$$

Hence, this factor depends on the properties of the host system through γ_p (or θ_p) and C_p^ε. Another representation of the coupling factor is its normalization with ω_{oc}, defining the second power of the EMCF as

$$\alpha^2 = \frac{\omega_{oc}^2 - \omega_{sc}^2}{\omega_{oc}^2} = \frac{K_c^2}{1 + K_c^2} \ . \tag{1.14}$$

1.2.3 Dynamic capacitance

In control theory, the relation between an input signal and the output signal of a system without feedback, also called plant transfer function, is of importance for the design of the controller. For the electromechanical system displayed in Figure 1.3, not only the properties of the SDOF structure itself but also its interaction with the piezoelectric transducer through the coupling coefficients impact this transfer function. The plant transfer function of a piezoelectric system, usually named dynamic capacitance, provides us with all necessary parameters to properly tune the shunt parameters. We recall Equation (1.6) and assume that the system is unforced ($f = 0$) [39]. Setting the piezoelectric charge and voltage into relation, we obtain the expression of the dynamic capacitance for the SDOF case [30]

$$\frac{q_p}{V_p} = -C_p^\varepsilon \left(\frac{1}{C_p^\varepsilon} \frac{\gamma_p^2}{ms^2 + k_s c} + 1 \right) = -C_p^\varepsilon \left(\frac{\omega_{oc}^2 - \omega_{sc}^2}{s^2 + \omega_{sc}^2} + 1 \right) = -C_p^\varepsilon \frac{s^2 + \omega_{oc}^2}{s^2 + \omega_{sc}^2} = C_p(s) \ . \tag{1.15}$$

In the static case, the dynamic capacitance reads

$$C_{p,static} = C_p(s = 0) = C_p^\varepsilon \frac{\omega_{oc}^2}{\omega_{sc}^2} = C_p^\varepsilon (1 + K_c^2) \ . \tag{1.16}$$

We have a closer look at this dynamic capacitance function in the SDOF case by means of the representation in Figure 1.5. The static value $C_{p,static}$ is greater than C_p^ε which is also referred to as the electrically blocked capacitance of the undeformed rod [40]. This blocked capacitance occurs at high frequencies where, in the absence of mechanical motions, the energy is stored only in electrical form. The pole of the dynamic capacitance function is the open-circuit frequency ω_{oc} while ω_{sc} corresponds to its zero. The better the electromechanical coupling, the greater the distance between these two frequencies

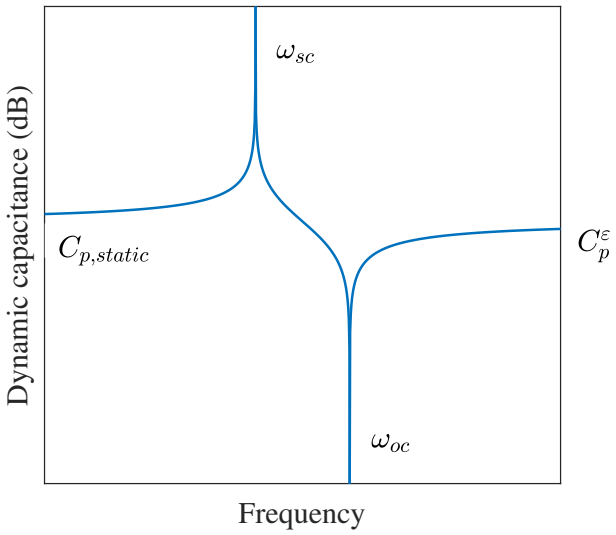

Figure 1.5: Example for a dynamic capacitance function of a piezoelectric structure in the SDOF case.

(cf. Equation (1.13)). Naturally, the EMCF of piezoelectric structures is limited and usually small, defining the limits of the control authority.

The reciprocal of Equation (1.15) yields the so-called dynamic elastance

$$\frac{V_p}{q_p} = \frac{1}{C_p(s)} = -\frac{1}{C_p^{\varepsilon}} \frac{s^2 + \omega_{sc}^2}{s^2 + \omega_{oc}^2} = E_p(s) \ . \tag{1.17}$$

Both transfer functions (Equations (1.15) and (1.17)) can serve as a basis to design a piezoelectric shunt controller for vibration attenuation of the host structure. They can be obtained easily from electrical measurements that only require the excitation of the structure via the piezoelectric transducer, acting both as an actuator and sensor.

1.3 Piezoelectric shunt damping

An electrical circuit connected to the piezoelectric host structure can be used to attenuate unwanted vibrations by dissipating the mechanical energy of the structure's motions after it has been converted to electrical energy. One refers to a shunt circuit whose transfer function is the electrical shunt impedance Z_{Shunt} (or admittance Y_{Shunt}) as depicted in Figure 1.6. The idea was first introduced by Forward in 1979 [41]. Ideally, a shunt circuit is designed in a way that it dissipates the electrical energy at the frequency at which undesired vibrations of the host structure appear. Common circuits are of either resistive (R shunt) or resistive-inductive (RL shunt) nature consisting of electrical elements such as resistors or inductors, possibly in combinations with capacitors. While a resistor can be considered as the electrical equivalent of a mechanical dashpot, adding an inductor may be seen as connecting an electrical mass to the structure. A piezoelectric RL shunt circuit is therefore often compared to a TMD [19].

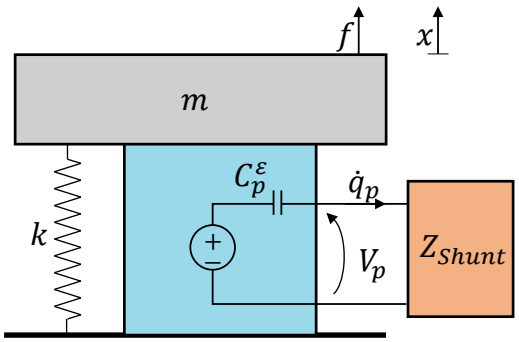

Figure 1.6: An SDOF piezoelectric system connected to a shunt impedance Z_{Shunt}.

1.3.1 Passivity

Moheimani and Fleming [42] stated that a shunt impedance is considered passive only if it does not introduce any additional energy into the system, reading

$$\int_0^\infty V_p(t) \cdot \dot{q}_p(t) dt \geq 0, \tag{1.18}$$

with $V_p(t)$ corresponding to the voltage and $\dot{q}_p(t)$ to the current in Figure 1.6. In a linear system, the passivity condition of the impedance $Z_{Shunt}(j\omega)$ reads [43]

$$\Re(V_p(i\omega) \cdot \dot{q}_p^*(j\omega)) \geq 0, \tag{1.19}$$

with $\dot{q}_p^*(j\omega))$ being the complex conjugate of $\dot{q}_p(j\omega))$. Alternatively, we can write

$$\Re(Z_{Shunt}(j\omega)) \geq 0 \quad \forall\omega \ . \tag{1.20}$$

$\Re$ defines the real part of a function whereas j denotes the unit imaginary number $j = \sqrt{-1}$. If the passive criterion given in Equations (1.18) to (1.20) is respected and the shunt transfer function positive-real, the system can be regarded as unconditionally stable [42] which significantly facilitates the practical application. Commonly, piezoelectric shunts only consist of electrical elements such as capacitors, resistors and inductors so they could be considered as passive damping solutions. However, some authors may disagree with this classification, since the required inductance values for shunts are often large and cannot always be realized using only analog components without a power supply [44]. In the context of this work we will hold to the above classic definition of passivity given that the theoretical control law according to which the shunt works remains passive. This is in line with definitions given, e.g., in [30, 42]. In shunt damping, passive applications are considered to be simple, low priced and easy to apply [27]. Furthermore, in contrast to active control approaches, a passive control does not run the risk of becoming unstable in the event of a disturbance.

1.3.2 Designing the shunt circuit

Over decades, various ideas for the design of a piezoelectric shunt impedance and the tuning of its parameters have been proposed. This section provides the reader with an overview of the most commonly-used approaches and details of the ones that build the basis for the developments in this work. It does not claim completeness with regard to all existing and common tuning approaches.

1.3.2.1 Resistive shunts

Electrical energy might be dissipated by connecting a resistor R to the electrodes of a piezoelectric transducer [19, 41, 45]. The shunt impedance then reads

$$Z_{Shunt,R}(s) = R \ . \tag{1.21}$$

Recalling Ohm's law

$$V = ZI, \tag{1.22}$$

with I corresponding to the electrical current $\dot{q}$ and Z being an arbitrary electrical impedance, Equation (1.10) then becomes

$$\begin{cases} (ms^2 + k_{oc})x - \theta_p q_p = f \\ Rq_p s + \frac{1}{C_p^\varepsilon} q_p - \theta_p x = 0 \ . \end{cases} \tag{1.23}$$

Inserting the second line of Equation (1.23) into the first yields the receptance function of the shunted system:

$$\frac{x}{f} = \left[ms^2 + k_{oc} - \frac{\theta^2}{Rs + \frac{1}{C_p^\varepsilon}} \right]^{-1} \ . \tag{1.24}$$

This receptance function can then, e.g., be minimized to find an optimal value for the free parameter R. Hagood et al. chose this parameter based on a pole-placement technique presented in [19]. Thomas et al. based their parameter optimization on a so-called fixed point [45]. Under a variation of the parameter R, this point is identical for each resulting frequency response function (FRF). By making this point the maximum of the receptance function, they derived an optimal value for R in a resistive shunt function [45]:

$$R_{opt,resistive} = \frac{1}{C_p^\varepsilon \omega_{sc} \sqrt{1 + \frac{K_c^2}{2}}} \ . \tag{1.25}$$

1.3.2.2 Resistive-inductive shunts

The impedance of an RL shunt is

$$Z_{Shunt,RL} = Ls + R \ . \tag{1.26}$$

We consider a series shunt so that inserting $Z_{Shunt,RL}$ into Equation (1.10) yields

$$\begin{cases} (ms^2 + k_{oc})x - \theta_p q_p = f \\ Lq_p s^2 + Rq_p s + \frac{1}{C_p^\varepsilon} q_p - \theta_p x = 0 \ . \end{cases} \tag{1.27}$$

The receptance function of the shunted system is

$$\frac{x}{f} = \left[ms^2 + k_{oc} - \frac{\theta_p^2}{Ls^2 + Rs + \frac{1}{C_p^\varepsilon}} \right]^{-1} . \tag{1.28}$$

We define the electrical resonance frequency

$$\omega_e = \sqrt{\frac{1}{C_p^\varepsilon L}}. \tag{1.29}$$

Ideally, in a properly-tuned shunt case, this frequency should be close to the targeted resonance frequency of the host system, causing the shunt circuit to resonate and dissipate electrical energy effectively via the resistor. As a result of the additional inductance, this receptance function has now two resonance peaks as well as two intersection points, also called fixed points. Depending on the choice of the parameter L, these fixed points might be of different amplitudes. One way to choose L is to aim for their peak values to be equal so that the resonance frequency of the uncontrolled system is centered between them. Figure 1.7a illustrates these two intersections of the different FRFs resulting from the different RL shunt-controlled systems. The yellow graph belongs to the case where L is chosen in a way that the fixed-points are of equal amplitude while the parameter R is set to zero. Once L is defined, the "optimal" damping might be chosen in different ways: Hagood and Flotow set R in a way that the amplitude at the electrical resonance frequency ω_e coincides with the amplitude of the two fixed points, resulting in a relatively flat receptance function [19]. Yamada et al. defined the optimal value for R by setting the two fixed points as maxima of the receptance function [46]. However, since this is not exactly feasible, they specified an optimal R value for each maximum separately to then use their the root mean-square (RMS) as the final optimal value. Following the same spirit, Thomas et al. refined their approach by finding an optimal value for R using a Taylor series expansion [45]. Their tuning rules are applied to an SDOF system example in Figure 1.7. It can be seen that, when the RL shunt is properly tuned, the fixed points are a good approximation of the receptance resonance peaks but that they do not coincide exactly with them. Moreover, both for [19] and [45], there remains a slight imbalance between the two resonant peaks and they do not feature an exact same amplitude value (cf. Figure 1.7).

In their work, Soltani et al. found optimal tuning rules that are not based on the fixed points [47]. They presented a closed-form mathematical expression for the amplitude of the two equal receptance peaks. This exact solution has then been subject to a minimization based on the H_∞ norm resulting in an expression for optimal RL shunt parameters [47, 48]. First, the parameter

$$r = \frac{\sqrt{64 - 16K_c^2 - 26K_c^4} - K_c^2}{8} \tag{1.30}$$

is introduced. With the help of this parameter, we can express the optimal values for the shunt inductance

$$L_{opt,resistive-inductive} = \frac{4K_c^2 + 4}{(3K_c^2 - 4r + 8)(\omega_{oc}^2 C_p^\varepsilon)} \tag{1.31}$$

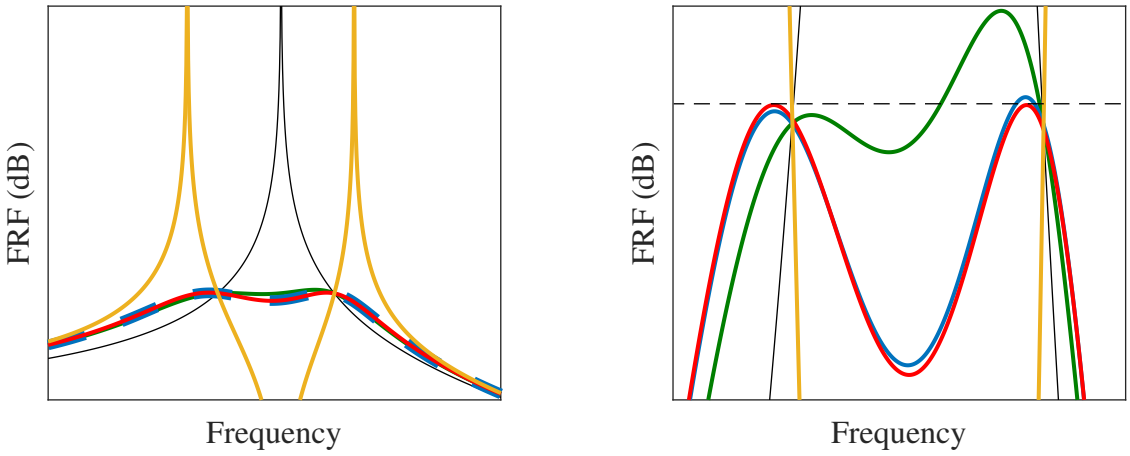

(a) Overview on the first mode. **(b)** Zoom view.

Figure 1.7: FRFs of an SDOF example. Uncontrolled (▬); controlled by an RL shunt tuned according to Hagood and Flotow (▬) [19], Thomas et al. (▪ ▪ ▪) [45] and Soltani et al. (▬) [47] (maximum peak amplitude in (▪ ▪ ▪)). (▬) corresponds to last case with $R = 0$.

and the optimal shunt resistance

$$R_{opt,resistive-inductive} = \frac{2\sqrt{2(K_c^2+1)[27K_c^4 + K_c^2(80-48r) - 64(r-1)]}}{(\omega_{oc}C_p^{\varepsilon})(5K_c^2+8)\sqrt{3K_c^2-4r+8}} \,. \tag{1.32}$$

The tuning rules presented in [47] build the basis for the developments of this work and have been applied to various shunt damping cases. Using these optimal parameters in the shunt circuit, exact equal peaks can be achieved as shown in Figure 1.7b. In Figure 1.8a, the FRF of a system controlled by an RL shunt designed according to the rules presented in Equations (1.30) - (1.32) is now compared to that of an SDOF system with an R shunt (cf. Equation (1.25)). A significantly greater amplitude reduction can be expected with an RL shunt, owing to the presence of two damped resonant peaks instead of one to which the remaining mechanical energy can be divided. However, as depicted in Figure 1.8b, the shunt performance is sensitive to variations of the shunt parameters, particularly to variations of L. A small change of 5 % of the inductance value can already cause a strong imbalance of the two resonance peaks and a detuning of the shunt. From a practical point of view, this means that great care must be taken to measure and identify the host system parameters, namely ω_{oc}, ω_{sc}, and C_p^{ε}.

1.4 Piezoelectric digital vibration absorbers

Although the use of piezoelectric RL shunt circuits represents an interesting damping solution, there exist limitations in the practical application. Recalling Equation (1.29) and considering the fact that capacitance values of piezoelectric patches are usually of the order of a few tens of nanofarad (nF) we see that high inductance values are needed to target low frequencies. These can easily exceed one Henry (H). Commercially available

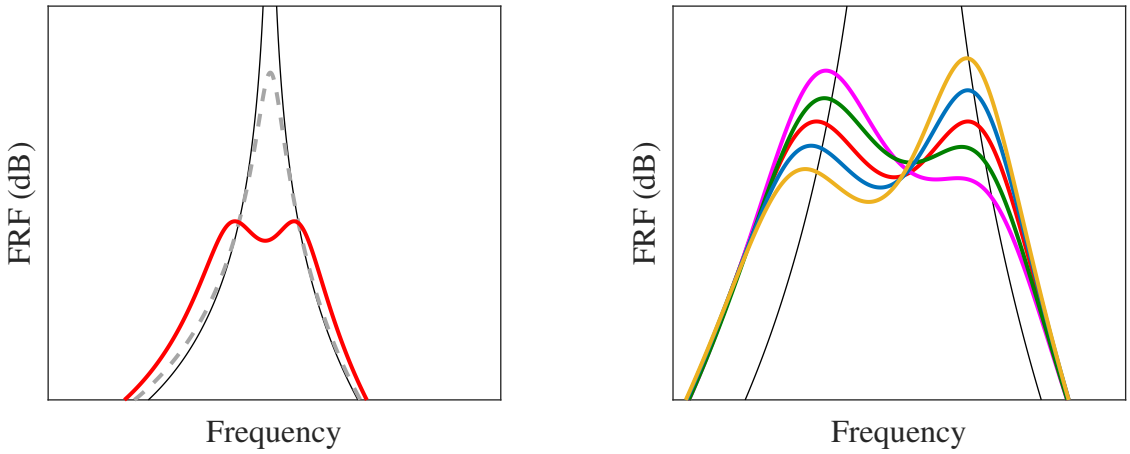

(a) Overview on the first mode. **(b)** Zoom view.

Figure 1.8: FRFs of an SDOF example. Uncontrolled (▬); controlled by an R shunt tuned according to [45] (▪ ▪ ▪); controlled by an RL shunt tuned according to [47] with $L = L_{opt}$ (▬), $L = 0.95L_{opt}$ (▬), $L = 0.975L_{opt}$ (▬), $L = 1.025L_{opt}$ (▬) and $L = 0.95L_{opt}$ (▬).

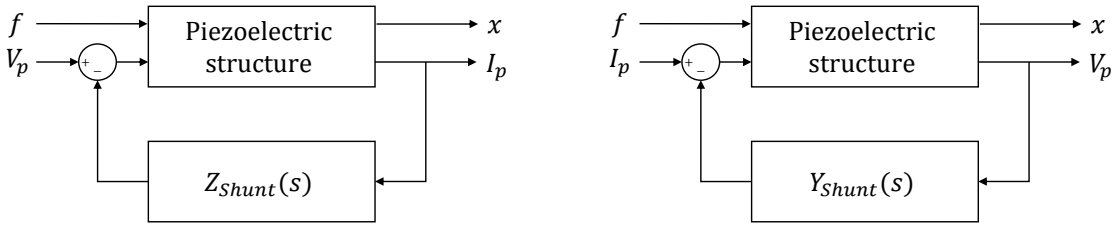

(a) **(b)**

Figure 1.9: Feedback formulation of a (a) shunt impedance, or (b) shunt admittance acting on a piezoelectric structure.

inductors rarely meet these requirements so that other solutions such as in-house designs [49, 50] need to be considered. However, if toroidal inductors are used, they are accompanied by practical difficulties such as winding resistances and capacitances, a temperature dependence and bulky dimensions [51]. An alternative is a synthetic inductor built from a gyrator and a capacitor [51–53]. Usually, these synthetic inductor elements are smaller in size but the gyrator consists of operational amplifiers (OpAmps) that need to be powered. In general, using analog electrical elements, the electrical shunt circuits can often become considerably large and cumbersome, particularly when multiple modes are targeted. In addition, values of analog components cannot be altered easily.

A shunt impedance Z_{Shunt} (or admittance Y_{Shunt}) acting on a piezoelectric structure can be seen as a feedback [54] as it is displayed in Figure 1.9. In the case of a shunt impedance, the piezoelectric transducer is sensing a current I_p to then act on the structure via a voltage V_p. The shunt transfer function defines the relation between a measured output and the imposed input and it thus functions as a controller. We build the open-loop by means of the current measured by the piezoelectric transducer and the voltage defined by this controller function. Thus, the plant is defined as the transfer function between these two

signals, when the external forcing f is set to zero. By looking at the problem from a control engineering point of view, it seems natural that the realization of the controller is not necessarily limited to an analog realization of an electrical circuit. Addressing the aforementioned problems that analog shunt circuits often pose, Fleming et al. proposed to synthesize not only the inductive part digitally but the entire shunt impedance [26]. This so-called synthetic impedance is a two-terminal device that is imposing any desired relation between the voltage V_p and the current I_p by simulating it in real time in a digital signal processing unit. A digital implementation of the shunt transfer function offers the user the possibility to emulate even sophisticated circuits and the shunt parameters can be easily adjusted to mistuning or changes in the host system. Synthetic impedances have already proven useful in various works. In [55], a multimodal shunt impedance was implemented digitally as a feedback controller. Giorgio et al. exploited a synthetic impedance for the realization of electrical networks to attenuate modes of mechanical structures by connecting multiple piezoelectric transducers to the network [56, 57]. Rosi et al. aimed for the attenuation of sound radiation of thin plates, also using a variety of patches together [58, 59]. Matten et al. implemented an R shunt on a plate structure with a synthetic impedance and discussed the technological constraints that may appear with a discretized shunt transfer function [60]. In [61], digital piezoelectric shunt controllers were used to create band gaps on a beam structure in order to damp their structural vibrations. In [62], Dal Bo et al. emulated multimodal shunt circuits in a digital controller that were optimized to consist of few elements. In order to mitigate the vibrations of nonlinear structures, Raze et al. synthesized a nonlinear shunt circuit and emphasized the benefits of flexibility using digital controllers [63]. In [30], the use of a piezoelectric DVA was discussed for different circuit designs and experimentally demonstrated on a beam structure. Using multiple DVAs on the same beam and aiming to target multiple modes simultaneously, Raze et al. realized electrical shunt networks exhibiting similar resonance frequencies as the host structures [64] and piezoelectric shunts tuned with a sequential procedure [65]. In this thesis, piezoelectric DVAs are exploited to operate on more complex mechanical structures. In the following sections, we will present their working principle and discuss their practical realization.

1.4.1 Working principle

As illustrated in Figure 1.10, a DVA consists of an analog board and a digital unit. The piezoelectric patch, acting both as a sensor and actuator, sends a voltage V_p to the DVA when activated by the vibrations of the host structure. This voltage signal is then received by the analog board of the DVA. In order to comply with the voltage limits of the digital unit and to avoid saturation of the OpAmps, the voltage signal needs to be scaled down, here by a factor α_{DVA} (cf. Figure 1.11). The signal can then be converted via an analog-to-digital-converter (ADC) and the desired input-output (I/O) relation is set in the digital unit. In this work, a dSPACE MicroLabBox [66] served as the digital unit and a piezoelectric shunt admittance Y_{Shunt} was imposed as the desired I/O. This function can be freely chosen and easily changed which represents a main advantage of a digital implementation. In addition, a controller gain g is added here to ensure that the DVA correctly emulates the desired shunt admittance. The signal is then sent from the digital unit to the analog board via a digital-to-analog-converter (DAC). Before the

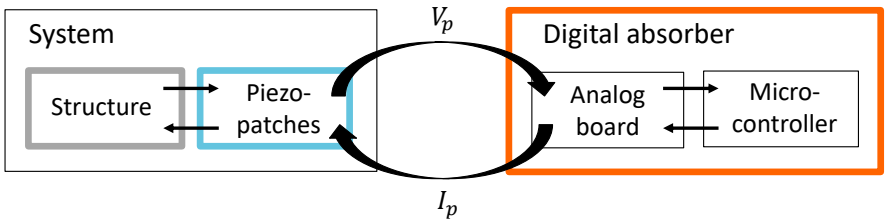

Figure 1.10: Schematic representation of a DVA acting on a structure via piezoelectric patches.

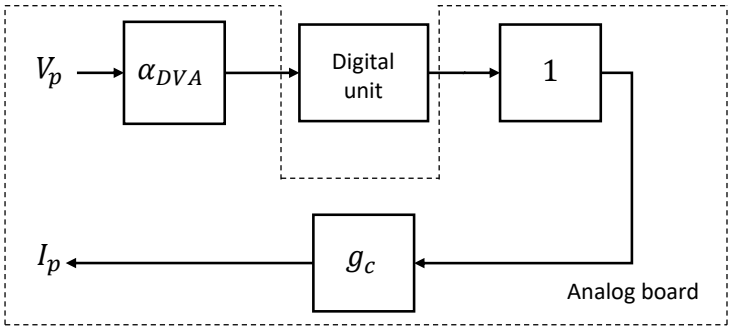

Figure 1.11: Schematic representation of the main operation steps of the DVA.

voltage is sent back to the transducer, it is multiplied by the current source gain g_c so that a current ($\dot{q}_p$) is sent to the piezoelectric patch and acts on the host structure. The I/O relation in the Laplace domain can then be expressed as:

$$I_p(s) = g\alpha_{DVA} g_c Y_{Shunt}(s) V_p(s) \ . \tag{1.33}$$

Since the desired relation is $I_p(s)/V_p(s) = Y_{Shunt}(s)$, we deduce

$$g = \frac{1}{g_c \alpha_{DVA}} \ . \tag{1.34}$$

1.4.2 Practical DVA realizations used in this work

In this work, experimental campaigns using DVAs were conducted on two bladed structures to damp their structural vibrations. The DVA design used in this context is presented in the following. It was based on Howland's current source [67] and schematized in Figure 1.12. High piezoelectric voltages are reduced by the factor α_{DVA} by means of the resistors $R_{p,1}$ and $R_{p,2}$:

$$\alpha_{DVA} = \frac{R_{p,2}}{R_{p,1} + R_{p,2}} \ . \tag{1.35}$$

The input and output voltages of OpAmp1, given by

$$V_{ADC} = \alpha_{DVA} V_p \ , \tag{1.36}$$

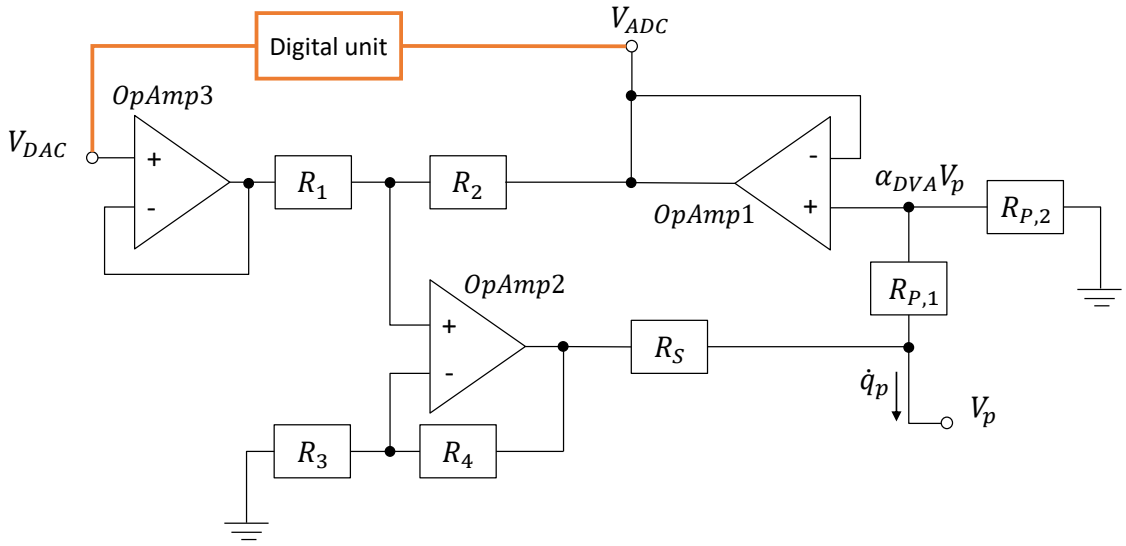

Figure 1.12: Circuit diagram of the DVA.

are identical and are fed to the ADC. We introduce an amplification gain

$$\beta = 1 + \frac{R_4}{R_3} \tag{1.37}$$

and an attenuation gain

$$\gamma = \frac{R_1}{R_1 + R_2}. \tag{1.38}$$

Based on the ideal OpAmp assumption [67], we can demonstrate that the injected current is a function of the DAC voltage as well as the load voltage given by the following relations:

$$\dot{q}_p = \frac{\beta(1-\gamma)}{R_s} V_{DAC} + \frac{(\alpha_{DVA}\beta\gamma - 1)(R_{p,1} + R_{p,2}) - R_s}{R_s(R_{p,1} + R_{p,2})} V_p = g_c V_{DAC} + \delta_c V_p \ . \tag{1.39}$$

Ideally, δ_c should be zero so that the current is only driven by V_{DAC}. Hence, the resistances are chosen to closely approach $\delta_c = 0$ but it is generally not possible to fulfill this condition exactly. Section 1.5 will discuss how this imperfection can be accounted for.

1.4.3 Practical applications of the DVA on bladed structures

The above presented DVA design is applied in this thesis for the damping attenuation of two bladed structures, namely of a bladed rail and a BluM. Both structures exhibit multiple piezoelectric patches, each of which was connected to a DVA mimicking a shunt circuit. The design allows for a current-driven control via each piezoelectric transducer, even if they have a common electrode which distinguishes them from those in e.g. Fleming's work [68]. An interaction between the DVAs, when multiple of them are used simultaneously, can be prevented by the fact that their current is injected via the electrode of the transducer that is not connected to a mutual ground. Five DVAs were realized on breadboards for the experimental setup with a bladed rail. The prototype of one of these

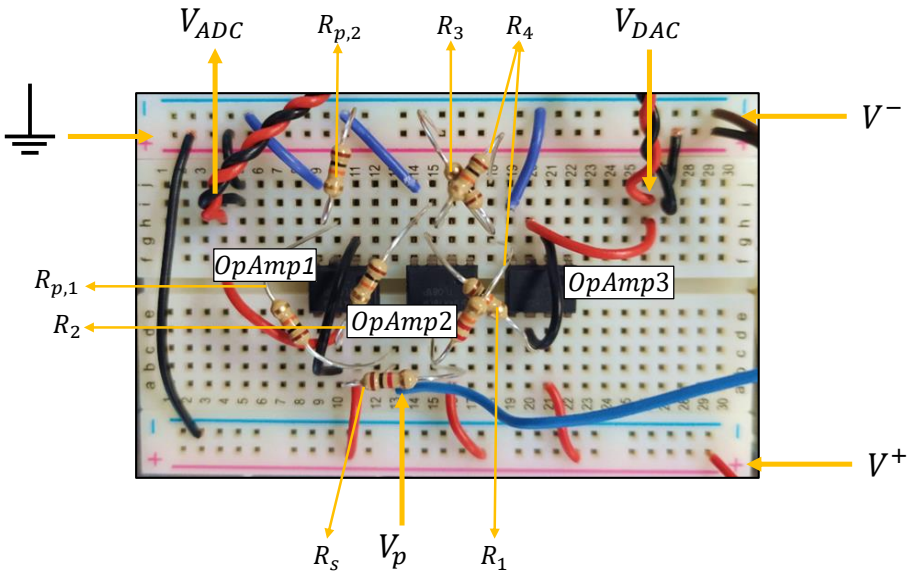

Figure 1.13: DVA prototype used in the experimental campaign on a bladed rail structure.

Resistor	Resistance [Ω] (bladed rail setup)	Resistance [Ω] (BluM setup)
R_1	10000	10000
R_2	10000	10000
R_3	10000	10000
R_4	34000	115000
R_s	2000	2610
$R_{p,1}$	10000	49900
$R_{p,2}$	10000	10000

Table 1.1: Resistances of the DVAs used in the experimental campaigns.

DVAs is displayed in Figure 1.13. TL081 OpAmps from Texas Instruments were used with the resistor values displayed in Table 1.1.

For the attenuation of the structural vibrations of a BluM, the DVA design was realized on printed circuit boards (PCB) (cf. Figure 1.14). The advantage of these PCBs is that the connections are properly fixed and the PCBs are more compact than a breadboard (44 mm × 43 mm). TI OPA445 and two additional power supply decoupling capacitors between the ground and both V^+ and V^- were used in this realization. The respective values for the resistances differ from the ones used in the bladed rail setup and are presented in the right column of Table 1.1. We note that the DVA design for the BluM was chosen with a so-called fail-safe solution, which means that in case of a power supply failure, the total resistance of the circuit forms an R shunt tuned toward the mean frequency of the first mode family of the structure. With this fail-safe solution integrated in the DVAs, a reduction of resonance peaks by about 1 dB is guaranteed even in the fully passive case.

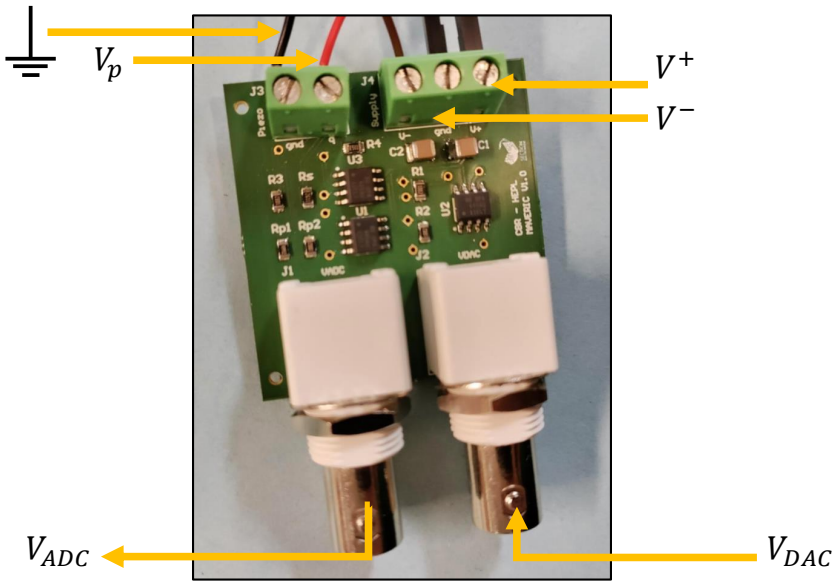

Figure 1.14: DVA on a printed circuit board design used for the experimental BluM structure.

1.5 Tuning the DVA accounting for imperfections in its electrical circuit

We now show that the transfer function implemented in the DVA can be tuned solely using the transfer function between V_{DAC} and V_{ADC}, which can easily be measured experimentally by the digital unit. Neither a numerical model of the structure to be controlled nor a detailed knowledge of the electrical circuit of the DVA are required by this tuning approach. It is particularly convenient for dealing with the complex systems treated in this thesis. In the ideal case ($\delta_c = 0$), the transfer function of the electromechanical system from V_{DAC} to V_{ADC} reads

$$Z_{p,EM}(s) = \frac{V_{ADC}}{V_{DAC}} = \frac{g_c \alpha_{DVA} V_p}{\dot{q}_p} = \frac{g_c \alpha_{DVA}}{s C_p(s)} \,. \tag{1.40}$$

This relation is illustrated in a block diagram from V_{DAC} to V_{ADC} in Figure 1.15. We observe that this plant transfer function is naturally related to the dynamic capacitance introduced in Section 1.2.3 and therefore contains all the necessary information to tune the shunt. If one were to identify a dynamic capacitance (or elastance) from the measured plant transfer function in this ideal case, one would find the same short- and open-circuit resonance frequencies and a scaled piezoelectric capacitance ($C_p^\varepsilon / g_c \alpha_{DVA}$).

Using this scaled capacitance in the tuning rules outlined in Section 1.3.2, one observes that the scaled parameters R and L would be multiplied by $g_c \alpha_{DVA}$. The shunt impedance and admittance would likewise be scaled by $g_c \alpha_{DVA}$ and $1/(g_c \alpha_{DVA})$, respectively. As discussed at the end of Section 1.4.1, the implemented transfer function (i.e. the term $g Y_{Shunt}(s)$ in Equation (1.33)) can thus be set equal to this scaled admittance to guarantee that the desired shunt impedance is emulated. In summary, $C_p(s)$, g_c and α_{DVA} do not need to be known individually, but their combination as the scaled piezoelectric

capacitance suffices to tune the transfer function implemented in the DVA. This scaled capacitance is directly identifiable from the measured plant transfer function. Conveniently, this practical rule turns out to be true as well when more complex shunts are used such as the ones presented in Chapter 2.

We now look in more detail at the inevitable case of the presence of imperfections in the resistances on the analog board. They can be interpreted as a conductance δ_c that acts in parallel with the dynamic capacitance as illustrated in Figure 1.16. Indeed, from Equations (1.35) and (1.39),

$$\frac{\dot{q}_p}{V_p} = sC_p(s) = g_c\alpha_{DVA}\frac{V_{DAC}}{V_{ADC}} + \delta_c \tag{1.41}$$

from which we deduce

$$\frac{V_{ADC}}{V_{DAC}} = \frac{g_c\alpha_{DVA}}{sC_p(s) - \delta_c} , \tag{1.42}$$

which corresponds to the situation depicted in Figure 1.15. We observe that this conductance plays the role of a constant in the dynamic impedance function and dominates the FRF at low frequencies. The effect that this conductance has on the FRF is the creation of a real pole, causing a change of slope of the transfer function for small s. This is illustrated on a simple example in Figure 1.17 where the FRF with $\delta_c = 0$ is compared to an FRF with $\delta_c \neq 0$. The ideal impedance function would behave as $\frac{1}{s}$ until the possible occurrence of a mechanical mode. In practice, this simple pole can be detected applying system identification methods on the measured dynamic impedance function. In particular, from Equation (1.16), the static value of the plant transfer function is $\frac{g_c\alpha_{DVA}}{\delta_c}$. It can therefore be identified, and the ideal-case plant transfer function can be retrieved as

$$\frac{g_c\alpha_{DVA}}{sC_p(s)} = \frac{1}{\frac{V_{DAC}}{V_{ADC}} + \frac{\delta_c}{g_c\alpha_{DVA}}} , \tag{1.43}$$

allowing for a tuning approach of the shunt admittance identical to the ideal case. Indeed, as illustrated in Figure 1.18, the imperfections of the DVA can be counteracted by neutralizing δ_c if the implemented digital transfer function is

$$\frac{V_{DAC}}{V_{ADC}} = Y_{DVA}(s) = \frac{Y_{Shunt}(s)}{g_c\alpha_{DVA}} - \frac{\delta_c}{g_c\alpha_{DVA}} . \tag{1.44}$$

This is confirmed when introducing this relation into Equation (1.39) and using Equation (1.35), we indeed obtain $\frac{\dot{q}_p}{V_p} = Y_{Shunt}(s)$ as desired. Therefore, also in the non-ideal case, it is possible to tune the implemented transfer function using only the measured plant transfer function.

1.6 Discretization of the controller function

Although the shunt circuit that is mimicked in the digital unit works according to a passive control law, instabilities might occur when using digital shunts. This is due to the occurrence of sampling delays introduced by the digital unit: a continuous voltage signal

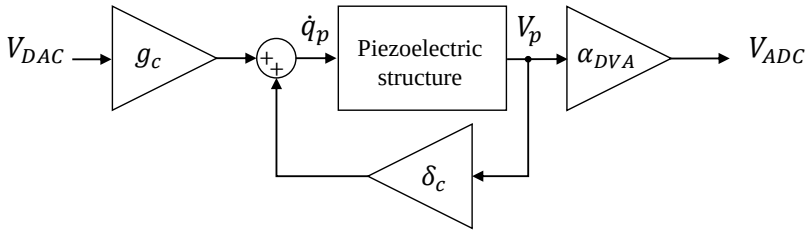

Figure 1.15: Feedback diagram for the measurement of the dynamic impedance with $\delta_c \neq 0$.

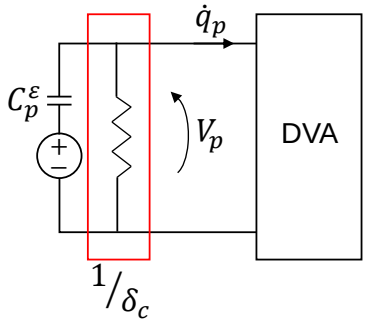

Figure 1.16: Effect of the imperfections of the resistances in the electrical circuit of the DVA. They can be modeled as a conductance δ_c (marked in red) in parallel with the piezoelectric capacitance.

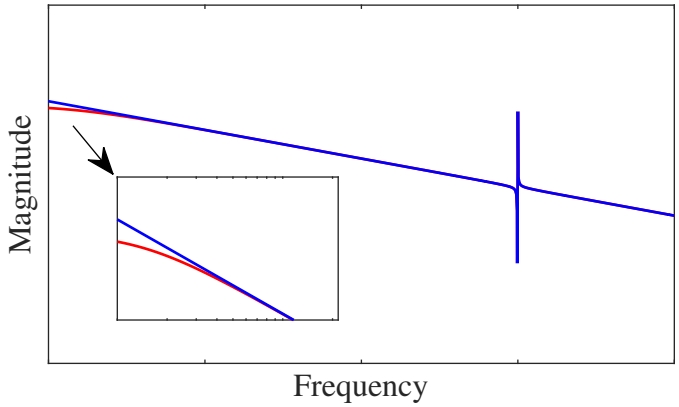

Figure 1.17: FRF example for a dynamic impedance with a perfect realization of the electrical circuit (cf. Equation (1.40))(—) and with imperfections in the resistances (Equation (1.42))(—). The x-axis scale is logarithmic. This example contains one mechanical mode.

is converted to a discrete one via an ADC. For the re-conversion to continuous time, this discrete signal is then held constant for each sampling time τ by a zero-order hold (ZOH), appearing as a staircase in Figure 1.19. An average over this ZOH representation results then in a shift of the initial continuous signal of $\frac{\tau}{2}$, also denoted delay. Hence, due to the ZOH, the continuous transfer function $H(s)$ differs from its discrete counterpart which can be interpreted as the actual transfer function that the controller imposes on the in-

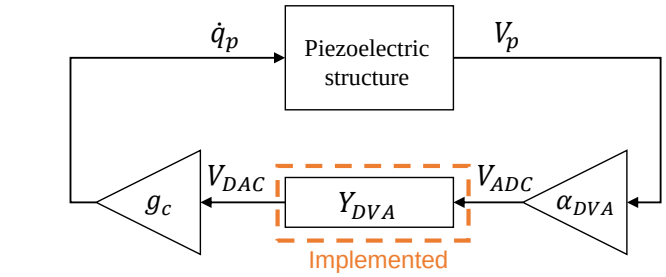

(a) $\delta_c = 0$.

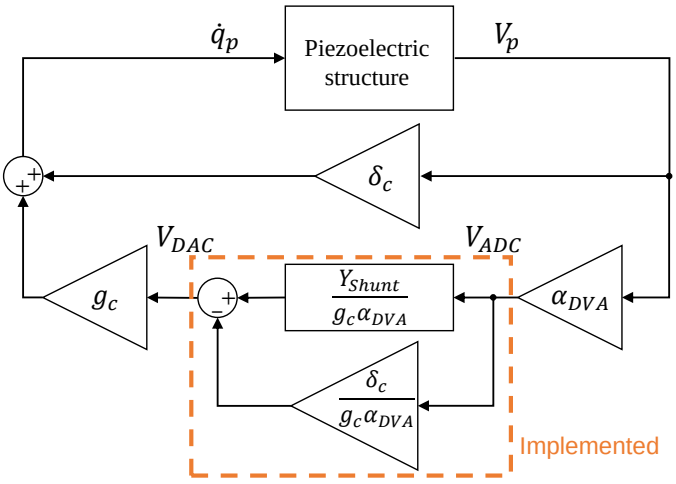

(b) $\delta_c \neq 0$.

Figure 1.18: Feedback diagram for the shunt admittance acting on the electromechanical structure.

put signal. These delay-induced modifications of the output also cause deviations of the closed-loop poles between the discretized and the continuous systems. This is schematically illustrated in Figure 1.20 where the root locus of a shunted controlled closed-loop system is displayed. The ideal poles, under the assumption that the delays are absent, are marked with an $\times$. The root locus is then displayed in red as a function of increasing τ. For a certain value of τ, the changes in the imposed transfer function can become critical for the integrity of the system: the poles cross the imaginary axis and shift from the left half of the s-plane to the right side so that the closed-loop system becomes unstable [69].

Delay-induced instabilities are a well-known problem in the field of control engineering and can occur if the discretization process is not performed accurately. Considering the sampling period $\tau = \frac{1}{f_s}$, the problem can be avoided by choosing f_s high enough to keep the delays small, as is often done in practice. However, the coupling factors in the piezoelectric shunt attenuation are naturally relatively small, so that the poles of the control loop are already close to the imaginary axis in the s-plane representation. Therefore, even small shifts of these poles can lead to a crossing of this axis and, consequently, to system instability. Especially when high frequencies are targeted, the hardware can become a limiting factor for the sampling frequency so that this parameter cannot be selected arbi-

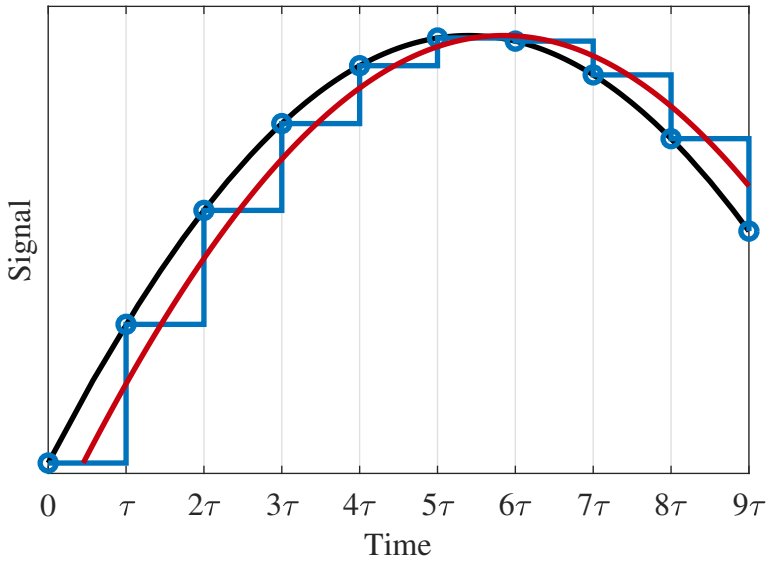

Continuous signal (▬), ZOH representation (▬) and average of the ZOH representation (▬) [30].

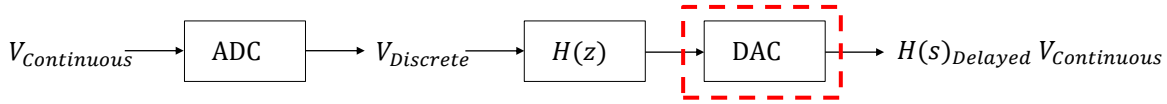

Figure 1.19: Schematical representation of the conversion of a continuous signal to a discrete signal and back.

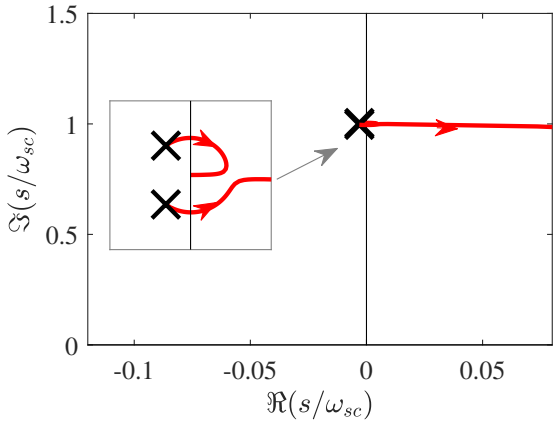

Figure 1.20: Root locus as a function of τ of a closed-loop system presented in the s-plane. The $\times$ mark the ideal poles of the system, assuming that $\tau = 0$ [30].

trarily high. In these cases, it is important to pay special attention to the discretization process.

The problem of instabilities was already tackled in [30] and [70] where a correction procedure was proposed anticipating the delay effects and modifying the shunt circuit admittance accordingly in order to counteract them. To this end, the continuous shunt admittance is first expressed as a rational function

$$Y_{Shunt}(s) = \frac{\sum_{m=0}^{N_s-1} b_m s^m}{\sum_{n=0}^{N_s-1} a_n s^n} \ , \tag{1.45}$$

with N_s being the number of poles in the shunt transfer function. The poles p_k of the ideal closed-loop when the system is shunted with this transfer function are then obtained by looking at the characteristic equation. In a next step, the expression for $Y_{Shunt}(s)$ is amended by the modification factors δ_{a_n} and δ_{b_m} and so that it reads

$$\tilde{Y}_{Shunt}(s) = \frac{\sum_{m=0}^{N_s} b_m(1+\delta_{b_m}) s^m}{\sum_{n=0}^{N_s} a_n(1+\delta_{a_n}) s^n} \ . \tag{1.46}$$

The purpose of these modification factors is to counteract the delay-induced modifications of the closed-loop. At this step, they are unknown and need to be defined. Knowing τ, the impact that the delays have on the closed-loop system controlled by $\tilde{Y}_{Shunt}$ can be anticipated. Comparing the closed-loop expression for the ideal case without delays and the case where delays are present, the following relationship is found:

$$\tilde{Y}_{Shunt}(p_k)\frac{1-e^{-\tau p_k}}{\tau p_k} = Y_{Shunt}(p_k) \ , \tag{1.47}$$

where p_k is representing a pole of the ideal closed-loop that should be maintained. In other words, the method looks for an expression for $\tilde{Y}_{Shunt}$ that allows the poles of the modified control loop to be the same as for the nominal, ensuring stability. This is done by forming a linear system of equations for $k = 1, ..., K$ based on Equation (1.47) and solving it for δ_{a_n} and δ_{b_m}. The modified shunt admittance $\tilde{Y}_{Shunt}(s)$ is then discretized with Tustin's method and implemented in the controller. This paragraph only provides a brief overview over the method proposed by Raze et al. [30, 70]. We refer the reader to the references for full mathematical details.

Different to the procedure described above, in this thesis we ensure closed-loop stability thanks to a novel procedure to *discretize* the shunt transfer function. It can be considered as a continuation of the work in [30] and [70], however, the focus is different: as explained before, in [30, 70], the shunt admittance was tuned and corrected in the continuous time domain to anticipate phase lags and discretized afterwards. In this work, the discrete shunt admittance is tuned directly using a pole-placement technique taking the ZOH discretization of the plant transfer function into account at first hand. The experimental campaigns discussed later in this mansucript confirmed that it is crucial to pay special attention to the discretization of the shunt admittance.

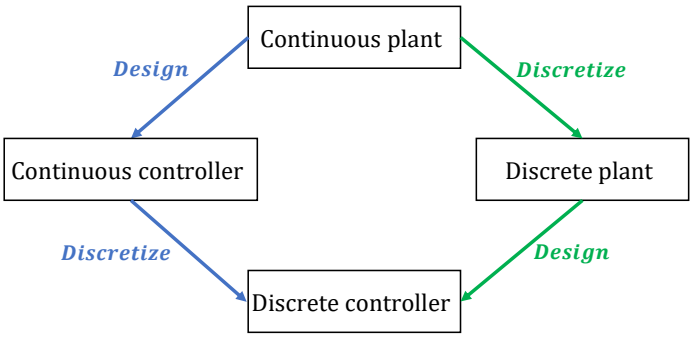

Figure 1.21: From a continuous plant to a discrete controller – two classic approaches [71].

1.6.1 From a continuous plant to a discrete controller design

To obtain a discrete controller function two classical paths can be followed, as shown in Figure 1.21. One could start with a continuous plant transfer function and design an ideal controller for it. This continuous controller is then discretized eventually. However, due to the discretization process, the discrete counterpart will differ from the desired continuous design and might even cause instabilities in the closed-loop system. Another option is to choose a controller based on the discrete plant transfer function. Here, one can take advantage of the fact that the plant and its ZOH discretization are known and include this knowledge in the controller design. The controller parameters are then directly chosen by means of the discrete plant. However, this controller will differ from an ideal one.

In this thesis, a method that attempts to combine the best of both worlds is presented: first, an optimal expression of the desired closed-loop transfer function is formed in continuous time and shunt parameters are derived. Then, in a second step, the closed-loop transfer function is formulated in discrete time consisting of discretizations of the plant transfer function and a discrete shunt admittance. This formulation enables us to find a discrete shunt admittance which ensures that the poles of discrete closed-loop transfer function are the discrete equivalent of the continuous one. The discretization procedure will be described in the following sections.

Formulation as a feedback problem

In Figure 1.22, the feedback presentation of a piezoelectric structure controlled by a shunt admittance Y_{Shunt}[†] from Figure 1.9 is now reconsidered for the discrete case using a discretized shunt admittance $Y_{Shunt}(z)$. In the following mathematical expressions, it is implied that a transfer function with the variable z represents a discretized version of its associated continuous-time transfer function.

In a first step, we simplify the model by only considering the electrical part of the piezoelectric structure and neglecting its mechanical properties, assuming that the structure is blocked and using C_p^ε. The plant of the feedback problem then becomes Z_p, namely the

[†]For the sake of simplicity and generality, Y_{Shunt} is herein considered instead of Y_{DVA}, neglecting the characteristics of the particular DVA realization in this work.

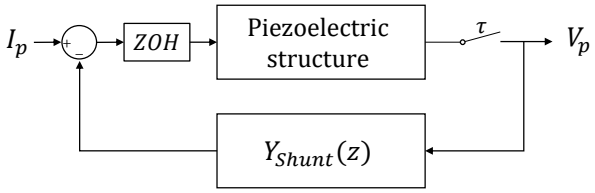

Figure 1.22: Feedback diagram of a discrete shunt admittance acting on a piezoelectric structure.

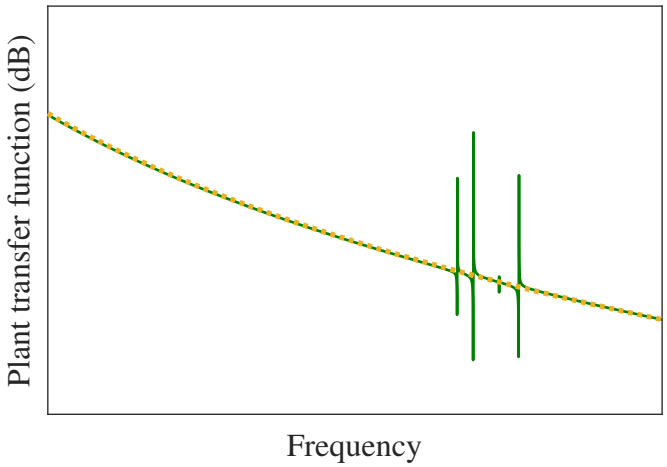

Figure 1.23: Example for a plant transfer function; (a) simplified, only taking the electrical part Z_p of the system into account (▬) and (b) considering the full electromechanical system $\frac{1}{sC_p(s)}$ (▬).

piezoelectric impedance. Its inverse is the piezoelectric admittance

$$Y_p(s) = Z_p^{-1}(s). \tag{1.48}$$

The simplification step is made based on the assumption that the electromechanical resonances are somewhat marginal compared to the general trend of the piezoelectric impedance whose amplitude is rapidly decreasing with increasing s:

$$Z_p(s) = \frac{1}{sC_p^{\varepsilon}} \,. \tag{1.49}$$

This trend is illustrated in Figure 1.23 for Equation (1.49) above and a multimodal example. By taking only the electrical part of the piezoelectric structure into account, a considerably simpler feedback problem can be formulated. It will be demonstrated later on an example that this assumption is justified by showing that the influence of the mechanical part does not have a significant impact on the performance of the shunt. The simplified feedback problem is illustrated in Figure 1.24a, where a discrete shunt admittance is acting on the piezoelectric impedance.

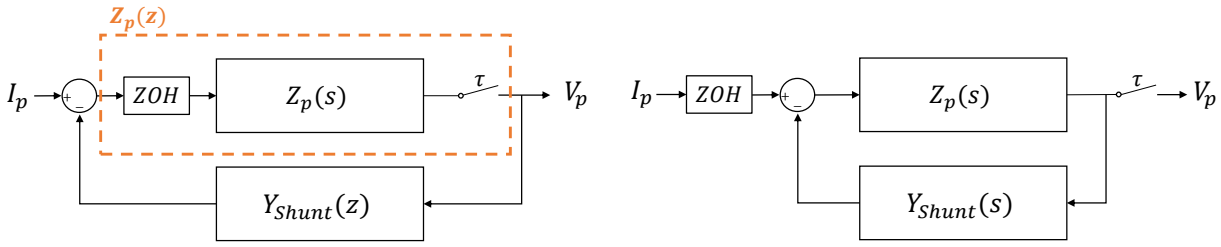

(a) **(b)**

Figure 1.24: The simplified feedback problem.

Following the left path of Figure 1.21, ideal shunt parameters are then found for a continuous controller. The characteristic equation for this new feedback formulation reads [72]

$$1 + Z_p(s)Y_{Shunt}(s) = 0 \ . \tag{1.50}$$

By premultiplying Equation (1.50) with Equation (1.48), we obtain the following expression for the roots of the characteristic equation:

$$Y_p(s) + Y_{Shunt}(s) = 0 \ . \tag{1.51}$$

This expression corresponds to the zeros of Norton's equivalent admittance [36] of a piezoelectric capacitance connected to a shunt circuit

$$Y_N(s) = Y_p(s) + Y_{Shunt}(s) \ . \tag{1.52}$$

This view allows us to express separately the different parts of the feedback problem, namely the shunt admittance and the plant transfer function, as it will be outlined below. The closed-loop transfer function can be obtained by forming the inverse of Equation (1.52):

$$\frac{1}{Y_N(s)} = \frac{Z_p(s)}{1 + Z_p(s)Y_{Shunt}(s)} \ . \tag{1.53}$$

If a DVA is used, the discrete-time transfer function of the closed control loop becomes

$$\frac{1}{Y_N(z)} = \frac{Z_p(z)}{1 + Z_p(z)Y_{Shunt}(z)}, \tag{1.54}$$

where $Z_p(z)$ is the ZOH-discretized counterpart of $Z_p(s)$ denoted by $\mathrm{ZOH}\{\cdot\}$, i.e., it represents the relation between I_p driven by a ZOH and the sampled V_p and is given by

$$Z_p(z) = \mathrm{ZOH}\{Z_p(s)\} \tag{1.55}$$

and $Y_{Shunt}(z)$ corresponds to the I/O relation that is imposed by the DVA. This expression is equivalent to the diagram in Figure 1.24a, as marked in orange.

General philosophy of the proposed discretization method

There exist on-hand methods to discretize a transfer function such as Tustin's method, the pole-zero matching technique or impulse-invariant mapping [69]. While these discretization methods might lead to good approximations of a discrete equivalent of $Y_{Shunt}(s)$, they cannot automatically ensure stability. In particular, if $\mathrm{D}\{\cdot\}$ denotes the selected discretization method (among any of the three aforementioned methods), one would have $Y_{Shunt}(z) = \mathrm{D}\{Y_{Shunt}(s)\}$, and the following inequality is generally true:

$$\mathrm{ZOH}\left\{\frac{1}{Y_N(s)}\right\} \neq \frac{\mathrm{ZOH}\{Z_p(s)\}}{1+\mathrm{ZOH}\{Z_p(s)\}\,\mathrm{D}\{Y_{Shunt}(s)\}}, \tag{1.56}$$

where the right-hand side represents the closed-loop transfer function of the discrete system (see Figure 1.24a). Hence, the dynamics of the discrete closed-loop system may significantly differ from the continuous one, which we assume satisfactorily represented by the left-hand side $\mathrm{ZOH}\left\{Y_N^{-1}(s)\right\}$ in this work. More problematically, if $Y_N^{-1}(s)$ has stable continuous closed-loop poles, $\mathrm{ZOH}\left\{Y_N^{-1}(s)\right\}$ is guaranteed to have stable discrete poles, but this does not extend to the discrete closed-loop system due to the inequality.

The proposed discretization method precisely aims at turning (1.56) into an equality. More specifically, it is sought to find $Y_{Shunt}(z)$ such that

$$\mathrm{ZOH}\left\{\frac{1}{Y_N(s)}\right\} := \frac{1}{Y_N(z)} = \frac{\mathrm{ZOH}\{Z_p(s)\}}{1+\mathrm{ZOH}\{Z_p(s)\}\,Y_{Shunt}(z)} := \frac{Z_p(z)}{1+Z_p(z)Y_{Shunt}(z)}, \tag{1.57}$$

i.e.,

$$Y_{Shunt}(z) = \frac{Z_p(z)Y_N(z)-1}{Z_p(z)}. \tag{1.58}$$

Equation (1.57) implies that the representations in Figures 1.24a and 1.24b are equivalent.

Classical discretization methods yield a discretized shunt admittance which approximate $Y_{Shunt}(s)$ well [69]. The proposed discretization method distinguishes itself from them by the fact that it also accounts for the plant transfer function $Z_p(z)$. As a consequence, owing to Equation (1.57), the discrete closed-loop transfer function is closer to the desired continuous one, and the discrete system has guaranteed stability.

The remainder of this section shows how to derive the coefficients of the transfer function $Y_{Shunt}(z)$ based on Equation (1.57) and demonstrates that the approach is well posed.

Discrete piezoelectric impedance

The ZOH discretization of Z_p, relating I_p and V_p that is sampled at multiples of τ, reads [69]

$$Z_p(z) = \mathrm{ZOH}\{Z_p(s)\} = \mathrm{ZOH}\left\{\frac{1}{sC_p^\varepsilon}\right\} = \frac{z-1}{z}\mathcal{Z}\left\{\frac{1}{s^2C_p^\varepsilon}\right\} = \frac{\tau}{C_p^\varepsilon}\frac{1}{z-1}\,. \tag{1.59}$$

$\mathcal{Z}$ is a shortcut notation denoting the z-transform of the sampled inverse Laplace transform.

Discrete shunt admittance

To be able to relate Equations (1.53) and (1.54), we express the discrete shunt admittance as a rational transfer function of the variable z by

$$Y_{Shunt}(z) = \frac{\sum_{m=0}^{N_s-1} b_m z^m}{\sum_{n=0}^{N_s-1} a_n z^n}, \tag{1.60}$$

where N_s is the number of poles of $Y_N^{-1}(s)$ and corresponds to twice the number of resonances of the electrical circuit. For a simple RL shunt, $N_s = 2$. It will be justified hereafter that the degrees of the numerator and denominator are equal, and consequently $Y_{Shunt}(z)$ represents a proper transfer function.

Discrete Norton's admittance

The ZOH discretization of the inverse of Norton's admittance reads [69]

$$\text{ZOH}\left\{\frac{1}{Y_N(s)}\right\} = \frac{z-1}{z}\mathcal{Z}\left\{\frac{1}{sY_N(s)}\right\} . \tag{1.61}$$

To express this relation more explicitly, a partial fraction expansion of $(sY_N(s))^{-1}$ can be obtained as

$$\frac{1}{sY_N(s)} = \sum_{k=1}^{N_s} \frac{r_k}{s-p_k} \tag{1.62}$$

where r_k is the residue of the transfer function $(sY_N(s))^{-1}$ at its pole p_k. Recalling that the z-transform of a transfer function with a simple pole is given by [69]

$$\mathcal{Z}\left\{\frac{1}{s+a}\right\} = \frac{z}{z-e^{-a\tau}}, \tag{1.63}$$

and using the linearity of the z-transform, the ZOH discrete version of Norton's admittance (cf. Equation (1.61)) is eventually obtained as

$$\text{ZOH}\left\{\frac{1}{Y_N(s)}\right\} = (z-1)\sum_{k=1}^{N_s}\frac{r_k}{z-e^{\tau p_k}} = \frac{(z-1)\sum_{k=1}^{N_s} r_k \prod_{i=1,i\neq k}^{N_s}(z-e^{\tau p_i})}{\prod_{k=1}^{N_s}(z-e^{\tau p_k})}. \tag{1.64}$$

At first sight, it may appear that this transfer function has both N_s poles and zeros and is thus not strictly proper. However, it can be shown that the numerator is actually of degree $N_s - 1$. Indeed, from Equations (1.52) and (1.62):

$$\frac{1}{sY_N(s)} = \frac{1}{s^2C_p^\varepsilon + sY_{Shunt}(s)} = \sum_{k=1}^{N_s}\frac{r_k}{s-p_k} . \tag{1.65}$$

To find the value of the sum of residues, we take the limit of $Y_N^{-1}(s)$ for $s \to \infty$,

$$\lim_{s\to\infty} \frac{1}{sC_p^\varepsilon + Y_{Shunt}(s)} = \sum_{k=1}^{N_s} r_k \ , \tag{1.66}$$

and analyze the asymptotic properties of Y_{Shunt}. Since it is the admittance of a passive circuit, it is a positive-real transfer function (cf. Section 1.3.1), and the degrees of its numerator and denominator cannot differ by more than one. Assuming that Y_{Shunt} is proper, meaning that the degree of the numerator is smaller than or equal to the one of the denominator, it becomes negligible in front of the piezoelectric admittance sC_p^ε when $s \to \infty$. In the opposite case, the admittance behaves asymptotically as cs where c is a constant. This constant must be positive because Y_{Shunt} is positive-real. In both cases, the left-hand side of this equation tends to zero and thus

$$\sum_{k=1}^{N_s} r_k = 0. \tag{1.67}$$

Hence, the coefficient associated with z^{N_s} in the numerator of Equation (1.64) vanishes, making this numerator a polynomial of degree $N_s - 1$. The discrete version of Norton's admittance thus has $N_s - 1$ zeros and N_s poles.

Discrete feedback problem

Using Equations (1.54), (1.59) and (1.60), the inverse of Norton's admittance can alternatively be expressed as

$$\frac{1}{Y_N(z)} = \frac{\dfrac{\tau}{C_p^\varepsilon} \displaystyle\sum_{n=0}^{N_s-1} a_n z^n}{(z-1) \displaystyle\sum_{n=0}^{N_s-1} a_n z^n + \frac{\tau}{C_p^\varepsilon} \sum_{m=0}^{N_s-1} b_m z^m} \ . \tag{1.68}$$

Since the numerator and denominator are of respective degrees $N_s - 1$ and N_s, using an admittance of the form of Equation (1.60) gives $N_s - 1$ zeros and N_s poles. Consequently, using a discrete admittance of the form of Equation (1.60) yields a transfer function similar to that given in Equation (1.64) in terms of number of poles and zeros.

Tuning of the shunt admittance

We now aim to enforce Equation (1.57) by equating Equations (1.64) and (1.68). The zeros $z_{z,k}$ of $Y_N^{-1}(z)$ are computed from Equation (1.64) and, from Equation (1.68), they must satisfy

$$\sum_{n=0}^{N_s-1} a_n z_{z,k}^n = 0, \qquad \forall k \in [1, \cdots, N_s - 1] \, . \tag{1.69}$$

Without loss of generality, these $N_s - 1$ equations can be solved for the N_s coefficients a_n by imposing

$$a_{N_s-1} = 1. \tag{1.70}$$

In this way, the poles of Norton's admittance are kept and a stable shunt admittance can be guaranteed. The poles $z_{p,k}$ of $Y_N^{-1}(z)$ are computed from Equation (1.64) and, from Equation (1.68), they must satisfy

$$(z_{p,k}-1)\sum_{n=0}^{N_s-1} a_n z_{p,k}^n + \frac{\tau}{C_p^\varepsilon}\sum_{m=0}^{N_s-1} b_m z_{p,k}^m = 0. \qquad \forall k \in [1,\cdots,N_s] \tag{1.71}$$

These N_s equations form a linear system that can then be solved numerically for the N_s coefficients b_m.

In summary, the tuning procedure follows:

1. Tuning of the continuous shunt admittance $Y_{Shunt}(s)$ and computation of Norton's admittance $Y_N(s) = sC_p^\varepsilon + Y_{Shunt}(s)$ (or direct tuning of Norton's equivalent admittance $Y_N(s)$).
2. Computation of the ZOH discretization of the inverse of $Y_N(s)$.
3. Computation of the poles $z_{p,k}$ and zeros $z_{z,k}$ of the discrete inverse Norton's admittance.
4. Determination of the coefficients of the discrete shunt admittance with Equations (1.69), (1.70) and (1.71).

A key advantage of this tuning and discretization procedure is that the closed-loop system stability is preserved due to that fact that the poles of the closed-loop transfer function are given by $z_{p,k} = e^{\tau p_k}$, which are stable if the original closed-loop poles of the continuous system p_k are stable.

1.6.2 Demonstration of the discretization procedure

The discretization effects of the shunt transfer function are now demonstrated on a fictitious SDOF example with the parameters $\omega_{oc} = 50\,\text{rad}$, $C_p^\varepsilon = 1$ and $\alpha = 0.1$. To this end, different discretization methods are compared for different τ:

- direct discretization of $Y_{Shunt}(s)$ without any correction using Tustin's method,
- discretization of a corrected $Y_{Shunt}(s)$ according to [70] using Tustin's method,
- tuning of $Y_{Shunt}(z)$ according to the tuning procedure presented in Section 1.6.1,
- tuning of $Y_{Shunt}(z)$ according to the tuning procedure presented in Section 1.6.1 without simplification; the impedance of the electromechanical system $\frac{1}{s}C_p(s)$ is considered as the plant transfer function.

The last method listed, working without the simplification, requires more explanation, which is given hereafter. Since the whole dynamic elastance of the electromechnical system is considered in this method, the poles and zeros related to the resonance frequencies of the mechanical modes are also included in Norton's equivalent admittance. In order to determine the shunt transfer function parameters, the additional zeros are not taken into

Sampling period τ [s]
$2 \times 10^{-5}\omega_{oc}^{-1} = 0.001$ s
$0.25\omega_{oc}^{-1} = 0.0031$ s
$0.75\pi\omega_{oc}^{-1} = 0.75\tau_{max} = 0.03$ s

Table 1.2: Values of the chosen sampling periods for the discretization study presented in Figure 1.25 presented in increasing order.

account. From Equation (1.54) we can see that the zeros of $\frac{1}{Y_N(z)}$ are the union of the zeros of $Z_p(z)$ and the poles of $Y_{Shunt}(z)$. Therefore, only a few of them can be changed by the choice of the shunt transfer function, while the others are fixed and may hence be discarded. On the other hand, following the spirit of the approach, the poles of the electromechanical system are taken into account for the choice of the shunt parameters. Equation (1.71) needs then to be solved with a least square error (LSE) optimization, considering that the number of present poles exceeds the number of the numerator coefficients of $Y_{Shunt}(z)$. Using this LSE optimization to determine these coefficients can then become a potential source of imprecision, especially for complex structures with numerous modes.

For the demonstration of the different discretization methods on an SDOF example, three different sampling periods are regarded corresponding to the different degrees of delay-induced changes in the discretized shunt admittances. We start with a sufficiently small value for τ that is increased until approaching the maximum value for τ_{max} according to the Nyquist-Shannon sampling theorem. It should be mentioned that approximating τ_{max} is a rather academic example chosen here to illustrate the different behaviors of the controllers. Normally, the sampling period should be chosen substantially smaller than its limit value, if possible. The values for the chosen sampling periods are listed in Table 1.2. The FRFs of the corresponding closed-loop systems are displayed in Figure 1.25. Significant differences between the discretization approaches can be observed. Even for a sufficiently small sampling period τ, the controller that has been discretized by Tustin's method without accounting for delays is slightly detuned. Increasing the sampling period stepwise shows that this controller quickly loses its efficiency (cf. Figure 1.25b). When τ_{max} is approached, both the discretization with Tustin's method and also the approach presented in [70] cannot provide a satisfying damping performance (cf. Figure 1.25c). However, the discretization method presented in Section 1.6.1 remains efficient. From Figure 1.25, it can also be observed that the simplification of the plant transfer function is justified: both FRFs of the closed-loop systems, one for the case where Z_p is the plant (▬), and one that considers the entire electromechanical system as a plant (▪ ▪ ▪) only differ slightly from each other. The poles of the closed-loop system in Figure 1.26 for a sampling period close to τ_{max} show that only the controller that has been discretized according to the approach presented in this chapter can ensure that the poles are located within the unit circle and, hence, that the closed-loop system is stable. In addition, it can be observed that the poles with and without simplification are almost identical.

Finally, the proposed discretization method is demonstrated on a more complex numerical example featuring multiple modes. In Figure 1.27, the receptance functions of a bladed

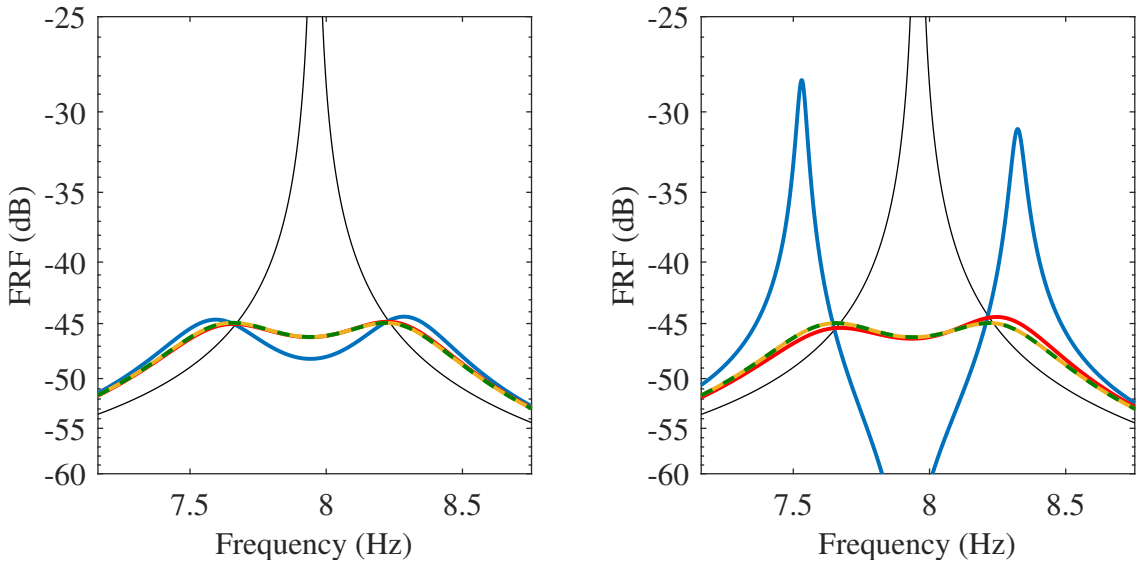

(a) $\tau = 0.001s$.

(b) $\tau = 0.25\omega_{oc}^{-1} = 0.0031s$.

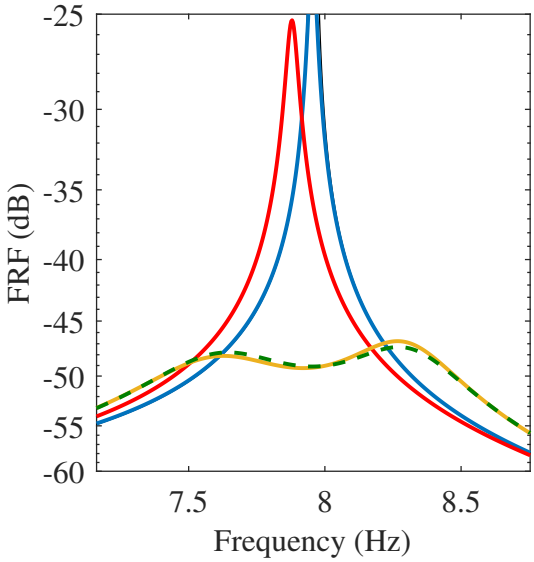

(c) $\tau = 0.75\pi\omega_{oc}^{-1} = 0.75\tau_{max} = 0.03s$.

Figure 1.25: Discretization effects illustrated on the FRF of an SDOF system (open-circuit (▬)) controlled by digital RL shunts discretized in different ways: Tustin's method (▬), according to [70](▬), according to Section 1.6.1 (▬) and according to Section 1.6.1 without simplification of the plant transfer function (▬)

rail model are displayed. This structure was also subject to experimental investigations in Chapter 3. The figure compares the open-circuit receptance with the FRF of the system controlled by a simple RL shunt targeting a mode located in the first group of modes, shown in the close-up (cf. Figure 1.27). The shunt transfer function was discretized with $\tau = \frac{1}{3}\omega_{oc}^{-1}$ according to the proposed method that takes advantage of the approximation of the plant. ω_{oc} corresponds to the targeted normalized resonance frequency which is located at 0.184. Figure 1.27 shows that the shunt controller yields a remarkable and

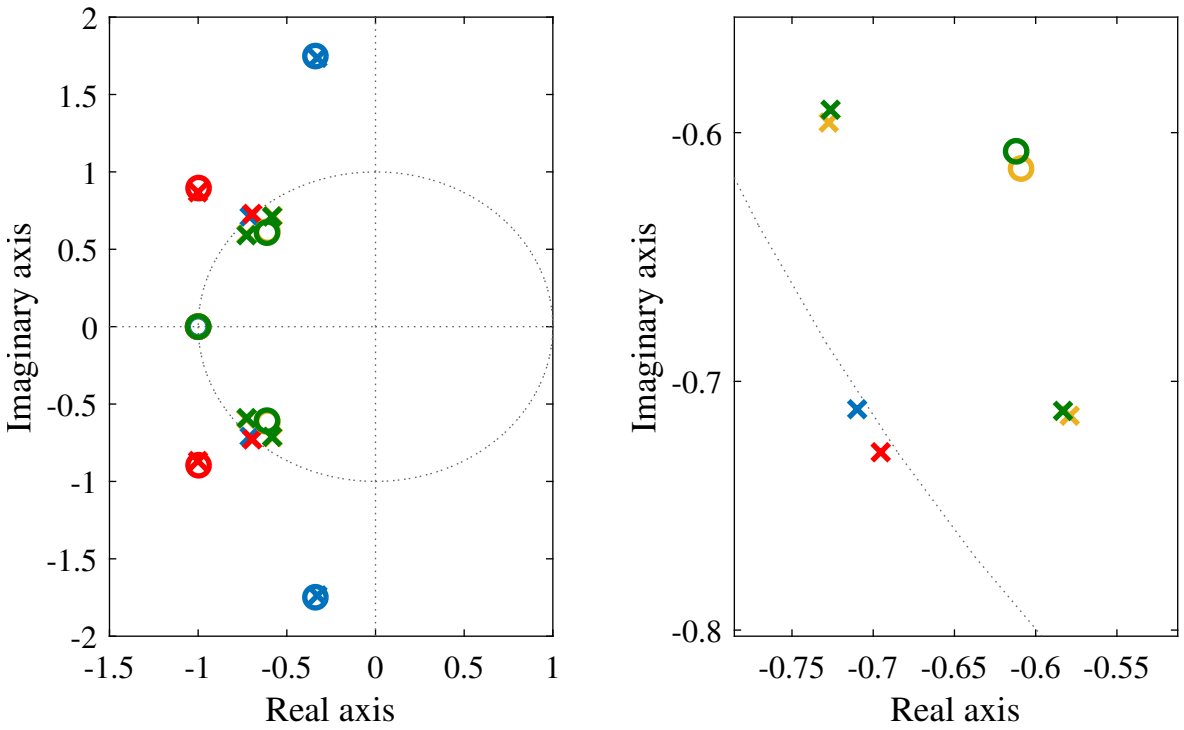

(a) Unit circle. **(b)** Zoom view.

Figure 1.26: Discretization effects illustrated in a pole-zero map for an SDOF system controlled by digital RL shunts. The shunt transfer function has been realized in different ways, setting $\tau = 0.75\tau_{max}$ and discretizing a) with Tustin's method (—), b) according to [70](—) c) according to Section 1.6.1 (—) and d) according to Section 1.6.1 without simplification of the plant transfer function (—). Poles of the respective closed-loop system are indicated with a $\times$ while zeros are marked by a $\circ$.

satisfying damping performance on the whole group of modes. We can conclude that the discretization method performs well for complex structures and is suitable for the applications used in this thesis. This will be confirmed later by the experimental results.

1.7 Conclusion

This chapter recalled important concepts and basic equations for piezoelectric shunt damping which is an attractive and relatively easy-to-implement solution for vibration mitigation. Different approaches to design the shunt controller were presented and discussed. Difficulties in the practical realization can be overcome by using a digital implementation of the shunt circuit as an alternative to often cumbersome analog shunt circuits. A digital absorber offers the user a considerable flexibility in the implementation and enables adaptivity of the controller parameters. The working principles of the DVA were presented as well as the practical realizations used in this work. Finally, a new discretization procedure for the shunt admittance that prevents delay-induced instabilities of the controlled system was proposed and validated numerically.

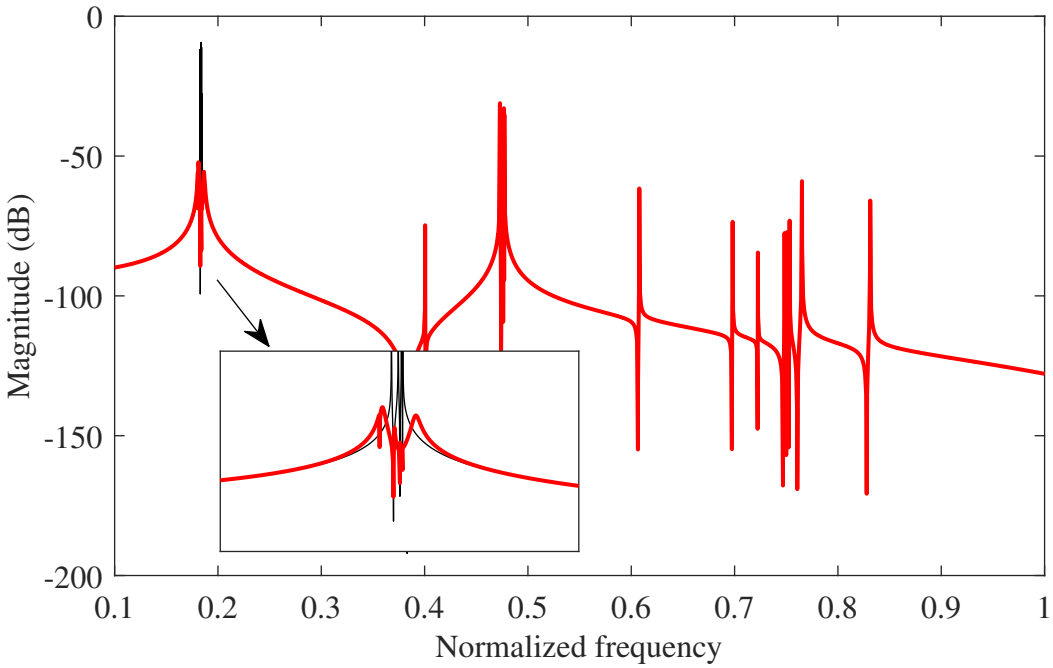

Figure 1.27: Blade tip FRFs of a numerical bladed rail model. (▬): open-circuit FRF and (▬): controlled by an RL shunt discretized by the proposed method.

Chapter 2

A multimodal vibration mitigation strategy for bladed structures

2.1 Introduction

After the introduction of piezoelectric shunt damping for an SDOF host system and the working principles of a DVA, we move to the multi-degree-of-freedom (MDOF) case. Specifically, bladed structures which can feature complex dynamics are considered in this chapter, because they will be studied experimentally in Chapters 3 and 4. In the first part, we provide an overview of their dynamic properties together with the existing damping approaches. The theory behind different multimodal damping strategies using multiple piezoelectric transducers is then presented with the aim to bring piezoelectric shunt damping one step closer to industrial applications.

2.2 Dynamic properties of bladed assemblies

Bladed structures are envisaged for their industrial relevance and in view of the challenges posed by their dynamic properties. Bladed structures often appear in the context of cyclic structures that are widely encountered in, e.g., wind turbines, power stations and turbo-molecular pumps. Such structures also constitute the core of turbojet engines through the stages of compressors, stators, and turbines. A full description of the functioning of such systems can be found in [73].

2.2.1 Cyclic symmetric structures

The main mathematical feature of a cyclic structure is that a portion of it (also called fundamental sector) is repeated $(N-1)$ times around an axis to form a closed structure with N sectors as schematized in Figure 2.1. Due to their symmetric properties, the physical coordinates can be translated into cyclic ones. Such a change of variables enables us to describe the system in terms of nodal diameters [74]. For linear systems, the equations of motion become uncoupled for each nodal diameter. The $0-$th nodal diameter corresponds to a deformed shape of the structure where all sectors move in unison. On the contrary, for the $\frac{N}{2}$ nodal diameter (if N is even), the adjacent sectors have opposite motion. Both cases correspond to non-degenerated nodal diameters. The other cases ($[1, \frac{N}{2}-1]$ if N

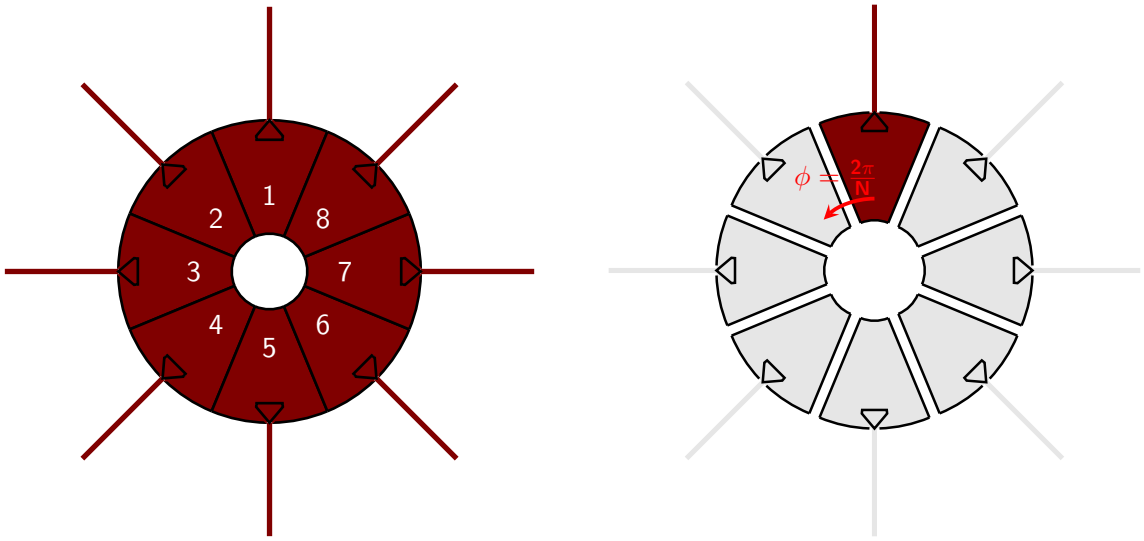

Figure 2.1: (a): Full cyclic symmetric structure, (b): Cyclic properties.

is even and $[1, \frac{N-1}{2}]$ otherwise) are called degenerated nodal diameters [75]. As a consequence, their deformed shapes correspond to traveling waves. The different deformed shapes of the example presented in Figure 2.1 are illustrated for the first flexural mode in Figure 2.2.

2.2.2 Blade modes and mode families

Another feature of structures exhibiting multiple blades of the same shape and size is that the natural frequencies of the blade modes appear in groups, also called mode families, for which each mode features a different nodal diameter. The corresponding dynamics can be analyzed by plotting the nodal diameters over the natural frequencies of the structure, as displayed in Figure 2.3 for a numerical model of a BluM, discussed in [30]. The BluM structure will be the subject of experimental investigations in Chapter 4. For a low number of nodal diameters, the natural frequencies appear scattered. These modes belong to the drum-dominated modes. For a higher number of nodal diameters, the structural motions are dominated by the blade modes, and the drum support only participates to a small extent. The horizontal lines in the diagram indicate that a large number of modes appears around specific ranges of frequencies. For illustration, the mode shapes of two bending modes (1B and 2B) and the first torsional mode (1T) of the blades are displayed in Figure 2.4. The high modal density of two mode families, namely the 1B and 1T families, is illustrated in Figure 2.5. The drum modes appear around these mode families.

In general, the excitation of blade modes in mode families should be avoided to, e.g., prevent material fatigue. If this is not possible, damping of these modes is of the upmost importance. The usual source of excitation for bladed structures comes from aerodynamic forces resulting from the engine's rotation, subjecting them to periodic rotational excitation at a frequency that is a multiple of the engine order. For rotating structures, the natural frequencies may change with rotational speed because of spin softening, pre-stress,

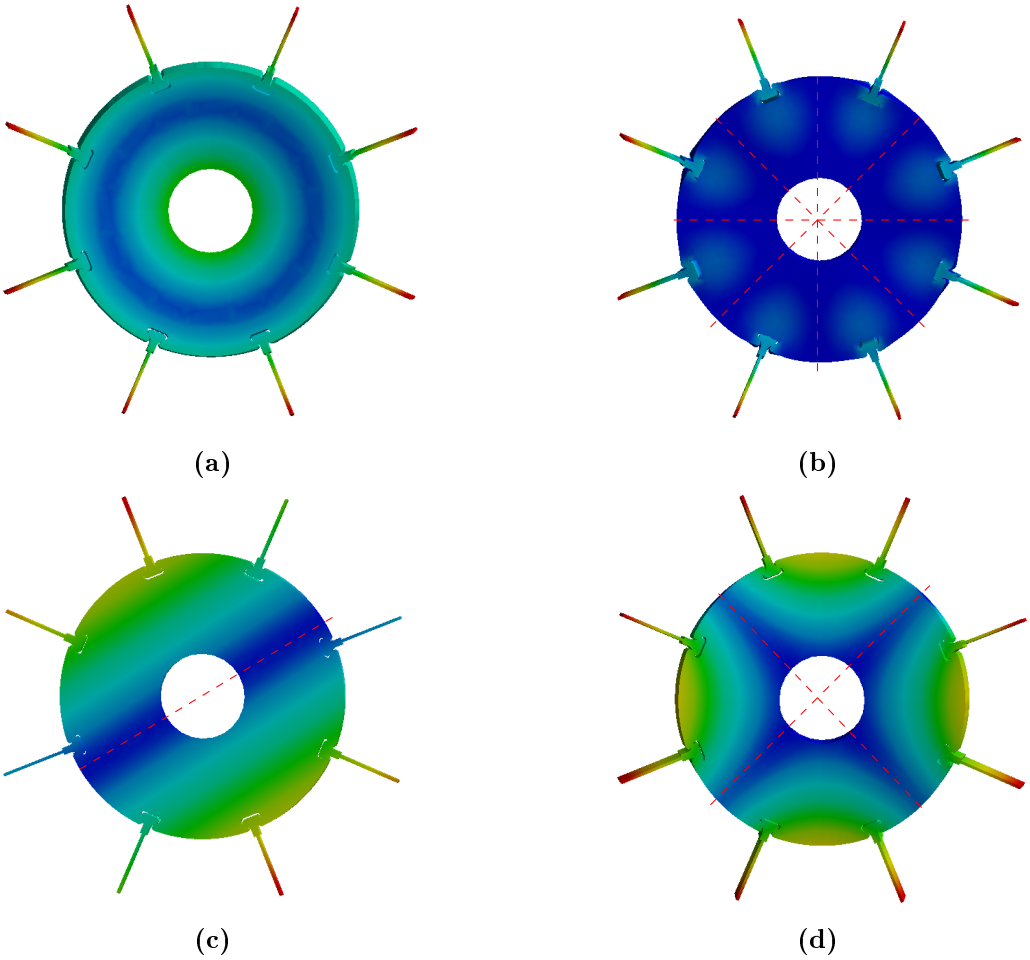

Figure 2.2: First edgewide flexural mode of the cyclic symmetric structure presented in Figure 2.1 (a): 0th nodal diameter (movement in unison), (b): $\frac{N}{2}$th nodal diameter (alternating motion), (c): 1st nodal diameter (forward), and (d): 2nd nodal diameter. The third nodal diameter is not illustrated for brevity. Red lines represent the lines where the motion is equal to 0 (at the time the motion is represented).

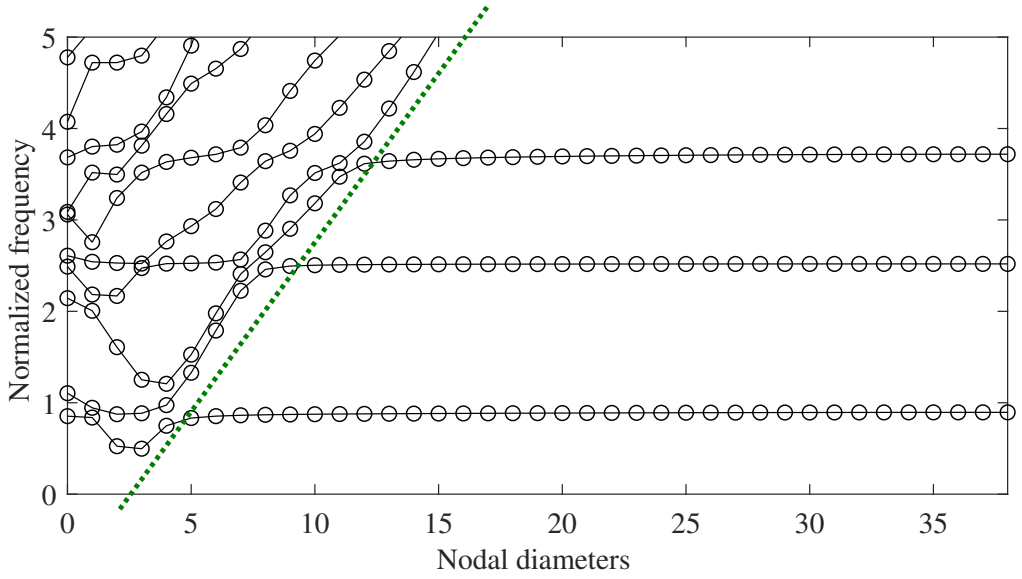

Figure 2.3: Natural frequency versus number of nodal diameter diagram of the BluM. Modes on the left-hand side of the green dashed line are considered as being drum-dominated whereas the ones on the right-hand side are blade-dominated [30]. For confidential reasons, the frequencies have been normalized with respect to the first natural frequency of the cantilever blade.

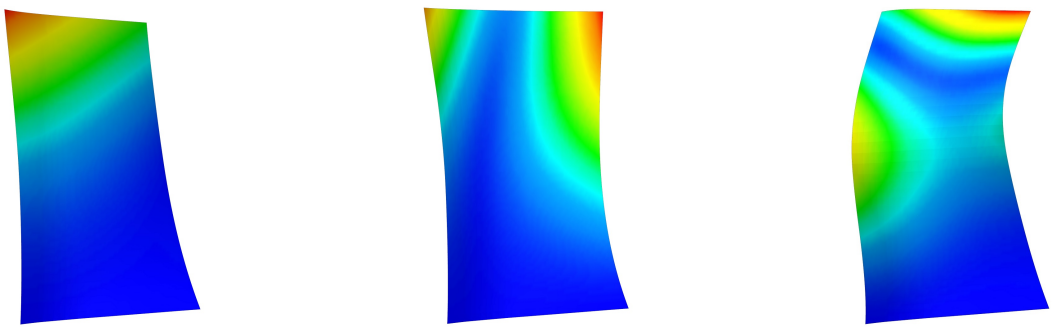

(a) **(b)** **(c)**

Figure 2.4: Mode shapes of the first (bending 1B) (a), second (torsion 1T) (b) and third (bending 2B) (c) cantilevered blade modes [30].

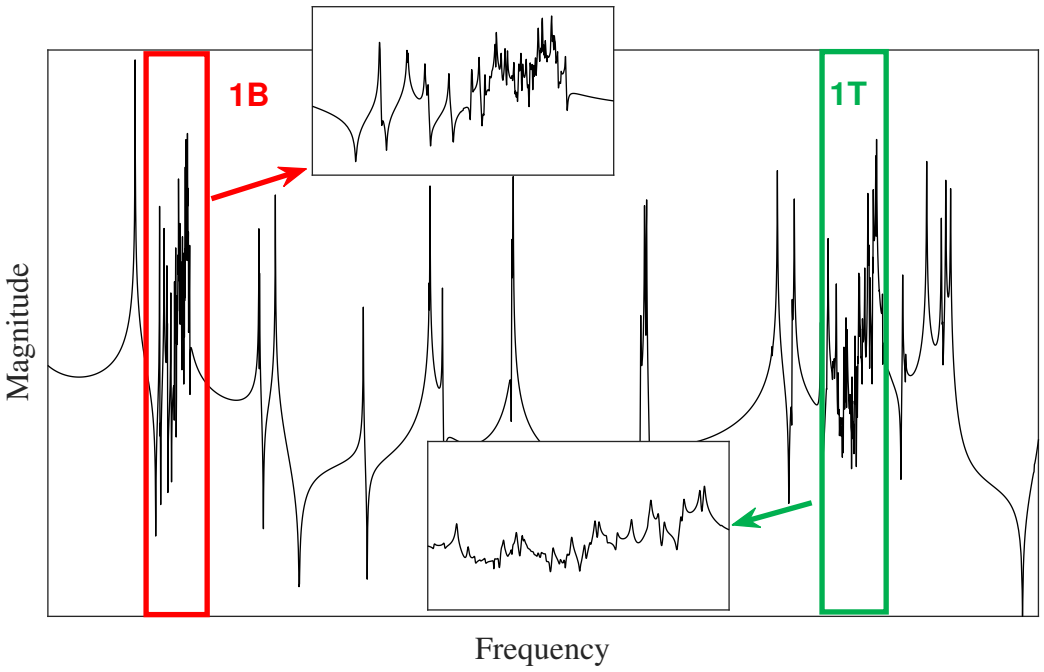

Figure 2.5: FRF measured at a blade tip of a BluM with an excitation force at the drum. The 1B and 1T mode families are marked in red and green, respectively.

Coriolis and gyroscopic effects [76]. In addition, Coriolis effect may, for high rotational speeds and for some specific cases, remove the occurrence of mode families [77]. The evolution of natural frequencies is typically represented with a Campbell diagram. Overall, the frequency versus number of nodal diameters diagram as well as the Campbell diagram are usually used for the load assessment of these structures [75]. We note that the rotational effects are disregarded in the framework of this thesis because the experimental campaign was conducted on a BluM at rest.

2.2.3 Applications to turbomachinery and damping approaches

The theory about the dynamic behavior of cyclic symmetric structures is fully described in [74] but only holds true if each repeated sector is identical. However, in practice, due to, e.g., manufacturing tolerances, material irregularities and wear of the system, small differences may exist between the sectors. This is referred to as random mistuning; it can be detrimental as localization phenomena can occur [78, 79]. An FRF illustrating mistuning around one mode family is represented in Figure 2.6. It can be seen that the modes are still close together, but that their frequencies change and may become more scattered. In the presence of mistuning, the notion of nodal diameters remains relevant to describe the mode shapes of the structure. However, the equations of motion become fully coupled. Research was conducted to characterize mistuned cyclic structures. In [80], the authors proposed a methodology to identify geometric mistuning. A similar approach was used in [81] and it was demonstrated that mistuning from the boundary conditions can also have a significant impact on the mode shapes. Recently, a methodology using a neural network was proposed [82], which shows that this research is still relevant in the

scientific community.

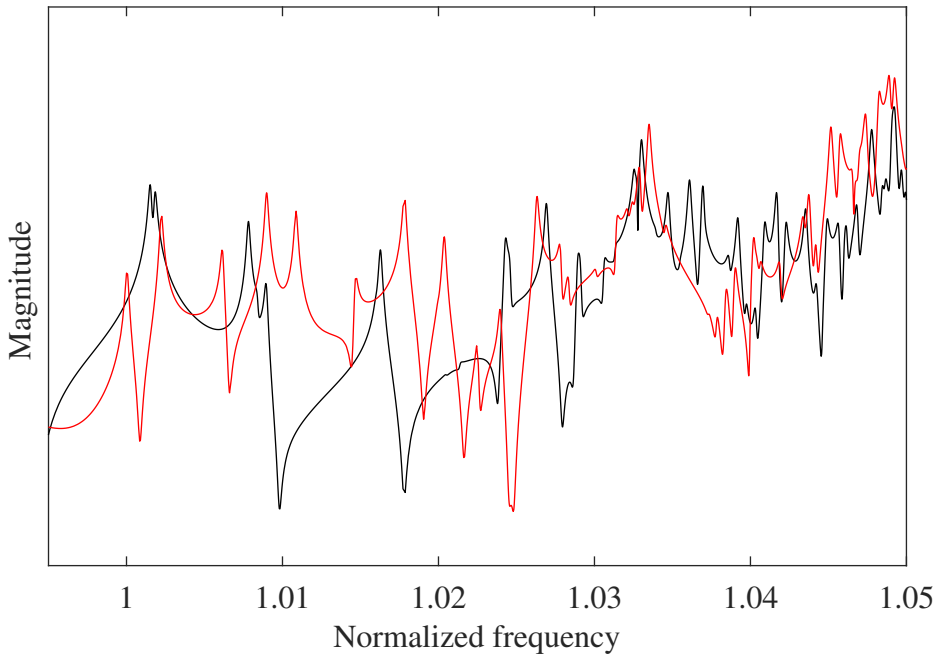

Figure 2.6: FRFs measured at a blade tip of a BluM with an excitation force at the drum: perfect cyclic symmetric (▬) and mistuned (▬) cases. The focus is on the first mode family and the frequency was normalized with respect to first resonance family of this mode group.

The BluM, used in the low-pressure compressor of aircraft engines, was already the subject of several studies in [32, 83–85]. Its manufacturing process comprises two steps, namely the production of the drum followed by friction welding of the blades [86]. The same procedure is used for BLISKs with a disk instead of a drum. Besides a weight reduction of the order of 25 %, the BluM and BLISK also offer improved aerodynamic efficiency. Moreover, the occurrence of fretting fatigue at the interfaces between drum/disk and blades can be avoided, a typical reason for the failure of such structures [65, 87].

One consequence of the manufacturing process is that BluMs/BLISKs have extremely low structural damping and are thus more prone to detrimental vibrations and high-cycle fatigue problems. For this reason, mitigating their vibrations is important in order to avoid failure and prevent deterioration. Different strategies for vibration mitigation of bladed structures have been developed over the years. The most popular one is to attach small mechanical devices that dissipate energy via friction. Blade root attachments are a possibility when considering bladed drums/disks [88] (cf. Figure 2.7a), but they cannot be applied to single-piece designs where the interface between the blades and the disk/drum is no longer present. Underplatform dampers [89, 90] (cf. Figure 2.7b[†]) and friction ring dampers [91] (cf. Figure 2.7c) constitute good candidates for vibration reduction without disturbing the airflow going through the engine. A thorough review of these techniques

[†]The underplatform dampers geometry is exaggerated to match the low number of sectors.

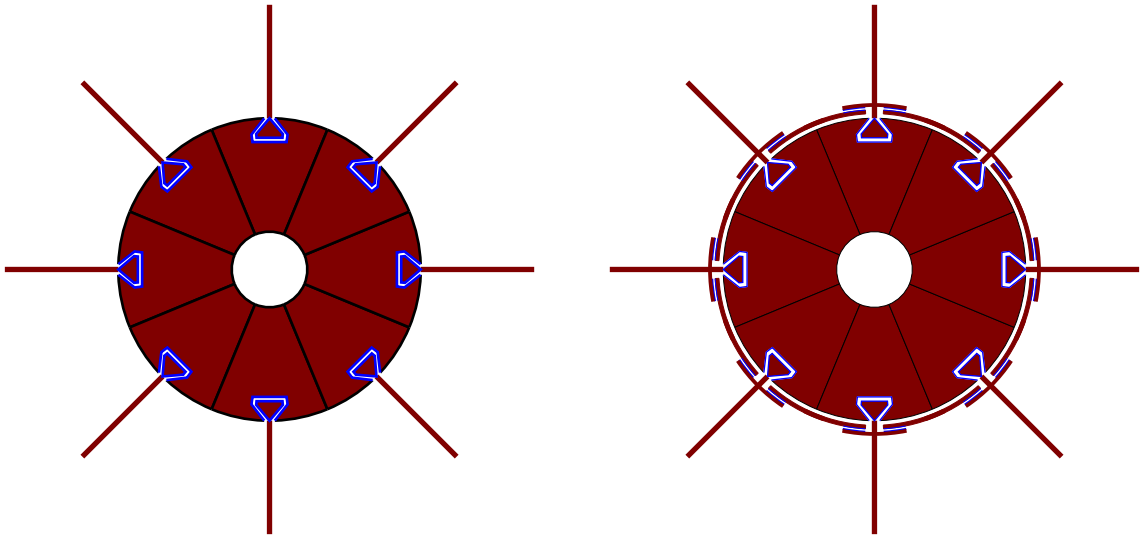

(a) Cyclic structure with dovetail attachments.

(b) Cyclic structure with underplatform dampers.

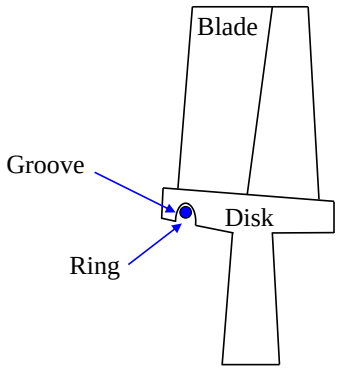

(c) Friction ring dampers [42].

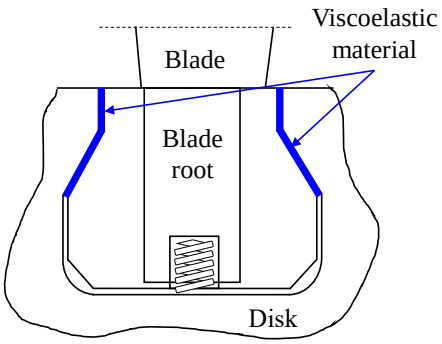

(d) Damping with viscoelastic materials [93].

Figure 2.7: Different damping solutions for bladed structures.

can be found in [92]. However, two main difficulties arise when exploiting friction damping. First, energy dissipation is achieved when a relative displacement is obtained between the structures. Therefore not all modes can be targeted. Second, numerical prediction of vibration reduction can be challenging as nonlinear solvers must be used, complicating the design process. Another possible damping solution utilizes viscoelastic materials [93] placed between the blade root and the disk as illustrated in Figure 2.7d. For single-piece designs, viscoelastic coating can be used. However, due to their material properties, their effectiveness varies with temperature with the result that this damping solution is not applicable for high temperatures [32]. Another interesting vibration mitigation approach is the modification of the blade profile so as to create an acoustic black hole effect [94]. The method allows for an amplitude reduction of a large number of vibration modes. Nevertheless, this comes at the expense of a loss of aerodynamic efficiency.

For the past two decades, strategies based on piezoeletric shunt damping were also considered. Tang and Wang placed piezoelectric patches on each blade of a bladed disk, shunting them to either a passive resonant shunt or an active-passive hybrid network [95].

In [96, 97], piezoelectric networks were exploited for multimodal vibration mitigation of bladed disks. The authors proposed a multi-circuit network that was designed analytically by means of an analysis of the host system. This approach proved also effective in the case of mistuning. Later, Liu et al. compared piezoelectric shunts with piezoelectric networks acting on a bladed disk structure in [98]. They concluded that both methods can damp the vibrations of the systems effectively, with the network approach being more efficient in the case of an excitation of a non-engine order. In [99], Kauffman and Lesieutre introduced a damping strategy that detunes the resonance frequencies of the blades. Using piezoelectric shunt circuits, they switched between open- and short-circuit states of the patches every time the resonance frequency was approached by the excitation. The method was demonstrated experimentally on blades mounted in a stationary frame, using titanium flat plates with surface-mounted piezoelectric patches. One limitation of this method is that the excitation frequency must be known since the switching mechanism depends on the knowledge of the rotor speed. Choi et al. used an RLC shunt circuit realized via a digital controller to damp the structural vibrations of a high-speed turbomachinery fan blade [100, 101]. In their implementation, two piezoelectric patches were placed to the blade surface, one functioning as a sensor and the other as an actuator. After a thorough study of the best suited patch material and their position, they demonstrated the damping performance of the digital shunts in a spin test on two GEnx blades. In [102] passive electrical shunt circuits were connected to the blades of a simplified rotor model, one circuit shunted to one blade. Two frequencies were targeted by one circuit tuned using numerical optimization. Thierry et al. demonstrated the efficiency of piezoelectric shunts on a turbojet fan blade [103]. They mounted a parallel connection of multiple piezoelectric patches in a mosaic on the blade surface and shunted them to a single RL shunt. In all the aforementioned strategies, the position of the patches was chosen on the blades itself, which is not a viable solution for industrial applications, since interaction with the airflow must be avoided. To overcome this issue, the transducers can be incorporated directly in the blades [104]. However, this solution considerably complicates the manufacturing process. Recently, Rossi et al. proposed to cover blades of a BLISK with piezoelectric patches to then impose a voltage distribution that intentionally caused a disturbance of the inlet flow of the fan. In numerical simulations, they were able to demonstrate that the stresses occurring at resonant frequencies can be reduced using this method [105].

In order to avoid disturbing the airflow, piezoelectric patches can be installed inside the drum/disk under the blade roots, as illustrated for a BluM in Figure 2.8. This was achieved by Mokrani et al. [32, 85], Zhou et al. [106] and Viguié et al. [107]. Placing the patches in this way provides an acceptable compromise between the aerodynamic performance and the electromechanical coupling. Considering this positioning strategy, Mokrani connected multiple piezoelectric patches in parallel and shunted them with piezoelectric shunt circuits [83]. Doing so, the values required for the inductances could be reduced while achieving a satisfying damping performance over the first group of blade modes. Yet, the approach could not prove robust against mistuning. In [106], Zhou et al. designed piezoelectric shunt circuits mimicking a nonlinear energy sink. Their method proved to be robust and effective over a large frequency band and could also reduce the required inductance values in comparison with a linear resonant shunt circuit. However, a non-

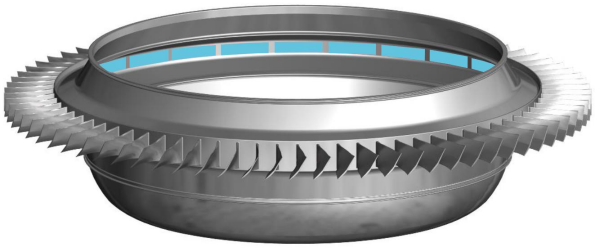

Figure 2.8: Piezoelectric patches (blue) installed under the blade roots inside the drum of a BluM structure (modified from [32]).

linear damping solution adds significant complexity to the design problem. Paknejad et al. utilized pairs of piezoelectric patches installed under the blade roots of a bladed rail structure to damp their structural vibrations with PPF controller [108]. In [109], Jamshidi et al. installed such piezoelectric transducer pairs in the drum of a BluM structure and achieved a remarkable reduction of their structural vibrations using IFF controller [109]. Both controllers work according to active control laws. In [30], through detailed numerical simulations, Raze proved the efficiency of different piezoelectric tuning strategies on a BluM. To the best of our knowledge, a digital realization of a passive piezoelectric shunt circuit has never been applied to a real cyclic bladed structure.

2.3 Multimodal vibration mitigation with multiple piezoelectric transducers

In order to mitigate the vibrations of bladed structures, strategies to target several modes with multiple piezoelectric DVAs are presented in this section. Tackling multiple modes with one or more piezoelectric shunt circuits has already been attempted in various studies. One possibility to damp multiple modes simultaneously is to individually shunt each transducer using a single RL circuit [110]. There also exist different circuit topologies for targeting multiple modes using a single piezoelectric shunt. The main idea is to make the circuit resonate at several frequencies. Edberg et al. designed a two-mode shunt by adding a second parallel LC branch to a simple RL shunt circuit [44]. Later, Hollkamp extended this design to an arbitrary number of electrical frequencies, proposing a layout of RLC branches in parallel [111]. Different designs of current blocking circuits have been discussed over the last decades [112, 113]. These circuits force the current to flow through a desired shunt branch for a particular frequency by blocking the other branches via filters. In [114], Behrens et al. proposed a current flowing circuit design. Other multimodal shunt designs consist of Cauer networks [115] or a series–parallel impedance structure [116]. In view of the often large number of electrical components, such shunt circuits were also emulated digitally [117]. Raze et al. demonstrated the effectiveness of a DVA acting on multiple modes and presented a simplified current-blocking approach [117]. An alternative to target multiple modes is to look at the problem from a control design perspective and design the shunt as a feedback controller [118].

In contrast to single RL shunts, multi-mode circuits may be hard to tune. Often, numerical optimization is used to define the values of the electrical components [119–121]. Berardengo et al. presented an approach for an optimal multimodal piezoelectric shunt impedance that was based on matrix inequalities [122]. In [111], a transfer function was considered for each mode to be damped. This function was then minimized while taking into account the other modes by weighting factors. With the focus on the reduction of the number of elements in an electrical circuit, Bo et al. proposed a design tool for electrical multimodal shunt circuits based on optimization, using one transducer [62]. Multiple piezoelectric transducers might also be used to tackle the problem, often in the context of electrical networks. A decentralized multiport synthetic impedance was designed by Moheimani et al. that was shunted to multiple piezoelectric elements [55]. Giorgio et al. exploited a digital implementation of a shunt admittance that targeted multiple modes of one- and two-dimensional structures. They used a multiterminal network interconnecting multiple piezoelectric transducers. Their aim was to design a network that was equivalent to a set of single transducers so that common tuning rules for the electrical parameters could be used [56, 57]. The same approach was later applied to the control of sound radiation by Rosi et al. [58, 59]. Furthermore, they found optimal positions of the transducers for the mitigation of multiple modes by optimizing the modal controllability. In his work, Mokrani addressed the problem of targeting closely spaced modes of a BluM consisting of 76 blades [32]. He proposed to target a mean frequency of the frequency range of interest and tune multiple piezoelectric absorbers to it. This idea will be adapted later in this chapter and extented from one to multiple mode families. Recently, a shunt calibration method was introduced by Toftekær and Høgsberg that also takes into account the influence of non-resonant vibration modes to achieve a more precise tuning [123].

In this thesis, we aim to exploit multimodal shunt damping approaches for vibration mitigation of structures featuring high modal density. This poses a distinct challenge since an optimal current flow might not be guaranteed if different shunt branches are resonating at similar frequencies. In addition, when using multiple DVAs, the patch-to-shunt function distribution needs to be evaluated. For the tuning strategies presented hereafter, several DVAs connected each to a piezoelectric transducer are used.

2.4 Basic electromechanical equations for the multimodal case

In order to obtain a model of an electromechanical structure, the finite element (FE) method can be used [124]. If $\mathbf{x}$ and $\mathbf{f}$ represent a vector of K generalized mechanical degrees of freedom (DOFs) and a vector of generalized mechanical loading, respectively, the governing equations of a piezoelectric structure are

$$\mathbf{M}\ddot{\mathbf{x}} + \mathbf{K_{sc}}\mathbf{x} + \boldsymbol{\gamma_p} V_p = \mathbf{f}, \tag{2.1}$$

$$\boldsymbol{\gamma_p}^T \mathbf{x} - C_p^{\varepsilon} V_p = q_p \ . \tag{2.2}$$

$\mathbf{M}$ represents the mass matrix, $\mathbf{K_{sc}}$ is the stiffness matrix with the electrodes of the transducer in short-circuit and $\boldsymbol{\gamma_p}$ is the electromechanical coupling vector. The Laplace

transform of Equations (2.1) and (2.2) reads

$$(\mathbf{M}s^2 + \mathbf{K_{sc}})\mathbf{x} + \boldsymbol{\gamma}_\mathbf{p} V_p = \mathbf{f}, \tag{2.3}$$

$$\boldsymbol{\gamma}_\mathbf{p}{}^T \mathbf{x} - C_p^\varepsilon V_p = q_p \ . \tag{2.4}$$

We consider the model of an ideal voltage source (cf. Equation (1.10)):

$$\begin{aligned} (\mathbf{M}s^2 + \mathbf{K_{oc}})\mathbf{x} - \boldsymbol{\theta}_\mathbf{p} q_p &= \mathbf{f}, \\ \boldsymbol{\theta}_\mathbf{p}{}^T \mathbf{x} - \frac{1}{C_p^\varepsilon} q_p &= V_p, \end{aligned} \tag{2.5}$$

where

$$\mathbf{K_{oc}} = \mathbf{K_{sc}} + \frac{1}{C_p^\varepsilon} \boldsymbol{\gamma}_\mathbf{p} \boldsymbol{\gamma}_\mathbf{p}{}^T, \quad \boldsymbol{\theta}_\mathbf{p} = \frac{1}{C_p^\varepsilon} \boldsymbol{\gamma}_\mathbf{p} \ . \tag{2.6}$$

If the matrix $\boldsymbol{\Phi}_\mathbf{sc}$ contains the short-circuit mode shapes and the diagonal matrix $\boldsymbol{\Omega}_{\mathrm{sc}}$ contains the short-circuit natural frequencies, we obtain the following relations:

$$\boldsymbol{\Phi}_{\mathrm{sc}}^T \mathbf{M} \boldsymbol{\Phi}_{\mathrm{sc}} = \mathbf{I}, \qquad \boldsymbol{\Phi}_{\mathrm{sc}}^T \mathbf{K}_{\mathrm{sc}} \boldsymbol{\Phi}_{\mathrm{sc}} = \boldsymbol{\Omega}_{\mathrm{sc}}^2 \ . \tag{2.7}$$

The expression for the dynamic capacitance in a multimodal case can then be obtained for an unforced structure ($\mathbf{f} = \mathbf{0}$) by condensing the mechanical equation into the electrical one using Equations (2.3), (2.4) and Equation (2.7). The multimodal dynamic capacitance reads

$$\begin{aligned} -\left[C_p^\varepsilon + \boldsymbol{\gamma}_p^T \boldsymbol{\Phi}_{\mathrm{sc}} \left(s^2 \mathbf{I} + \boldsymbol{\Omega}_{\mathrm{sc}}^2 \right)^{-1} \boldsymbol{\Phi}_{\mathrm{sc}}^T \boldsymbol{\gamma}_p \right] V_p = \\ -C_p^\varepsilon \left[1 + \sum_{k=1}^{K} \frac{\gamma_{\phi,k}^2}{C_p^\varepsilon} \frac{1}{s^2 + \omega_{\mathrm{sc},k}^2} \right] V_p = C_p(s) V_p = q_p, \end{aligned} \tag{2.8}$$

with the modal coupling coefficients $\gamma_{\phi,n}$ given by

$$\boldsymbol{\gamma}_p^T \boldsymbol{\Phi}_{\mathrm{sc}} = [\gamma_{\phi,1} \cdots \gamma_{\phi,K}] \ . \tag{2.9}$$

The example of a 3-DOF system is given in Figure 2.9. It can be seen that the values of $C_p(s)$ differ according to the frequency at hand and that the value of C_p^ε is approached stepwise from mode to mode starting at $C_{p,static}$.

We now consider the case when multiple piezoelectric transducers are connected to a structure with $\mathbf{f} = \mathbf{0}$. Under the assumption that all other transducers are in open circuit, we take the Laplace transforms of Equations (2.3) and (2.4). Inserting the former equation into the latter yields an expression of the dynamic capacitance:

$$C_p(s) = \frac{q_p}{V_p} = -C_p^\varepsilon \frac{\prod_{m=1}^{M} (s^2 + \omega_{oc,m}^2)}{\prod_{m=1}^{M} (s^2 + \omega_{sc,m,p}^2)} \ . \tag{2.10}$$

$\omega_{sc,m,p}$ is the m^{th} natural frequency of the structure when transducer p is in short circuit and every other transducer is in open circuit; $\omega_{oc,m}$ is the corresponding open-circuit frequency. Its inverse is the dynamic elastance in the multimodal case:

$$E_p(s) = \frac{1}{C_p(s)} \ . \tag{2.11}$$

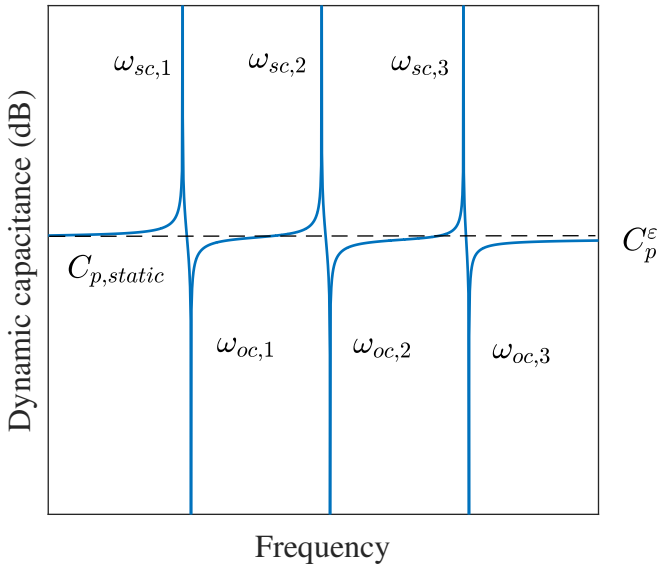

Figure 2.9: An example of a dynamic capacitance function of piezoelectric structure for a fictitious 3-DOF system.

Finally, a dynamic capacitance function is obtained for each transducer p which provides information about the electromechanical coupling with the modes of the structure (cf. Equation (2.8)). We gather these different C_p^ε in a dynamic capacitance matrix with dimensions $P \times P$. Here, the p^{th} diagonal entry for $s = 0$ gives information about the static capacitance of transducer p:

$$C_{p,static} = \left(\mathbf{C}_p(0)\right)_{pp} . \tag{2.12}$$

2.5 Shunt tuning strategies

2.5.1 One mode family

If only the modes of one mode family are targeted, each mode is controlled via a single series RL shunt. For the tuning of the shunt parameters, two different approaches are proposed, namely the isolated mode and mean shunt strategy.

Isolated mode strategy

In the isolated mode strategy, the RL shunt parameters are tuned based solely on the H_∞ norm, taking into account the actual resonance frequency of the mode. Following the tuning strategy from Section 1.3.2.2, equal peaks of the receptance function are targeted. The electromechanical coupling factor in a setup with multiple transducers is derived. As it is the rate of converted energy by the piezoelectric material, it is different for each piezoelectric transducer. For a given patch p, the EMCF reads

$$K_{c,m,p}^2 = \frac{\omega_{oc,m}^2 - \omega_{sc,m,p}^2}{\omega_{sc,m,p}^2} . \tag{2.13}$$

Using the tuning rules introduced in Equations (1.30) - (1.32) with $K_{c,m,p}$ and $\omega_{oc,m}$ and a blocked modal capacitance, the values for the inductance $L_{m,p}$ and the resistance $R_{m,p}$ of a single shunt branch can be calculated. For a maximum vibration mitigation and control over the structure, each shunt is connected to the transducer p that features the largest EMCF with the target mode.

Mean shunt strategy

Another option to target a family of closely spaced modes is a mean shunt strategy. The idea, initially introduced by Mokrani [32], takes advantage of the high modal density. It is adapted in this work by tuning each shunt according to a so-called mean frequency built as the average of the M targeted resonant open-circuit frequencies $\omega_{oc,m}$

$$\widehat{\omega}_{oc,\mathbf{m}} = \frac{1}{M} \sum_{m \in \mathbf{m}} \omega_{oc,m} \ . \tag{2.14}$$

The M mechanical modes are indexed by $\mathbf{m}$. A mean effective electromechanical coupling factor (MEMCF) is computed by averaging the EMCF over the M modes defined by P transducers:

$$\widehat{K}^2_{c,\mathbf{m}} = \sum_{p=1}^{P} \frac{1}{M} \sum_{m \in \mathbf{m}} \frac{\omega^2_{oc,m} - \omega^2_{sc,m,p}}{\omega^2_{sc,m,p}} \ . \tag{2.15}$$

Eventually, the shunt parameters can be calculated according to Equations (1.30) - (1.32) using $C_{p,static}$ (Equation (2.12)) and the derived mean parameters $\widehat{K}_{c,\mathbf{m}}$ and $\widehat{\omega}_{oc,\mathbf{m}}$ from Equations (2.14) and (2.15). Due to the fact that each patch is used to target all the modes of a family, the optimal patch to target a mode does not have to be determined as in the isolated mode strategy; the application of the mean shunt strategy is thus truly straightforward.

2.5.2 Multiple mode families

When multiple mode families and/or separate modes are targeted, a shunt circuit design possessing multiple branches is to be considered. In this work, each circuit branch resonates with one mode of a family and/or a support mode. For good damping performance, the interference between the different shunt branches of a circuit is to be avoided. To this end, the targeted modes of one circuit should be located away from each other. This is one of the reasons why the modes of one mode family are not targeted by the same multi-staged circuit. The current blocking approach proposed by Raze et al. [117] is exploited herein in combination with either the isolated mode or the mean shunt strategy. The shunt circuit is schematized in Figure 2.10. One stage consists of an RL shunt branch and a notch filter which is tuned toward one of the targeted frequencies, in ascending order. By providing an infinite impedance at the targeted frequency, the LC filters ensure that the current flows through the appropriate shunt branch. Since multiple piezoelectric transducers operate simultaneously, several multi-stage shunt circuits are implemented, as shown for a BluM in Figure 2.11. The number of shunt circuits therefore corresponds to the number of piezoelectric patches used. Each circuit stage is then tuned to one frequency, either single or mean, from a specified mode family and/or an isolated mode

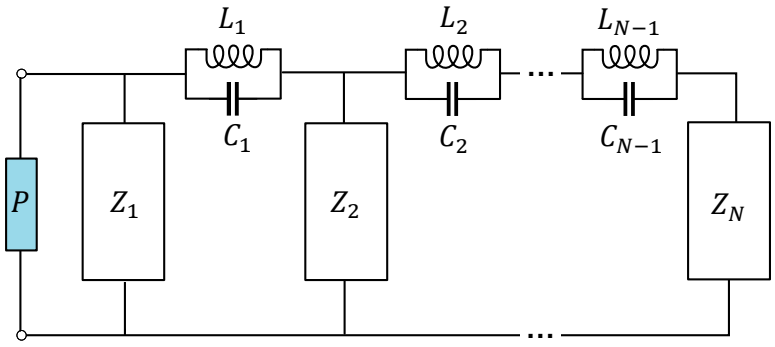

Figure 2.10: Electrical circuit for the multistage current blocking approach tuned toward N resonant modes. One stage consists of a the shunt impedance Z_N and a notch filter.

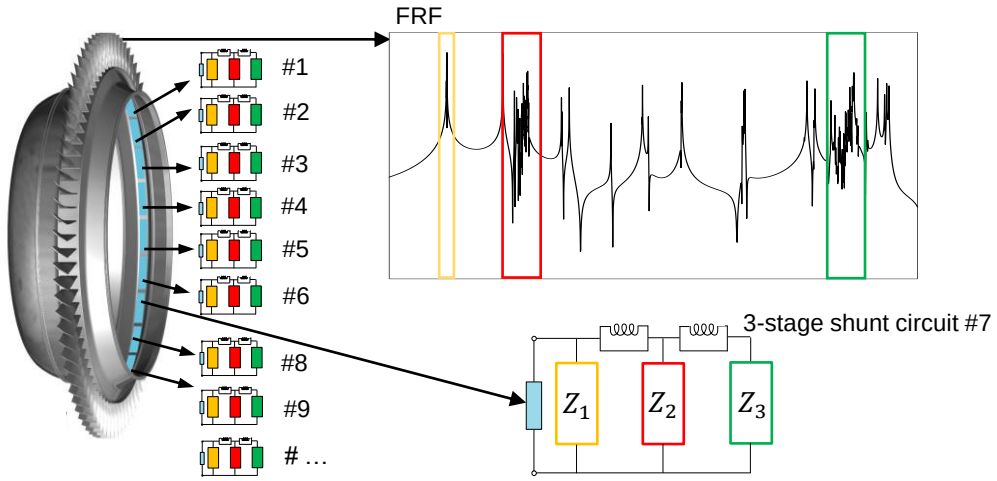

Figure 2.11: Exploitation of several multi-stage shunt circuits on a BluM example. The circuits operate simultaneously, being connected to different piezoelectric patches. One stage each is tuned toward a particular frequency (range) of the host structure FRF.

such as a drum mode. As a final result, the same frequency ranges are targeted by various shunt branches that belong to different circuits. Doing so, the interaction between branches is mitigated, and a high level of control performance can be provided[†].

When using a multi-stage shunt circuit, the different stages have an impact on what is to be considered the respective plant transfer function from the point of view of the individual shunt branches. To take this into account, a sequential tuning of the different circuit stages is adopted to determine the respective shunt parameters. This method was first introduced by Raze et al. in [117] and is exploited herein.

Modeling the dynamic elastance from a shunt branch point of view

In the tuning procedure, an equivalent electromechanical structure as well as a fictitious optimal shunt branch are identified at each state n of the network (cf. Figure 2.12). In this

[†]In practice, an ideal current flow cannot always be guaranteed.

way, common shunt tuning formulas can be used to tune the parameters of this optimal shunt circuit which are eventually translated to physical parameters in the context of the overall circuit. The relation between the piezoelectric transducer and a specific shunt branch can be expressed by a transfer matrix $\mathbf{G}$:

$$\begin{bmatrix} V_s \\ sq_s \end{bmatrix} = \mathbf{G} \begin{bmatrix} V_p \\ sq_p \end{bmatrix} = \begin{bmatrix} g_{11}(s) & g_{12}(s) \\ g_{21}(s) & g_{22}(s) \end{bmatrix} \begin{bmatrix} V_p \\ sq_p \end{bmatrix}. \tag{2.16}$$

The two-port network theory [125] is used to model an electrical network from the respective shunt branch point of view. Due to the presence of different circuit stages, this electrical network has to be considered and updated at each tuning step. V_s is the voltage across a shunt branch and q_s the charge flowing through it. From Equation (2.16), the dynamic elastance E_s is derived as it is seen from a currently regarded shunt branch:

$$\frac{V_s}{q_s} = s\frac{g_{12}(s) + \frac{V_p}{sq_p} g_{11}(s)}{g_{22}(s) + \frac{V_p}{sq_p} g_{21}(s)} \,. \tag{2.17}$$

Under the assumption that this expression is similar to Equation (2.11) for a single transducer p, Equation (2.17) can be approximated around a specific resonance frequency as

$$\frac{V_s}{q_s} \approx -\frac{1}{\tilde{C}_p^{\varepsilon}} \frac{s^2 + \tilde{\omega}_{sc}^2}{s^2 + \tilde{\omega}_{oc}^2}. \tag{2.18}$$

$\tilde{C}_p^{\varepsilon}$, $\tilde{\omega}_{sc}$ and $\tilde{\omega}_{oc}$ are the characteristics of an equivalent dynamic elastance from the point of view of the n^{th} shunt branch. They correspond to the equivalent piezoelectric structure in Figure 2.12. Using $\tilde{\omega}_{sc}$ and $\tilde{\omega}_{oc}$, a branch-specific EMCF, can be formed:

$$\tilde{K}_c^2 = \frac{\tilde{\omega}_{oc}^2 - \tilde{\omega}_{sc}^2}{\tilde{\omega}_{sc}^2} \,. \tag{2.19}$$

This quantity can help to assess the control authority over the mode that is targeted by this specific branch. For more accuracy, Equation (2.18) can be expanded by adding an inductance $\tilde{L}$ and a resistance $\tilde{R}$

$$\frac{V_s}{q_s} \approx -\tilde{L}s^2 - \tilde{R}s - \frac{1}{\tilde{C}_p^{\varepsilon}} \frac{s^2 + \tilde{\omega}_{sc}^2}{s^2 + \tilde{\omega}_{oc}^2} \,. \tag{2.20}$$

$\tilde{L}$ and $\tilde{R}$ are parameters of the equivalent piezoelectric structure (cf. Figure 2.12) as it is seen from the n^{th} shunt branch. Alternatively, in order to model a capacitive behavior, the equivalent piezoelectric structure might be expressed as

$$\frac{q_s}{V_p s} = \frac{1}{s} \frac{g_{22}(s) + \frac{V_p}{sq_p} g_{21}(s)}{g_{12}(s) + \frac{V_p}{sq_p} g_{11}(s)} \,, \tag{2.21}$$

which represents the inverse of Equation (2.17). Similarly to Equation (2.20), it can then be modeled using a conductance $\tilde{G}$ and a reluctance $\tilde{B}$:

$$\frac{q_s}{V_p s} \approx -\frac{\tilde{B}}{s^2} - \frac{\tilde{G}}{s} - \tilde{C}_p^{\varepsilon} \frac{s^2 + \tilde{\omega}_{oc}^2}{s^2 + \tilde{\omega}_{sc}^2} \,. \tag{2.22}$$

Network identification

To identify the parameter values of the equivalent piezoelectric structure, the true elastance from Equation (2.17) is fitted to the model. The identification procedure was first presented in [117] and is described hereafter for completeness.

At first, a best network model needs to be found that will be used to fit the parameters. For an elastive model, this procedure consists of fitting the parameters from Equation (2.20) to the true elastance given in Equation (2.17). Respectively, the parameters from Equation (2.22) are fitted to Equation (2.21) in the capacitive case. To decide whether an elastive or capacitive model should be chosen, the distance from the frequency of interest ω_0, which could, e.g., be a resonance frequency ω_{sc}, to the poles or zeros of the elastance is evaluated. It follows a comparison between (1) the sum of the distances from the frequency of interest to the two closest surrounding poles with the respective distances to (2) the two closest surrounding zeros to this frequency. If the former is greater than the latter, the network is modeled as an elastive type. Otherwise, a capacitive network is assumed.

If a dynamic elastance is to be fitted, the following expression is approximated:

$$\frac{V_s}{q_s} = -\tilde{L}s^2 - \tilde{R}s - \frac{1}{\tilde{C}_p^\varepsilon}\frac{s^2+\tilde{\omega}_{sc}^2}{s^2+\tilde{\omega}_{oc}^2} = \frac{\tilde{L}s^4 + \tilde{R}s^3 + \left(\tilde{L}\tilde{\omega}_{oc}^2 + \frac{1}{\tilde{C}_p^\varepsilon}\right)s^2 + \tilde{R}\tilde{\omega}_{oc}^2 s + \frac{\tilde{\omega}_{sc}^2}{\tilde{C}_p^\varepsilon}}{s^2+\tilde{\omega}_{oc}^2} \,. \tag{2.23}$$

The idea is then to retain a pole p and a zero z from the true elastance which are chosen to be the closest from the frequency ω_0. The approximation function then reads

$$\frac{V_s}{q_s} \approx \frac{(as^2+bs+c)(s^2+2z_r s+z^2)}{s^2+2p_r s+p^2} \,. \tag{2.24}$$

Besides the conditions for p and z, additional conditions are imposed by the interpolation. The identification procedure can then be summarized as follows:

1. Consider the actual V_s/q_s and set the pole p that is closest to $j\omega_{sc}$ (of magnitude p and real part p_r) to $\tilde{\omega}_{oc}$.

2. Find the closest zero V_s/q_s (of magnitude z and real part z_r) to this p.

3. We build the function $f(s) = (s^2+2p_r s+p^2)/(s^2+2z_r s+z^2)V_s/q_s$. The constants a, b and c are determined by fitting $f(s)$ in a LSE sense to a frequency range that comprises p and z.

4. Setting Equations (2.23) and (2.24) equal yields the parameters $\tilde{R}$, $\tilde{L}$, $\tilde{\omega}_{oc}$, $\tilde{\omega}_{sc}$ and $\tilde{C}_p^\varepsilon$.

When a mean shunt is used, step 4 has be to executed for every mode of the targeted frequency range and then averaged according to Equations (2.14) and (2.15). Likewise, an average of the parameters $\tilde{R}, \tilde{L}$ and $\tilde{C}_p^\varepsilon$ must be formed. The identification procedure for a capacitive model differs slightly and is described in detail in Appendix A.

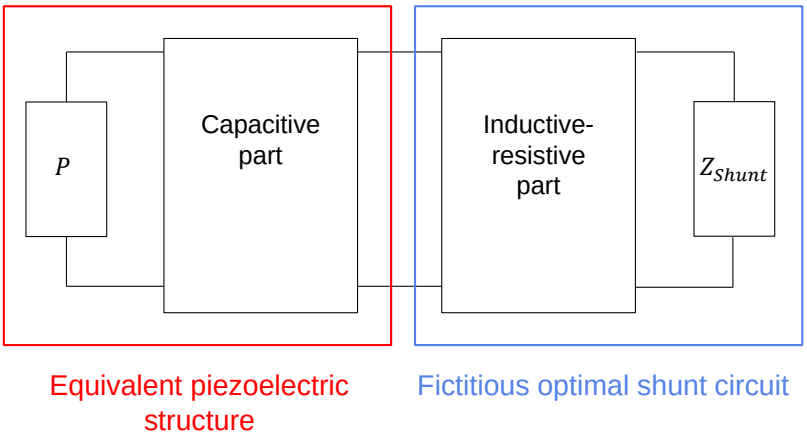

Figure 2.12: Schematics of the tuning procedure for the multimodal current blocking approach. The circuit can be regarded in two parts: an equivalent piezoelectric structure and a fictitious optimal shunt that is to be tuned.

Optimal shunt parameters

Eventually, the optimal parameters of the shunt branch can be calculated from the equivalent piezoelectric structure. Knowing $\tilde{C}_p^{\varepsilon}$, $\tilde{\omega}_{sc}$ and $\tilde{\omega}_{oc}$, either the isolated mode or the mean shunt strategy can be applied to determine the optimal shunt parameters R^* and L^* of the n^{th} fictitious shunt branch. Together with the parameters of the piezoelectric structure, they add up the to the physical shunt parameters [117]:

$$R = R^* - \tilde{R}, \qquad L = L^* - \tilde{L} \ . \tag{2.25}$$

This tuning procedure needs to be performed for all subsequent branches of the shunt until all parameters are determined.

2.6 Conclusion

This chapter presented the challenges that can be faced in vibration damping of complex structures. A specific focus was set on bladed structures. Different approaches for vibration mitigation of these structures exist, all of which have significant limitations, making this research topic still highly relevant. The damping solution chosen herein relies on piezoelectric shunt damping. In this thesis, the proposed innovation is twofold. First, the use of a DVA represents a compact, effective and versatile solution. Second, a tuning strategy targeting multiple modes of different mode families is proposed by incorporating a current blocking multimodal shunt circuit within the isolated mode and mean shunt strategies. In the following chapters, the proposed strategy will be demonstrated experimentally on two bladed structures, namely a bladed rail and a BluM.

Chapter 3

Experimental vibration mitigation of a bladed rail

3.1 Introduction

We now focus on the experimental application of the shunt tuning strategies introduced in Chapter 2. The shunt circuits were realized with DVAs (cf. Section 1.4.2 and 1.4.3) shunted to multiple transducers and acting simultaneously on the structure. The strategy presented in Chapter 2 is demonstrated using a bladed rail, a simplified version of an industrial bladed disk which also features low damping and mode families with a relatively high modal density. This chapter begins with a description of the experimental setup and the structure under investigation. A practical procedure is then outlined for the identification of the plant parameters, which is essential for the tuning of the shunts. Finally, the experimental damping performance of these shunts are presented. First, the focus is set on the first family of bending modes, including a robustness analysis of the shunts. Second, two mode families are targeted at the same time.

3.2 Experimental setup

The structure

The experimental structure is a 3D-printed steel support with five equidistant blades of the same shape. The bladed rail is displayed in Figure 3.1 and was already the subject of previous numerical investigations [30, 126]. The geometrical properties of the blades conform to current state-of-the-art designs for bladed disks [32]. In the experimental setup, both ends of the support structure (rail) were clamped by 3D-printed clamps made of PLA and fixed on an optical table. At the underside of the rail, five PIC151 (10 mm × 15 mm × 0.5 mm, Physik Instrumente) piezoelectric patches were glued with conductive glue since high strains are expected at this location [32].

One patch $\#i$ is connected to a respective DVA $\#i$, $i = 1, ..., 5$ (see Figure 3.3). Different pictures of the experimental set-up are shown in Figures 3.1 and 3.2. In addition, Figure 3.4 gives an overview of the patch arrangement in relation to the blade shape. For reasons of confidentiality, no further details on the dimensions of the structure can be provided.

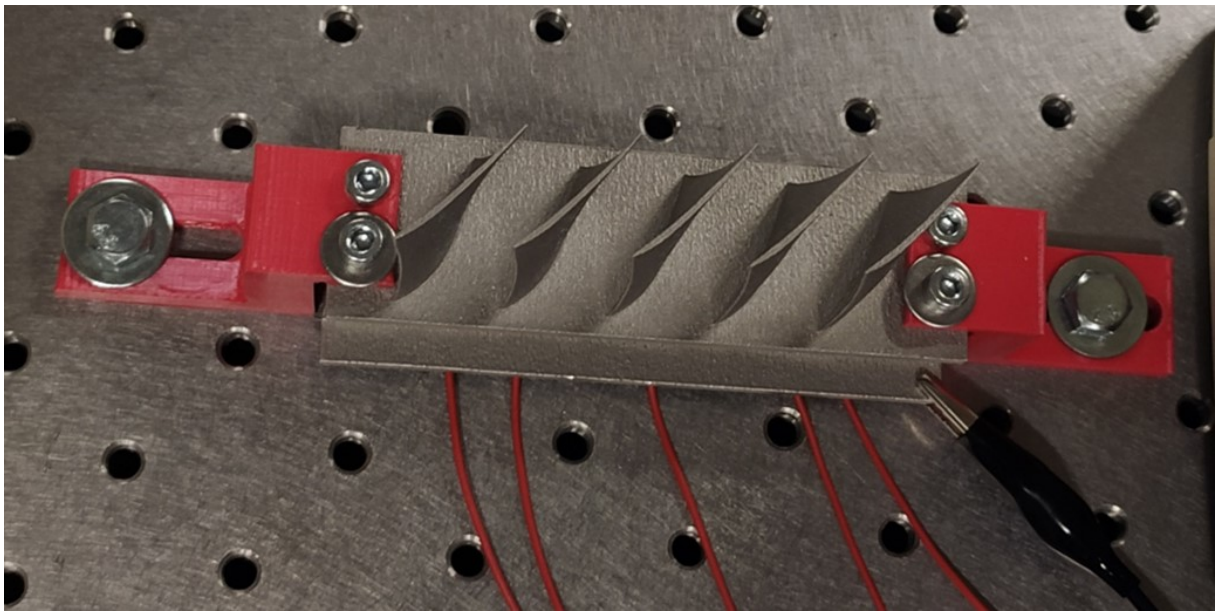

Figure 3.1: The bladed rail structure clamped to an optical table.

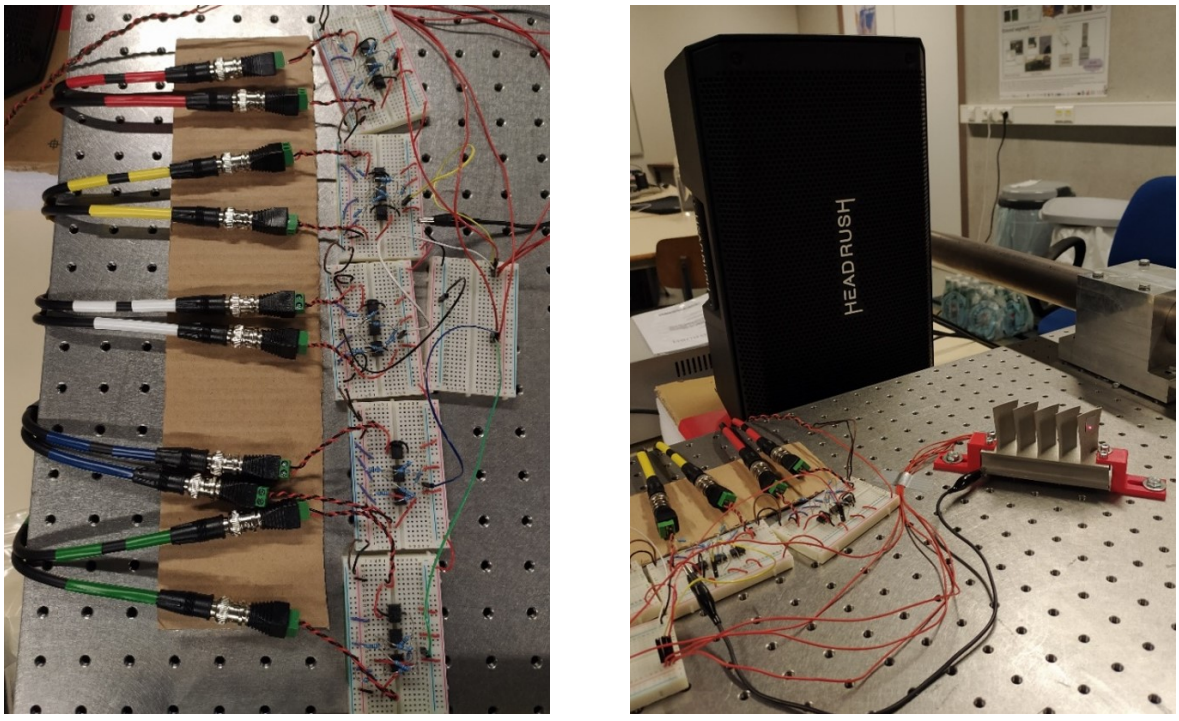

(a) **(b)**

Figure 3.2: Experimental setup for the experiments with the bladed rail. The five patches of the rail were connected to five DVAs (a). For acoustic excitation, the speaker in the background was used (b).

Equipment

The excitation signal was an acoustic sine sweep over the range of one or two mode families of the bladed rail, realized by a Headrush FRFR-108 Active Monitor speaker (cf.

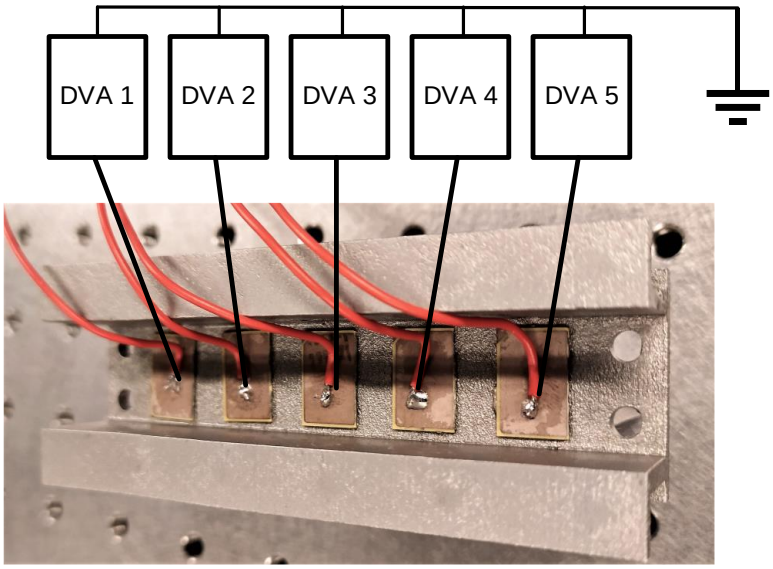

Figure 3.3: Schematics of the experimental setup: Five piezoelectric patches are glued to the bottom of the support structure at the locations of the blade roots. The patches are each connected to one DVA. The DVAs are grounded.

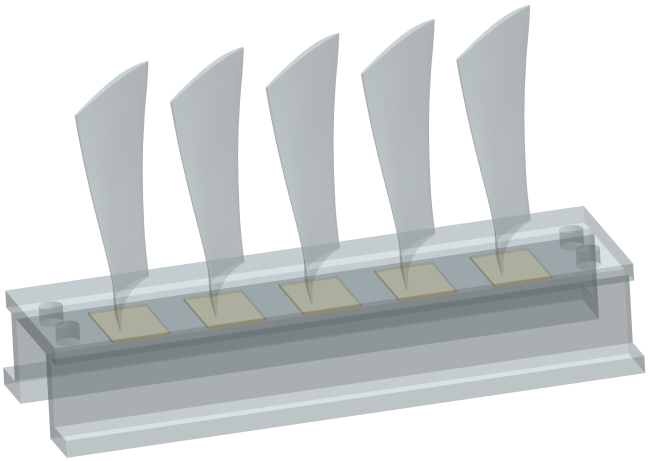

Figure 3.4: Layout of the experimental bladed rail with five piezoelectric patches glued on the rail at the locations of the blade roots.

Figure 3.2b). In order to assess the vibration reduction, a laser vibrometer was installed to measure the velocity at the first tip blade. The results were then post-processed in the Simcenter Testlab software. For the realization of the digital shunts, a controller board MicroLabBox from dSPACE and the associated software were used.

Dynamics of the bladed rail

In order to obtain an overview of the structure's dynamics and the locations of the mode families, the open-circuit FRF of the first blade tip was measured and analyzed. This was achieved by disconnecting the electrodes of the piezoelectric patches from the DVAs

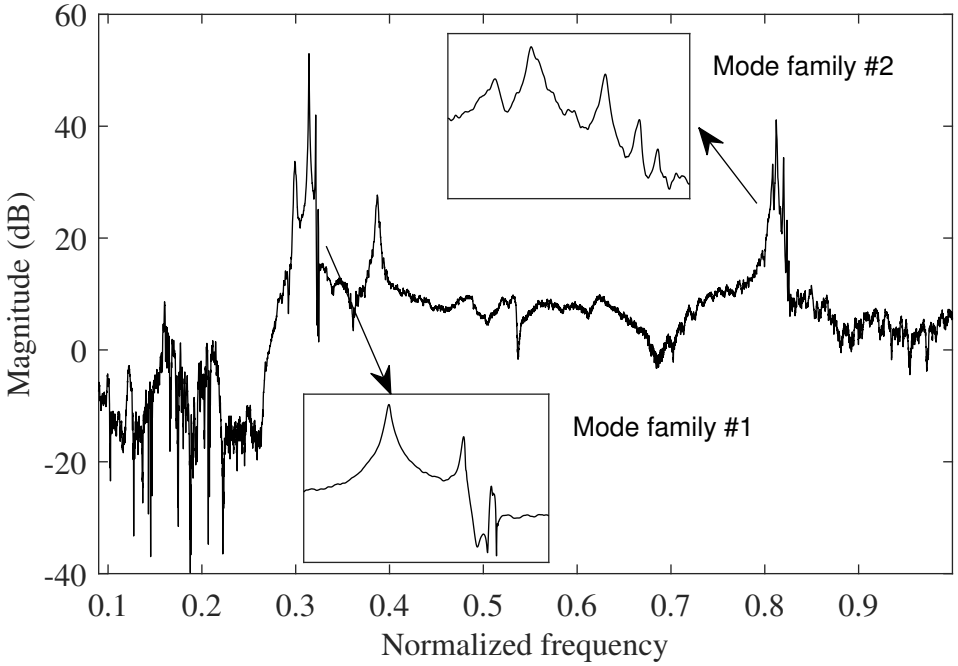

Figure 3.5: Open-circuit FRF of the first blade under a sine sweep acoustic excitation.

Family 1		Family 2	
Frequency	Damping ratio [%]	Frequency	Damping ratio [%]
0.3143	0.03	0.7943	0.05
0.3213	0.03	0.8146	0.03
0.3240	0.03	0.8200	0.02
0.3243	0.08	0.8237	0.02
-	-	0.8257	0.02

Table 3.1: Normalized resonance frequencies and associated damping ratios of the first and second mode families.

and exciting the structure with a sine sweep over the first two groups of bending modes and the first torsion modes. Their approximate location and their mode shapes could be characterized based on numerical simulations conducted in [127]. The focus of this study was on the first two mode families so that the sweep rate of the excitation was set to $0.5\,\mathrm{Hz\,s^{-1}}$ in their frequency range and to $10\,\mathrm{Hz\,s^{-1}}$ in the region of the other modes. Figure 3.5 shows the FRF of the first blade tip. Mode family #1 located between 0.30 and 0.33 is the first bending mode family. The second mode family between 0.79 and 0.83 is associated with the first torsion modes of the blades. The natural frequencies in the two targeted families are listed in Table 3.1. Since the structure has five blades, five modes are expected to be visible for each family. However, only four resonance peaks were visible for family #1. It was possible to account for this during the tuning procedure by targeting one mode with two patches.

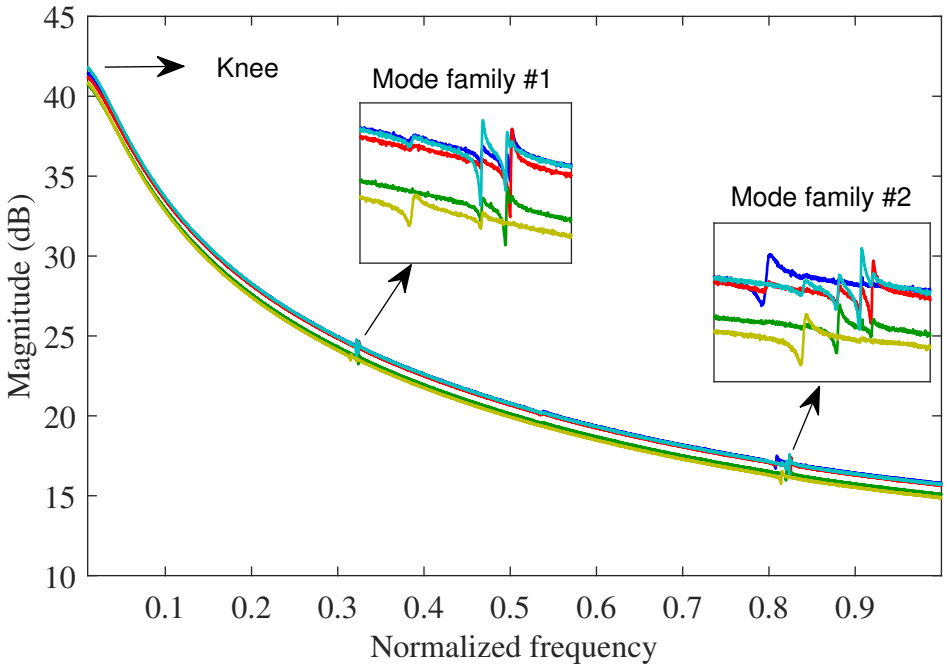

Figure 3.6: Dynamic impedances of the five piezoelectric patches in the frequency range up to mode family #1 and #2; P1 (—), P2 (—), P3 (—), P4 (—) and P5 (—).

Dynamic impedances and coupling assessment

In a first step, parametric models of the plant transfer functions are needed to obtain the system parameters required for shunt tuning and to evaluate the coupling. To this end, the structure was excited by a multisine excitation over the full frequency range via the piezoelectric patches. A multisine signal is periodic and composed of multiple sine waves that are harmonically related. Various frequencies can be excited at the same time with a user-defined amplitude and random phase [128]. The resulting transfer functions are the dynamic impedances of the electromechanical system (cf. Equation (1.42)). The measured impedances are presented in Figure 3.6, with a close-up on the mode families in Figure 3.7. On the basis of these dynamic impedances, state-space models of the plant transfer functions were identified for the different patches using the PolyMAX modal parameter estimation method [129] in a multiple-input multiple-output (MIMO) context. The method works with a stabilization diagram that allows the user to manually select the poles in a prescribed frequency range, facilitating the identification of closely-spaced modes. To this end, the frequency ranges of interest were predefined and curve fitting procedures with increasing model orders were performed up to a user-defined limit in each frequency range. The poles that were consistently identified with increasing model orders were then considered as stabilized poles. A selection of the stabilized poles was then performed by displaying these poles together with the measured FRFs in a stabilization diagram. The resulting stabilization diagrams for mode families #1 and #2 are presented in Figure 3.8. The procedure yields a good accuracy while avoiding to retain spurious poles in the identification process, making the user confident that the selected poles are close to the actual poles of the physical system. Evaluating the stabilization

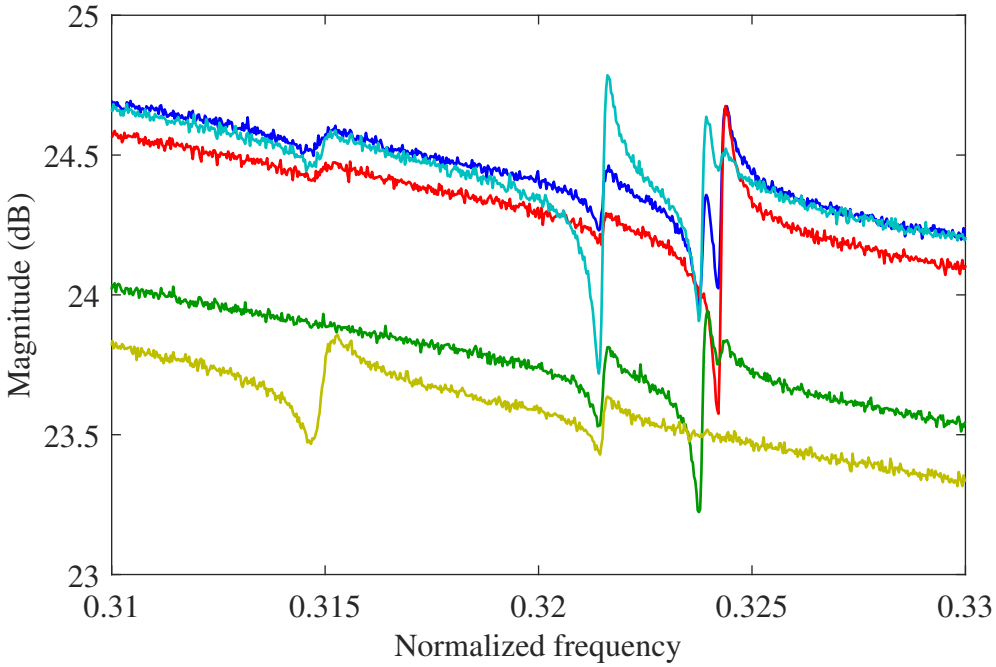

(a) Mode family #1.

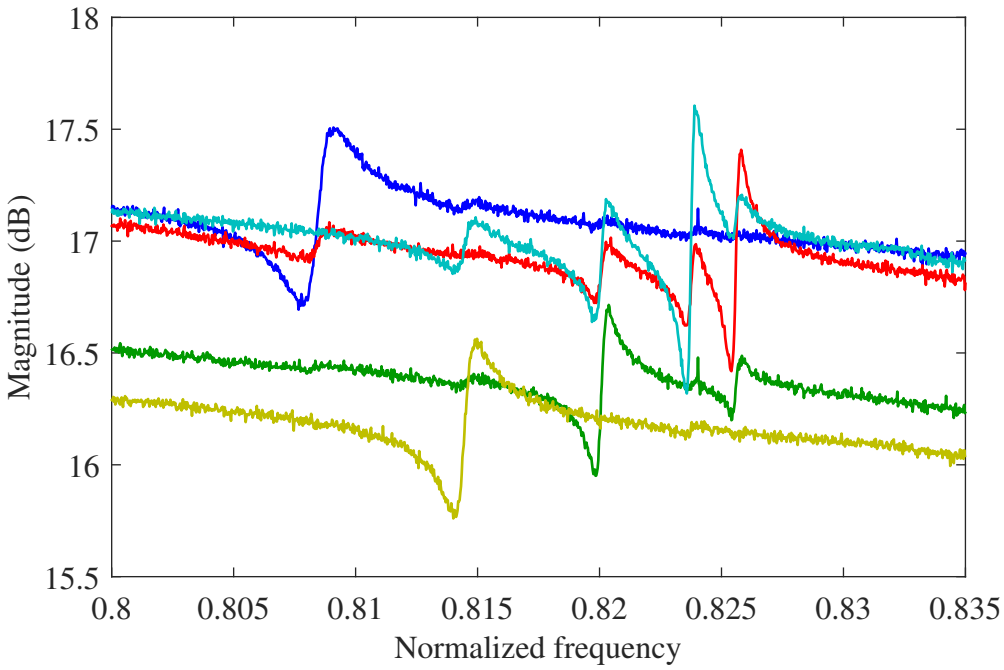

(b) Mode family #2.

Figure 3.7: Close-up views on the dynamic impedances of the five piezoelectric patches in the range of the mode families #1 and #2: P1 (—), P2 (—), P3 (—), P4 (—) and P5 (—).

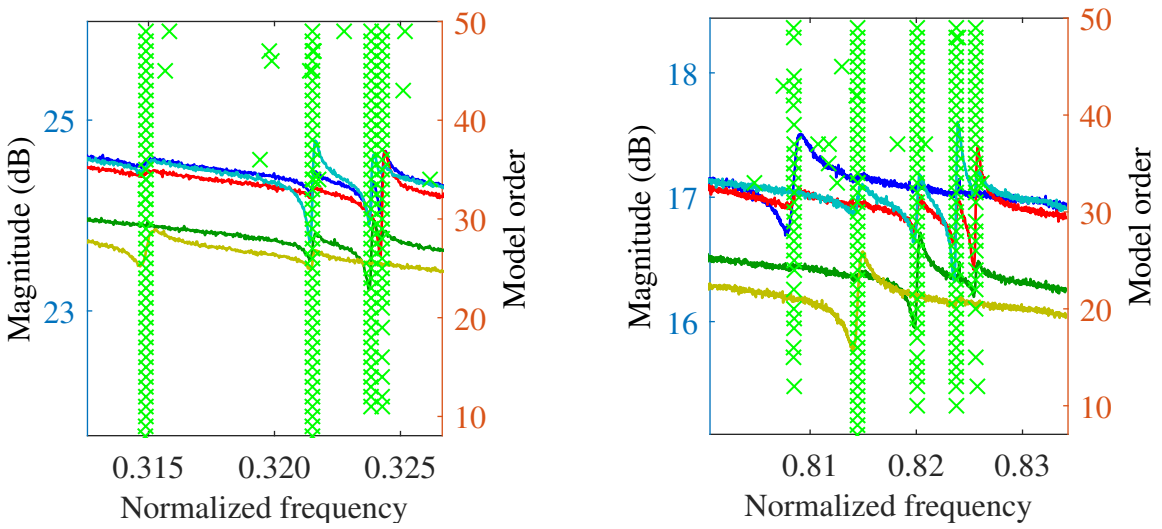

(a) Mode family #1 **(b)** Mode family #2

Figure 3.8: Stabilization diagram obtained with the PolyMAX method applied to measured dynamic impedances of the five piezoelectric patches: P1 (—), P2 (—), P3 (—), P4 (—) and P5 (—). The stabilized poles are displayed with a ×.

diagram results in a set of selected poles and corresponding participation factors. With the knowledge of these parameters, the corresponding mode shapes can then be obtained by expressing the measured FRFs in a partial fraction format and solving the equations in a least-squares sense [129], a procedure that is known as least-squares frequency-domain (LSFD) method [130].

In addition to the complex poles that correspond to the resonance frequencies of the electromechanical system, a simple pole is to be identified from the dynamic impedance measurements. This pole occurs at low frequencies and corresponds to a so-called 'knee' in the FRF caused by the imperfections of the DVA resistances, as discussed in Section 1.5 (cf. Figure 3.6). At the beginning of the system identification procedure, this knee is identified as a real pole by evaluating the trend of the measured impedances over the full frequency range. The PolyMAX method, originally designed to identify complex poles, was adapted to account for this real pole. The resulting state-space model is presented in a Bode plot in Figure 3.9.

From the knowledge of the identified resonance frequencies, the electrical coupling between the modes and the patches could be assessed with the EMCF (2.13) and an evaluation of the measured impedances in Figure 3.6. As outlined in Section 1.2.3, the identified zeros (poles) of the dynamic elastances are the short- (open-) circuit resonance frequencies of the electromechanical structure. If they are clearly visible in the transfer function, it can be concluded that there is a significant electromechanical coupling between a patch and the considered mode. Eventually, a mode is assigned to the patch with which the electromechanical coupling is the strongest, as shown in Table 3.2. For mode family #1, only four modes are visible in Figure 3.7a so that the fourth mode was targeted by two patches simultaneously. The results of the identification then served as the basis for the

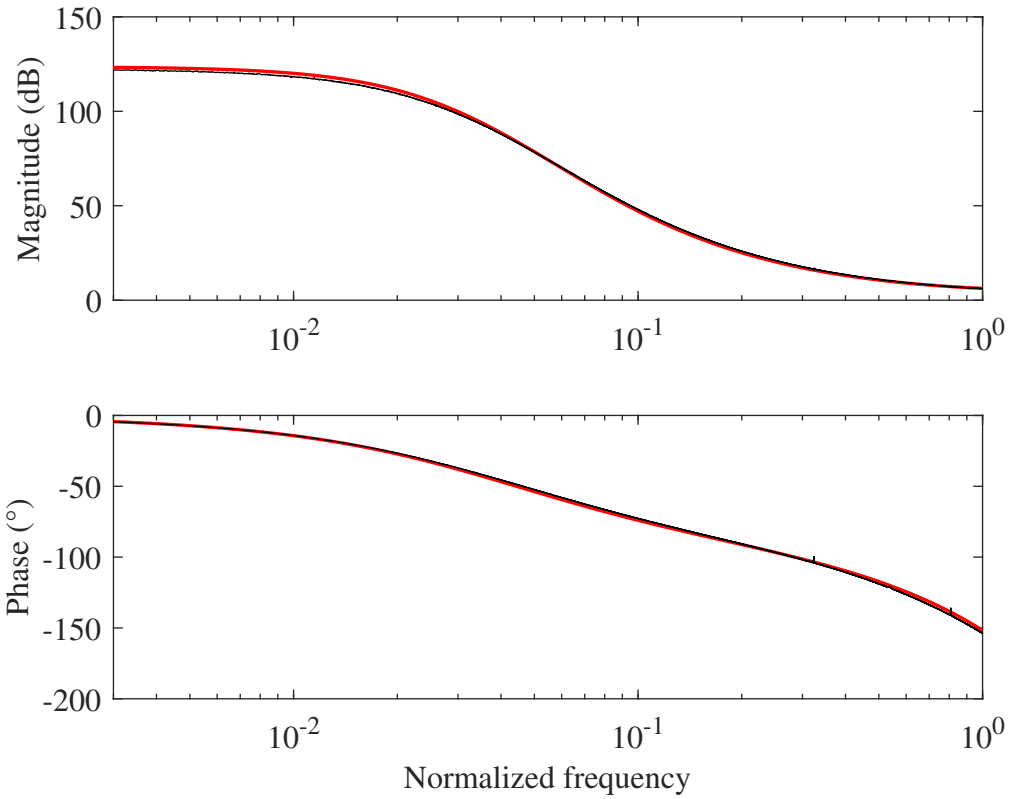

Figure 3.9: Bode plot of the measured dynamic impedance for patch 1 (▬) and the identified state-space model (▬) of the overall trend and the imperfection.

application of the proposed tuning strategies (cf. Section 2.5). The structural resonance frequencies and damping ratios identified by the PolyMAX method are listed in Table 3.1. The associated damping ratios are very low, i.e., on the order of 0.05%. As discussed in Chapter 2, this low damping is typical of bladed assemblies and justifies the use of additional damping devices. Since the identified damping ratios are small, damping was neglected in the tuning process. However, when damping cannot be neglected, methods that account for it can be employed during shunt tuning [131].

Mode family 1	
Mode	Patch
1	5
2	4
3	3
4	2 & 1
-	-

Mode family 2	
Mode	Patch
1	1
2	5
3	3
4	4
5	2

Table 3.2: Patch distribution per mode family.

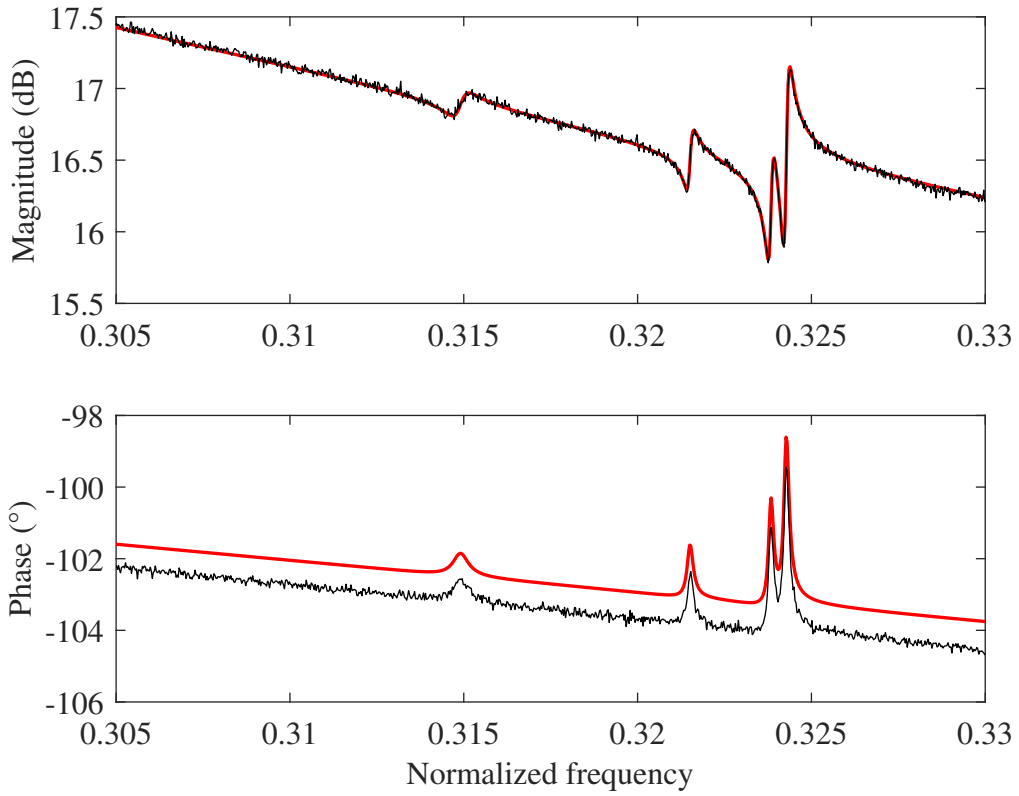

Figure 3.10: Bode plot of the measured dynamic impedance for patch 1 (▬) and the identified state-space model (▬) in the frequency range of mode family #1.

3.3 Summary of the shunt tuning procedure

The different steps for the design and implementation of the shunt transfer functions applied to the bladed rail sum up as follows:

1. Measurement of the dynamic impedance functions of all patches in a MIMO setup using multiple DVAs simultaneously (cf. Section 1.4.2).

2. System identification of the measured data using the PolyMAX method [129]. The identified parameters are the resonance frequencies (open- and short-circuit), damping ratios and values for δ_c that are then considered in the controller gain during the shunt implementation (step 5).

3. Coupling evaluation for each patch with the targeted modes and mode-to-patch distribution for the isolated mode strategy.

4. Design of the shunt transfer function $Y_{Shunt}(s)$ based on steps 1 and 2. The tuning rules from Section 2.5 and (if multiple mode groups are targeted) Section 2.5.2 are exploited in this step.

5. Discretization of $Y_{Shunt}(s)$ according to the procedure described in Section 1.6.1 and implementation of the shunts using the dSPACE software. The identified values for δ_c are considered directly by setting the controller gains.

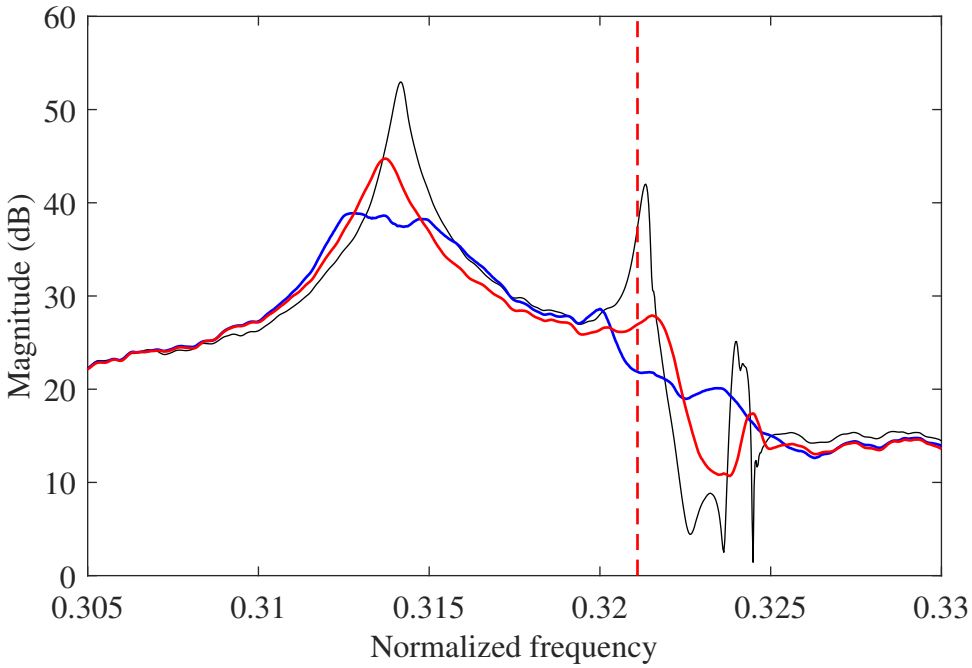

Figure 3.11: FRFs of the first mode family of the bladed rail: open circuit (—), shunted by the isolated mode (—) or mean shunt (—) strategies. The mean frequency is indicated in (- - -).

We note that this procedure relies solely on experimental measurements and the resulting identified data so that no numerical model of the structure is needed. This greatly facilitates the application of the method and makes it highly practical.

3.4 Experimental results

3.4.1 Mode family #1

The first mode family was first targeted, implementing a single series RL shunt circuit per DVA. In order to assess damping performance, the bladed rail was excited acoustically by a sine sweep, both in open-circuit and shunted configurations. The FRFs corresponding to isolated mode and mean shunt tuning are presented in Figure 3.11. A substantial reduction of the resonance amplitudes could be achieved with both approaches. However, the mean shunt strategy is more effective, particularly for the first mode, i.e., it yields a reduction of 14 dB in comparison to 8 dB for the isolated mode strategy. While both approaches performed similarly for the second mode (19 dB), for modes 3 and 4, the isolated mode and mean shunt strategies achieved a reduction of 8 and 12 dB, respectively. The mean frequency targeted by the mean shunt strategy was located in the vicinity of the third and fourth modes which explains the better performance. In addition, the influence of closely-spaced modes can somewhat compromise the attenuation performance of the isolated mode strategy so that a precise frequency target is not always possible.

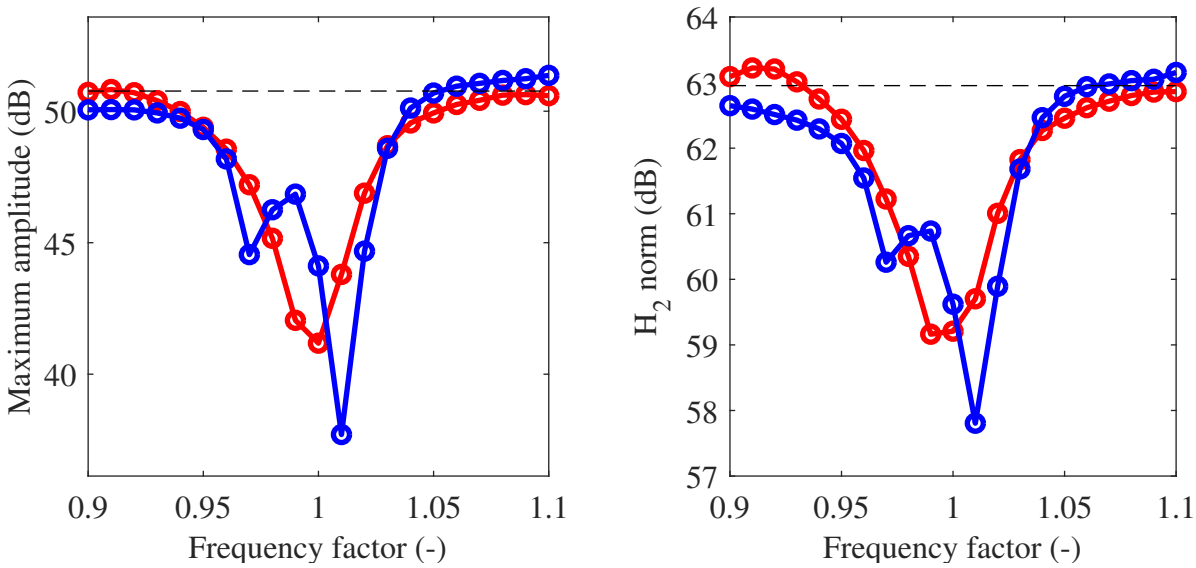

Figure 3.12: H_∞ (a) and H_2 (b) norms of the FRF for the first mode family of the bladed rail for different shunt frequencies. The isolated mode (—) and mean shunt (—) strategies are compared to the open-circuit case (▪ ▪ ▪).

3.4.2 Robustness study

In order to examine the robustness of the shunts, the performance was studied under changing conditions. First, the digital controller frequency was varied to account for errors that could happen during shunt tuning, e.g., due an inaccurate system identification. Second, the system was altered physically by adding masses to the blades to simulate mistuning.

3.4.2.1 Variation of the digital shunt frequency

The optimal frequencies of each shunt function were varied up to $\pm 10\,\%$. The performance was assessed based on two norms, namely the H_∞ (maximum amplitude) and the H_2 (area under the FRF) norm and is displayed in Figure 3.12. It can be observed that the optimal amplitude attenuation with the isolated mode strategy occurred at a frequency factor of 1.01 which can be attributed to a slight time variability of the setup. Comparing the evolution of the norms, it is visible that the mean shunt performance was consistently and smoothly decreasing with deviations of the frequency factor from the optimal value. This was not the case for shunts tuned according to the isolated mode strategy as there was an abrupt performance decrease at a frequency factor at 0.99. There may not have been sufficient coupling with this new mode for this particular frequency variation. The mean shunt could compensate better for this due to the averaging of the parameters. Generally, the damping performance of the two shunts can be considered effective up to frequency deviations of approximately $5\,\%$ with respect to the initially identified ones. If the shunts are detuned to a greater extent, the DVAs can even slightly amplify the resonance amplitudes in comparison to the uncontrolled case (cf. Figure 3.12).

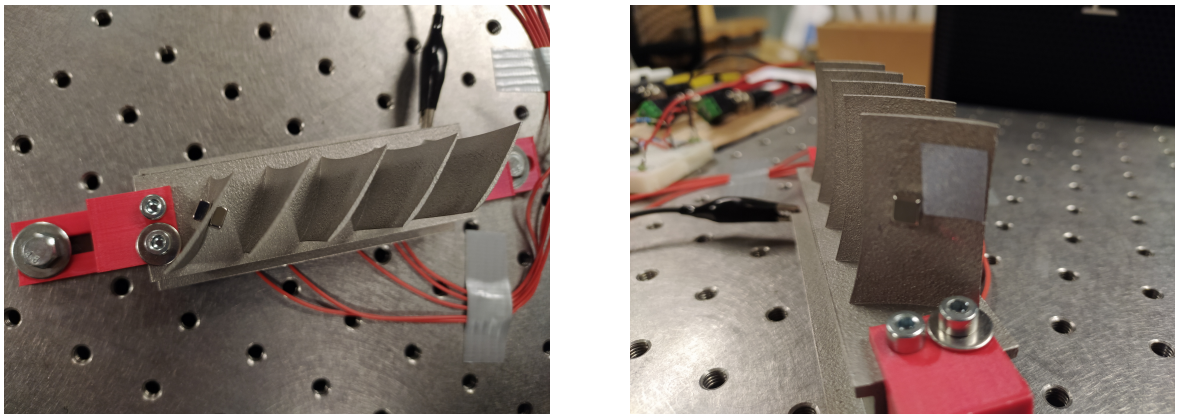

Figure 3.13: Modification of the bladed rail. A pair of magnets was added to the first blade in order to change the resonance frequencies of the blade modes.

3.4.2.2 Modification of one blade

In a next step, an additional mass in the form of a pair of magnets was added to the first blade of the structure as depicted in Figure 3.13. Approximately 45 % of the blade mass was added causing a shift of 2.7 % of the first resonance frequency of mode family #1. The FRFs of the initial and modified systems are presented in Figure 3.14. In addition, the FRFs of the detuned and retuned systems are shown both for the isolated mode (Figure 3.14a) and mean shunt strategies (Figure 3.14b). From Figure 3.14a it can be seen that a satisfactory damping reduction of all modes could be achieved using the retuned isolated mode strategy. On the other hand, a retuned mean shunt could only reduce the amplitude of the first resonance frequency by less than 1 dB (cf. Figure 3.14b). The modifications caused the resonance frequency of this mode to be relatively far from the other modes of the mode family. As the mean shunt strategy relies on a large proximity of the frequencies to be attenuated, it was less efficient in this case. However, a look at the direct comparison between the two proposed approaches in Figure 3.15 evidences that the performance of the mean shunt was clearly more robust on the other family modes in comparison to the isolated mode strategy owing its more broadband character.

3.4.2.3 Modification of all blades

All five blades of the structure were then modified with magnets. In order to model a non-uniform mistuning, they were placed differently for each blade as displayed in Figure 3.16. The mistuning caused a decrease in the first resonance frequency of 3.6 %. The resulting FRFs are presented in Figure 3.17. Again, the retuned isolated mode strategy proved successful amplitude attenuation of the first mode family. Conversely, the retuned mean shunts could not achieve the same damping performance as in the initial system. From Figure 3.17b, we can see that only modes 2 and 3 could be attenuated effectively while the damping performance on mode 1 was only slightly improved, as already observed in the previous section. On the other hand, there was even an increase in amplitude for mode 4. Regarding the new FRF of the open-circuit measurement, the mistuning caused an increase in the distance between the third and the fourth modes which had a distinct

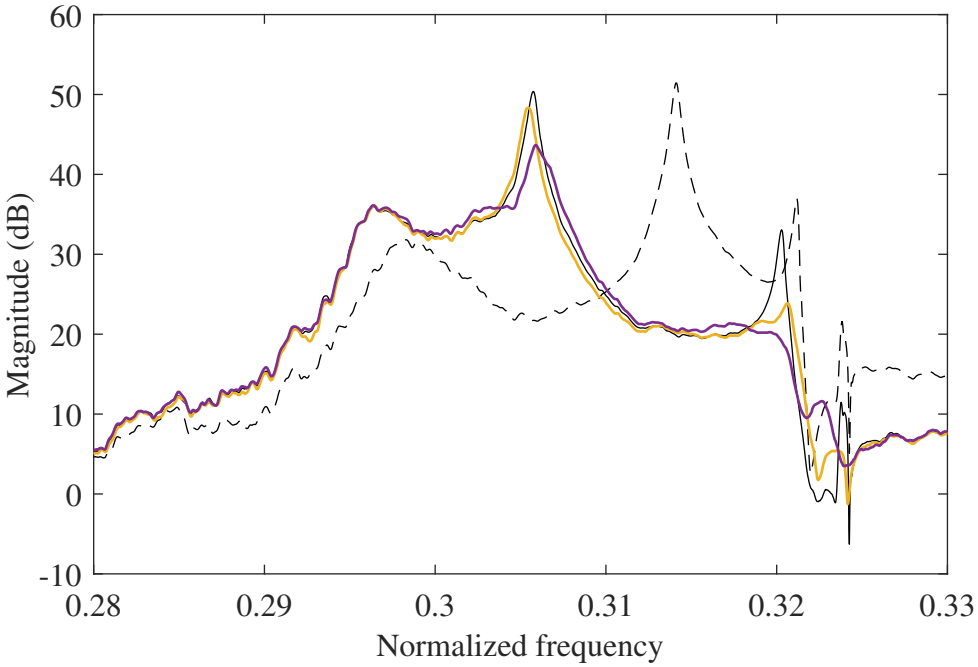

(a) Isolated mode strategy.

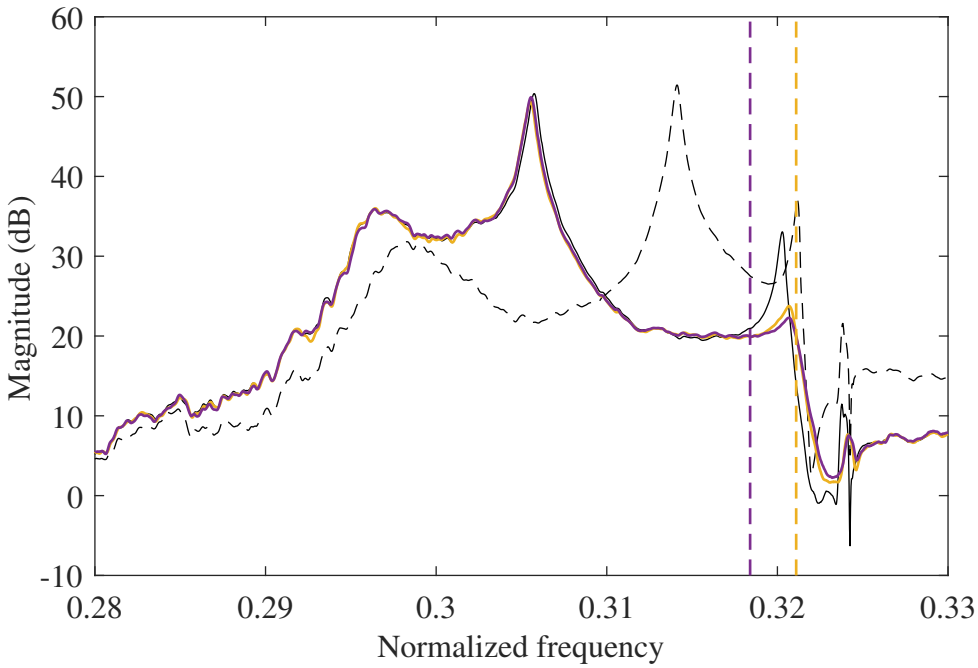

(b) Mean shunt strategy. (▪▪▪) and (▪▪▪) indicate the respective mean frequencies.

Figure 3.14: Robustness study (first blade mass modified): open-circuit FRFs of the initial (▪▪▪) and mistuned systems (▬), system controlled by the detuned (▬) and retuned (▬) shunts.

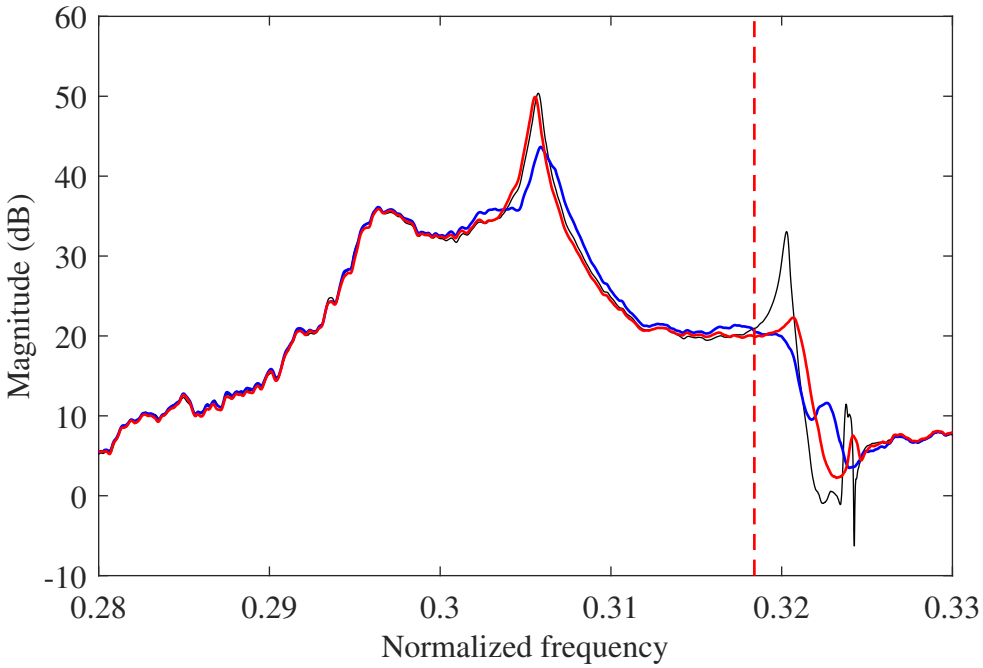

Figure 3.15: Robustness study (first blade mass modified): FRFs of the open circuit (modified) (▬), of the system shunted by an RL shunt (retuned) (▬) and of a mean shunt (retuned) (▬). The mean frequency is indicated in (▪ ▪ ▪).

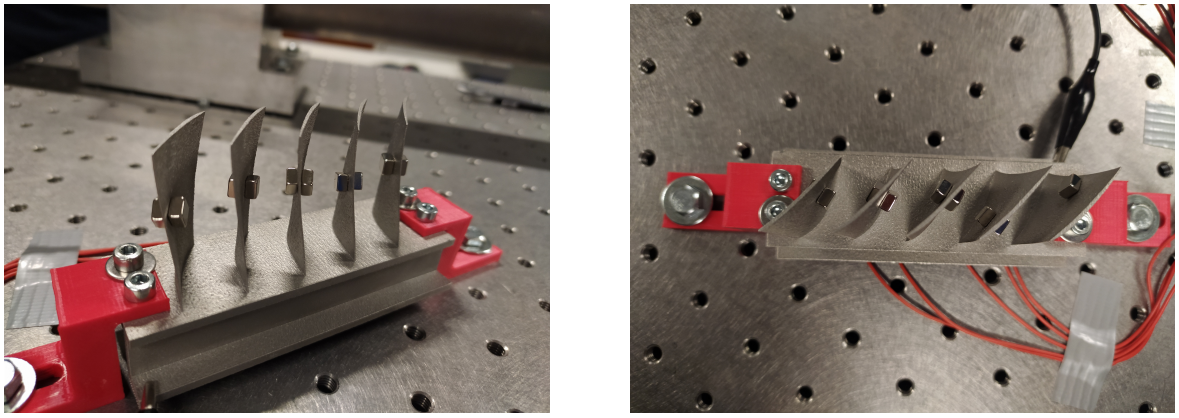

Figure 3.16: Modification of the bladed rail. A pair of magnets was added to each blade.

effect on the damping performance of the mean shunt. From these observations, it can be stated that this strategy becomes less efficient and is not necessarily robust when mistuning introduces a large gap between the targeted modes. A retuning of the shunts with this strategy might thus not always be advisable.

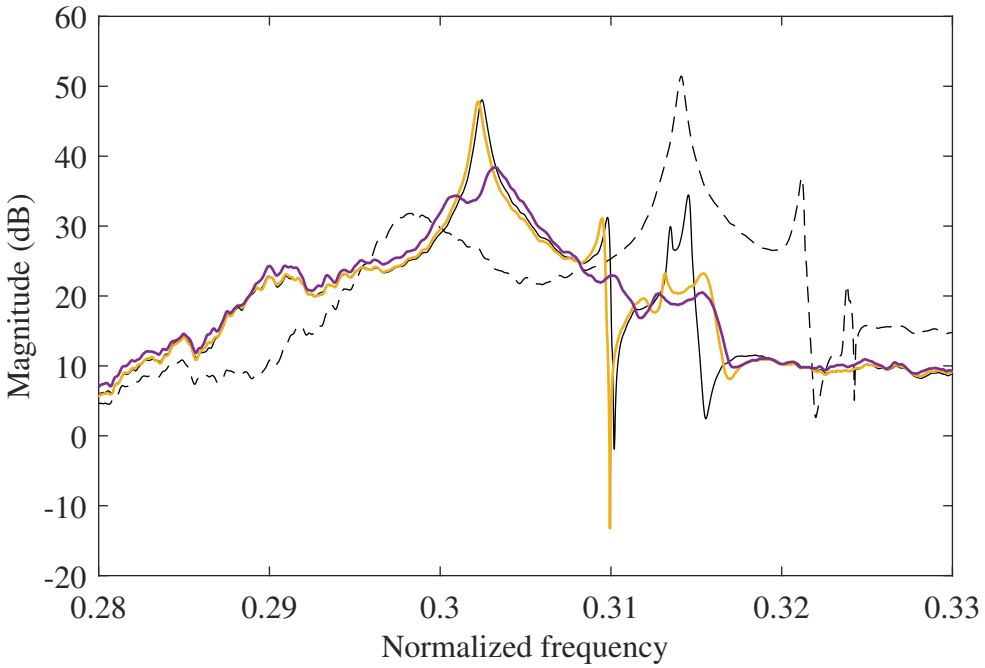

(a) Isolated mode strategy.

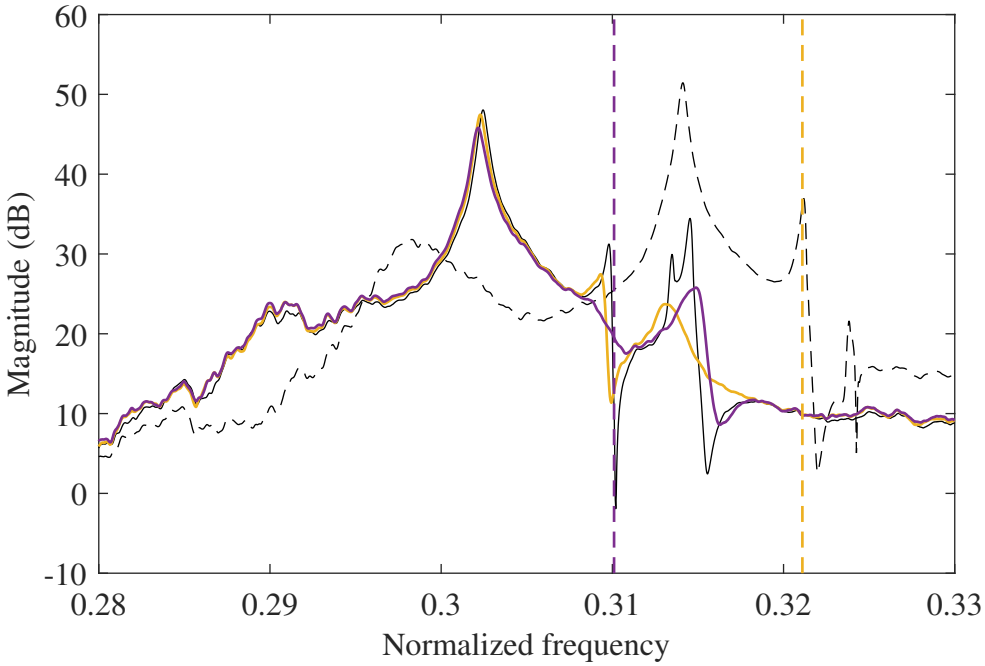

(b) Mean shunt strategy. (▪▪▪) and (▪▪▪) indicate the respective mean frequencies.

Figure 3.17: Robustness study (all blades modified): open-circuit FRFs of the initial (▪▪▪) and mistuned systems (▬), system controlled by the detuned (▬) and retuned (▬) shunts.

3.4.3 Vibration mitigation of two mode families

By exploiting a two-stage current blocking shunt circuit, the vibrations of two mode families could be attempted simultaneously. To this end, a single DVA targeted one mode per

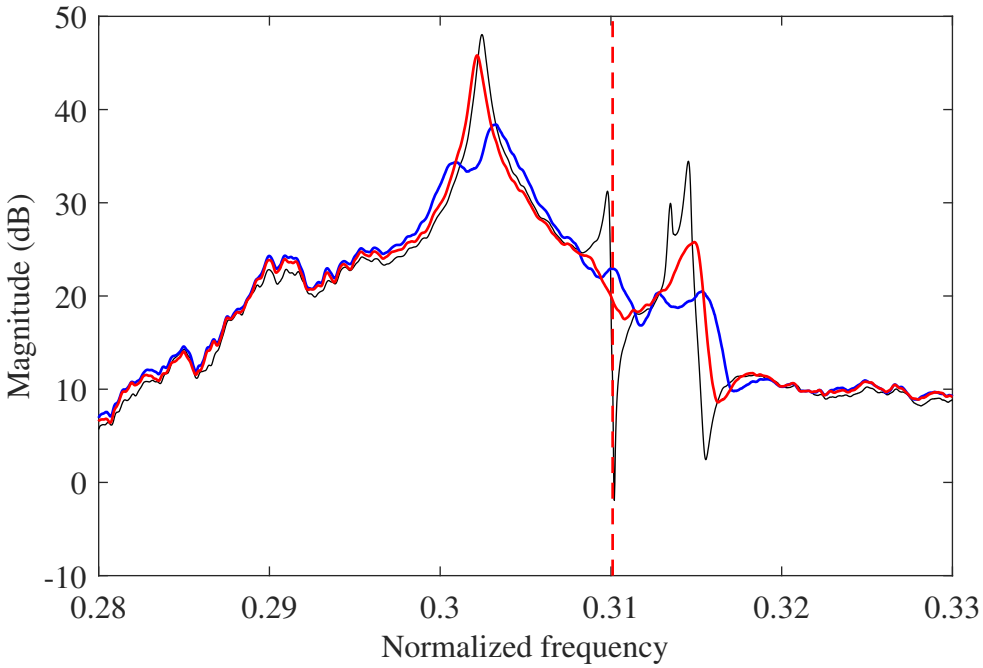

Figure 3.18: Robustness study (all blade masses modified): FRFs of the open circuit (modified) (▬), of the system shunted by an RL shunt (retuned) (▬) and of a mean shunt (retuned) (▬). The mean frequency is indicated in (▪ ▪ ▪).

family, following the isolated mode and the mean shunt strategy, respectively. The FRFs of the controlled systems are presented in Figure 3.19 for both mode families. The resonance amplitudes of the second mode family could be reduced by approximately 10 dB. This uniform and superior (in comparison with the first mode family) damping performance can be explained partly by the fact that the modes were more equally distributed in the frequency range. The damping performance for the second mode family comes at the cost of a somewhat lower performance of the shunts on the first mode family, particularly for the mean shunt approach. Considering an additional mode family and targeting multiple modes with one shunt circuit can thus lead to a decrease in the damping performance for certain frequencies compared to a single branch shunt circuit. This is due the fact that the control authority needs to be distributed over more modes. In addition, the current can possibly flow through other branches than the desired one when the complexity of the electrical circuit increases so that an optimal current flow might not always be guaranteed.

3.5 Conclusion

The multimodal tuning strategies proposed in Chapter 2 proved herein successful during the experimental testing of a bladed rail structure featuring different mode families with closely-spaced modes. Identifying the parameters of the host structure with the help of the PolyMAX method enabled the tuning of the shunt parameters. Subsequently, the magnitudes of 9 modes could be reduced by a factor ranging from 5 to 18 dB, depending on the mode or tuning strategy considered. A robustness study on the first mode family showed that the shunts performed satisfactorily for changes of the resonance frequencies

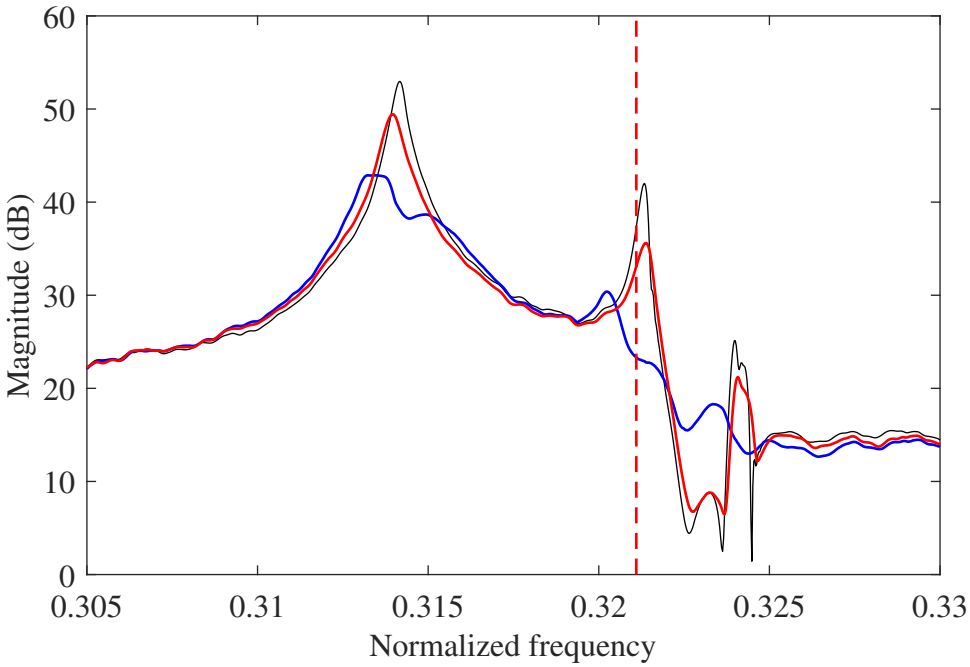

(a) Mode family #1.

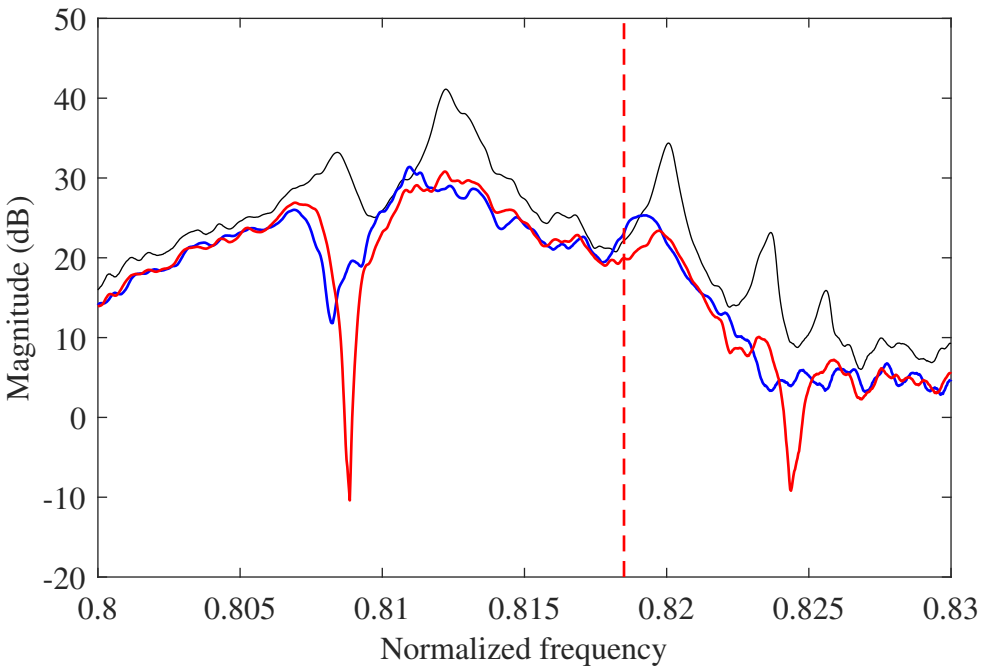

(b) Mode family #2.

Figure 3.19: FRFs of the bladed rail with open-circuited (—) patches or shunted with current blocking circuits in the range of the mode families #1 and #2. Isolated mode (—) and mean shunt (—) strategies.

up to 5 %, making the method robust toward a certain degree of structural mistuning. Thanks to the use of DVAs, the shunt parameters could be easily adapted, highlighting the flexibility of a digital implementation.

Chapter 4

Experimental vibration mitigation of a BluM

4.1 Introduction

After the bladed rail in Chapter 3, the application of interest is now the BluM structure introduced in Section 2.2. It possesses 76 blades; it thus features significantly more vibration modes and also a greater number of piezoelectric patches. This structure was already investigated experimentally by Mokrani et al. [83–85]. In their works, gyrator circuits were used in the synthetic inductors realizing the RL shunts. The structure was excited harmonically without contact using voice coil actuators, and small permanent magnets attached to blade tips. 28 piezoelectric patches were installed in the drum. In order to overcome the need of impractically high inductances, they implemented parallel loops of piezoelectric shunts when targeting specific single resonance frequencies [32, 83]. Further, they addressed the problem of closely-spaced modes through the mean shunt strategy, used as a basis technique for the tuning strategies in Section 2.5 [32, 84]. They observed that mistuning was present in the BluM structure, which impaired damping performance. In contrast to these studies based on analog circuits, our research relies on a digital shunt realization using DVAs, which, in addition to increased tuning flexibility, eliminates the need for synthetic inductors. The isolated mode and mean shunt strategies presented in Section 2.5 are exploited in this chapter to mitigate the vibrations of the BluM.

This chapter is organized as follows. First, the BluM structure and the different setup configurations used for the numerical and experimental studies are described in Section 4.2. In Section 4.3, the results of the numerical study are presented. Sections 4.4.1 and 4.4.2 include a description of the experimental setup together with the dynamic properties of the experimental BluM. The results of the system identification procedure at the root of the shunt tuning strategy are discussed in Section 4.4.3. The chapter ends with Section 4.4.4 which discusses the experimental results including performance and robustness analyses.

4.2 The BluM structure

The BluM structure investigated in this work is a compressor stage of an airplane rotor provided by Safran Aero Boosters [132]. The BluM is made of an alloy of titanium and exhibits 76 blades. 28 patches PI-PIC255 were fixed in the support drum under the blade roots, with one patch covering approximately three blades. Here, one electrode of a patch was connected to the BluM structure. The drum itself is connected to an electrical ground. The patch dimensions are 40 mm × 10 mm × 200 µm. During the experimental campaign, only 16 out of the 28 available patches could be used simultaneously, corresponding to the 5 configurations illustrated in Figure 4.1. Patches marked in red were individually shunted to a DVA. The remaining 12 patches were left in open circuit.

For the sake of industrial confidentiality, any sensitive data about such as response levels and frequencies of the structure is normalized in what follows.

4.3 Numerical study

An FE model of the BluM that was already used for numerical investigations in [30] is considered in this section, featuring a modal damping of 0.01 %. From the ideal case without any mistuning, three different variants of the model were created, each introducing mistuning by arbitrarily adding small masses to the blades of the BluM. While their locations were varied, the total number of masses and mass points remained similar, i.e., between 13 and 16 with an average of 3 g. As displayed in Figure 4.2, mistuning resulted in lower resonance frequencies that also appeared more spread. Mode families #1 and #2 are clearly visible in this figure, represented by an almost horizontal line around frequencies 1.0 and 2.5. Based on the numerical simulations conducted using the Siemens NX software [133], state-space models were built. To this end, 25 FRFs were calculated considering the excitation force F_y in Figure 4.3. The locations were chosen to be evenly distributed over the circumference of the BluM.

For the presentation of the results, the amplitude reduction was assessed by comparing the average of the H_2 norm of the 25 FRFs of the system in open circuit and of the controlled system in the frequency range of the targeted modes. For all simulations, only the mean shunt strategy was exploited with single RL shunts tuned toward the mean frequency of mode family #1. This family was considered to be between frequencies 1.00 and 1.08.

The case without mistuning is first considered. Figure 4.4 shows the evolution of the amplitude reduction as a function of the number of active piezoelectric patches. The piezoelectric patches with the lowest mean coupling factors (over all modes) were removed in the different cases. For a small number of patches, the amplitude reduction increases sharply. Already with 6 patches, the FRF amplitudes are reduced by approximately 50 %. Then, the increase is less impressive. This indicates that it might not be necessary to use all patches simultaneously.

The mean coupling factors averaged over all modes of family #1 are displayed for each piezoelectric patch in Figure 4.5. The overall mean of these EMCF per patch is also

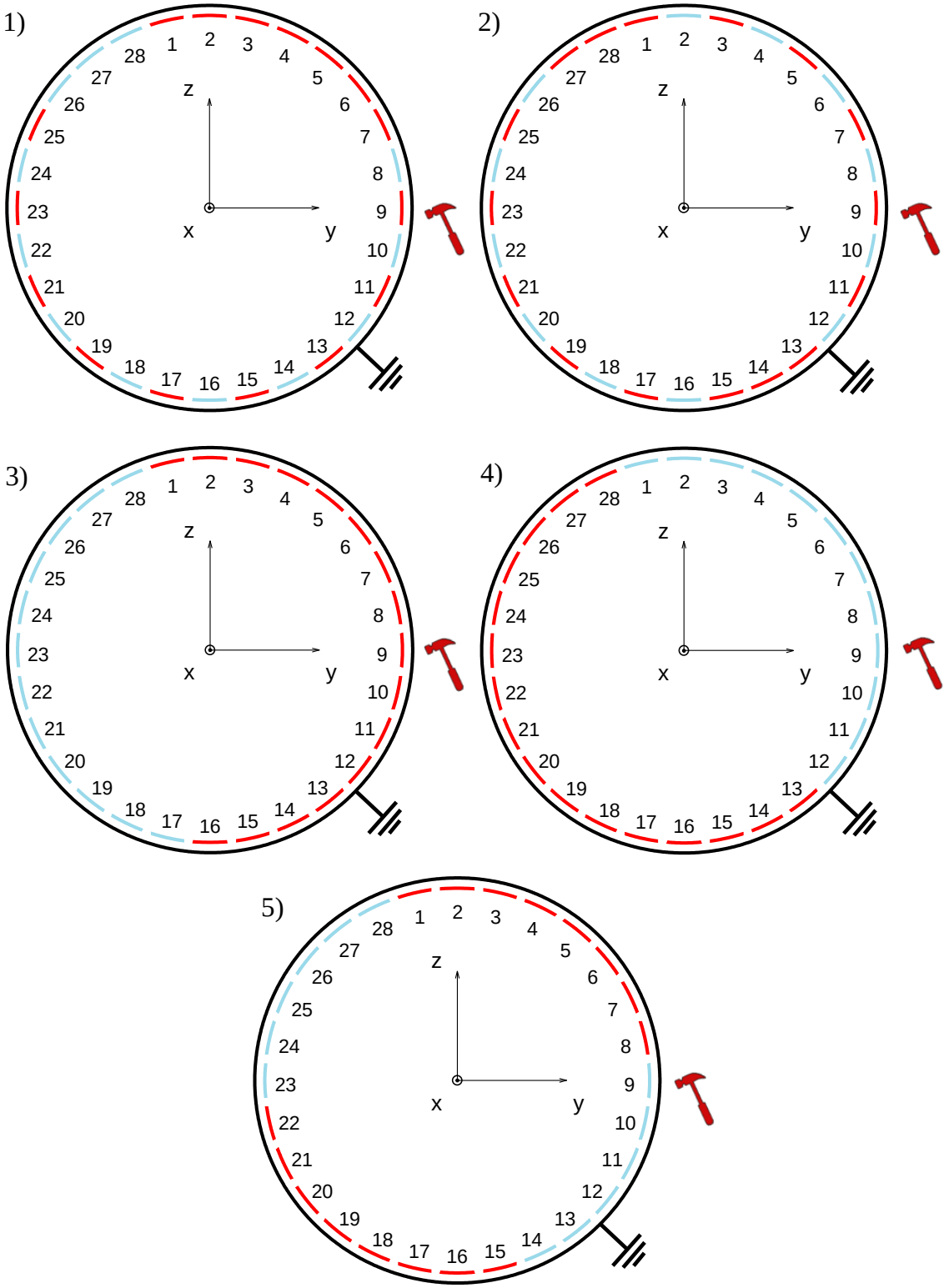

Figure 4.1: Different configurations of the piezoelectric patches. Red indicates that the corresponding patch is used. The numbers 1-5 refer to the respective configuration. The hammer indicates the impact location.

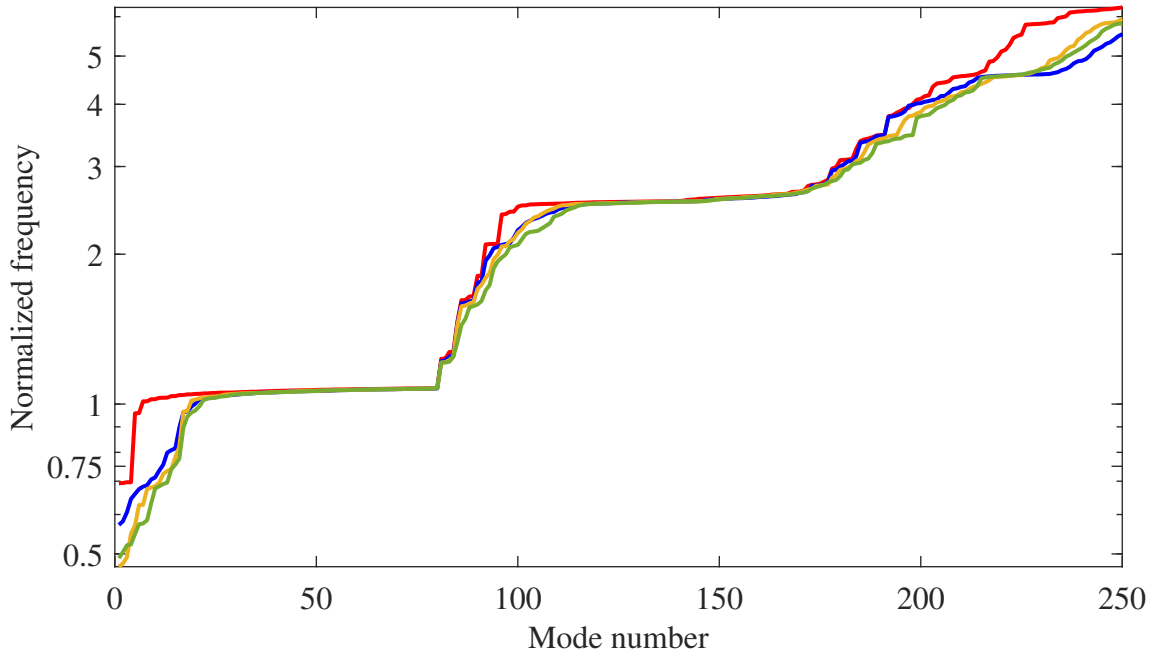

Figure 4.2: BluM frequencies (normalized with respect to the first resonance frequency of mode family #1). No mistuning (—), mistuning case #1 (—), #2 (—) and #3 (—).

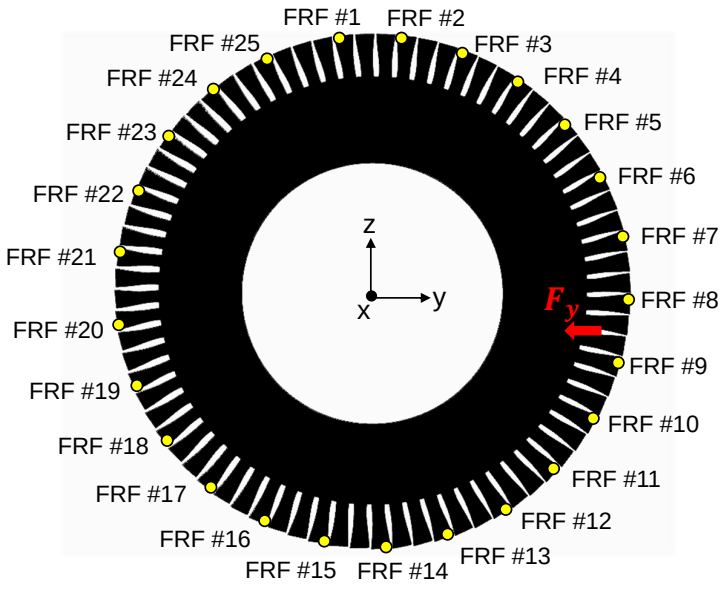

Figure 4.3: Positions where the FRFs were measured. The receptance functions are between the excitation force F_y and the tip displacements in the x direction.

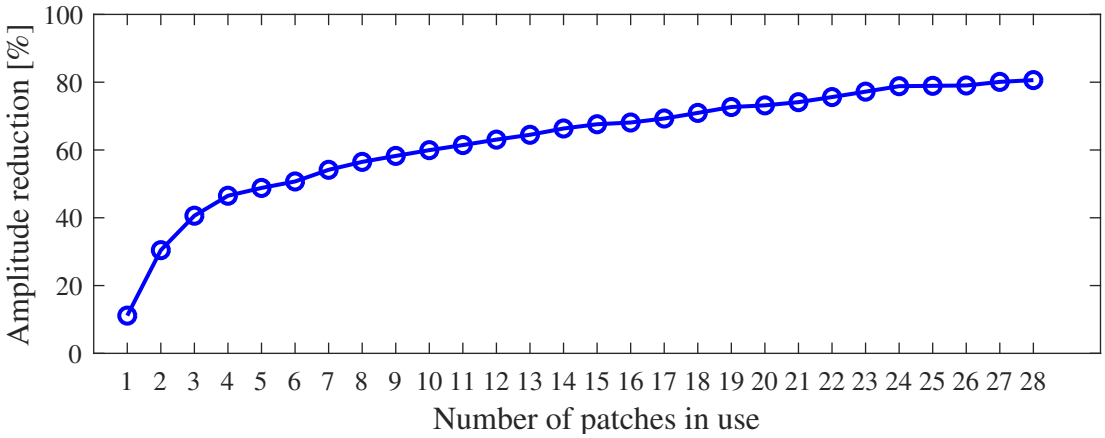

Figure 4.4: Amplitude reduction for mode family #1 as a function of the number of active piezoelectric patches (case without mistuning).

represented. In the absence of mistuning, the figure shows that (i) the deviation from the mean is much smaller and (ii) the coupling is better. The overall mean EMCF for the different mistuned cases remain similar, being approximately 17 % smaller than without mistuning. For some patches, the coupling factors are significantly smaller than the overall mean, which can be explained by the localization of vibrational energy induced by mistuning [134].

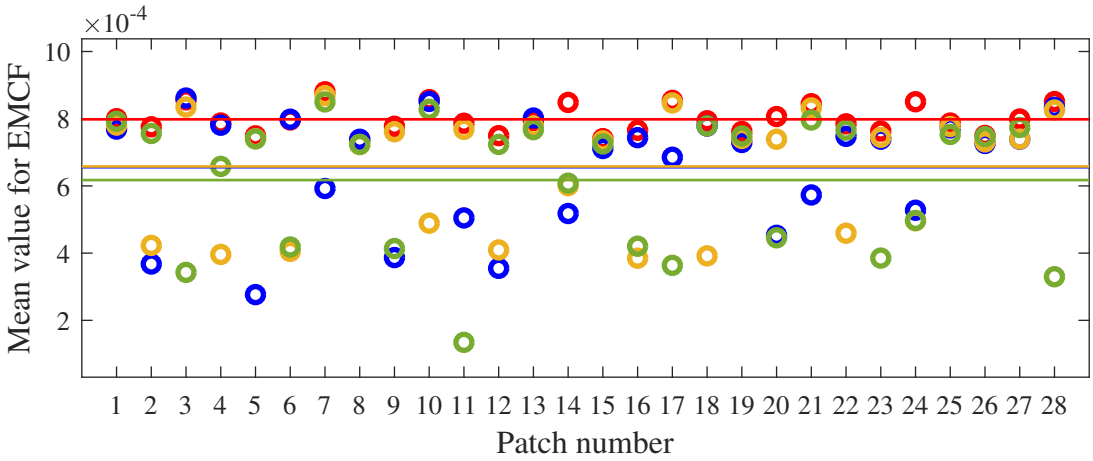

Figure 4.5: Mean coupling factors averaged over all modes of family #1: no mistuning (—), mistuning case #1 (—), #2 (—) and #3 (—). The mean coupling factor over all patches is represented using a horizontal line.

Efficiency of patch configurations

The amplitude reduction for mode family #1 obtained with different patch configurations and different mistunings is displayed in Figure 4.6. It is important to note that the shunts were tuned optimally for each mistuned case. All patch configurations lead to a mean amplitude reduction of more than 60 %. In addition, a reduction of at least 40 % can be

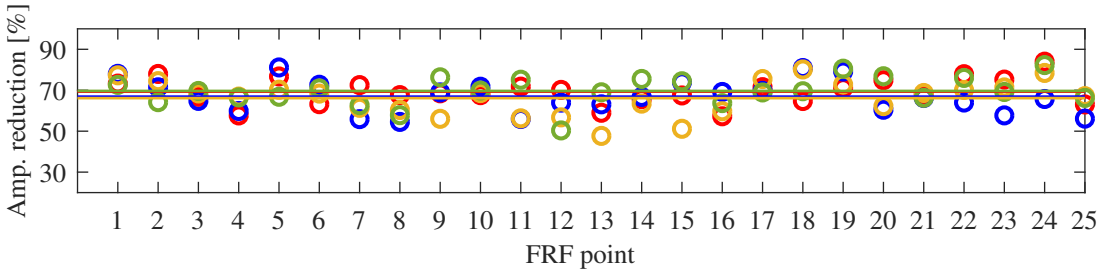

(a) Patch configuration 1.

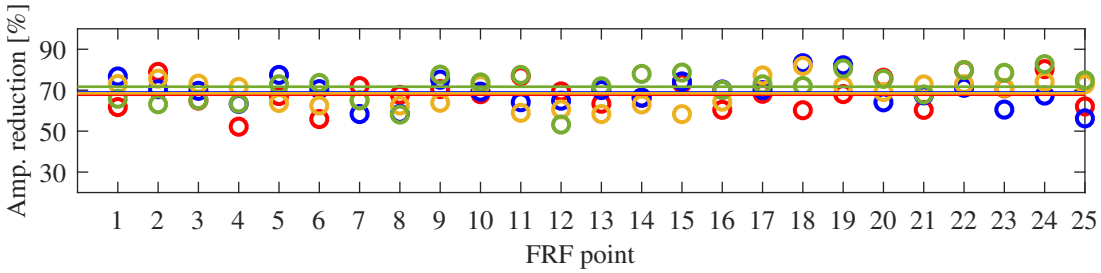

(b) Patch configuration 2.

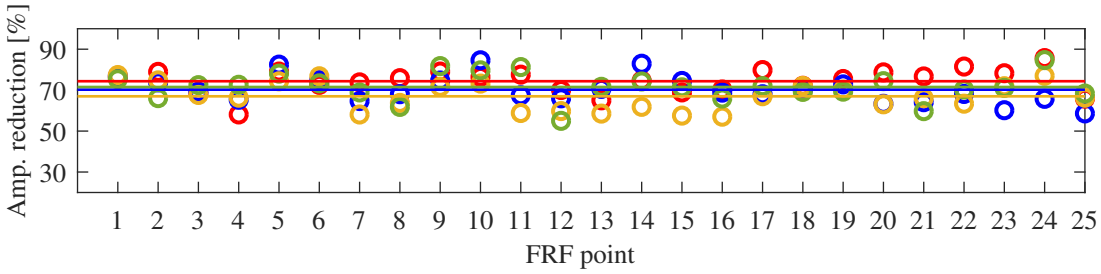

(c) Patch configuration 3.

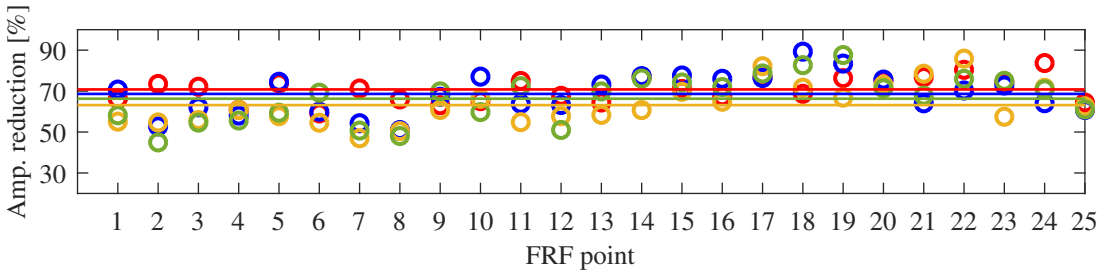

(d) Patch configuration 4.

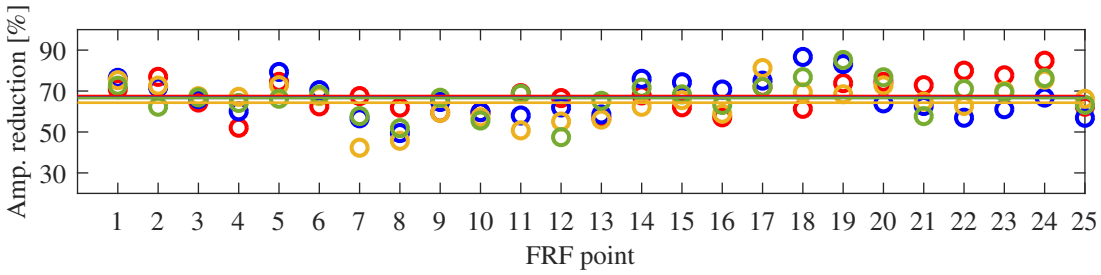

(e) Patch configuration 5.

Figure 4.6: Amplitude reduction for mode family #1. No mistuning (—), mistuning case #1 (—), #2 (—) and #3 (—). All shunts were tuned optimally. The mean amplitude reduction per patch configuration is represented using a horizontal line.

achieved in the worst case scenario. Although the coupling is better without any mistuning, this does not translate into any improvement in terms of amplitude reduction. The similar damping performance can be explained by Figure 4.4, i.e., if enough patches are used, a strong amplitude reduction can be expected even in the presence of mistuning.

Figure 4.7 presents a comparison between the different patch configurations. It confirms our previous findings, i.e., when considering the mean value of the amplitude reduction, all patch configurations yield excellent damping performance. Moreover, no configuration seems to significantly outperform the other configurations.

For illustration, Figure 4.8 depicts the FRFs of four points distributed around the BluM for patch configuration 3 and mistuning #1. The magnitudes were normalized with respect to the FRF amplitude of the first mode of mode family #1. A relatively important and broadband amplitude reduction can be achieved over the whole frequency range of mode family #1. We just note that the amplitude reduction is somewhat smaller around the frequency 1.07 for FRF #7 and #20.

Finally, we stress that this study does not claim to be a comprehensive statistical investigation, but it can rather be seen as a support study for the experimental campaign.

Robustness of patch configurations

In this section, the robustness of damping performance is assessed by using systematically the shunts tuned when no mistuning is present. Unlike the previous section, no shunt retuning is thus achieved when mistuning is introduced. The resulting amplitude reductions are depicted in Figure 4.9. All configurations are relatively robust toward mistuning, providing a mean amplitude reduction of more than 60 %. For obvious reasons, the deviations from the mean are greater than when the shunts are retuned. Again, no patch configuration significantly outperforms the other ones. The receptance of point #10 in Figure 4.10 shows that the amplitude of almost all resonance peaks could be significantly reduced both in the tuned (no mistuning) and detuned (mistuning #1) cases, highlighting that the shunts do not necessarily have to be retuned.

Targeting two mode families

Finally, using the current blocking circuit presented in Chapter 2.5.2, two mode families of the BluM were targeted with the mean shunt strategy. A mistuned BluM structure (case #1) was subject to 16 shunts in patch configuration 3. The results are presented in Figure 4.11 by means of FRF #10. The FRF shows that both mode family #1 (located around normalized frequency 1) and #2 (located around normalized frequency 2.5) could be attenuated with the multi-stage shunt design. Reductions of the resonance amplitudes of up to 20 dB and 15 dB, respectively, could be achieved. Comparing this amplitude reduction on mode family #1 with these obtained using single shunts (cf. Figure 4.10b), we note that there is a loss in damping performance. Using a passive control law, this loss in performance for this mode group can be explained by the fact that the available control authority is now distributed over two frequency ranges. However, the reductions of the resonance amplitudes remain highly satisfying.

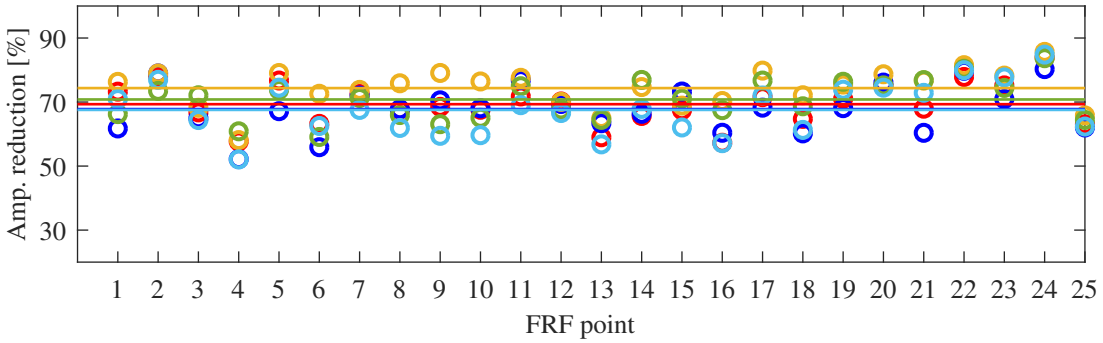

(a) No mistuning.

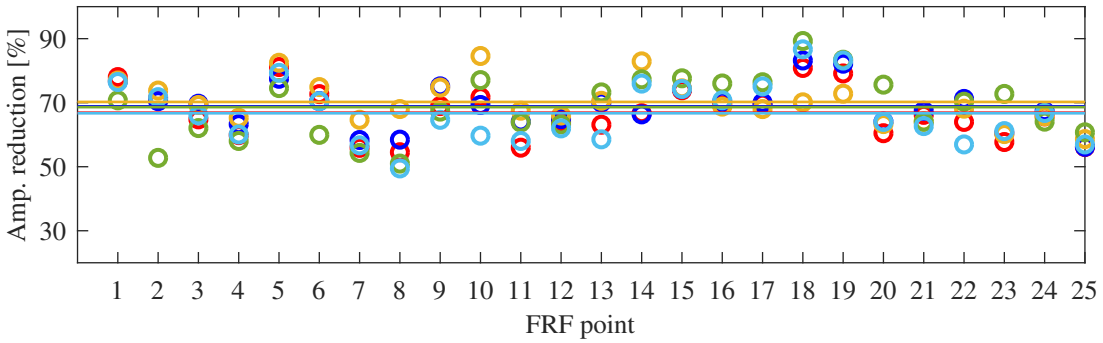

(b) Mistuning case #1.

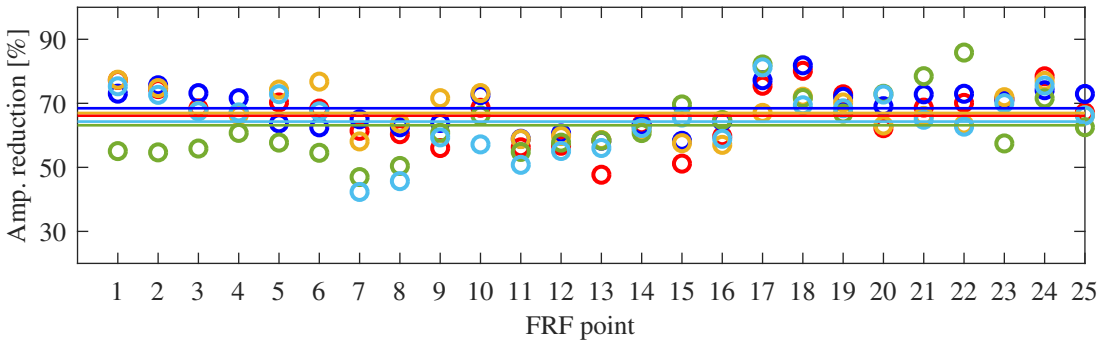

(c) Mistuning case #2.

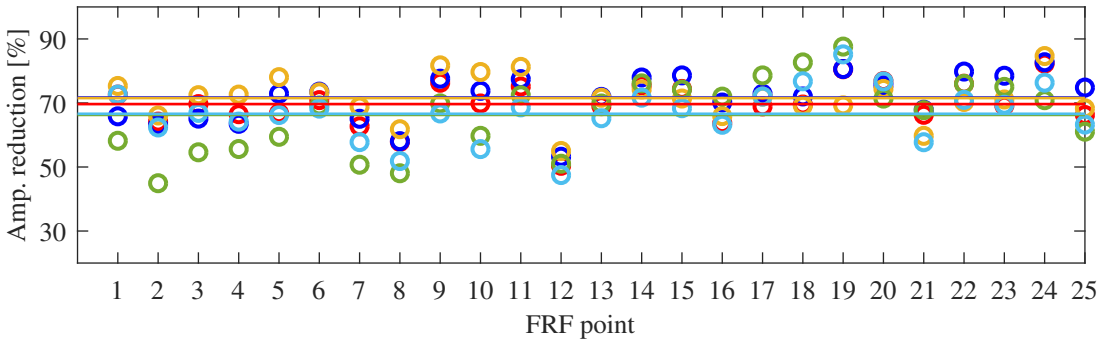

(d) Mistuning case #3.

Figure 4.7: Amplitude reduction for mode family #1. Patch configuration 1: (—), 2: (—), 3: (—), 4: (—) and 5: (—). All shunts were tuned optimally. The mean value per mistuning case is represented using a horizontal line.

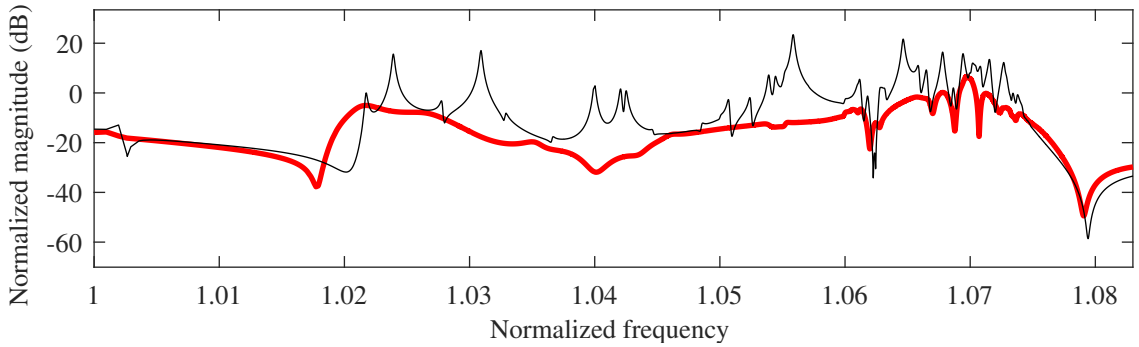

(a) FRF #1.

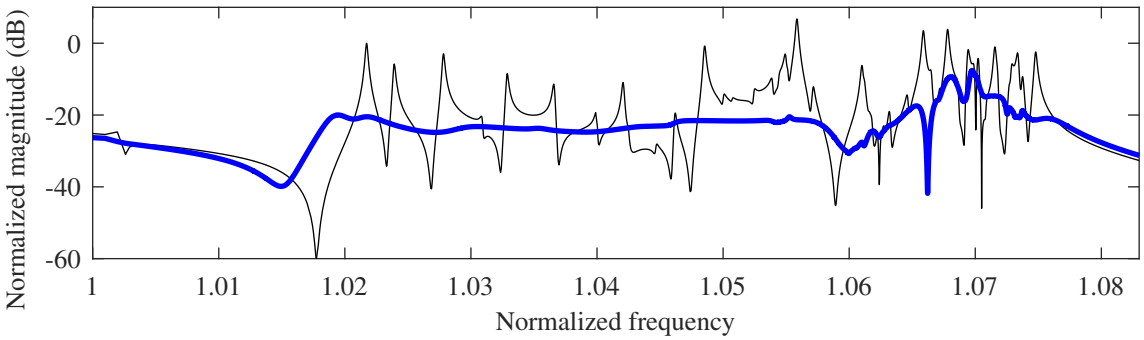

(b) FRF #7.

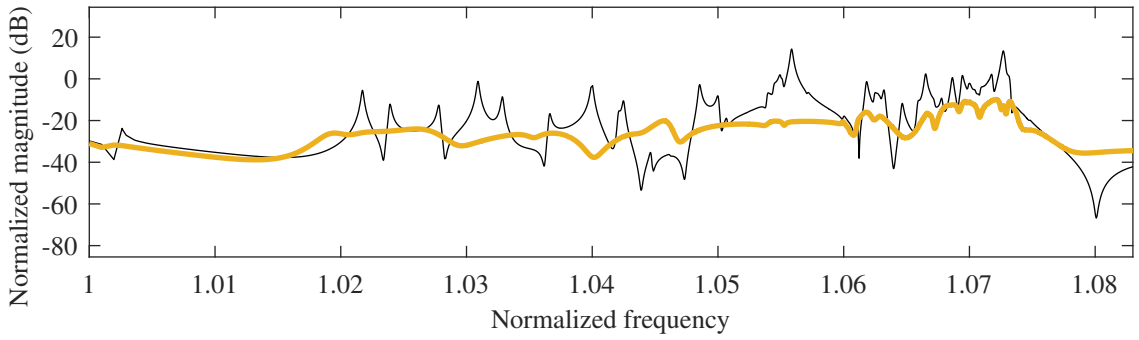

(c) FRF #14.

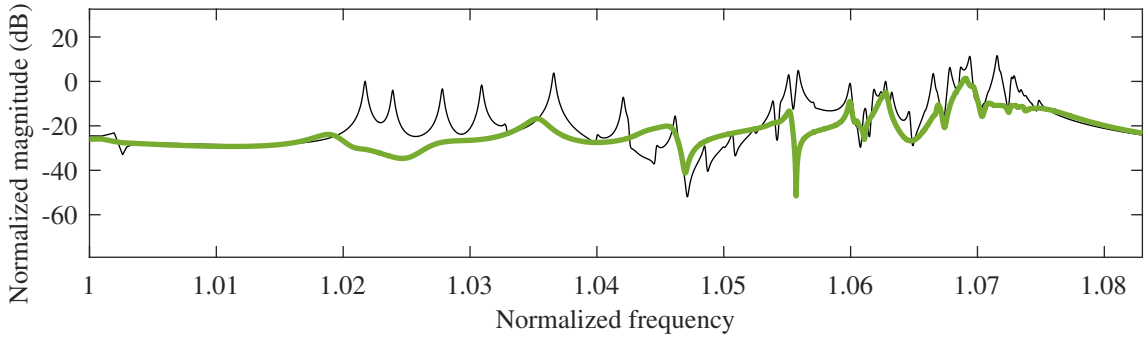

(d) FRF #20.

Figure 4.8: FRF for patch configuration 3 and mistuning #1.

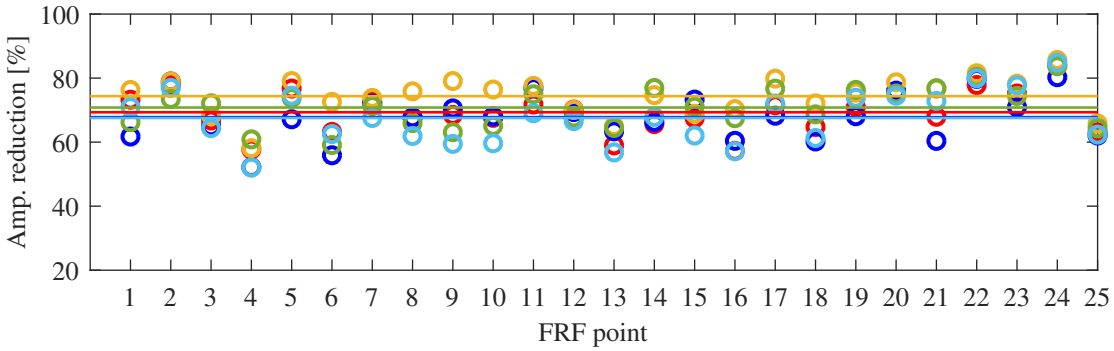

(a) No mistuning.

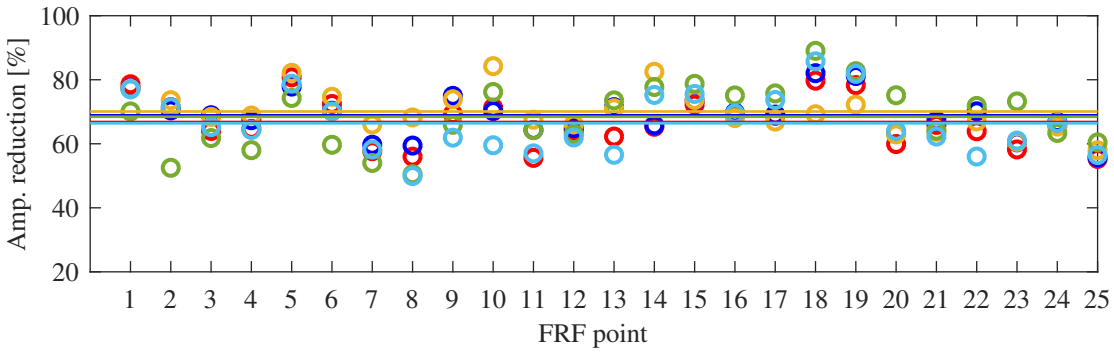

(b) Mistuning case #1.

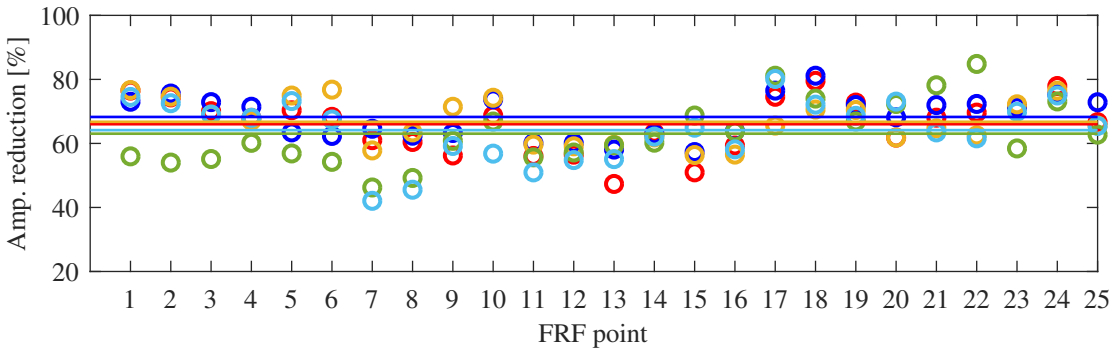

(c) Mistuning case #2.

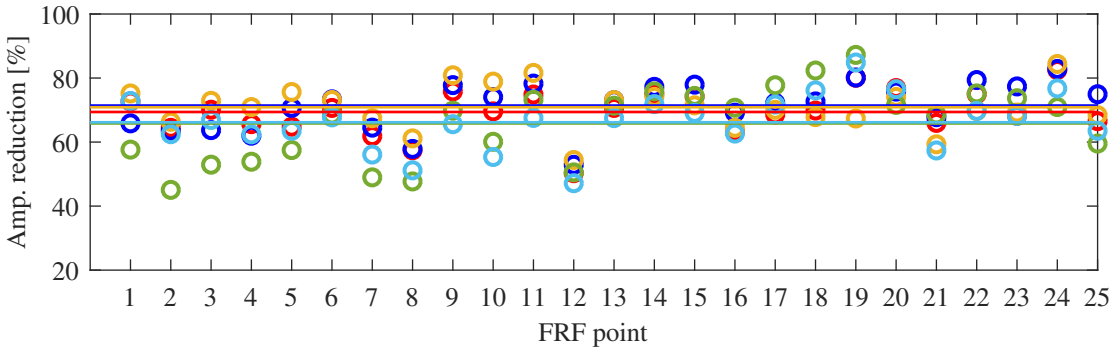

(d) Mistuning case #3.

Figure 4.9: Amplitude reduction for mode family #1. Patch configuration 1: (—), 2: (—), 3: (—), 4: (—) and 5: (—).

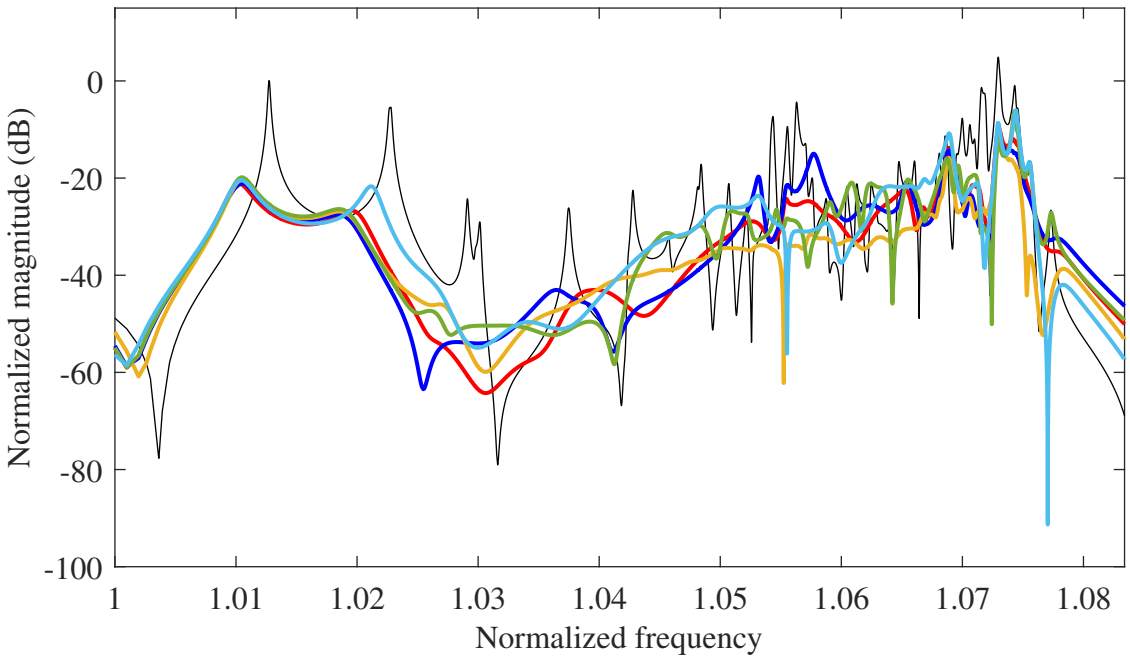

(a) No mistuning.

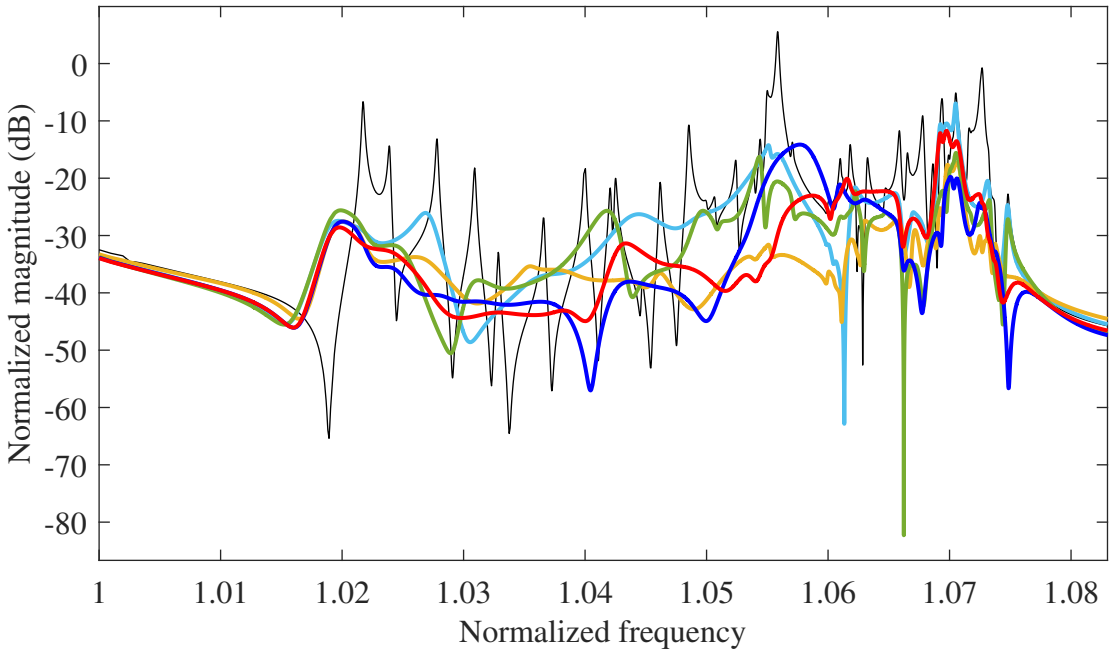

(b) Mistuning case #1.

Figure 4.10: FRF #10. Patch configuration 1: (—), 2: (—), 3: (—), 4: (—) and 5: (—).

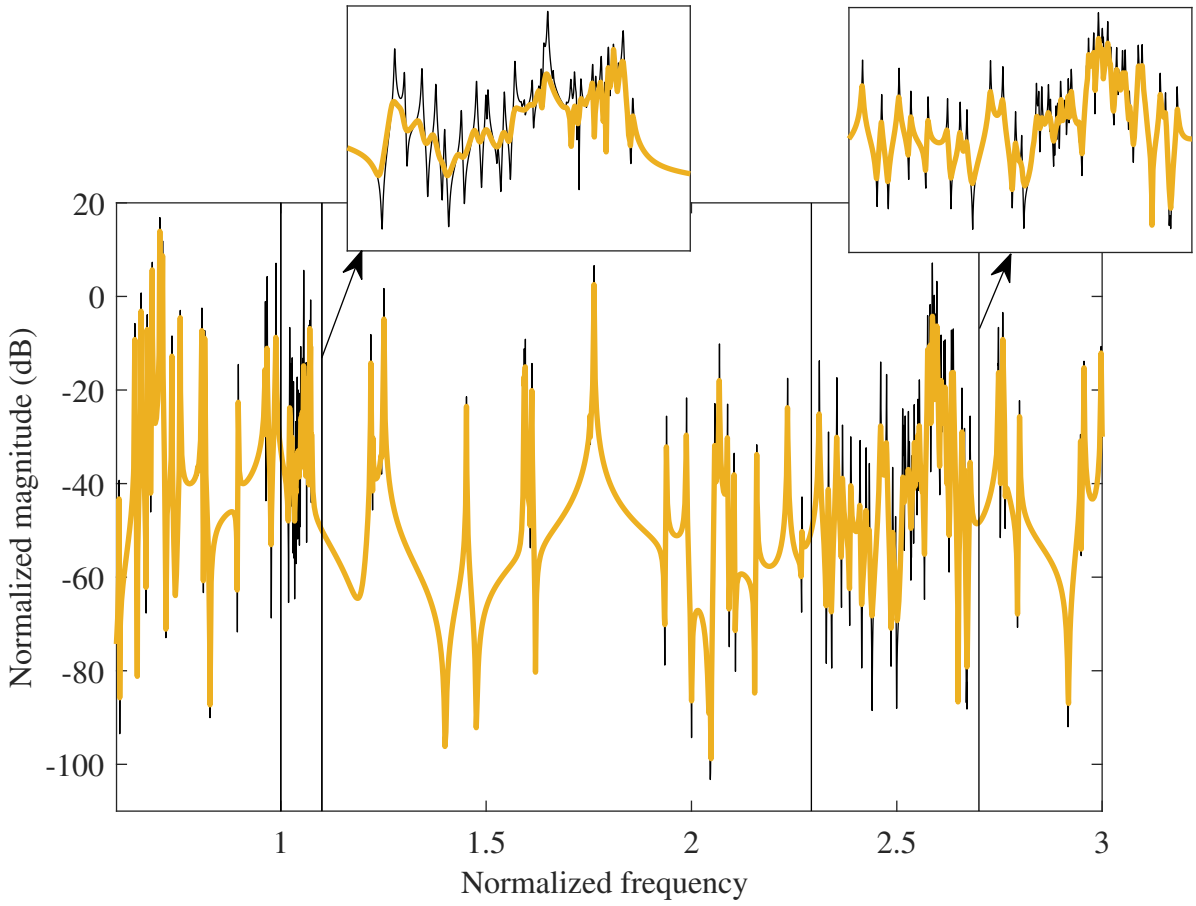

Figure 4.11: FRF #10 of a mistuned BluM (case #1). The uncontrolled case (▬) is compared to a system controlled by multi-stage shunt circuits using patch configuration 3 (▬).

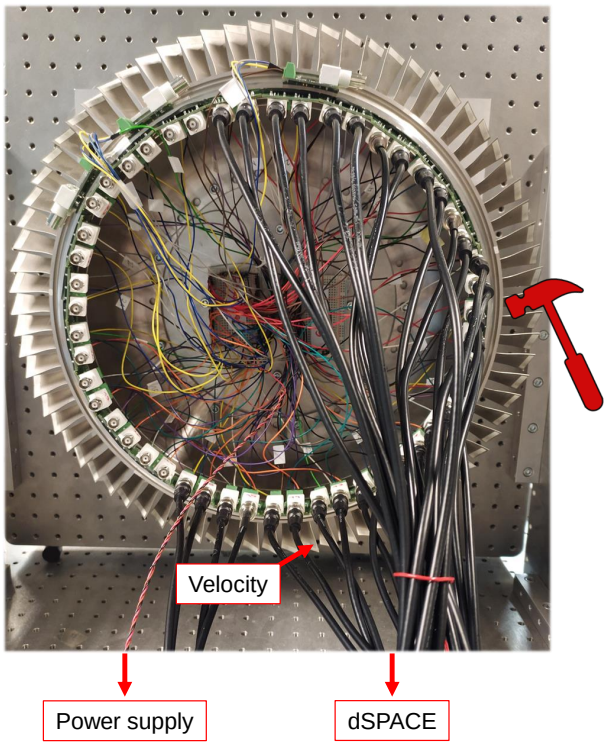

(a) Photograph of the BluM setup with DVAs. The hammer indicates the location of the excitation and the arrow refers to the location of the tip velocity measurement.

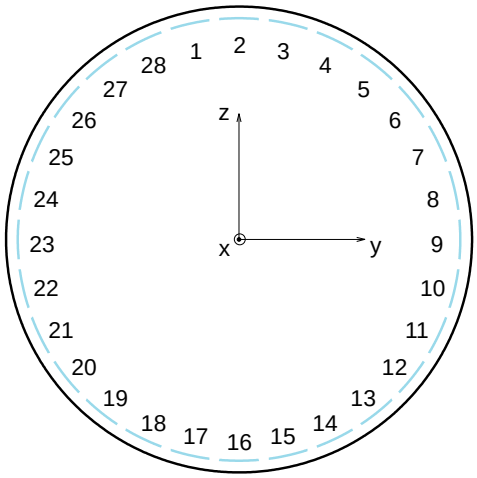

(b) Overview of the patch distribution.

Figure 4.12: The BluM structure.

4.4 Experimental study

4.4.1 Experimental setup

A photograph of the BluM structure is provided in Figures 4.12a and 4.13. The patch distribution in Figure 4.12b corresponds to the one used in the numerical study. Figure 4.14 gives an overview over the whole experimental setup including the clamping and a close-up on the patch fixation. Using conductive glue, the piezoelectric patches were installed inside the drum, one electrode being connected to the BluM structure. The clamping of the drum was realized by screwing it on a metal plate that was vertically fixed on an optical breadboard. This optical breadboard was then mounted on an optical table, building the electrical ground. An impulsive force located at the outer part of the drum below patch #9 was applied using a hammer (five runs per FRF). A laser vibrometer measured the tip velocity at a blade tip at the bottom of the BluM close to patch #15. The magnets that were mounted at the blade tips to excite the structure [83–85] were initially retained and eventually modified in the course of the robustness study. The digital shunts were implemented via a dSPACE MicroLabBox, and the Simcenter Testlab software was used for data acquisition and post-processing. Since the MicroLabBox has only 16 DAC output channels, only 16 of the 28 patches of the BluM were used simultaneously. As

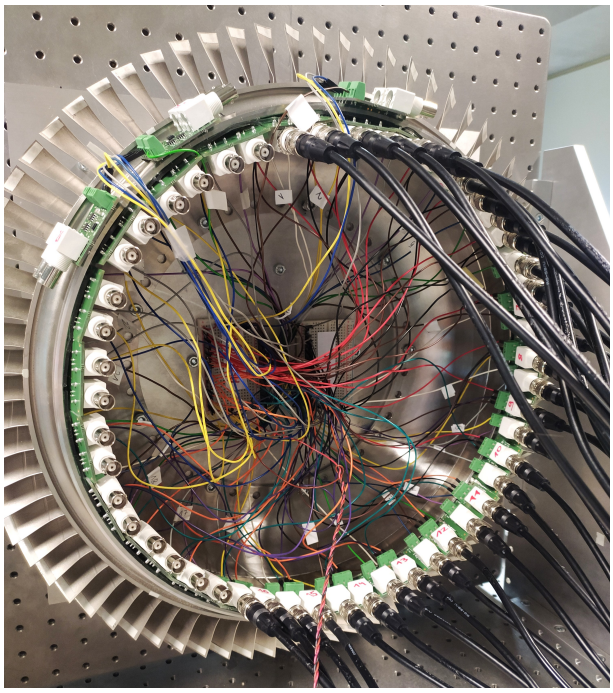

Figure 4.13: Experimental setup of the BluM with DVAs - side view.

already mentioned earlier and discussed in [83–85], the BluM is inevitably mistuned. For this reason, the patch configurations in Figure 4.1 were used, in line with the numerical simulations in Section 4.3.

4.4.2 BluM dynamics

Figure 4.15 presents the FRF (mobility) when the piezoelectric patches are in open circuit. The resonance frequencies and amplitudes are normalized with respect to the frequency and peak amplitude of the first mode of the first bending mode family located between 1 and 1.06. The second family of BluM modes comprising torsional modes is not visible because the laser measured the velocity at the center of the blade. The third mode family consisting of the second bending modes of the blades is located after 2.5. Between these families, isolated modes of the drum support appear. Our focus for vibration mitigation is on the first mode family comprising 35 visible resonance peaks and the surrounding drum modes. This mode family features closely-spaced modes with predominantly low damping. The subsequent mode families are located at higher frequencies, requiring high sampling frequencies that cannot be straightforwardly achieved using the available hardware.

4.4.3 Dynamic impedances and coupling assessment

To assess the electromechanical coupling, the dynamic impedance function is considered for each shunted patch. A total of 16 dynamic impedances were measured per patch configuration. To this end, the BluM was excited via a piezoelectric patch, resulting in one set of measurements per configuration. Considering the available working memory of the MicroLabBox, this sequential excitation was necessary in order to simultaneously measure with 16 patches. The excitation signal was a multisine in the frequency interval

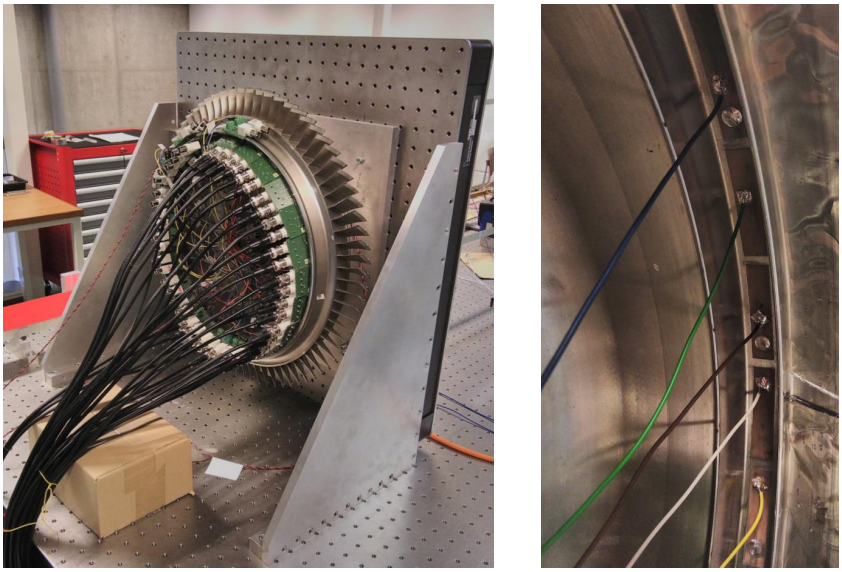

Figure 4.14: View on the whole experimental setup of the BluM with DVAs and its clamping realization (left) and a close-up on the patch fixation inside the drum (right).

0-4.4. RMS amplitudes were chosen for each patch individually to avoid saturation of the DVA and to achieve an overall uniform excitation with all transducers combined. With $n = 400000$ samples per period and a sampling rate $fs = 10000\,\mathrm{Hz}$, a frequency resolution of $0.05\,\mathrm{Hz}$ was obtained. One multisine realization was averaged over $P = 10$ periods [128].

The dynamic impedance measurement of patch 1 for patch configuration 3 is plotted in Figure 4.16. The mode families #1 and #3 are visible whereas mode family #2 cannot be observed. The dynamic impedances for the first mode family for the 16 piezoelectric patches are presented in Figure 4.17. Each patch features good coupling with the different modes. Besides, there is no coupling with all 76 blade modes in any patch. One possible reason for this is the presence of mistuning in the BluM. The dynamic impedances for the other patch configurations in Appendix B present similar characteristics.

Plant models were identified using the PolyMAX method [129], as in Section 3.2. During the identification process, the relations between the patches were not taken into account since the off-diagonal FRF terms are relatively small and thus easily corrupted by noise. The stabilization diagram for patch configuration 3 is plotted in Figure 4.18. The identified modes for all patch configurations are listed in Table 4.1. The table also includes the modes of an altered BluM setup used later for a robustness study. It contains the modes of the first mode family as well as drum modes at frequencies < 1. Modes that appear after mode family #1 are not listed herein since they are not targeted by the shunts. Comparing the stabilization diagram in Figure 4.18 with Figure 3.8, we see that the multiplicity of modes complicates the identification of the stabilized modes. In addition, not every patch features a good coupling with each identified mode (cf. Figures 4.17 and 4.18). We also note that the signal-to-noise ratio is smaller in comparison to the measurements conducted on the bladed rail, representing a further complication for the

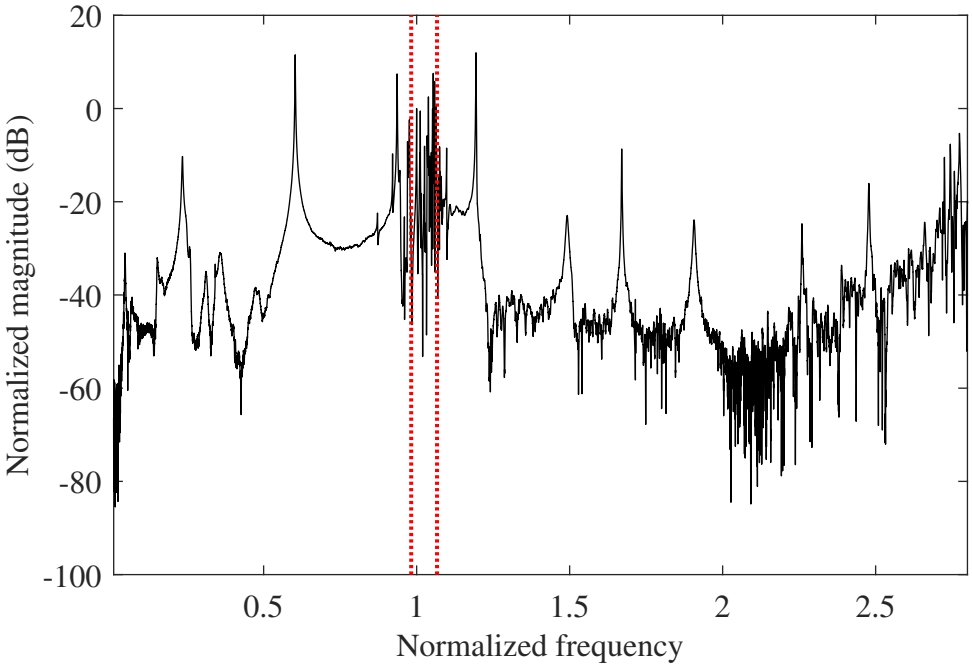

(a) Whole frequency range.

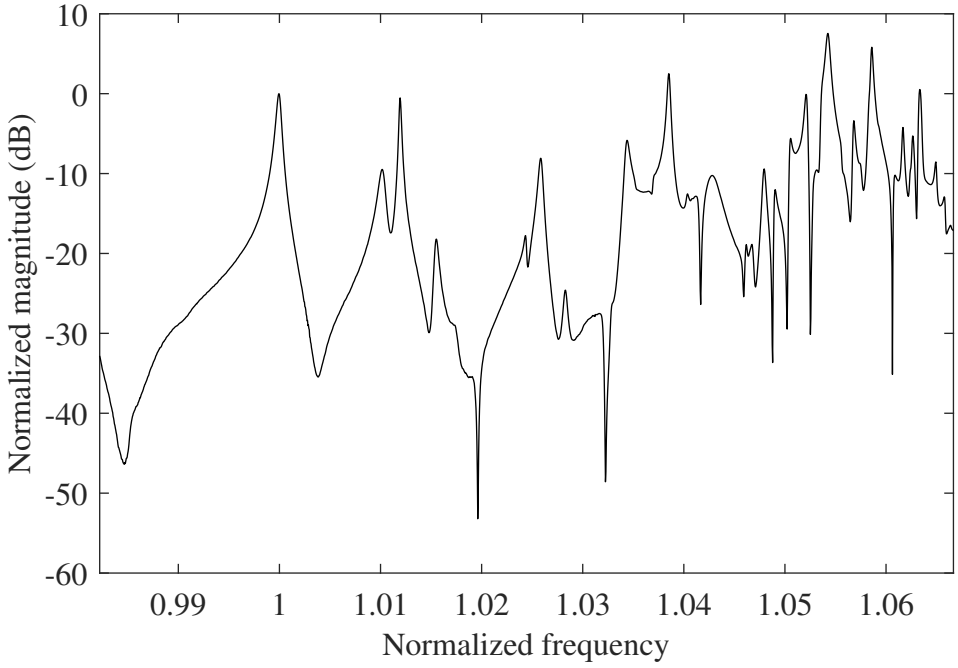

(b) Mode family #1.

Figure 4.15: Open-circuit FRF of the BluM.

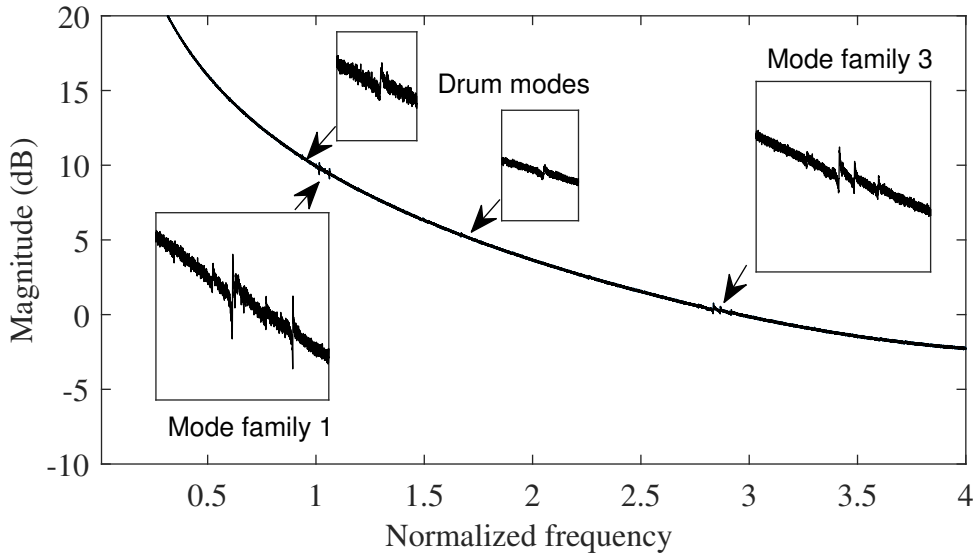

Figure 4.16: Dynamic impedance of piezoelectric patch 1 in patch configuration 3.

identification process.

The identified state-space model comprising the general trend of the dynamic impedance function is presented in Figure 4.19. The model features a relatively good fit of the magnitude, but it is 0.4 dB lower than the measurements in the frequency range of the mode family. In addition, the phase has errors of approximately 5°, and the general trend is not captured correctly. A possible reason for this disagreement is noise at low frequencies. Nevertheless, these errors were corrected when the identified complex poles were incorporated in the model. This is shown in the Bode plots of Figure 4.20. A good agreement between the measurements and the model can be obtained both for the magnitude and the phase. However, the phase plot reveals that not all modes that feature a coupling with this patch were identified in the model, e.g., around the frequencies 1.026 and 1.046.

The identified models provided the parameters of the electromechanical system necessary for coupling evaluation and shunt tuning. The damping ratios were generally around 0.04% for configuration 3. In addition, following the isolated mode strategy, the patch-to-mode distribution is listed in Table 4.2. This distribution was chosen in such a way that no mode was targeted twice.

4.4.4 Performance of the shunts

4.4.4.1 Mode family #1

To mitigate the resonant vibrations of the first mode family, the isolated mode and mean shunt strategies were applied to the BluM. Table 4.3 presents the different mean frequencies used for each patch configuration. Figure 4.21 displays the FRF (mobility) of the uncontrolled and controlled systems for patch configuration 3 (see Figures B.5-B.8 in Appendix B for the other patch configurations). Both strategies yield excellent performance with reductions of the resonance peak amplitudes up to 10 dB. Vibration attenuation

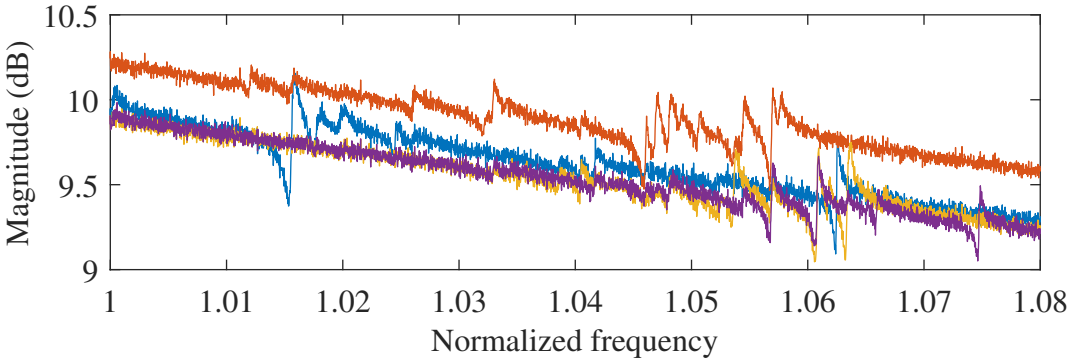

(a) Patch 1 (—), patch 2 (—), patch 3 (—) and patch 4 (—).

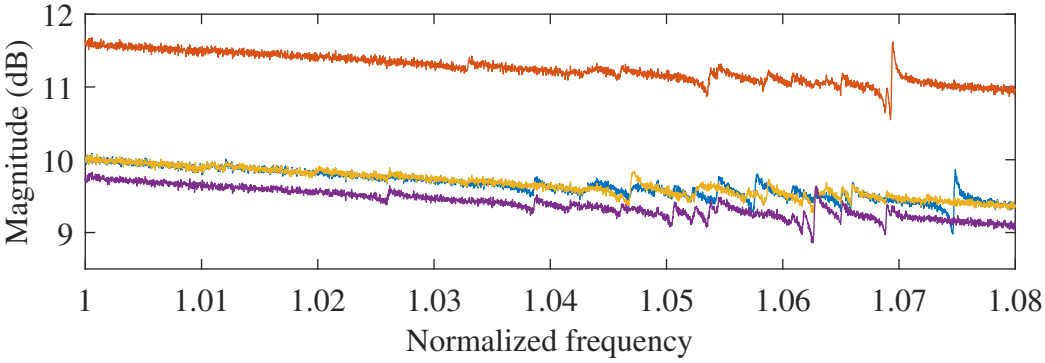

(b) Patch 5 (—), patch 6 (—), patch 7 (—) and patch 8 (—).

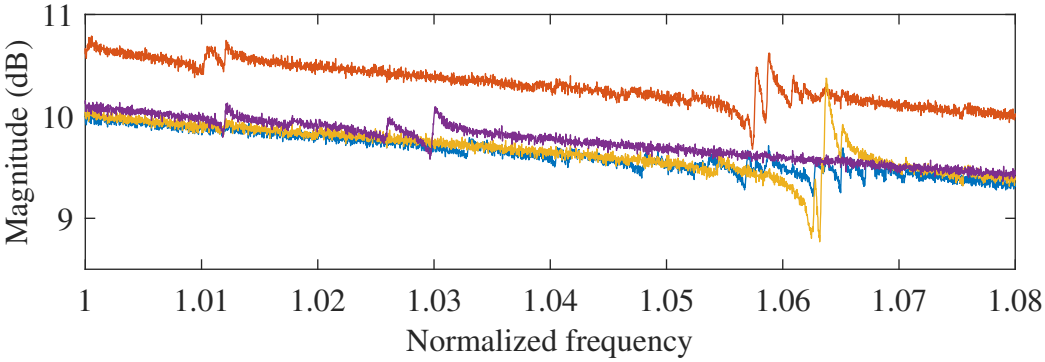

(c) Patch 9 (—), patch 10 (—), patch 11 (—) and patch 12 (—).

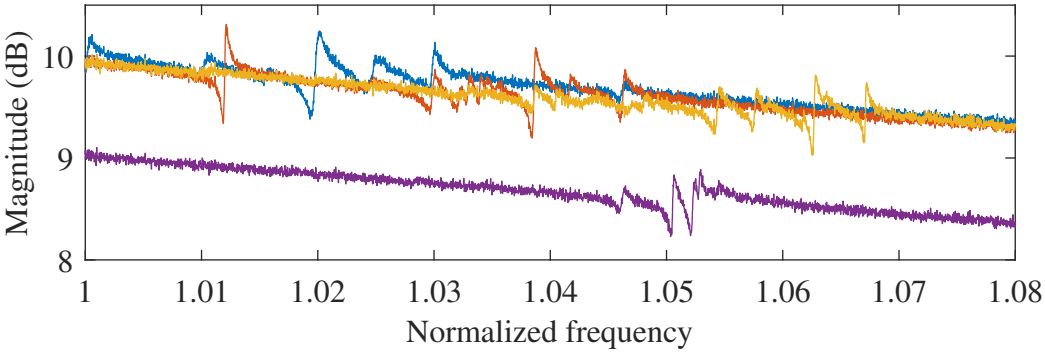

(d) Patch 13 (—), patch 14 (—), patch 15 (—) and patch 16 (—).

Figure 4.17: Dynamic impedance of patches 1-16 for patch configuration 3.

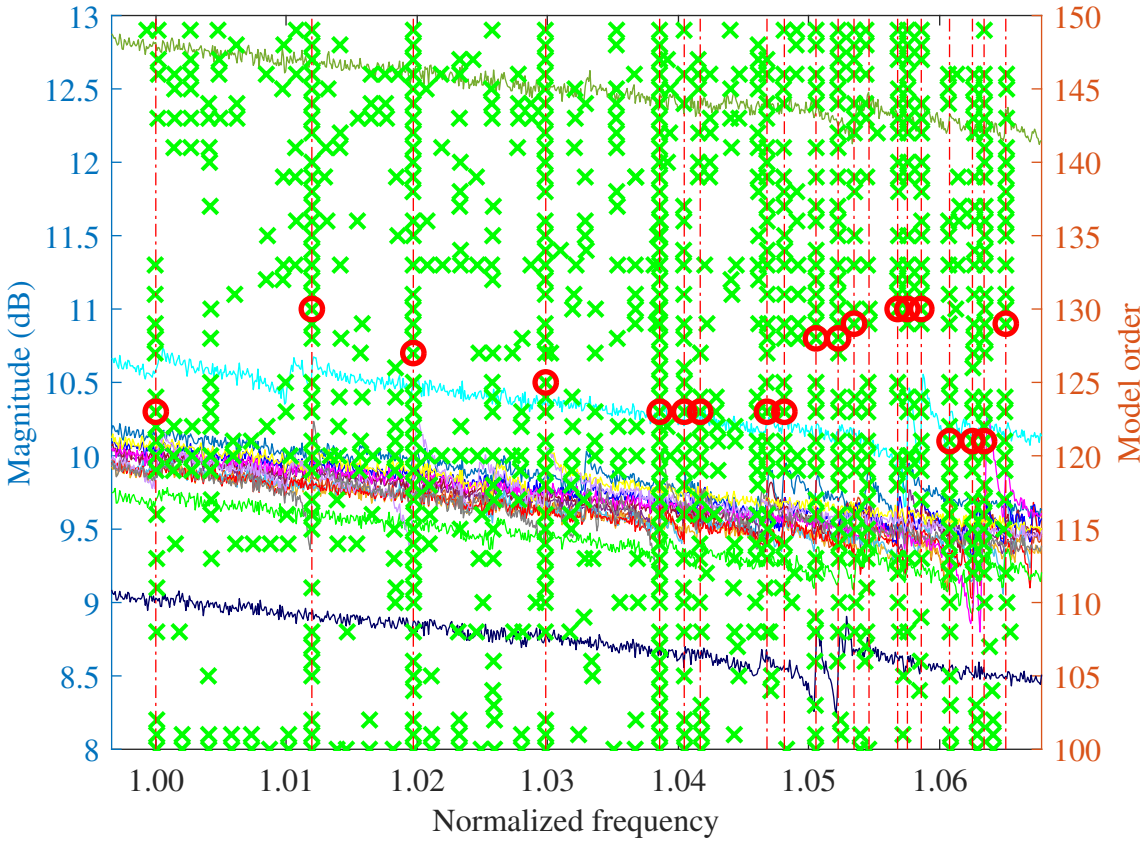

Figure 4.18: Stabilization diagram for patch configuration 3. ×: stabilized poles; ○ and (▪ ▪ ▪) at the corresponding frequency: identified poles. Since the individual transfer functions are indistinguishable in this plot, they are not noted in the legend.

	Normalized frequency						
Mode number	Conf. 1	Conf. 2	Conf. 3	Conf. 4	Conf. 5	Conf. 3 (altered)	Conf. 5 (altered)
1	0.603	0.603	0.602	0.604	0.9213	0.602	0.603
2	0.872	0.921	0.921	0.872	0.937	0.998	0.938
3	0.921	0.936	0.960	0.921	0.100	1.008	0.976
4	0.936	0.960	1.000	0.936	1.012	1.011	0.987
5	0.960	1.000	1.012	1.012	1.015	1.016	0.998
6	1.000	1.010	1.020	1.016	1.018	1.019	1.008
7	1.010	1.012	1.030	1.018	1.012	1.022	1.014
8	1.012	1.016	1.033	1.020	1.024	1.025	1.017
9	1.016	1.018	1.039	1.024	1.026	1.030	1.019
10	1.018	1.020	1.041	1.026	1.028	1.032	1.022
11	1.020	1.025	1.047	1.028	1.032	1.034	1.025
12	1.024	1.026	1.048	1.030	1.034	1.036	1.027
13	1.026	1.029	1.051	1.032	1.038	1.039	1.029
14	1.028	1.030	1.054	1.033	1.040	1.042	1.032
15	1.030	1.032	1.057	1.034	1.042	1.048	1.034
16	1.032	1.034	1.059	1.035	1.046	1.049	1.040
17	1.034	1.039	1.063	1.037	1.049	1.053	1.042
18	1.039	1.046	1.065	1.039	1.052	1.056	1.044
19	1.040	1.049	1.069	1.040	1.054	1.061	1.047
20	1.044	1.051	1.075	1.042	1.058	1.064	1.049
21	1.046	1.053	1.098	1.044	1.060	1.074	1.053
22	1.047	1.057	1.102	1.046	1.063	1.075	1.057
23	1.049	1.059	-	1.047	1.065	1.098	1.059
24	1.051	1.061	-	1.049	1.067	-	1.061
25	1.053	1.063	-	1.051	1.069	-	1.064
26	1.057	1.065	-	1.053	1.075	-	1.065
27	1.059	1.069	-	1.054	-	-	1.068
28	1.061	1.075	-	1.056	-	-	1.071
29	1.063	1.099	-	1.057	-	-	1.074
30	1.069	-	-	1.061	-	-	1.075
31	-	-	-	1.062	-	-	1.079
32	-	-	-	1.075	-	-	1.082

Table 4.1: Identified mode frequencies of the initial and altered systems.

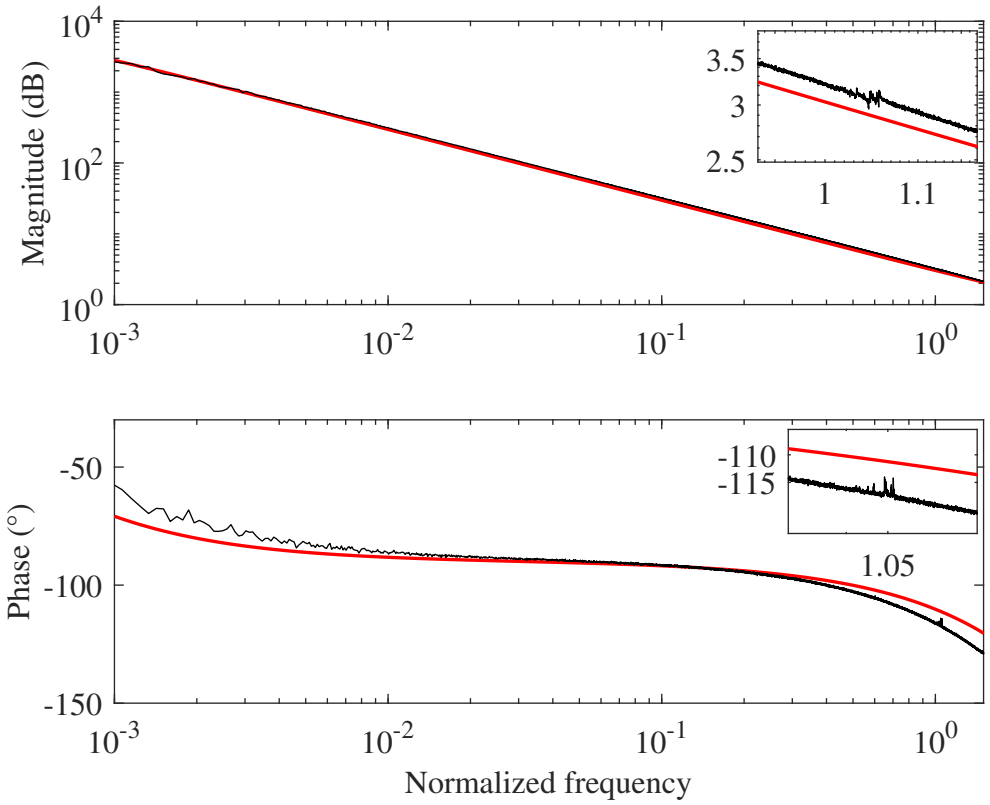

Figure 4.19: Bode plot of the dynamic impedance for patch 1/configuration 3 (▬) and the identified model (▬) of the overall trend and the imperfection knee.

	Mode number					
Patch number	Conf. 1	Conf. 2	Conf. 3	Conf. 4	Conf. 5	Conf. 3 (Robustness)
1	6	9	11	7	6	6
2	4	15	14	4	2	10
3	12	19	21	13	11	21
4	15	11	20	19	14	16
5	16	20	19	20	15	14
6	18	16	18	24	17	13
7	8	18	11	9	8	8
8	19	29	17	25	18	17
9	13	27	14	22	28	14
10	20	23	22	15	26	12
11	22	25	16	6	25	5
12	26	22	17	29	23	18
13	21	14	7	31	16	19
14	23	17	6	33	22	18
15	3	24	9	28	19	14
16	11	21	12	30	29	22

Table 4.2: Patch-to-mode distribution for the isolated mode strategy.

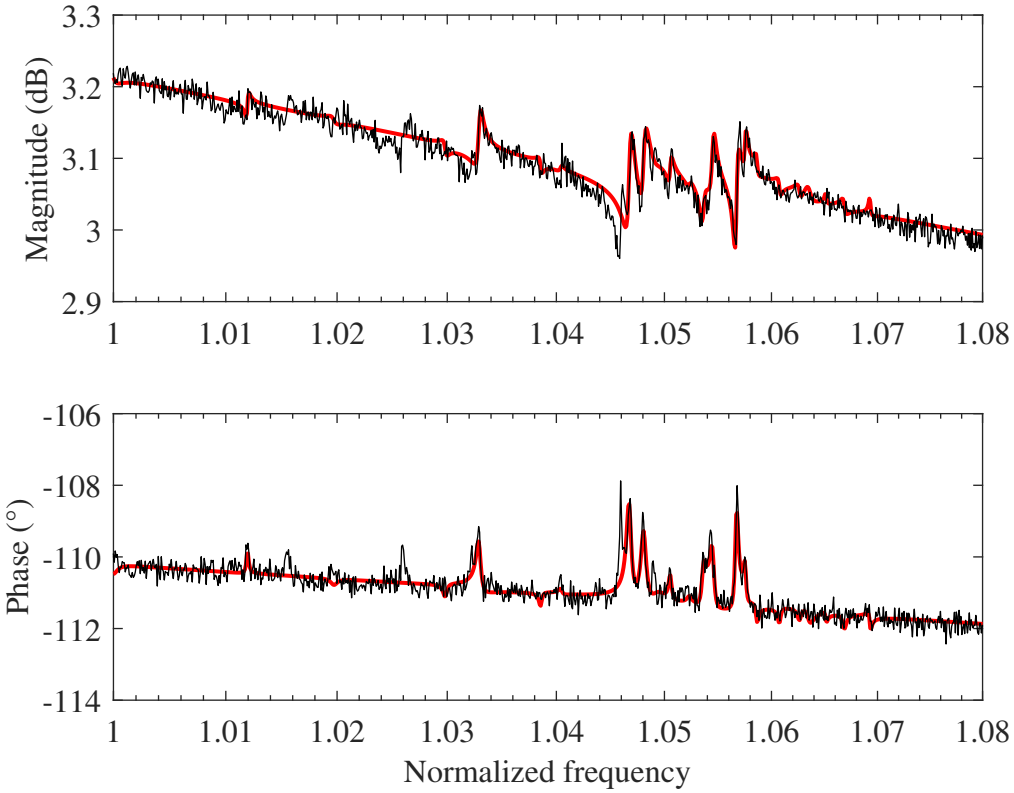

Figure 4.20: Bode plot of the dynamic impedance for patch 1/configuration 3 (▬) and the identified model (▬).

is particularly high between normalized frequencies 1.02 and 1.07 where the modes are very close to each other. This is due to two reasons, i.e., the mean frequency lies in this interval, and the coupling for these modes is stronger, as indicated in Table 4.2.

To compare the different patch configurations, the FRF are displayed in Figures 4.22 and 4.23, and the H_2 norms of the FRF are given in Table 4.4. For better visualization, a linear scale is used for the vertical axis. The magnitudes were normalized with respect to the peak magnitude of the first mode of family #1. Overall, the different configurations yield very good damping performances. However, it is clear that configuration 3 provides the best vibration attenuation results leading to a relatively uniform reduction without important dropouts. Conversely, configuration 4 which can be seen as complementary to configuration 3 (see Figure 4.1) features such dropouts, e.g., at 1.054. The same holds true for the other configurations, partly explaining the difference between the H_2 norms. A possible explanation for these differences can be, e.g., the excitation location centered at the localized patch distribution in configuration 3. Here, the coupling might be strong. The setup has also uncertainties and asymmetries due to mistuning and possible irregularities due to the fixation of the patches (uneven distribution of the conductive glue), which can possibly influence the coupling with specific modes. It is thus difficult to draw general conclusions regarding the performance for different patch configurations. In addition, the numerical study did not evidence particularly favorable configurations either.

Configuration	Mean frequency
1	1.038
2	1.040
3	1.044
4	1.028
5	1.041

Table 4.3: Mean frequencies targeted by the mean shunt strategy.

Configuration	H_2 norm	
Open circuit	221.52	
-	Isolated mode	Mean shunt
1	166.24	164.84
2	184.80	190.45
3	143.45	147.64
4	194.08	157.95
5	161.99	155.47

Table 4.4: Amplitude reduction measured through the H_2 norm between 0.9778 and 1.0667.

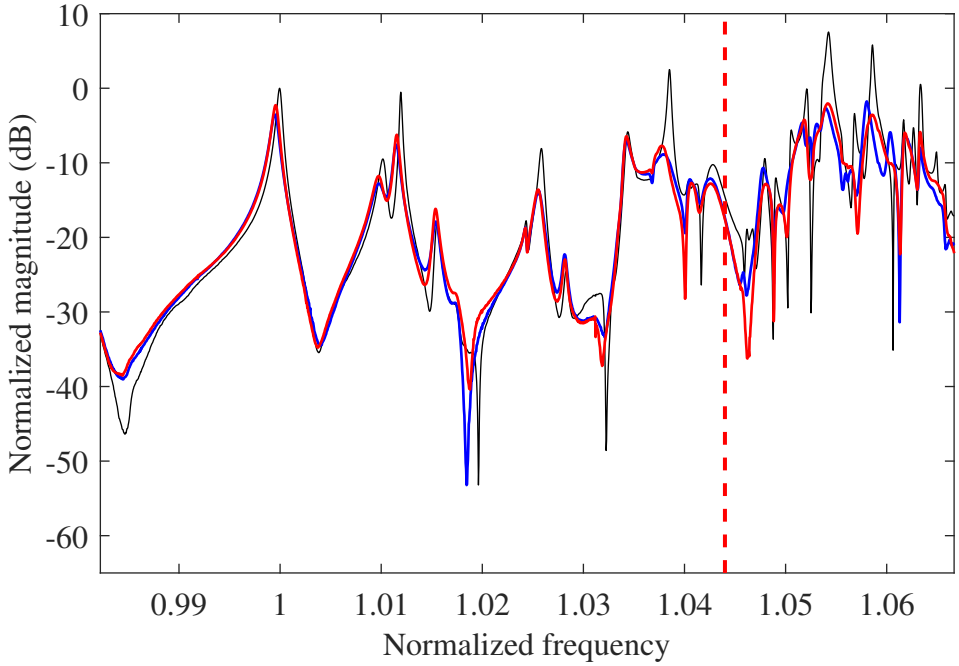

Figure 4.21: FRFs for patch configuration 3. Open circuit (—), isolated mode (—) and mean shunt (—). The mean frequency is represented using (- - -).

4.4.4.2 Robustness study

To evaluate the robustness of the previous results, some of the small magnets mounted on the blade tips in [83–85] were detached. A total number of 14 magnets with a mass of 1.3 g were removed at the locations indicated in Figure 4.24. This resulted in a change in the resonance frequencies of up to 0.7 %, as shown in Figure 4.25. In the following figures, the frequencies and amplitudes remain normalized with respect to the first resonance frequency of mode family #1 in the initial configuration.

Both the isolated mode and mean shunt strategies with patch configuration 3 were applied to the altered system, considering the original shunt transfer function (referred to as detuned case) and a retuned design based on newly identified system parameters. Their respective performance is compared in Figure 4.26.

For the detuned case, we observe similar damping performance (from 5 to 10 dB) between 0.99 and 1.05. However, certain resonance peaks, e.g., at 1.008, 1.011, and 1.027, feature no or only a small amplitude reduction. At 1.019, one can even observe an increase in the resonance amplitude. Around 1.044, both approaches yield large amplitude reductions. For the mean shunt strategy, this is because this frequency range is specifically targeted. For the isolated mode strategy, it turns out that several shunts were also tuned toward frequencies close to 1.044. For frequencies starting from 1.05, there was less coupling with the modes than in the initial BluM. The mean shunt strategy is clearly more robust than the isolated mode strategy in this frequency range.

Overall, both strategies could be retuned successfully, as confirmed in Figure 4.26b. However, as for the detuned case, no significant amplitude reduction could be achieved for the

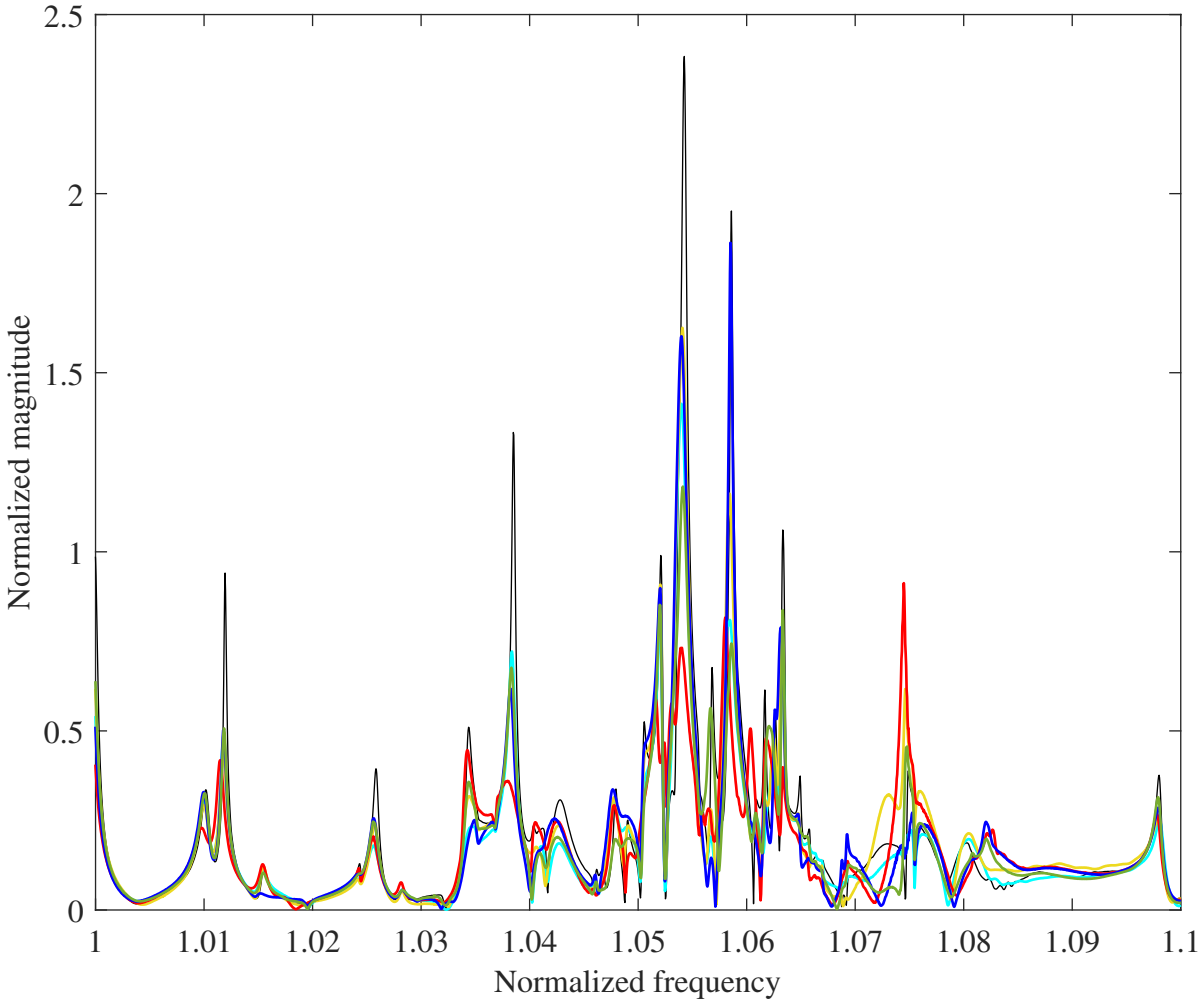

Figure 4.22: FRFs: open circuit (—), isolated mode strategy, configurations 1 (—), 2 (—), 3 (—), 4 (—) and 5 (—).

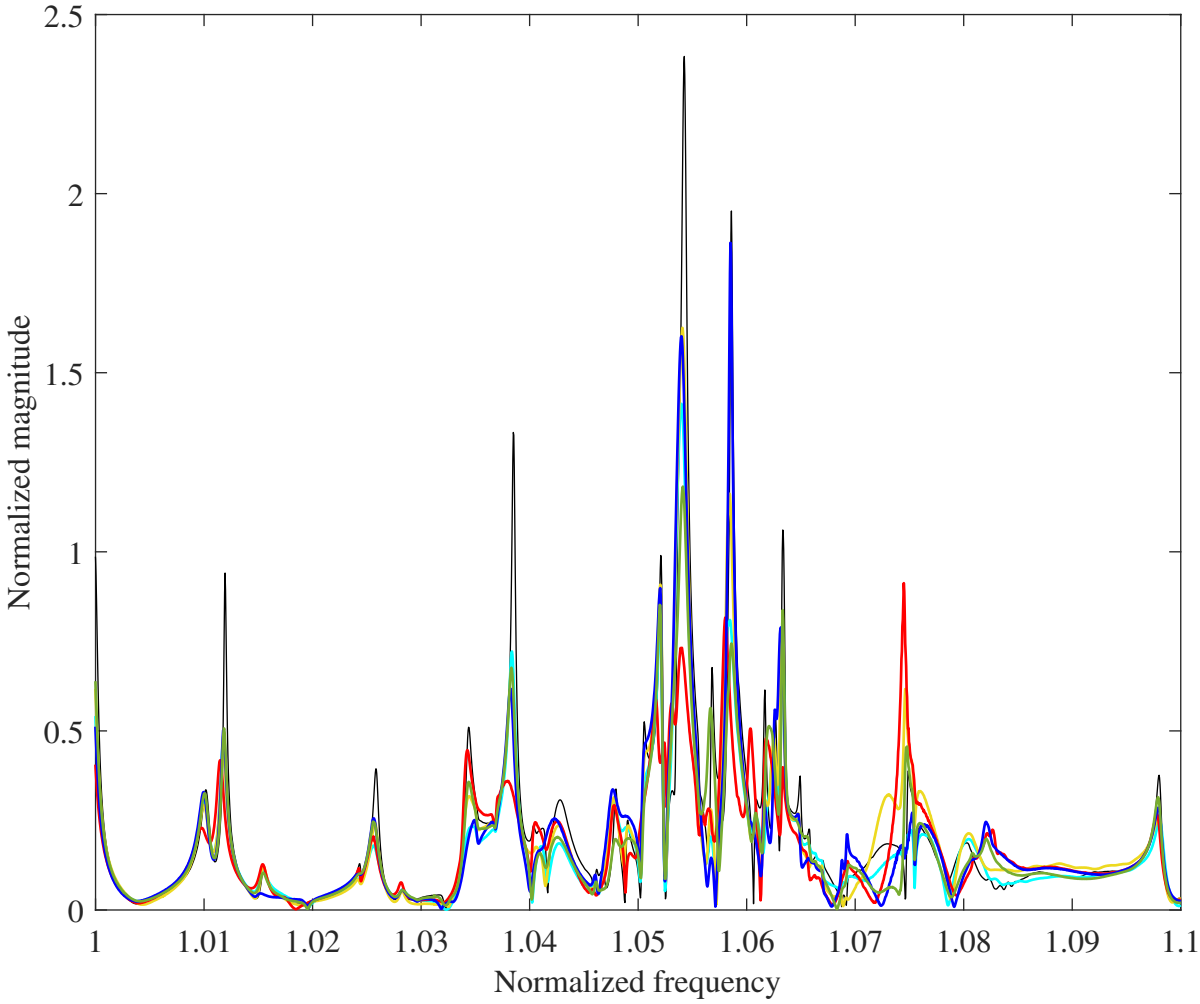

Figure 4.23: FRF: open-circuit (—), mean shunt strategy, configurations 1 (—), 2 (—), 3 (—), 4 (—) and 5 (—).

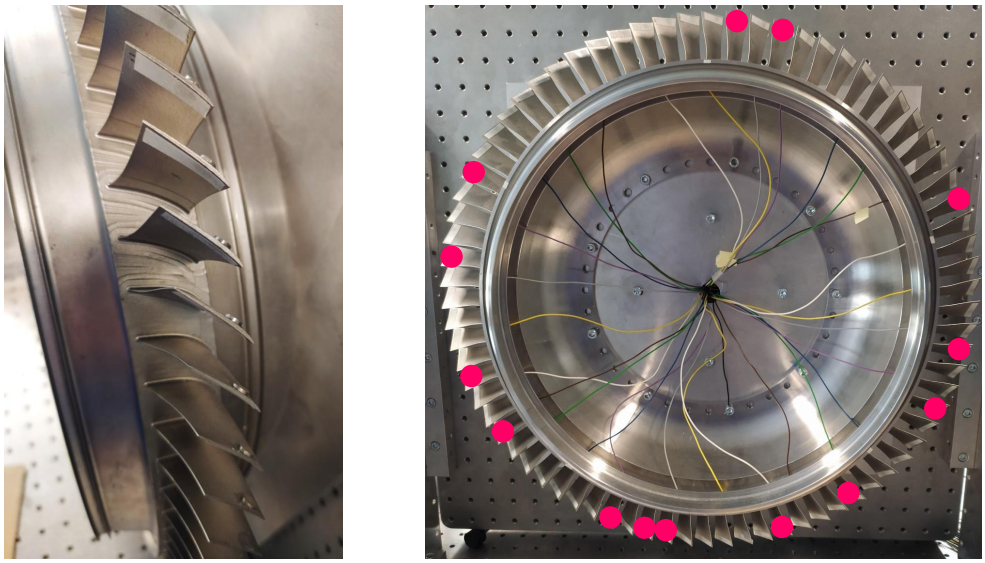

Figure 4.24: Locations where magnets were removed.

resonances after 1.05. It can also be observed that the mean shunt strategy clearly leads to better vibration attenuation, particularly in the range of the mean frequency (1.019).

Figure 4.27 which plots the FRFs of the BluM controlled by detuned and retuned mean shunts evidences the influence of the mean frequency. For instance, the mode at 1.057 could be attenuated with the detuned mean frequency (1.044) whereas this was not possible for the retuned mean frequency (1.019). Figure B.9 shows the same comparison for the isolated mode strategy.

4.4.4.3 Targeting multiple modes with one shunt circuit

Thanks to the multi-stage current blocking circuit presented in Section 2.5.2, not only the modes of family #1 but also the modes of the drum support can be targeted with one shunt circuit with different stages.

Two-stage shunt circuit

The mean shunt strategy was applied to mode family #1 along with an individual RL shunt targeting the drum mode at 0.602 in patch configuration 3. The resulting FRFs in Figure 4.28 evidence a reduction in resonance amplitude for both the drum mode (7.5 dB) and the mode family (amounting to 12 dB especially between 1.040 and 1.065).

We note that the use of the multimodal two-stage shunt circuit leads to a certain loss of control authority over the first mode family, as can be seen from the fact that the resonance amplitudes were somewhat less reduced compared to the single shunt case (up to 5 dB). In addition, as already mentioned in Section 2.5.2, the use of a multi-stage shunt circuit can lead to some imprecision in the tuned shunt branches due to the fact that an ideal current flow cannot always be guaranteed since the stages might interact.

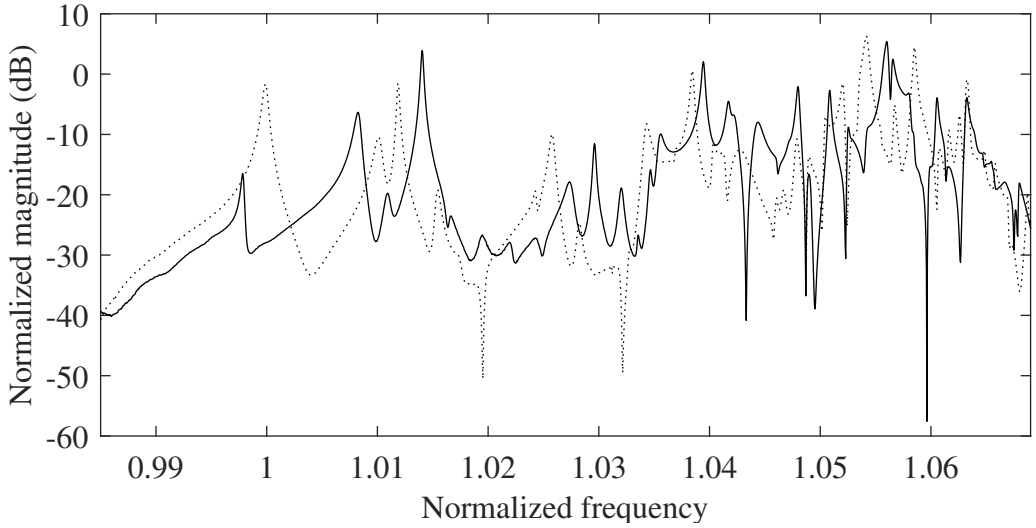

Figure 4.25: Open-circuit FRFs of the initial (▪ ▪ ▪) and altered systems (▬).

Three-stage shunt circuit

Two drum modes were then targeted together with mode family #1 by implementing a shunt circuit comprising three stages. To this end, we consider patch configuration 5 due to the fact that it features a good coupling with multiple drum modes. The patch configuration was applied to the altered BluM configuration used for the robustness study in Section 4.4.4.2. The identified modes for this setup are listed in the last column of Table 4.1. The first identified drum modes, namely 0.603 and 0.938, were targeted by the first stages of the shunt circuit whereas the last stage was tuned toward the mean frequency of mode family #1 (1.040). The resulting FRF in Figure 4.29 shows that the resonance amplitudes of the drum modes could be successfully attenuated (3.5 dB and 6 dB, respectively). Moreover, the amplitudes of almost every resonance peak of the mode family could be reduced by amounts ranging from 3 dB to 11 dB.

4.5 Conclusion

The objective of this chapter was multimodal shunt damping with multiple transducers, each connected to a DVA. The tuning strategies developed in Section 2.5 were successfully validated numerically and experimentally using a complex industrial structure, the BluM. Specifically, the resonant vibrations of mode family #1 together with one or two drum modes were attenuated thanks to the multi-stage shunt design presented in Section 2.5.2. This chapter also studied carefully the influence of different parameters, including the number/configuration of piezoelectric patches and mistuning. For instance, numerical simulations showed that the attenuation performance is already satisfactory with 7 patches. In addition, all patch configurations could provide an overall uniform and substantial damping performance with a mean attenuation of the FRF amplitudes of about 70 % and a minimum attenuation of 40 %, this even in the presence of mistuning. For the experimental BluM, reductions of the resonance magnitudes mostly ranged from 4 dB to 10 dB.

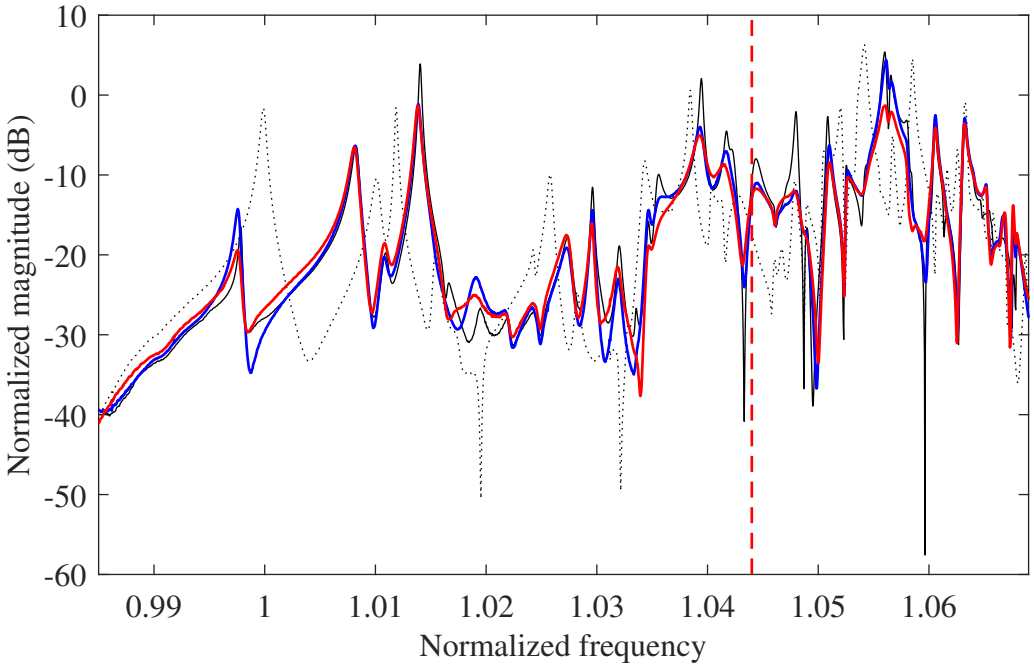

(a) Detuned shunts.

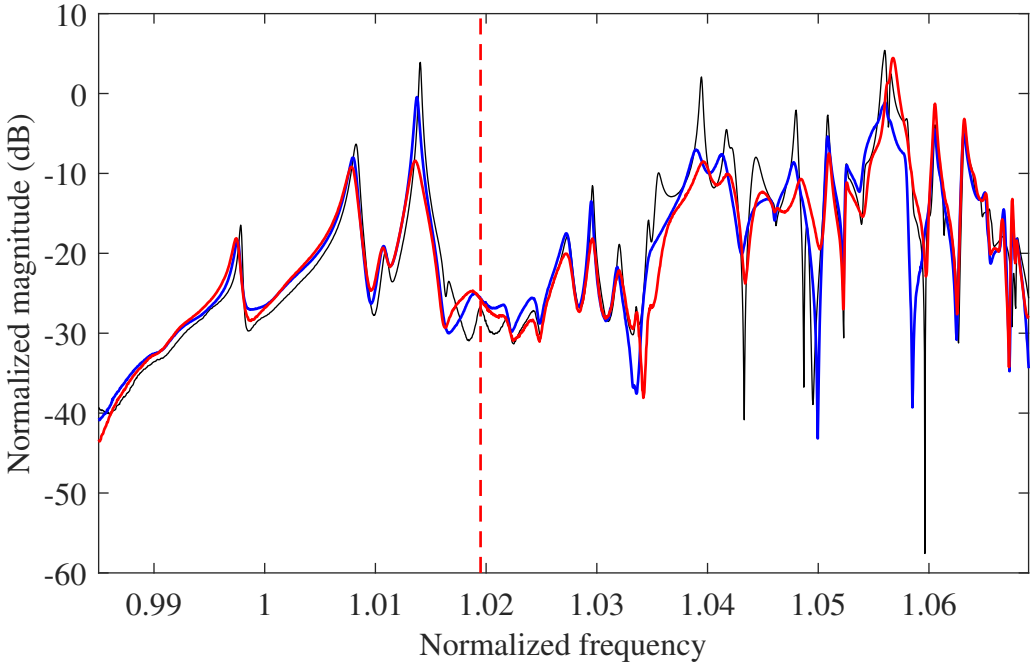

(b) Retuned shunts.

Figure 4.26: Robustness study. Initial open-circuit FRF (▪▪▪), open-circuit FRF of the altered system (▬), isolated mode strategy (▬) and mean shunt strategy (▬). The mean frequency is represented using (▪▪▪).

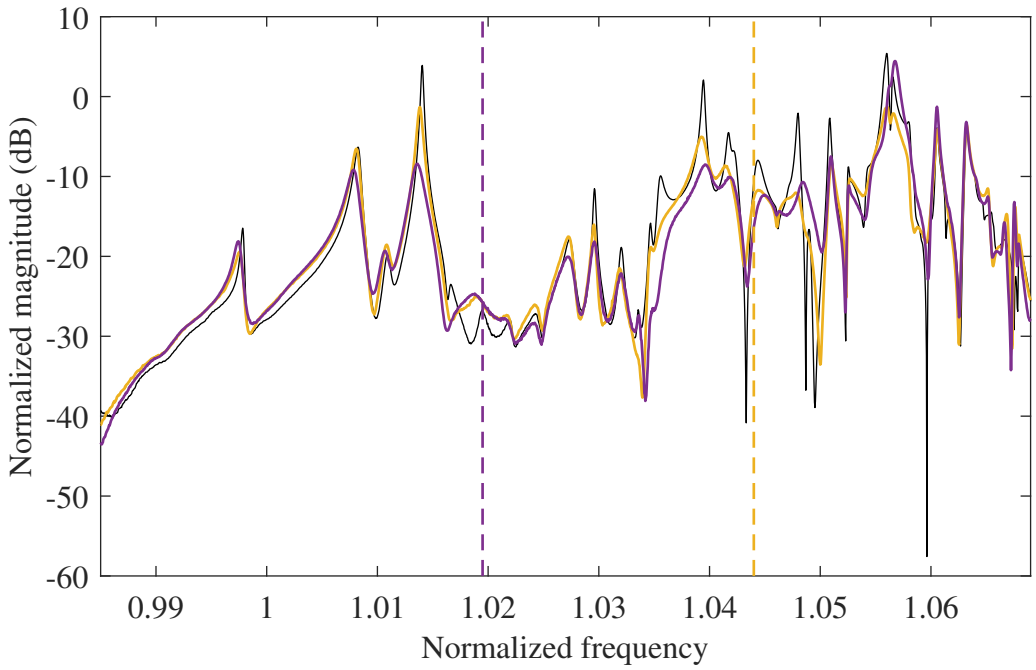

Figure 4.27: Open-circuit FRF of the altered system (—) and FRFs of the system controlled by detuned mean shunts (—) and retuned mean shunts (—). The mean frequencies are represented using (- - -) and (- - -), respectively.

Both the isolated mode and mean shunt tuning strategies proved efficient in the different cases investigated. However, the tuning procedure for the mean shunt strategy is significantly faster. Indeed, unlike the isolated mode strategy, a coupling evaluation and a mode-to-patch distribution are not needed. All in all, the preference should thus be given to the mean shunt strategy.

The digital implementation of the shunts offers great advantages over the analog shunt circuits used in [83–85]. Indeed, in this study, the DVAs allowed for a rapid and easy retuning of the shunt when mistuning was introduced. Also, the DVAs are very compact when realized on a PCB.

This chapter proposed a proof of concept that can be used as a basis for more robust industrial implementation. Further research could, e.g., automate the system identification procedure to progress toward self-tuning DVAs. It would also be of interest to study the impact of different measurement locations and types of excitation on shunt performance. A good candidate is engine order excitation which better reflects the BluM's operational conditions. Finally, a rotating BluM could also be envisioned where energy harvesting from the rotational energy could be used to power the DVAs.

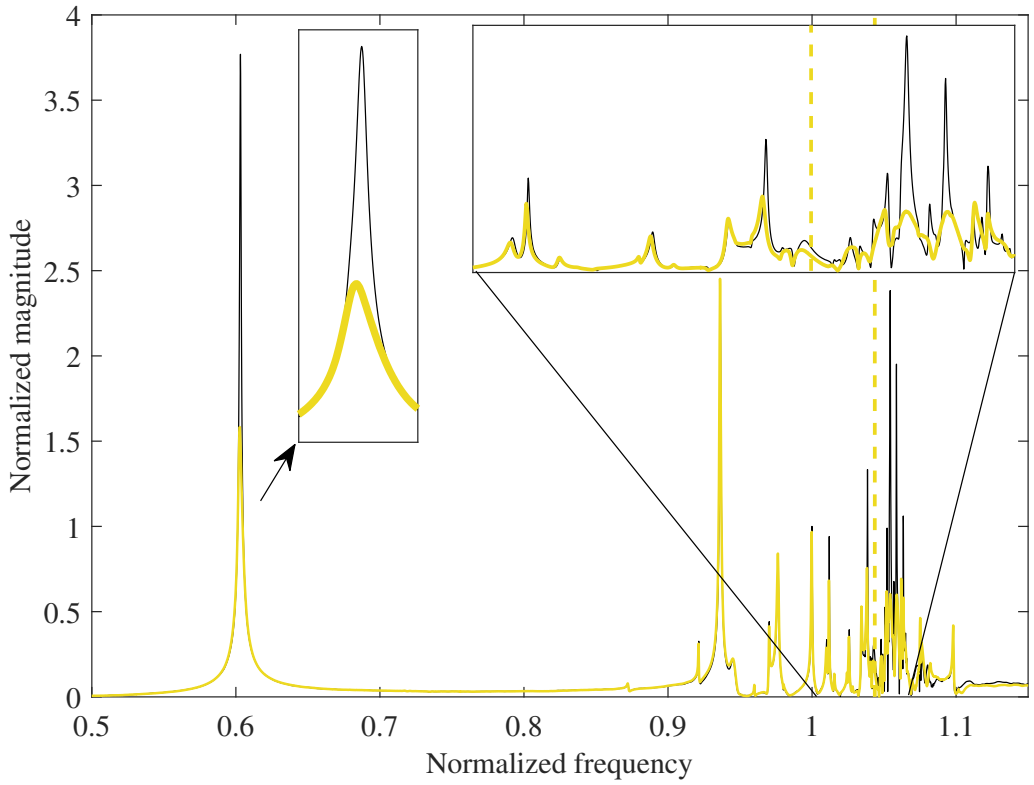

(a) Whole frequency range.

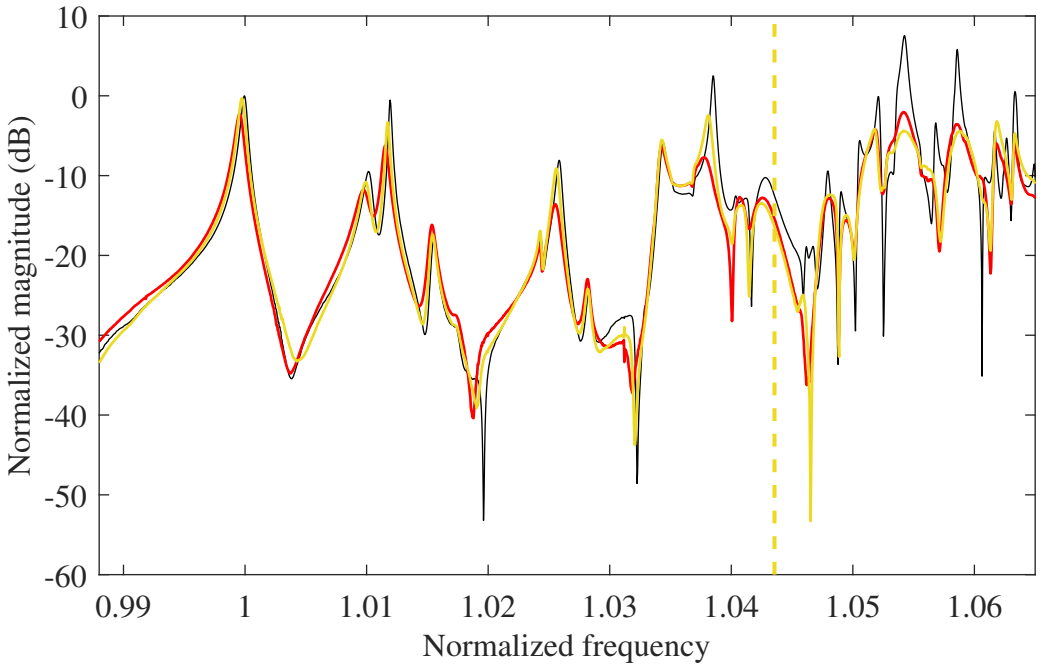

(b) Close-up on mode family #1. Comparison with single mean shunts (▬).

Figure 4.28: FRFs of the uncontrolled system (▬) and of the system controlled by a two-stage current blocking circuit (▬). The targeted mean frequency is represented using (▬).

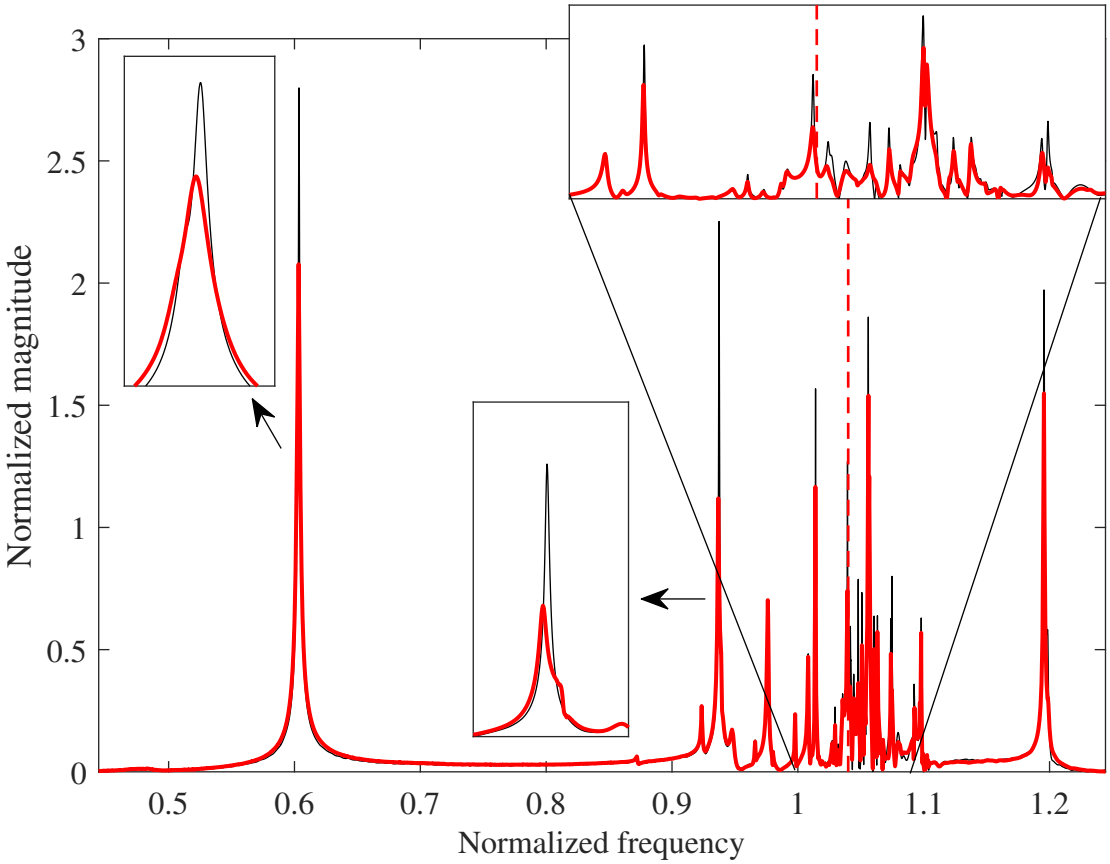

(a) Whole frequency range.

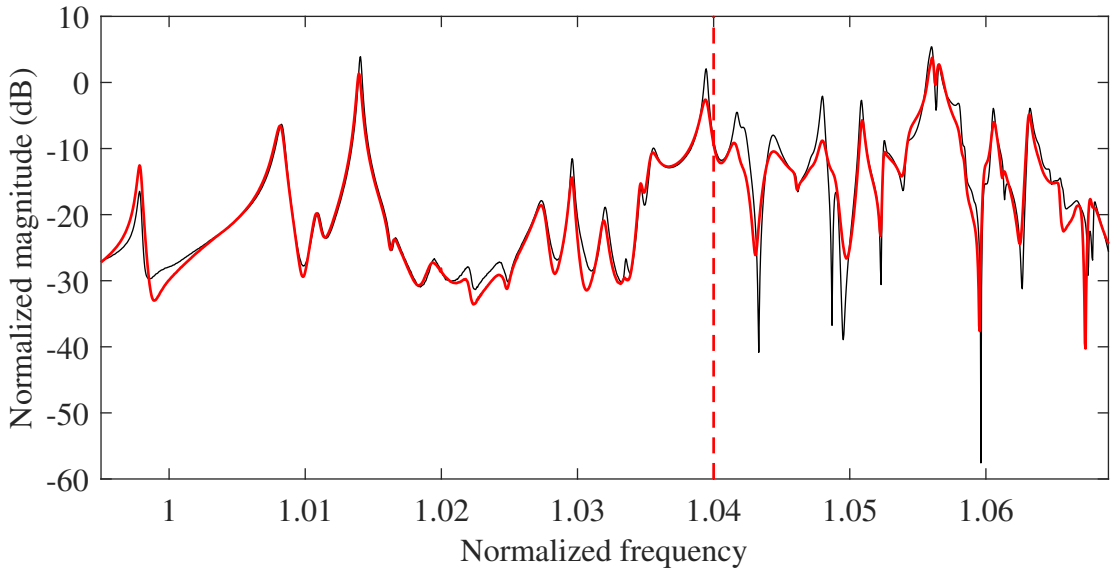

(b) Close-up on mode family #1.

Figure 4.29: FRFs of the uncontrolled system (▬) and of the system controlled by a three-stage current blocking circuit (▬). The targeted mean frequency is represented using (▬).

Chapter 5

Exact H_∞ tuning rule for a positive position feedback controller

5.1 Introduction

In the previous chapters, passive control laws were applied to structures featuring different levels of complexity. This chapter focuses on active control methods which have the advantage of improving the control authority over the system. However, since active controllers can potentially introduce additional energy into the system, special attention must be paid to stability conditions.

To allow for damping performance enhancement, this chapter discusses the possibility to add an active component to classical RL shunts, namely a negative capacitance, to form an NCRL shunt. In this context, classic H_∞ tuning rules for passive RL shunts are first extended to this case. In a second step, a parallel between the control parameters of an NCRL shunt and of a PPF controller is drawn. This parameter equivalence is subsequently used to translate the shunt tuning rules to PPF controllers with the aim to provide exact H_∞ tuning rules and a closed-form expression of the maximum amplitude of the receptance function. Using these newly-derived tuning rules, a thorough comparison between NCRL shunts and PPF controllers is performed using an SDOF example. Owing to their considerably greater stability margins, we then focus solely on the PPF controller for the evaluation of the performance of these tuning rules.

5.2 Enhancing the damping performance of RL shunts with a negative capacitance

The damping performance of classical RL shunts, which operate according to a purely passive control law, is limited by the coupling between the mechanical structure and the piezoelectric transducer. Consequently, an improvement of this coupling, characterized by the EMCF, can augment control performance. To achieve this, an NC can be added in series or parallel to the shunt circuit.

The concept of an NC was first introduced by Forward [18]. The author aimed to compensate for the inherent capacitance of electromechanical transducers coupled to vibrating mechanical structures using an NC circuit in parallel to a piezoelectric transducer. Bondoux cancelled the electrical reactance in simple R shunt circuits with an NC alone and eventually compared it to an RL shunt [135]. Tang and Wang implemented an NC in series with the piezoelectric material to improve the damping performance of resonant shunts [136]. They adapted the shunt tuning rules based on the common intersection points (fixed points) of the FRF for passive RL shunts first introduced by Hagood and von Flotow [19]. Behrens et al. presented a thorough theoretical analysis of a controller consisting of an R shunt with an NC. Their results were demonstrated using a plate structure whereas the NC value was chosen to be as close as possible to the stability limit [137]. Fleming and Moheimani designed active shunt impedance based on LQG and H_∞ synthesis techniques. In their work, they noticed some similarities between these active impedances and an NC [27]. Neubauer et al. compared different circuit compositions of series NCRL shunts in order to point out the stability limits and the enhanced damping performance. They provided experimental validations with a vibrating mass mounted on a piezoelectric stack actuator [138]. In their study, the optimal shunt parameters were also derived by means of the fixed-points tuning rule. Later, de Marneffe and Preumont compared a series and a parallel configuration of an NC and concluded that the series implementation is more robust [28]. Their theoretical results were verified by experiments on a truss structure where the NC values were chosen so that 90 % of the stability limit was reached. In addition, they compared an NCRL shunt to the classical active approach of an integral force feedback (IFF) controller. It could be shown that the IFF controller leads to better damping performance than the shunt [28]. Berardengo et al. derived more complex formulations for the dynamic capacitance of the piezoelectric transducer in order to take multiple modes and their influence into account and to design a robust electrical network by using a real circuit to realize the NC. They proposed different designs for RL shunts with an NC in parallel or series as well as a circuit with two NC in parallel-series combinations. Eventually, their findings were validated using a cantilever steel beam [39, 139]. Subsequently, Berardengo et al. proposed a solution for multimodal shunt damping with R shunts connected to an NC (RNC shunts) and to an inductance L. Instead of tuning L toward a monomodal control, the inductor was used to improve the broadband attenuation of the RNC shunt being relatively robust to detuning [140]. The method was demonstrated numerically and experimentally. Recently, Sugino et al. realized an NC circuit with a digital controller to create programmable bandgaps in a beam [141]. Both the synthetic impedance and the NC need to be powered [138]. This is why piezolectric NCRL shunts, although working according to a passive control law, are sometimes classified in the active control field.

In this chapter, the exact H_∞ tuning rule for RL shunts, first proposed by Soltani et al. [47] (cf. Section 1.3.2.2), are extended to the case when an RL shunt is connected in series to an NC. An equivalence between a PPF controller and an NCRL shunt is then put forward in order to translate this tuning rule to the active control case. Finally, a comparison between the two approaches is provided, highlighting the superiority of the PPF controller for practical applications.

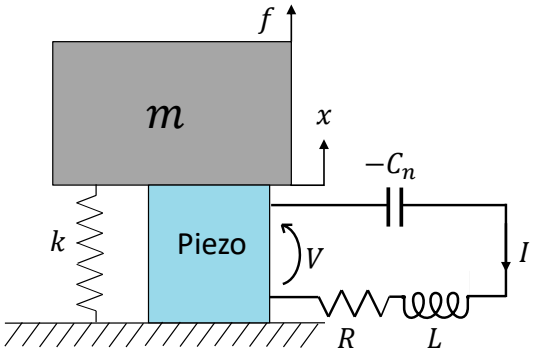

Figure 5.1: SDOF system with a series RL shunt in series with an NC.

5.2.1 The NCRL shunt

We reconsider the example of a piezoelectric SDOF structure similar to the one in Figure 1.6, now connected to a series RL shunt in series with an NC as displayed in Figure 5.1. The equations of motion for the passive part of the system are given in Equation (1.27), with θ_p characterizing the amount of energy that is transformed between the piezoelectric transducer and the mechanical system [19]. We recall the definition of the dimensionless EMCF given in Equation (1.13), or, alternatively normalized with the open-circuit resonance frequency in (1.14). This coupling factor is defined by means of the fixed properties of the host system, namely θ_p and C_p^ε. The maximum amplitude of the forced response of the controlled system is determined by the EMCF, as it is taken into account for the definition of the shunt parameters [47]. If an NC is added to the shunt circuit, the electromechanical coupling can be increased and the shunt performance is enhanced [28]. For a piezoelectric transducer connected to a passive RL shunt circuit in series with a negative capacitance C_n, the relation between the voltage and the charge is given by

$$\left(Ls^2 + Rs - \frac{1}{C_n}\right) q_p = V_p \ . \tag{5.1}$$

The electrical part of Equation (1.27) adapted to the case when an NC is used reads

$$Ls^2 q_P + Rsq_p + \frac{1}{C_{eff}} q_p - \theta_p x = 0 \ , \tag{5.2}$$

with the effective capacitance [39]

$$\frac{1}{C_{eff}} = \frac{1}{C_p^\varepsilon} - \frac{1}{C_n} \ . \tag{5.3}$$

With this additional parameter, the shunt parameters R and L now need to be tuned in dependence of C_n to obtain an optimal damping performance. We write the transfer function from the disturbance force to the displacement using the first line of Equation (1.27) and Equation (5.2)

$$\frac{x}{f} = \left[ms^2 + k_{oc} - \frac{\theta_p^2}{Ls^2 + Rs + \frac{1}{C_{eff}}}\right]^{-1} \ . \tag{5.4}$$

Introducing the electrical frequency and the damping ratio of the shunt, Equation (5.4) can be rewritten in dimensionless form

$$\omega_e^2 := \frac{1}{C_{eff}L}, \quad 2\omega_e\zeta_e := \frac{R}{L} \tag{5.5}$$

so that [48]

$$x_{st} := \frac{f}{k_{oc}}, \quad \tilde{\alpha}^2 := \frac{\theta_p^2 C_{eff}}{k_{oc}}, \quad \nu_e := \frac{\omega_e}{\omega_{oc}}, \quad \hat{s} := \frac{s}{\omega_{oc}} \ . \tag{5.6}$$

The tilde refers to the case when an NC is used. Using Equations (5.5) and (5.6), the transfer function of the SDOF system with an NCRL shunt reads

$$h(\hat{s}) = \frac{x}{x_{st}} = \left[\hat{s}^2 + 1 - \frac{\tilde{\alpha}^2}{\frac{\hat{s}^2}{\nu_e^2} + 2\zeta_e\frac{\hat{s}}{\nu_e} + 1}\right]^{-1} \ . \tag{5.7}$$

With Equations (1.14), (5.3) and (5.6), the EMCF, enhanced by an NC is now

$$\tilde{\alpha}^2 = \frac{\theta_p^2 C_p^\varepsilon}{k_{oc}}\frac{C_{eff}}{C_p^\varepsilon} = \alpha^2\left[1 - \frac{C_p^\varepsilon}{C_n}\right]^{-1} \ . \tag{5.8}$$

Its value is greater than the EMCF of the initial system, when $C_p^\varepsilon < C_n < \infty$. Due to the relation

$$\tilde{K}_c^2 = \frac{\tilde{\alpha}^2}{1-\tilde{\alpha}^2} \ , \tag{5.9}$$

the short-circuit normalized EMCF is also increased.

5.2.2 H_∞ tuning rules for RL shunts with NC

The exact H_∞ tuning rules for passive RL shunts presented in Section 1.3.2.2 are now extended to the NCRL case. There is now an additional free parameter $\tilde{\alpha}$ that is fixed in the first place in order to find optimal values for ν_e and ζ_e. This is done by minimizing the H_∞ norm of the transfer function $h(i\hat{\omega})$. $\hat{\omega}$ represents a circular frequency normalized by ω_{oc} given in Equation (5.7):

$$\min_{\nu_e,\zeta_e}\|h(j\hat{\omega}_e)\|_\infty \rightarrow \text{find } \nu_e, \zeta_e \text{ such that } \ |h(j\hat{\omega}_{e,A})| = |h(j\hat{\omega}_{e,B})| \equiv h_0 \ .$$

Here, h_0 is the maximum amplification of two equal resonance peaks at the dimensionless frequencies $\hat{\omega}_{e,A}$ and $\hat{\omega}_{e,B}$. It can be expressed as function of the effective EMCF [47]:

$$h_0 = \frac{8}{\tilde{\alpha}\sqrt{2\sqrt{54\tilde{\alpha}^4 - 144\tilde{\alpha}^2 + 64} + 9\tilde{\alpha}^2 + 16}} \ . \tag{5.10}$$

Equation (5.10) can then be solved for $\tilde{\alpha}$, being equivalent to

$$135h_0^4\tilde{\alpha}^8 - 864h_0^4\tilde{\alpha}^6 + 1152h_0^2\tilde{\alpha}^4 + 2048h_0^2\tilde{\alpha}^2 - 4096 = 0 \ . \tag{5.11}$$

Equation (5.11) is a quartic equation in $\tilde{\alpha}^2$ that is solvable in closed-form. This means that a coupling coefficient $\tilde{\alpha}^2$ can be deduced for a desired amplification h_0 by solving Equation (5.11).

By minimizing the peak amplitude h_0, we find a value for $\tilde{\alpha}$ so that

$$\frac{\partial h_0}{\partial \tilde{\alpha}} = 0 \ . \tag{5.12}$$

Using Mathematica [142], we obtain:

$$\frac{\partial h_0}{\partial \tilde{\alpha}} = -\frac{4\left(\frac{216\tilde{\alpha}^3-288\tilde{\alpha}}{\sqrt{54\tilde{\alpha}^4-144\tilde{\alpha}^2+64}}+18\tilde{\alpha}\right)}{\tilde{\alpha}\left(9\tilde{\alpha}^2+2\sqrt{54\tilde{\alpha}^4-144\tilde{\alpha}^2+64}+16\right)^{3/2}} - \frac{8}{\tilde{\alpha}^2\sqrt{9\tilde{\alpha}^2+2\sqrt{54\tilde{\alpha}^4-144\tilde{\alpha}^2+64}+16}} \ . \tag{5.13}$$

Equations (5.10) and (5.12) are solved for $\tilde{\alpha}$, yielding

$$\tilde{\alpha}_{opt} = 2\sqrt{\frac{2}{15}} \ . \tag{5.14}$$

Inserting $\tilde{\alpha}_{opt}$ in Equation (5.10), we obtain a quantification of the minimum attainable dimensionless H_∞ norm:

$$h_{0,opt} = \sqrt{5} \ . \tag{5.15}$$

With $\tilde{\alpha}_{opt}$, we can also define the shunt parameters ν_e and ζ_e, expressed as a function of $\tilde{K}_c^2$ (cf. Equation (5.9)). To this end, the tuning rules provided by Soltani et al. [47] can be used to find the optimal shunt parameters. The intermediate parameter r is found with Equation (1.30), using $\tilde{K}_c^2$ instead of K_c^2. The optimal frequency and damping ratios then read

$$\nu_e = \sqrt{\frac{3\tilde{K}_c^2 - 4r + 8}{4\tilde{K}_c^2 + 4}} \tag{5.16}$$

and

$$\zeta_e = \frac{\sqrt{27\tilde{K}_c^4 + 80\tilde{K}_c^2 + 64 - 16r\left(4 + 3\tilde{K}_c^2\right)}}{\sqrt{2}\left(5\tilde{K}_c^2 + 8\right)}, \tag{5.17}$$

Finally, a theoretical optimal value for C_n can be derived with Equations (5.8) and (5.14):

$$C_{n,opt} = C_p^\varepsilon \left[1 - \frac{\alpha^2}{\tilde{\alpha}_{opt}^2}\right]^{-1} \ . \tag{5.18}$$

Using Equation (5.5), physical shunt parameters R and L can be calculated for a series shunt. They are a function of C_{eff}, ω_{oc}, ν_e and ζ_e.

5.3 Equivalence between an RL shunt with an NC and a PPF controller

Another way to attenuate vibrations is to control a structure with an active damping device such as a PPF controller [21]. This approach acts like a filter, controlling a displacement with an actuation force [22, 143, 144]. As already implied in the name, the

position coordinate is measured by a sensor and positively fed to both the compensator and eventually back to the structure via an actuator [144, 145]. Three controller parameters, namely the pole frequency, the damping ratio and the controller gain, need to be defined for a second-order PPF. The controller acts on the system as a low-pass filter and is rolling off at higher frequencies. Hence, there is no risk to excite higher-order modes with a PPF controller which is an interesting feature of the approach [72]. Moreover, it can be designed using solely experimentally obtained transfer functions, eliminating the need to create analytical models of the plant structure. Goh and Caughey provided a comparison between velocity feedback and PPF controllers, stating that the latter yields a more robust closed-loop system [22]. All these properties make the PPF an attractive solution for the mitigation of structural vibrations.

Different strategies can be followed for the choice of the controller parameters. In [22], the authors aimed for maximum attainable closed-loop damping that was combined with tuning filters in the multimodal case. A self-sensing PPF controller with a piezoelectric patch acting simultaneously as a sensor and actuator was proposed by Dosch et al. [146]. An optimization algorithm was then used to determine the controller parameters aiming for optimal damping of the resonance amplitude of the receptance function [146, 147]. Kwak and Han investigated the possibility of using a genetic algorithm to find optimal PPF parameters [148]. In their work, solely the controller frequency was varied, whereas the remaining parameters remained fixed, which is a notable drawback of their study. Enríquez-Zárate et al. proposed a controller design with an a priori defined damping factor and chose the controller gain with the focus on ensuring system stability [149]. A common tuning approach for the controller parameters is to focus on the pole frequency ensuring that the controller resonates at the host structure's natural frequency [150]. For a maximum flatband response, a fifth-order Butterworth filter for a specific frequency might be used to design the PPF controller [151]. In their work, Paknejad et al. aimed to optimize all three controller parameters opting for maximum damping [152]. It is widely known that PPF controllers increase the low-frequency sensitivity of the controlled system, resulting in a growth of the static response [153]. To limit this static softening, Paknedjad et al. minimized the H_2 norm of the receptance for the final controller design. Alternatively, the problem can be addressed by expressing the PPF filter in a fractional-order format [154, 155]. A feedforward control that is counteracting the increasing static response might become an option, if the user has a good knowledge of the system dynamics [156]. Recently, MacLean et al. studied how a desired damping performance, the static softening and system stability interact with each other [153]. In [157], Den Hartog's fixed-points theory was adapted to tune a PPF controller. Similarly to the resonant piezoelectric shunt controller, the receptance function of the controlled system exhibits two resonance peaks around the targeted frequency. Using the tuning rules in [157], the resonance peaks then feature an approximately equal amplitude. Yet, an exact solution in the H_∞ sense is not provided.

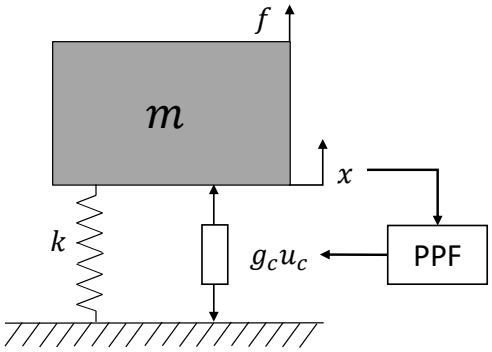

Figure 5.2: SDOF system with a PPF controller.

5.4 Parameter equivalence between NCRL and PPF controllers

The SDOF system is now controlled by a PPF controller as displayed in Figure 5.2 with a collocated sensor-actuator pair. We obtain the following equations of motion

$$\begin{cases} mxs^2 + kx = f + \omega_c^2 g_c u_c \\ (s^2 + 2\omega_c\zeta_c s + \omega_c^2)u_c = x \end{cases}, \tag{5.19}$$

with the control signal u_c, the damping ratio ζ_c, the controller frequency ω_c and the controller gain g_c. The second line of Equation (5.19) is then inserted in the first so that

$$(ms^2 + k)x = f + \frac{\omega_c^2 g_c x}{s^2 + 2\omega_c\zeta_c s + \omega_c^2}. \tag{5.20}$$

Equation (5.20) is then divided by x. The reciprocal of this expression yields the receptance function

$$\frac{x}{f} = \left[ms^2 + k - \frac{\omega_c^2 g_c}{s^2 + 2\omega_c\zeta_c s + \omega_c^2}\right]^{-1}. \tag{5.21}$$

With [48]

$$x_{st} := \frac{f}{k},\ \omega_0 := \sqrt{\frac{k}{m}},\ \hat{s} := \frac{s}{\omega_0},\ \nu_c := \frac{\omega_c}{\omega_0},\ g := \frac{g_c}{k}, \tag{5.22}$$

Equation (5.21) can be rewritten in dimensionless form:

$$\frac{x}{x_{st}} = \left[\hat{s}^2 + 1 - \frac{g}{\frac{\hat{s}^2}{\nu_c^2} + 2\zeta_c\frac{\hat{s}}{\nu_c} + 1}\right]^{-1}. \tag{5.23}$$

Comparing Equations (5.7) and (5.23), we can see that the controller parameters of an NCRL shunt and those of a PPF controller play the same role in the receptance function. This parameter equivalence is provided in Table 5.1. Interestingly, a dynamical similarity was already pointed out by Agnes [145]. In this work, a *full equivalence* of the tuning parameters and the receptance functions is stated. To demonstrate this equivalence, a SDOF host system is controlled by an NCRL shunt and a PPF controller, both tuned with the optimal parameters in Table 5.1. The results in Figure 5.3 evidences that the receptance functions are identical, confirming our finding.

Shunt	$\tilde{\alpha}^2$	ν_e	ζ_e
PPF	g	ν_c	ζ_c

Table 5.1: Equivalence between the dimensionless parameters of an NCRL shunt and a PPF controller.

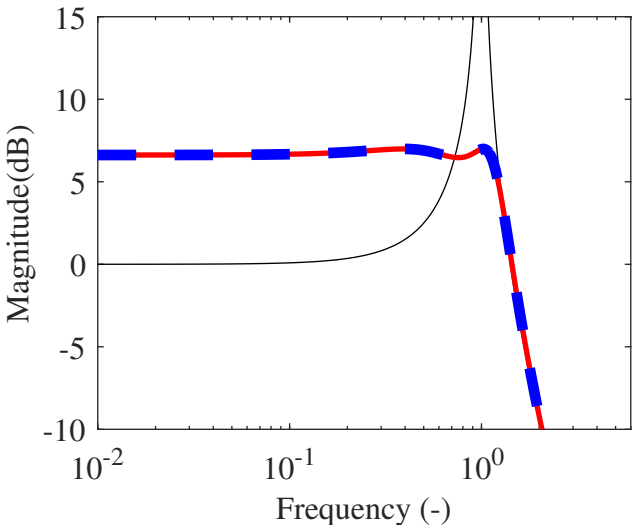

Figure 5.3: Receptance function of a dimensionless SDOF system in the uncontrolled case (▬)) and controlled by an NCRL shunt ($\alpha = 0.1$) (▪ ▪ ▪) and a PPF controller (▬)). Both are tuned according to H_∞ tuning rules.

5.5 Limitations of the parameter equivalence

In the previous section, it was shown that an NCRL shunt and a perfectly collocated PPF exhibit identical receptance functions when the parameter equivalence of 5.1 is considered. However, this equivalence is only valid up to certain limits. This becomes clear when assessing the stability limits of the two approaches. In the following, two different viewpoints to investigate stability are discussed. To this end, we regard the open-loop transfer functions of the two systems. They can be derived by means of the feedback diagrams displayed in Figure 5.4. For the NCRL shunt, the transfer function $G(s)$, also known as the dynamic impedance of the piezoelectric transducer, can be derived from Equation (1.10) and the expression of k_{sc} (cf. Equations (1.9) and (1.11)):

$$G_{Shunt}(s) = \left.\frac{V_p}{sq_p}\right|_{f=0} = -\frac{1}{sC_p^\varepsilon}\frac{s^2+\omega_{sc}^2}{s^2+\omega_{oc}^2} \,. \tag{5.24}$$

It is the relation between sq_p and V_p when the external forcing f is set to zero. The feedback $Y_{Shunt,NC}(s)$ then reads

$$Y_{Shunt,NC} = \frac{1}{Ls + R - \frac{1}{sC_n}} \,. \tag{5.25}$$

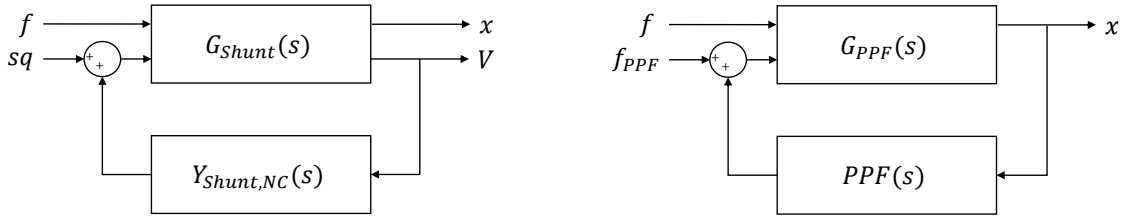

(a) Piezoelectric NCRL shunt. **(b)** PPF controller.

Figure 5.4: Feedback control of a host system with different control approaches.

Equations (5.24) and (5.25) are now combined to obtain the open-loop transfer function in dimensionless form (with Equations (5.5) and (5.6))

$$H_{ol,Shunt}(\hat{s}) = -G_{Shunt}(\hat{s})Y_{Shunt,NC}(\hat{s}) = \frac{\hat{s}^2+1-\alpha^2}{\hat{s}^2+1}\frac{\frac{\tilde{\alpha}^2}{\alpha^2}}{\frac{\hat{s}^2}{\nu_e^2}+2\zeta_e\frac{\hat{s}}{\nu_e}+1-\frac{\tilde{\alpha}^2}{\alpha^2}} . \tag{5.26}$$

For the PPF controller, the plant transfer function G_{PPF} is derived from Equation (5.19) as the relation between the controller force $f_{PPF} = \omega_c^2 g_c u_c$ and the displacement x when $f = 0$:

$$G_{PPF}(s) = \frac{1}{ms^2+k} . \tag{5.27}$$

In the PPF case, the feedback is a second-order filter:

$$PPF(s) = \frac{g_c\omega_c^2}{s^2+2\omega_c\zeta_c s+\omega_c^2}. \tag{5.28}$$

With Equations (5.27) and (5.28), and the parameters in Equation (5.22), the open-loop transfer function is written in dimensionless form:

$$H_{ol,PPF}(\hat{s}) = -G_{PPF}(\hat{s})PPF(\hat{s}) = -\frac{1}{\hat{s}^2+1}\frac{g}{\frac{\hat{s}^2}{\nu_c^2}+2\zeta_c\frac{\hat{s}}{\nu_c}+1} . \tag{5.29}$$

Case 1: Only $\tilde{\alpha}^2$ and g are varied

Following the spirit of the parameter equivalence, the controller gains $\tilde{\alpha}^2$ and g are varied in the same way. The characteristic equation for the NCRL shunt can be derived from Equation (5.26)

$$1+\frac{\hat{s}^2+1-\alpha^2}{\hat{s}^2+1}\frac{\frac{\tilde{\alpha}^2}{\alpha^2}}{\frac{\hat{s}^2}{\nu_e^2}+2\zeta_e\frac{\hat{s}}{\nu_e}+1-\frac{\tilde{\alpha}^2}{\alpha^2}} = 0. \tag{5.30}$$

It can be rewritten so that

$$(\hat{s}^2+1)\left(\frac{\hat{s}^2}{\nu_e^2}+2\zeta_e\frac{\hat{s}}{\nu_e}+1-\frac{\tilde{\alpha}^2}{\alpha^2}\right)+\left(\hat{s}^2+1-\alpha^2\right)\frac{\tilde{\alpha}^2}{\alpha^2} = 0 \tag{5.31}$$

and

$$(\hat{s}^2+1)\left(\frac{\hat{s}^2}{\nu_e^2}+2\zeta_e\frac{\hat{s}}{\nu_e}+1\right)-\tilde{\alpha}^2 = 0. \tag{5.32}$$

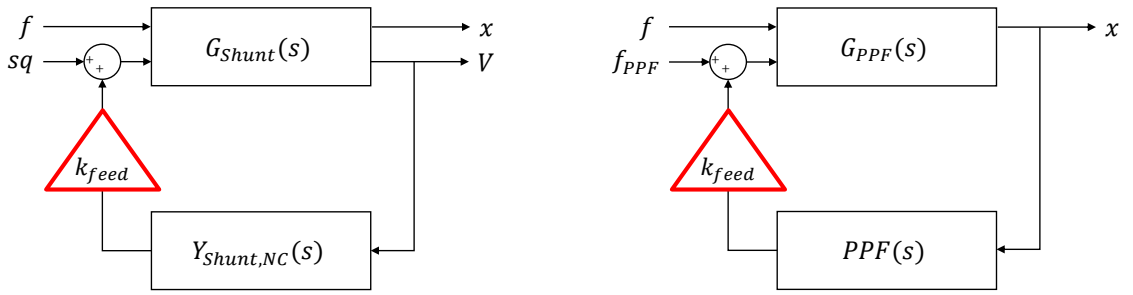

(a) Piezoelectric RL shunt with NC. **(b)** PPF controller.

Figure 5.5: Feedback control with a loop gain with a piezoelectric RL shunt with different control approaches.

For the PPF, we obtain the characteristic equation from Equation (5.29)

$$1 - -\frac{1}{\hat{s}^2+1}\frac{g}{\frac{\hat{s}^2}{\nu_c^2}+2\zeta_c\frac{\hat{s}}{\nu_c}+1} = 0, \tag{5.33}$$

rewritten as

$$(\hat{s}^2+1)\left(\frac{\hat{s}^2}{\nu_c^2}+2\zeta_c\frac{\hat{s}}{\nu_c}+1\right) - g = 0. \tag{5.34}$$

From classic control theory it is known that the roots of this characteristic equation correspond to the poles of the controlled system [69]. Given the equivalence between $\tilde{\alpha}^2$ and g, a comparison between Equations (5.32) and (5.34) reveals that both approaches lead to the same closed-loop poles. Thus, varying them in the same way, also leads to the same root locus. For the shunt, this variation in $\tilde{\alpha}^2$ only could be interpreted as a global mismatch between the shunt parameters and the NC. For the PPF controller, changing g would already correspond to a change of the loop gain.

Case 2: An additional loop gain is introduced and varied

The stability of the controlled systems may be studied by introducing an additional loop gain k_{feed} that is varied while the controller parameters are kept constant. The schematics are displayed in Figure 5.5. In the context of a practical implementation, the variation of a loop gain is of great interest for stability investigations of the controller. This analysis allows for investigating the effects of possible delays in the feedback loop that can change the characteristics of the controller function and impact the dynamics of the closed-loop system [70]. If the controlled system does not have a large enough tolerance to these delays or other disturbances in the loop, instabilities can occur. We consider $k_{feed} = 1$ as the optimal case. Based on Figure 5.5 and the previous developments, the characteristic equation for the NCRL shunt can be derived from Equation (5.30) so that

$$1 + k_{feed}H_{ol,Shunt}(\hat{s}) = 1 + k_{feed}\frac{\hat{s}^2+1-\alpha^2}{\hat{s}^2+1}\frac{\frac{\tilde{\alpha}^2}{\alpha^2}}{\frac{\hat{s}^2}{\nu_e^2}+2\zeta_e\frac{\hat{s}}{\nu_e}+1-\frac{\tilde{\alpha}^2}{\alpha^2}} = 0, \tag{5.35}$$

or,

$$(\hat{s}^2+1)(\frac{\hat{s}^2}{\nu_e^2}+2\zeta_e\frac{\hat{s}}{\nu_e}+1) - k_{feed}\tilde{\alpha}^2 + \frac{\tilde{\alpha}^2}{\alpha^2}(k_{feed}-1)(\hat{s}^2+1) = 0. \tag{5.36}$$

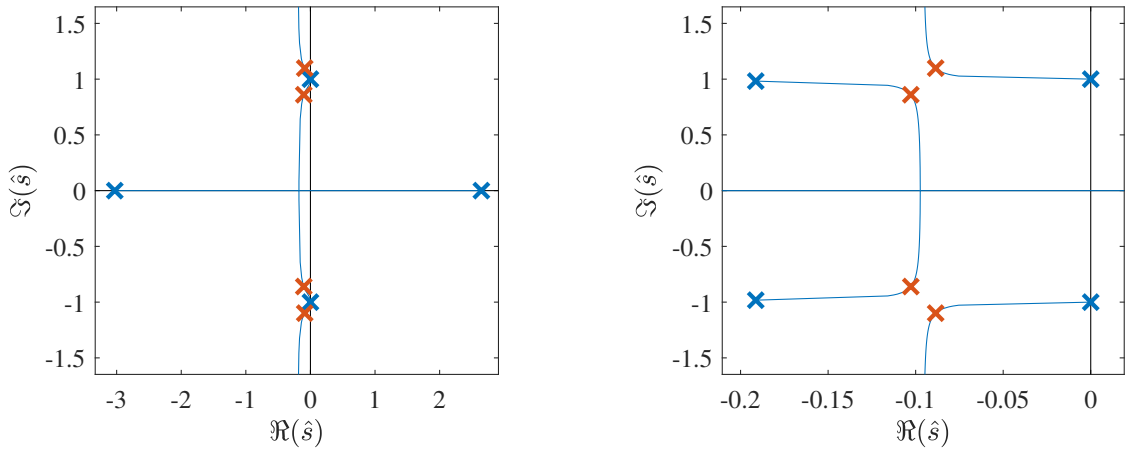

(a) RL shunt with NC ($\alpha = 0.1$). **(b)** PPF.

Figure 5.6: Root loci of of the controlled systems for variations of k_{feed}. Open-loop poles: ×, and poles of the closed-loop system: ×.

For the PPF controller, we obtain

$$1 + k_{feed} H_{ol,PPF}(\hat{s}) = (\hat{s}^2 + 1)\left(\frac{\hat{s}^2}{\nu_c^2} + 2\zeta_c \frac{\hat{s}}{\nu_c} + 1\right) - k_{feed} g = 0. \tag{5.37}$$

Comparing Equations (5.36) and (5.37) reveals that, for $k_{feed} \neq 1$, the characteristic equations of the two controllers differ from each other so that, for the same variation of k_{feed}, the systems exhibit different closed-loop poles. Only in the perfectly tuned case with $k_{feed} = 1$, their roots are identical and the closed-loop stability is the same for both approaches. This can be explained by the influence that the loop gain has on the polynomials in the characteristic equation. Equation (5.36) shows that, for the NCRL shunt, the zeroth and the second-order terms of the $\hat{s}$-polynomials are influenced by k_{feed}. In contrast, for the PPF controller, only the zeroth-order term of the polynomial in $\hat{s}$ is affected by k_{feed} (cf. Equation (5.37)). The root loci of the controlled systems in the s-plane are plotted in Figure 5.6. Indeed, the root loci evolve differently for $k_{feed} \neq 1$. For the NCRL shunt, the open-loop poles of the plant are located along the imaginary axis, whereas one of the controller's poles lies in the right half plane (cf. Figure 5.6a). Finally, when the loop is closed, their initial directions are reversed in the root locus due to the positive feedback. On the other hand, all poles of the PPF controller are located in the left half plane.

In summary, for the non-ideally tuned case, the proposed parameter equivalence does not always hold true leading to different performances (and stability margins) of the two approaches.

5.5.1 Stability and stability margins

For the stability investigations of the closed-loop system, the open-loop transfer functions given in Equations (5.26) and (5.29) are reconsidered. In previous works [28, 158], it was shown that, given that the damping ratio and optimal frequency are greater than zero, the

controller could only be destabilized by $\tilde{\alpha}$ or g. Considering the NCRL shunt, the initial electromechanical coupling characterized by α needs to be taken into account. Relatively large values of α can ensure a better control authority and thus a more robust system. However, systems controlled by piezoelectric RL shunts usually exhibit low coupling. In [28], de Marneffe and Preumont define a theoretical stability limit for NCRL shunts, stating that the closed-loop system is stable when

$$C_n > \frac{\omega_{oc}^2}{\omega_{sc}^2} C_p^{\varepsilon} \ . \tag{5.38}$$

The system becomes unstable if the negative stiffness of the transducer, represented by the capacitance ($\omega_{oc}^2 C_p^{\varepsilon}/\omega_{sc}^2 = C_n$), cancels out the structure's stiffness (as it is seen from the transducer) [28]. Comparing this condition with the value for $C_{n,opt}$ proposed in Equation (5.18), we deduce that the optimal value for the NC is already close to this limit. A look at Equation (5.8) reveals that $\tilde{\alpha}^2 = 1$ when the stability limit is reached. Hence, stability is ensured as long as $\tilde{\alpha}^2 < 1$. This explanation can be translated to the PPF controller. Similarly to [28], Krenk et al. derived the stability limit for the PPF controller by means of the overall structural stiffness [159]. In their work, Zhao et al. defined the limit for the controller gain directly to $g < 1$ [158].

If the theoretical closed-loop stability is a necessary condition, it is not sufficient to ensure satisfactory control performance. In practical applications, uncertainties and unmodeled dynamics need to be taken into account during controller design through adequate stability margins. We can derive these margins from the open-loop transfer functions [69]. A comparison between Equations (5.26) and (5.29) shows that the open-loop transfer functions for the NCRL shunt and the PPF controller are not identical. For the PPF controller, the plant transfer function is only represented by the mechanical system whereas the whole electromechanical system is considered as a plant in the shunt approach. This perspective is based on the actual practical application of piezoelectric shunts.

Based on the parameter equivalence listed in Table 5.1, the tuning rules from Equations (5.14) and (5.16) - (5.18) can be used for both the NCRL shunt and the PPF controller. Bode plots of the open-loop transfer functions in this optimal tuning scenario are plotted in Figure 5.7. $H_{ol,Shunt}(\hat{s})$ and $H_{ol,PPF}(\hat{s})$ evolve differently, and significantly greater stability phase margins are featured by the PPF controller around the resonance frequency. The phase margins as a function of $\tilde{\alpha}$ are displayed in Figure 5.8. The PPF controller yields phase margins between 60° and 80° whereas the NCRL shunt features very small phase margins when $\tilde{\alpha}$ is greater than $\alpha = 0.1$. If the optimal value (5.14) is reached, the theoretical phase margin is even smaller than 1°. This would not only render the NCRL shunt prone to instabilities caused by modeling errors or errors made during the controller design but also to delays generated by a digital controller. To avoid this, $\tilde{\alpha}$ must be chosen smaller than $\tilde{\alpha}_{opt}$ in practical applications. It can be concluded that the PPF controller is clearly more robust and represents the only viable solution for practical applications of the proposed tuning rule.

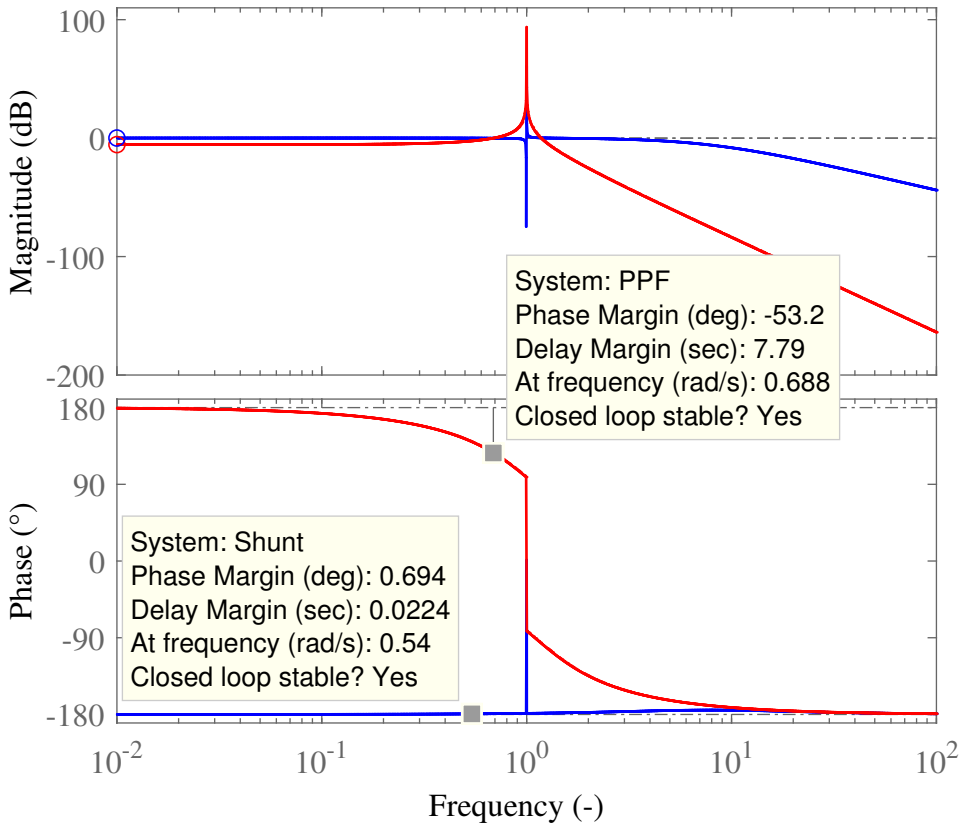

Figure 5.7: Bode plots of the open-loop transfer functions of a dimensionless SDOF system ($\alpha = 0.1$) with an NCRL shunt (▬) and a PPF controller (▬)) tuned according to H_∞ tuning rules.

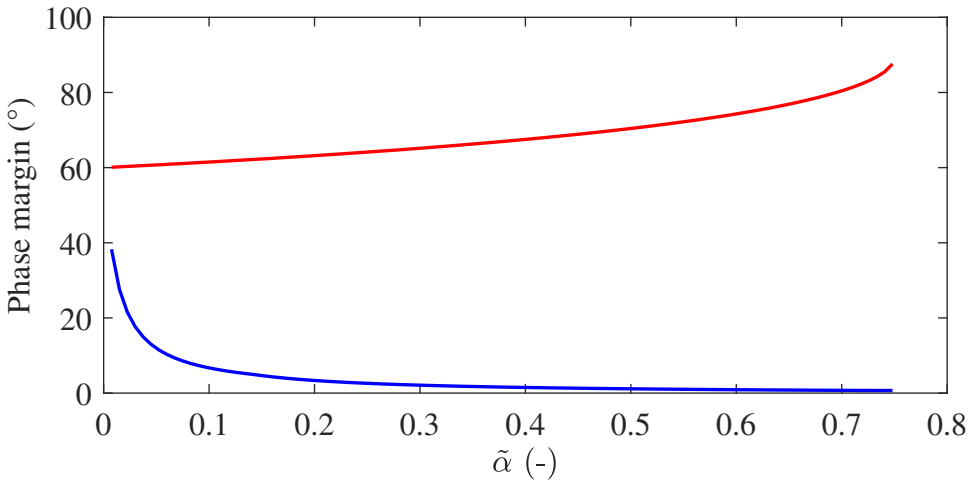

Figure 5.8: Phase margins for the open-loop transfer functions of the NCRL shunt (▬) and the PPF controller (▬) for variations of the parameter $\tilde{\alpha}$.

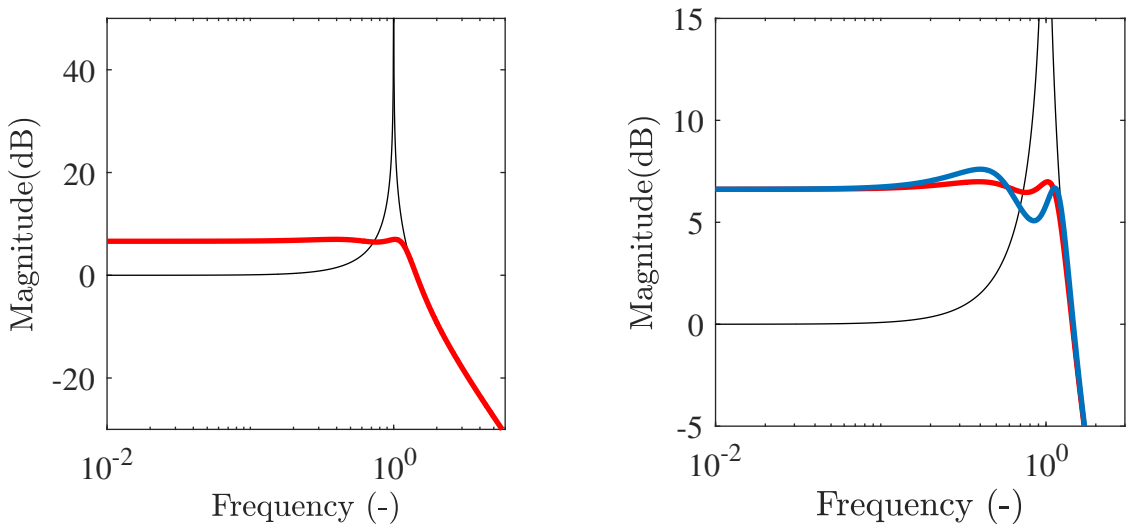

Figure 5.9: FRFs between the structural response and external force of a SDOF system. Uncontrolled (▬), controlled by a PPF controller with exact H_∞ rules (▬) and by a tuning based on fixed points (▬).

5.6 Performance of the H_∞ tuning rule for the PPF controller

For performance assessment, the receptance functions of the uncontrolled (1.10) and controlled (5.23) systems are displayed in Figure 5.9a. The FRF of the PPF controlled system now presents two resonance peaks that are equal in amplitude instead of one. In comparison to the uncontrolled system, the resonance amplitudes could be very significantly decreased. However, this amplitude reduction comes at the price of an increased static response which can be explained by examining Equation (5.23) at low frequencies:

$$h(0) = \frac{1}{1-g} \,. \tag{5.39}$$

The growth of the static response is a well-known side effect of the PPF controller and was widely discussed in the research community [152, 154–156]. In Figure 5.10, the FRF of the SDOF system controlled by PPF with different gains are shown. For $g < g_{opt}$, the growth of the static response can be reduced but, as a trade-off, the resonance amplitudes feature greater magnitudes.

In [47], it was concluded that an equal-peak design could only be ensured for values of $\tilde{\alpha} < \tilde{\alpha}_{max} = 0.74815$, corresponding to $g_{max} = 0.5597$ for the PPF controller. The maximum amplitude h_0 of the receptance function and the static response are plotted in Figure 5.11 for different gain values g. In fact, for values $g > g_{max}$, the maximum resonance amplitude occurs at $\hat{s} = 0$, corresponding to the static response. Therefore, the minimum amplitude for g_{opt} defined in Equation (5.15) is indeed an absolute minimum.

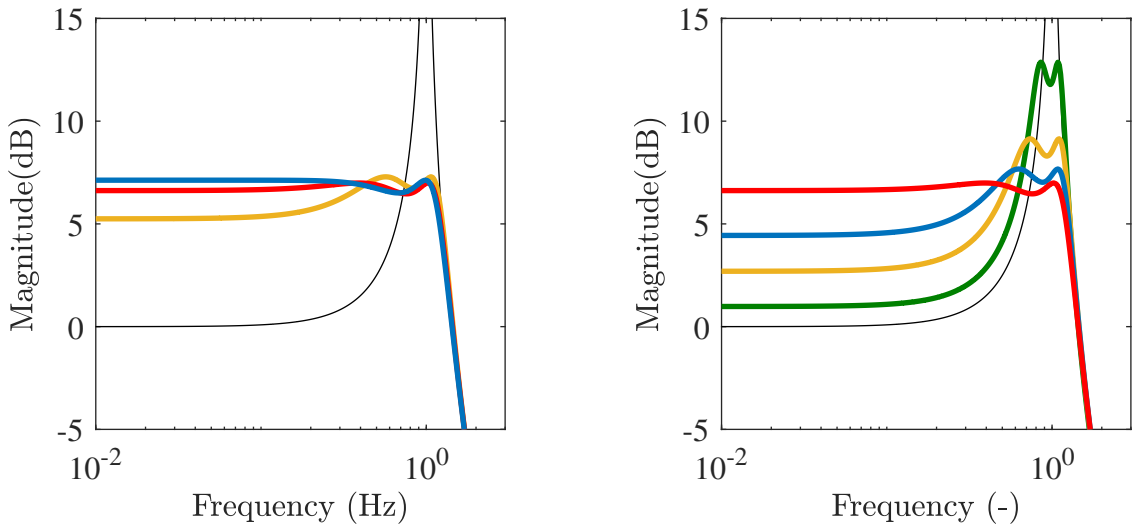

(a) FRF for $g = 0.85g_{opt}$ (—), $g = g_{opt}$ (—) and $g = 1.046g_{opt} = g_{max}$ (—).

(b) FRF for $g = 0.2g_{opt}$ (—), $g = 0.5g_{opt}$ (—), $g = 0.75g_{opt}$ (—) and $g = g_{opt}$ (—).

Figure 5.10: FRFs between the structural response and the external disturbance voltage of the SDOF system controlled by a PPF controller with different gain settings. The uncontrolled response is represented with (—).

Finally, the H_∞ tuning rule is compared to the fixed-points-based tuning method presented by Zhao et al. [157, 158]. In their work, the authors do not define a specific optimal gain value but propose to choose the controller gain to be as large as possible without violating the stability limit. As it was shown before, this significantly increases the static response. Hence, g must finally be set to a smaller value. For the comparison, the gain of both controllers are equal to g_{opt}. The FRF of the controlled systems are presented in Figure 5.9b. As expected, the fixed-points method does not yield exactly equal amplitudes of the resonance peaks. However, due to the choice of the gain values, an identical amplitude of the static response is obtained. Thus, the tuning rule proposed herein can also serve as a guidance for the choice of a concrete gain value when other tuning methods are used.

5.7 Conclusion

In this chapter, it was demonstrated that the receptance function of an NCRL shunt and of a collocated PPF controller are identical. Based on this result, an equivalence between their parameters was derived. Subsequently, the exact H_∞ tuning rule proposed in [47] for passive RL shunts was extended to active control by introducing a tuning parameter, namely the effective electromechanical coupling factor or the controller gain. A closed-form expression of the receptance (featuring two peaks of equal amplitude) was then obtained. A lower bound for the H_∞ norm of the controlled response was derived, which highlights the inherent performance limits of the NC and PPF.

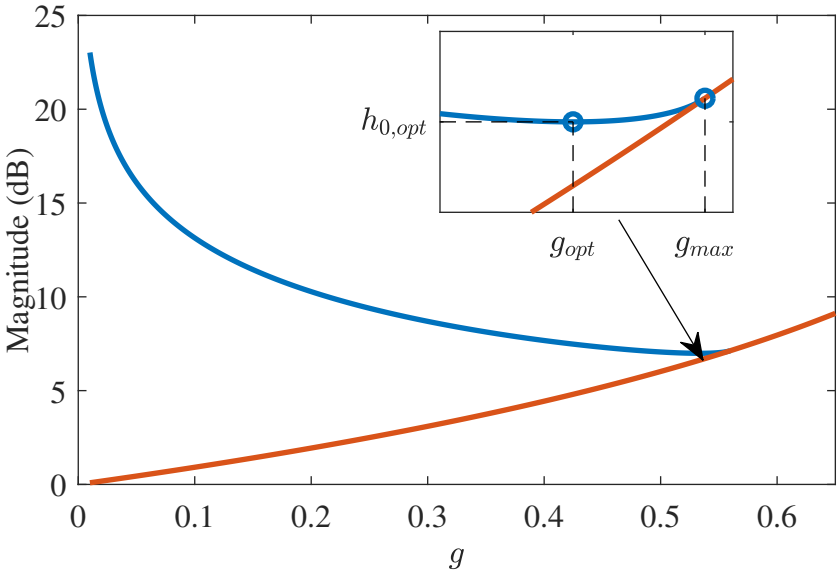

Figure 5.11: Maximum amplitude h_0 (—) and static response (—) of the controlled SDOF system as a function of the gain g.

The NCRL shunt and the PPF controller were also compared in terms of their stability margins and the open-loop transfer functions of the controlled system. The analogy between the two approaches only holds true in terms of their governing parameters and receptance functions but not for their stability margins. The reason is that the plant and feedback transfer functions are defined differently. From the stability investigations, it could be concluded that the use of an optimal NCRL shunt yields extremely small phase margins so that it cannot safely be applied in practice. The NC value should thus be chosen as a trade-off between the desired performance and the required robustness of the controlled system. Conversely, the stability margins of the optimal PPF controller are sufficiently large for practical applications.

Because this chapter focused on an SDOF host structure, the MDOF case is discussed in the next chapter.

Chapter 6

H_∞ tuning rule for a positive position feedback controller: the multi-degree-of-freedom case

6.1 Introduction

Conventionally, PPF controllers are tuned toward a selected resonant frequency of the host system, so that it may seem natural to model the host system as an SDOF system. Yet, for real structures, such an approximation is not always valid since the influence of other structural modes can influence the controller efficiency. For reliable and optimal damping performance, the influence of these modes must be taken into account when tuning the PPF parameters.

The task was approached in different ways in the research community. A common practice is to consider a simplified version of the host system, truncated in the frequency range of interest. There are several ways on how to account for the influence of the out-of-band modes. For the case of a collocated controller, Clark described two possibilities [160]. One is to model the out-of-bandwidth dynamics by a single mode that is acting as a feedback on the truncated host system. The alternative option is to introduce a feedthrough to a state-space model that incorporates the total displacement contribution of the out-of-band modes. To define this contribution, the pole-zero pattern of the open-loop transfer function was analyzed with the aim to find the system poles that were of importance for the bandwidth of interest and to then enforce them. Similarly, Moheimani et al. proposed to add a feedthrough term to the truncated host system model in the context of multivariable PPF controllers acting on a structure [161]. Recently, Silva et al. [162] used particle swarm optimization to tune the PPF parameters in a MIMO setup. Their tuning was based on a reduced-order model of the structure. In [163], the authors placed a PPF controller in series with a fictitious spring in a simplified numerical beam model. The added fictitious stiffness represented the influence of the higher-order modes. The PPF controller was then tuned based on the simplified model and could successfully introduce system damping. Fenik and Starek accounted for the contribution of the non-targeted vibration modes by including a constant as a correction to the optimal PPF controller parameters [164]. They achieved a closed-loop damping but, as already discussed in Sec-

tion 5.3, a drawback of their study is that they expressed the controller gain as a function of the controller frequency and damping ratio and found an optimum only for these two parameters. Their work additionally included a tuning strategy that incorporates the dynamics of other PPF controllers acting simultaneously, in descending order with respect to their natural frequencies [164].

From a piezoelectric shunt damping perspective, the influence of higher-order modes can be taken into account by using the dynamic capacitance to tune the shunt parameters [39, 165, 166]. Following the spirit of the comparison between a PPF controller and piezoelectric shunts, we will adapt this idea in this chapter to the active PPF control case. Specifically, we tune the parameters of the PPF controller aiming for a minimization of the H_∞ norm of the modal amplitude of the targeted mode. This chapter is structured as follows. First, a procedure to obtain the correction factors accounting for the influence of higher-order modes is presented. The effectiveness of the proposed correction procedure and the H_∞ tuning rule for a PPF controller are then studied, using a cantilever beam structure.

6.2 Correction procedure to account for higher-order modes

An MDOF system controlled by a PPF controller can be expressed with the following set of equations of motion in modal space:

$$\begin{cases} (s^2\mathbf{I} + \mathbf{\Omega}^2)\boldsymbol{\eta} = \mathbf{f} + \mathbf{w}\omega_c^2 g_c u_c \\ (s^2 + 2\zeta_c\omega_c s + \omega_c^2)u_c = \omega_c^2 g_c x_s \\ x_s = \mathbf{v}^T\boldsymbol{\eta} \end{cases} . \tag{6.1}$$

where $\mathbf{v}^T$ and $\mathbf{w}$ are vectors denoting the position of the sensor and of the actuator, respectively. $\mathbf{I}$ is the identity matrix, and $\mathbf{\Omega}$ is a diagonal matrix with the resonance frequencies. $\boldsymbol{\eta}$ is the vector of modal amplitudes, and x_s is the sensor signal. $\boldsymbol{\eta}$ is partitioned such that

$$\boldsymbol{\eta}^T = [\,\boldsymbol{\eta}_{<i}^T,\ \eta_i,\ \boldsymbol{\eta}_{>i}^T\,] . \tag{6.2}$$

In this case, the subscript i specifies the targeted mode. Consequently, the modal amplitudes of lower and higher frequency modes are influenced by $\boldsymbol{\eta}_{<i}$ and $\boldsymbol{\eta}_{>i}$, respectively. In the same way, we can partition the vectors $\mathbf{v}$ and $\mathbf{w}$:

$$\mathbf{v}^T = [\,\mathbf{v}_{<i}^T,\ v_i,\ \mathbf{v}_{>i}^T\,] \quad \text{and} \quad \mathbf{w}^T = [\,\mathbf{w}_{<i}^T,\ w_i,\ \mathbf{w}_{>i}^T\,] . \tag{6.3}$$

We consider the first line of Equation (6.1) and set $\mathbf{f} = 0$. For $\boldsymbol{\eta}_{<i}$, $\mathbf{\Omega}$ is small in relation to $s^2\mathbf{I}$ so that we can assume the dominating term is

$$s^2\boldsymbol{\eta}_{<i} = \mathbf{w}_{<i}\omega_c^2 g_c u_c . \tag{6.4}$$

For $\boldsymbol{\eta}_{>i}$, we obtain

$$\mathbf{\Omega}_{>i}^2\boldsymbol{\eta}_{>i} = \mathbf{w}_{>i}\omega_c^2 g_c u_c, \tag{6.5}$$

by discarding the $s^2\mathbf{I}$ term. The sensed signal x_s is then written with Equation (6.2), so that

$$x_s = \mathbf{v}_{<i}^T \boldsymbol{\eta}_{<i} + v_i \eta_i + \mathbf{v}_{>i}^T \boldsymbol{\eta}_{>i}. \tag{6.6}$$

Inserting Equations (6.4) and (6.5) in Equation (6.6) yields

$$x_s = \frac{1}{s^2}\mathbf{v}_{<i}^T \mathbf{w}_{<i} \omega_c^2 g_c u_c + v_i \eta_i + \mathbf{v}_{>i}^T \boldsymbol{\Omega}_{>i}^{-2} \mathbf{w}_{>i} \omega_c^2 g_c u_c. \tag{6.7}$$

We introduce the auxiliary variables

$$\frac{\kappa_{<i}}{s^2} = \mathbf{v}_{<i}^T \frac{1}{s^2} \mathbf{w}_{<i} \quad \text{and} \quad \kappa_{>i} = \mathbf{v}_{>i}^T \boldsymbol{\Omega}_{>i}^{-2} \mathbf{w}_{>i}, \tag{6.8}$$

and insert Equation (6.7) into Equation (6.1):

$$\begin{cases} (s^2 + \omega_i^2)\eta_i = w_i \omega_c^2 g_c u_c \\ \left(s^2 + 2\zeta_c \omega_c s + \omega_c^2 - \omega_c^2 g_c \kappa_{>i} - \omega_c^2 g_c \kappa_{<i} \frac{1}{s^2}\right) u_c = v_i \eta_i \end{cases}. \tag{6.9}$$

In this work, the focus is set on the first structural mode so that $\kappa_{<i} = 0$. The following relations are introduced:

$$\hat{u}_c = \frac{u_c}{v_i}, \quad \hat{\omega}_c^2 = \omega_c^2 - \omega_c^2 g_c \kappa_{>i}, \quad \hat{g}_c = \frac{\omega_c^2 g_c w_i v_i}{\hat{\omega}_c^2}, \quad \hat{\zeta}_c = \frac{\zeta_c \omega_c}{\hat{\omega}_c}, \tag{6.10}$$

so that Equation (6.9) reads

$$\begin{cases} (s^2 + \omega_i^2)\eta_i = \hat{\omega}_c^2 \hat{g}_c \hat{u}_c \\ \left(s^2 + 2\hat{\zeta}_c \hat{\omega}_c s + \hat{\omega}_c^2\right) \hat{u}_c = \eta_i \end{cases}. \tag{6.11}$$

Conveniently, we note that Equation (6.9) now has the same form as Equation (5.19). Hence, we can use the formulas for the tuning of the controller parameters presented in Section 5.2.2. With Equation (6.10), corrected parameters for the PPF controller in the MDOF case are obtained:

$$g_c = \frac{\hat{g}_c}{v_i w_i + \kappa_{>i} \hat{g}_c}, \quad \omega_c^2 = \frac{\hat{\omega}_c^2}{1 - g_c \kappa_{>i}}, \quad \zeta_c = \frac{\hat{\zeta}_c \hat{\omega}_c}{\omega_c}. \tag{6.12}$$

The tuning steps for the PPF controller in the MDOF can then be summarized as follows:

1. Identification of the system parameters ω_i, w_i, v_i and $\kappa_{>i}$.
2. Computation of the optimal PPF controller parameters $\hat{\omega}_c$, $\hat{\zeta}_c$ and $\hat{g}_c$, using ω_i as in an SDOF case according to the tuning rules defined in Section 5.2.2.
3. Correction of the controller parameters according to Equation (6.12).

All system parameters used in this tuning and correction procedure can be easily determined using state-of-the-art system identification methods. This is a clear advantage of this method, as it makes it widely and easily applicable. Compared to [160], it can be applied to different sensor-actuator configurations. However, we note that the correction factors depend on the measured plant transfer function and that the equal-peak design is enforced only on one modal coordinate. As a result, the controller performance depends on the setup choice together with the sensor/actuator positions, and the method cannot inherently ensure an equal-peak design.

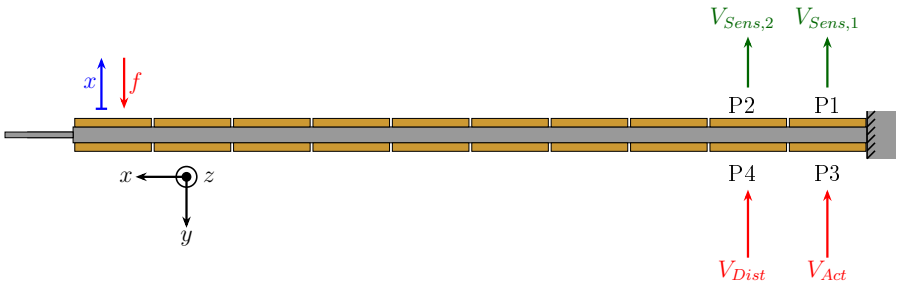

Figure 6.1: Top view of the cantilever beam setup.

6.3 Numerical demonstration on a cantilever beam

The cantilever steel beam schematized in Figure 6.1 is considered for the numerical and experimental demonstration of the tuning rules. The structure was already the subject of other studies, often in the context of nonlinear dynamics, where the thin lamina at the right end of the beam (cf. Figure 6.1) served to induce nonlinear behavior (see, e.g., [63, 166]). To this end, this lamina was clamped. In this work, we left it in a free configuration to remain in a linear motion regime. Table 6.1 lists the properties of the cantilever beam model that was used for the numerical simulations. They are consistent with the properties of the experimental setup. The two piezoelectric patches P1 and P2 located on one side of the beam close to the clamping served as voltage sensors. Patch P3 is the voltage actuator for the controller whereas P4 is a voltage actuator exciting the structure with a disturbance voltage. A displacement sensor was located at the end of the cantilever beam.

The FE model of the cantilever beam structure was built according to the method presented in [124]. It consists of Euler-Bernouilli beam elements and accounts for displacements along the x- and y- axes and rotations around the z-axis incorporating three DOFs per node (axial, transversal, rotation). Considering their motions as negligible, the other DOF were not taken into account. Using a discretization of one element per millimeter for both the beam and the lamina, we obtain a model with 4437 DOFs. To simplify this model and reduce the computational effort, a Craig-Bampton-based model order reduction was used [166]. Finally, all electrical DOFs of the patches and one interface mechanical DOF were maintained together with 20 vibration modes. In addition, the model considers a modal damping of 0.2 %. For the evaluation of the controller performance, we analyze the transfer functions from the disturbance voltage to the tip displacement and from a disturbance force at the beam tip to the tip displacement. Figure 6.2 shows that the numerically-obtained and experimentally-identified open-loop plant transfer functions are in satisfactory agreement, justifying the previous assumptions made for the numerical model.

6.3.1 Plant transfer functions

A configuration with a collocated sensor-actuator pair yields an alternating pole-zero pattern in the open-loop transfer function. Good stability margins can be expected from this pattern [167]. Figure 6.3 features the plant transfer functions obtained with pseudo-collocated (P1 to P3) and non-collocated (P2 to P3) cases. In the pseudo-collocated

Property	Value
Cantilever steel beam	
Length	700 mm
Cross-sectional area	14 mm × 14 mm
ρ	7850 kg m^{-3}
E	210 GPa
Thin steel lamina	
Length	100 mm
Height	14 mm
Thickness	0.5 mm
ρ	7850 kg m^{-3}
E	210 GPa
Piezoceramic PSI-5A4E patches	
Length	67 mm
Height	14 mm
Thickness	2 mm
ρ_p	7800 kg m^{-3}
E_p	66 GPa
d_{31}	-190×10^{-12} m V^{-1}
ε_0	8.854 pF m^{-1}
ε_{33}^S	$1531\varepsilon_0$
Gap between the patches	3 mm
Distance P_1/P_3 to clamping	1 mm

Table 6.1: Properties of the numerical and experimental cantilever beams and the four piezoceramic patches glued to it.

Mode number	1	2	3
Resonance frequency [Hz]	24.28	42.13	152.9

Table 6.2: Resonance frequencies of the numerical cantilever beam.

case, P1 and P3 are at the same location in the x-direction, but on either side of the beam. Since the in-plane transverse motions could disturb the alternating pole-zero pattern at high frequencies, it is described by the additional term *pseudo*. In what follows, however, we refer to this case as collocated, as the numerical study in this work is not affected by these possible perturbations. In Figure 6.3, it can be observed that both collocated and non-collocated configurations feature an alternating pole-zero pattern. We note that this is beneficial, but definitely not a general feature for the non-collocated case.

Table 6.2 lists the resonance frequencies obtained by means of the plant transfer functions. In this study, we focus on the first bending mode of the cantilever beam. Figure 6.3 shows the first two system poles are relatively close to each other. A tuning of the PPF controller parameters using an SDOF approximation might thus not lead to optimal damping performance.

6.3.2 Collocated versus non-collocated setups

We now regard the response of the controlled systems to assess the performance of the PPF controller tuned according to the MDOF H_∞ tuning rule. The FRFs for the collo-

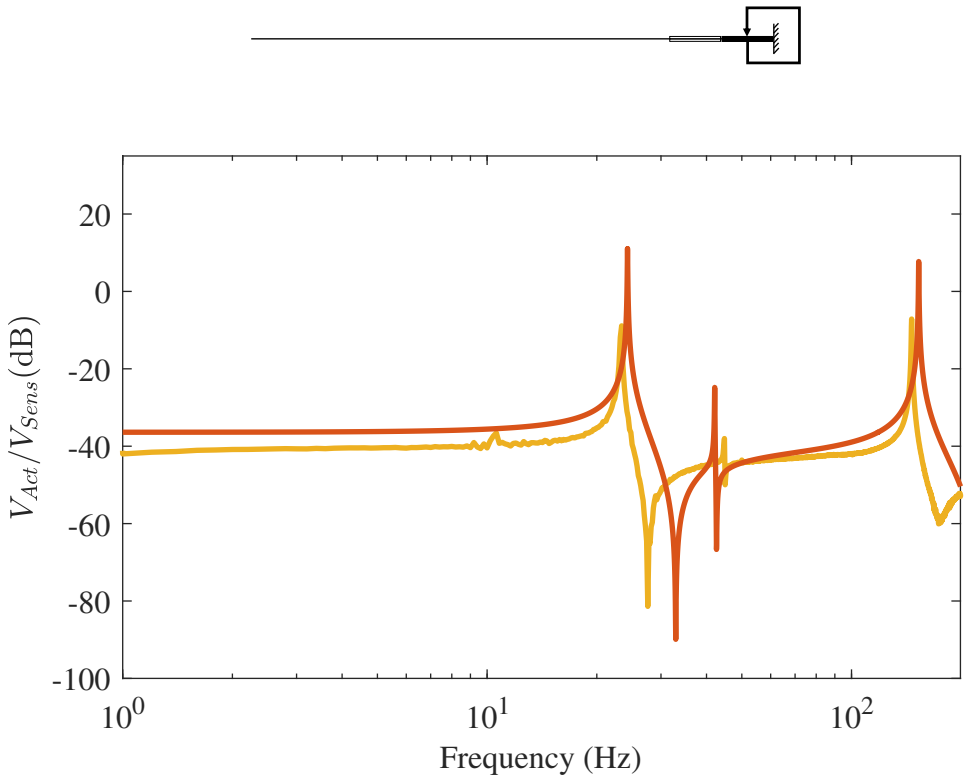

Figure 6.2: Plant transfer functions from P1 to P3 obtained by numerical simulations (—) and experimental measurements (—).

cated and non-collocated configurations are displayed in Figure 6.4.

When a disturbance voltage was applied to the beam via P4, both configurations caused a reduction in resonance amplitude of about 40 dB. However, the increase in static response which is expected for the PPF controller can only be observed for the non-collocated case. As shown by the torque distribution sketched in Figure 6.5, the piezoelectric disturbance actuator applies a torque on the structure that can only be sensed in the beam section of P4 (assuming that the in-plane displacements are small herein). Consequently, for the static case, only the P2 sensor can detect the disturbance and activate the controller. In addition, we note that the two resonance peaks, clearly visible in the SDOF example in Figure 5.9b, are more difficult to observe in this example. The reason for this is the increased static response as well as the influence of the modes occurring at higher frequencies.

When the disturbance was induced at the beam tip via a force, both configurations yielded a reduction of the resonance amplitude of 47 dB. Since mainly the first bending mode was activated by the force at the beam tip, the influence of the other modes was decreased, and the controller could enforce two equal peaks. This illustrates that the choice of FRF used for performance evaluation is of great importance.

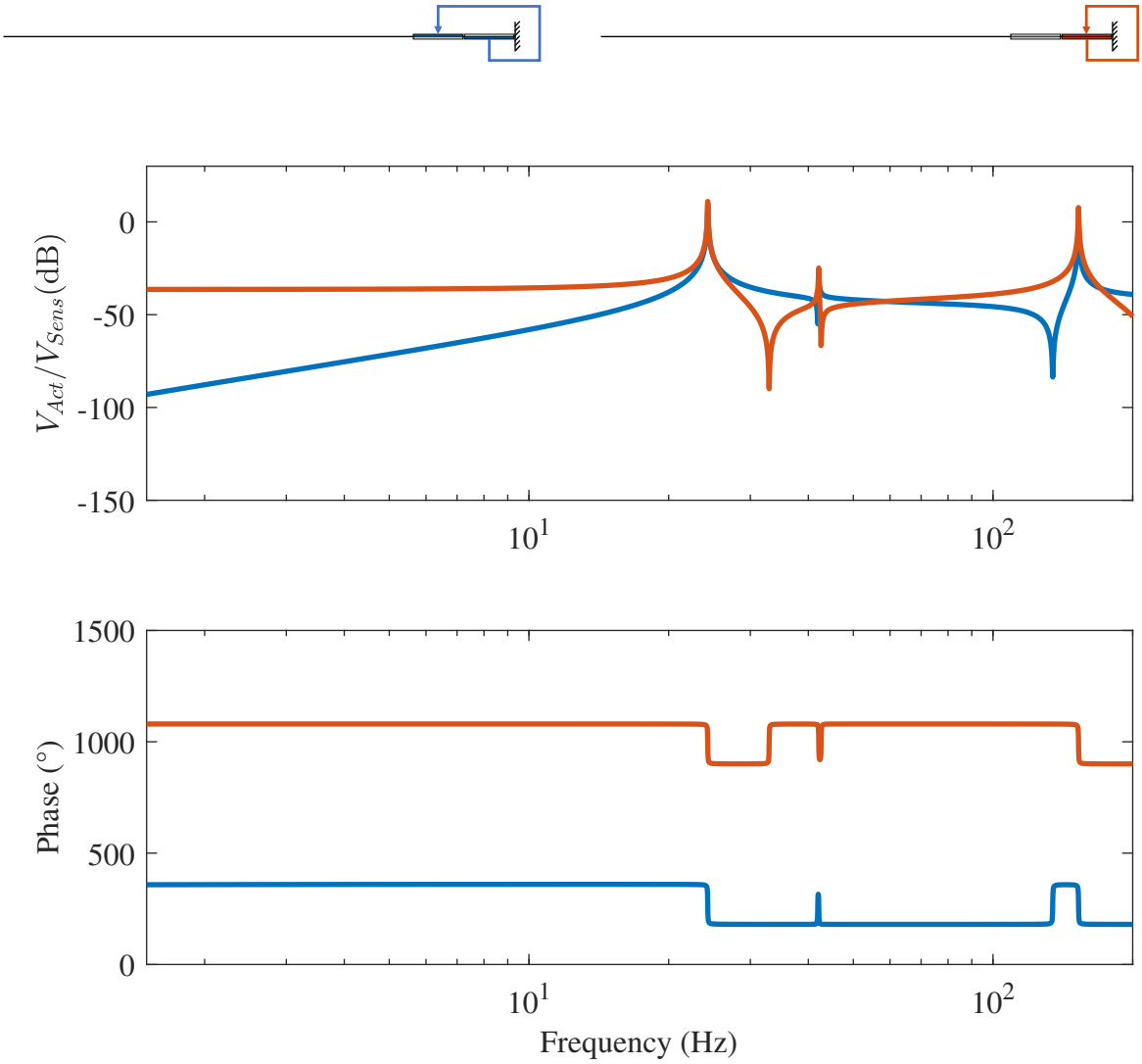

Figure 6.3: Bode plot of the plant transfer functions of the numerical beam. Non-collocated (P2 to P3) (—) and pseudo-collocated (P1 to P3) (—).

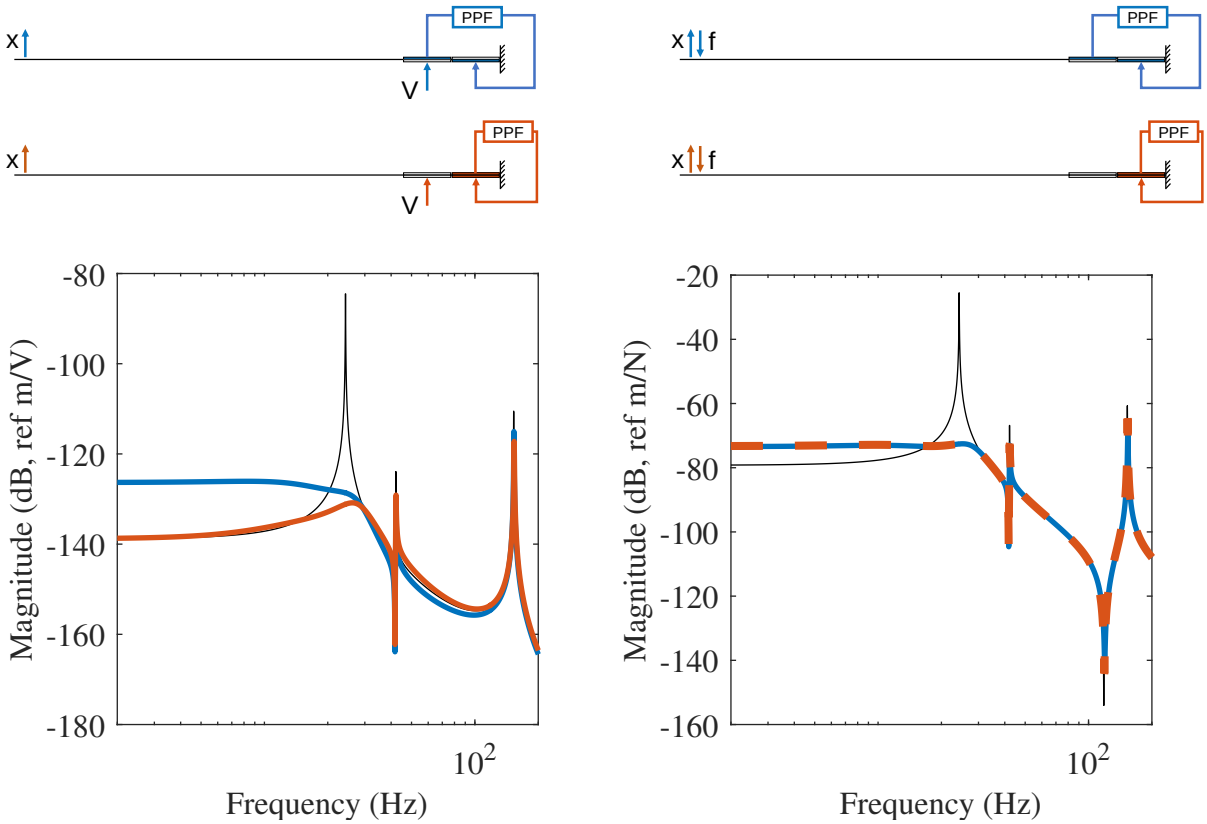

(a) From disturbance voltage (P4) to tip displacement

(b) From disturbance force at the beam tip to tip displacement

Figure 6.4: FRFs of the numerical beam. Uncontrolled (—); controlled by a PPF accounting for the influence of higher-order modes in a non-collocated (—) and pseudo-collocated (—) setup.

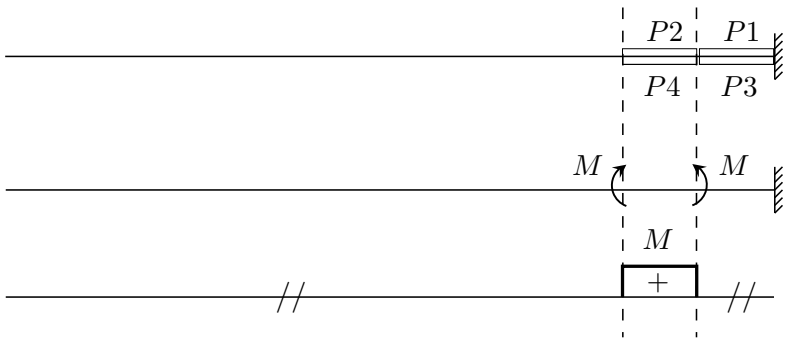

Figure 6.5: Schematics of the cantilever beam when P4 is injecting a disturbance voltage (static case).

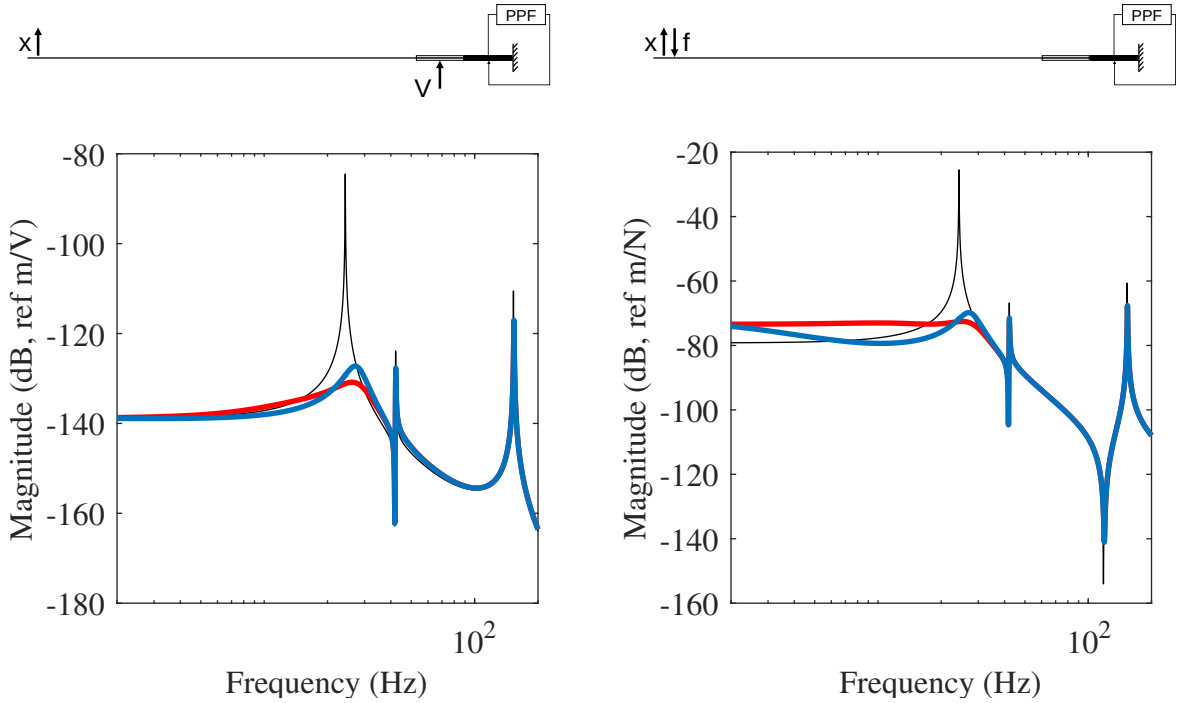

(a) From disturbance voltage (P4) to tip displacement

(b) From disturbance force at the beam tip to tip displacement

Figure 6.6: FRFs of the numerical beam. Uncontrolled (—); PPF controller accounting for higher-order modes (—) or not (—).

6.3.3 Influence of higher order modes

To demonstrate the importance of the inclusion of higher-order modes, the receptance functions for the system connected to a PPF controller tuned with and without the higher-mode corrections are plotted in Figure 6.6. Thanks to the correction, amplitude reduction could be enhanced by 5.5 dB and 3.5 dB, respectively. Moreover, a strong detuning of the PPF controller can be observed if the influence of higher-modes is not taken into account, since the second mode is close to the targeted one.

6.3.4 Variations of the controller gain

In a next step, the controller gain was varied for the collocated case, similarly to what was carried out in Figure 5.10. Small variations of the controller gain are first considered, see Figure 6.7a. When a disturbance voltage is acting, the FRF shows an imbalance between the two resonance peaks, also in the optimal case. As discussed earlier, possible reasons for this are the influence of other structural modes and the static response that was not amplified. On the other hand, for the disturbance force, the receptance function shows that an equal-peak design could be better approached. This is partly because the static response was magnified here, as is typical for the PPF controller. Second, the influence of the higher-order modes on the system dynamics was reduced at this input location. The theoretical developments for PPF controllers in Section 5.6 can be found in this transfer function. For example, the optimal controller gain yielded the best damping performance.

Variations of the controller gain in a larger range are displayed in Figure 6.7b. The FRF shows that setting the gain to g_{opt} resulted in the highest reduction of the maximum receptance amplitude in both cases. Yet, as expected from the previous results, the FRF obtained from a disturbance voltage did not feature an increased static response so that the trade-off with the reduction of the resonance amplitude cannot be observed in this example; the resonance peaks are unbalanced as anticipated. For the FRF from the tip force to the displacement at beam tip, two-well balanced resonance peaks emerge. Again, the modal coordinate to which the controller was tuned is strongly dominant in this FRF. We can clearly see the trade-off between the growth of the static response and reduction of the resonance amplitude for different gain factors.

6.3.5 Comparison with the fixed-point method

We conclude the numerical study with a comparison between the proposed tuning method with the fixed-points method, as in Figure 5.9b. The correction factors for the higher modes were applied to both methods. The resulting FRFs are displayed in Figure 6.8. The exact H_∞ tuning rule is slightly more efficient (1 dB) than the fixed-points method. Moreover, the two resonance peaks are better balanced for the H_∞-based controlled system. From these results, we can also state that the value for g_{opt} in Equation (5.14) and the correction factors for out-of-band modes can also be used for the fixed-points method. Whereas the difference between the two methods may not seem significant in terms of performance, the developments in this work provide not only a new tuning rule with a well-defined optimal gain value, but also a mathematically exact solution for the SDOF case.

6.4 Experimental demonstration on a cantilever beam

The experimental beam corresponds to the same cantilever beam that was used in the previous section. The experimental setup is presented in Figure 6.9. One piezoelectric patch next to the clamping served as an actuator whereas the adjacent one induced the disturbance voltage. Both opposite patches were employed as sensors, namely sensors 1 and 2. The former (latter) corresponds to the (non-)collocated configuration. Voltage amplifiers magnified the disturbance signals by a factor ten. These gains are accounted for in the FRFs to enable a fair comparison with the numerical results. The digital controller unit dSPACE MicroLabBox realized the excitation signals, acquired the measurement signals and served for the implementation of the controller function. An accelerometer measured the response at beam tip. The signal was then integrated twice to obtain a displacement.

6.4.1 Plant transfer functions

For the identification of the system parameters, the plant transfer functions were measured through the excitation of the system from 1 Hz to 200 Hz using a multisine signal with an RMS amplitude of $A = 0.5V$. The signal consisted of $N = 20000$ samples per period, $P = 20$ periods and $R = 10$ realizations [128]. With a sampling rate of 4000 samples per

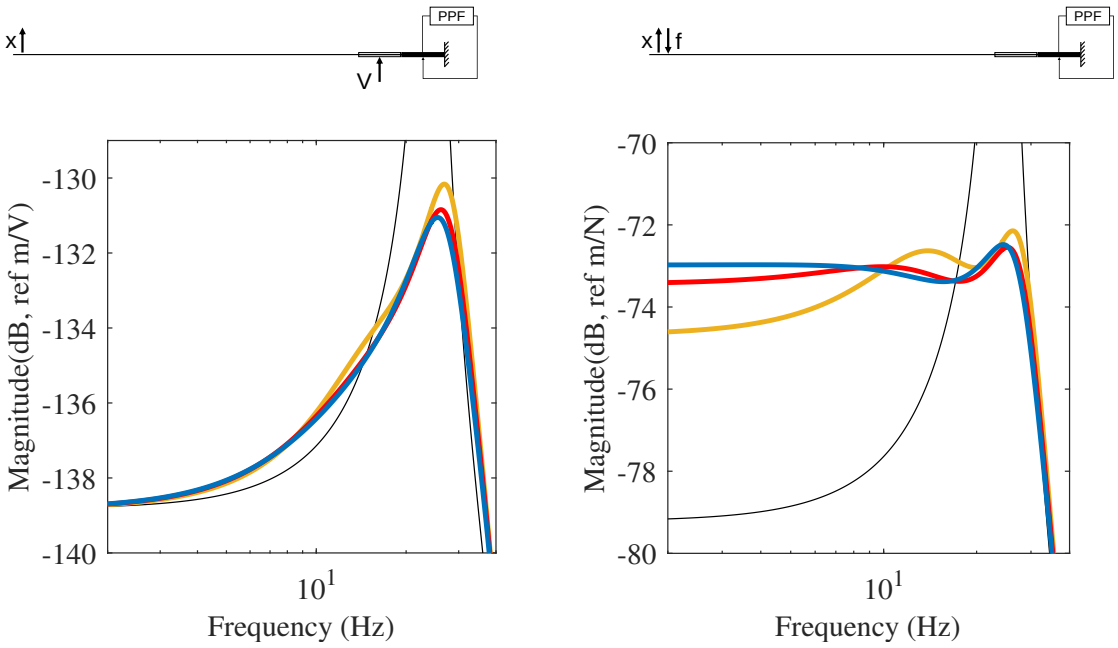

(a) Gain variations of $g = 0.85g_{opt}$ (—), $g = g_{opt}$ (—) and $g = 1.046g_{opt} = g_{max}$ (—).

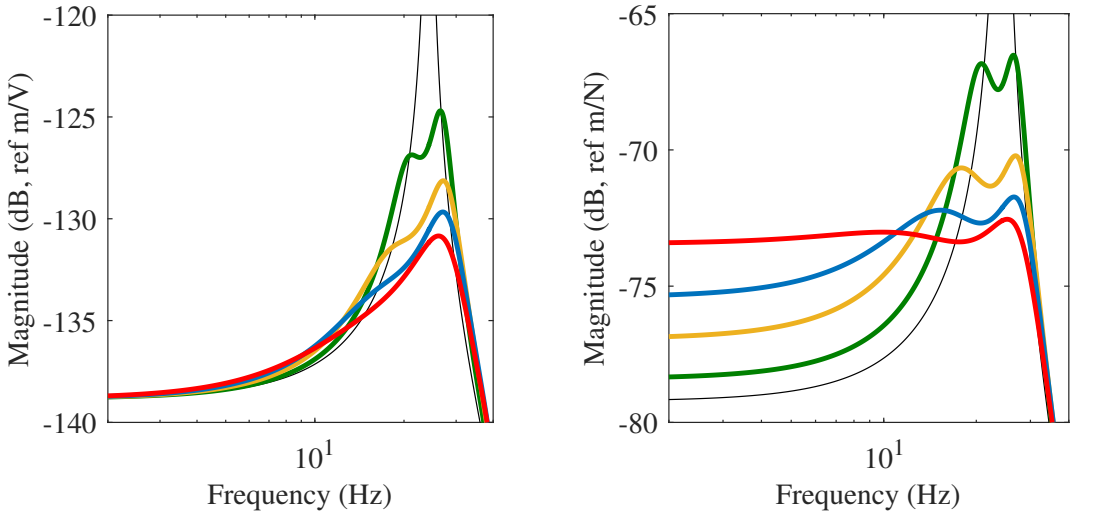

(b) Gain variations of $g = 0.2g_{opt}$ (—), $g = 0.5g_{opt}$ (—), $g = 0.75g_{opt}$ (—) and $g = g_{opt}$ (—).

Figure 6.7: FRFs between the structural response and the external disturbance voltage of the numerical beam controlled by a PPF with different gains (uncontrolled response: —).

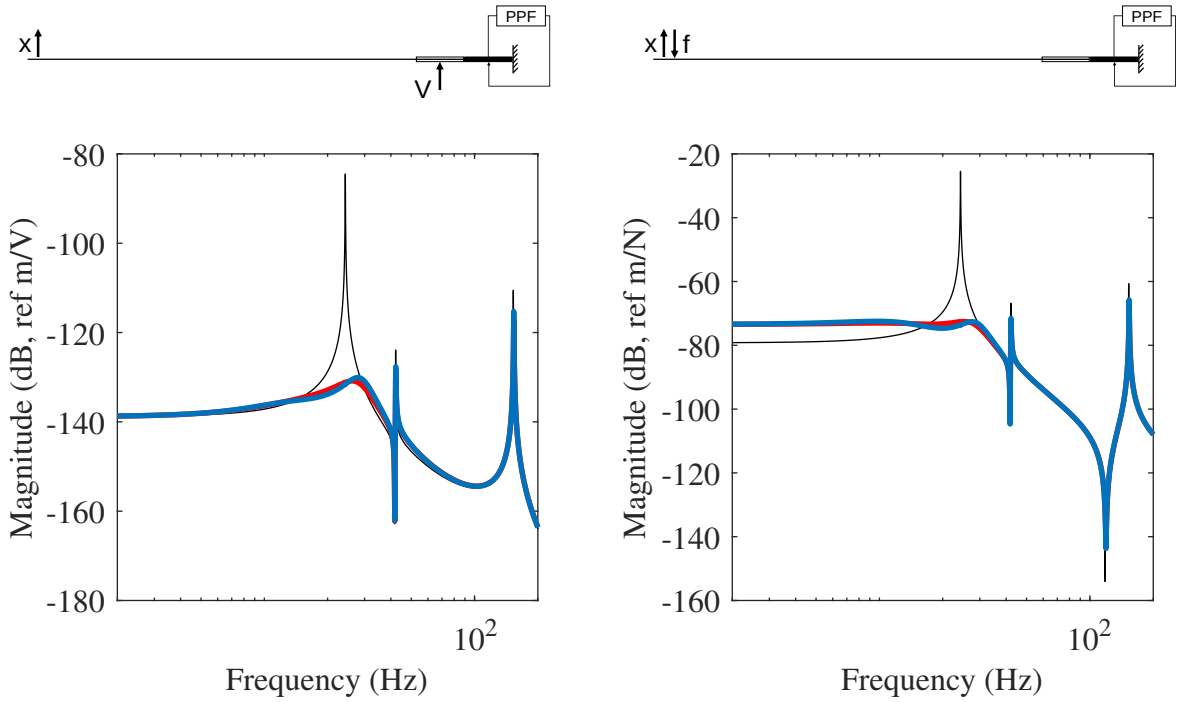

(a) From disturbance voltage (P4) to tip displacement

(b) From disturbance voltage (P4) to tip displacement

Figure 6.8: FRFs of the numerical beam. Uncontrolled (▬); controlled by a PPF controller tuning using H_∞ rule (▬) or the fixed-points method (▬).

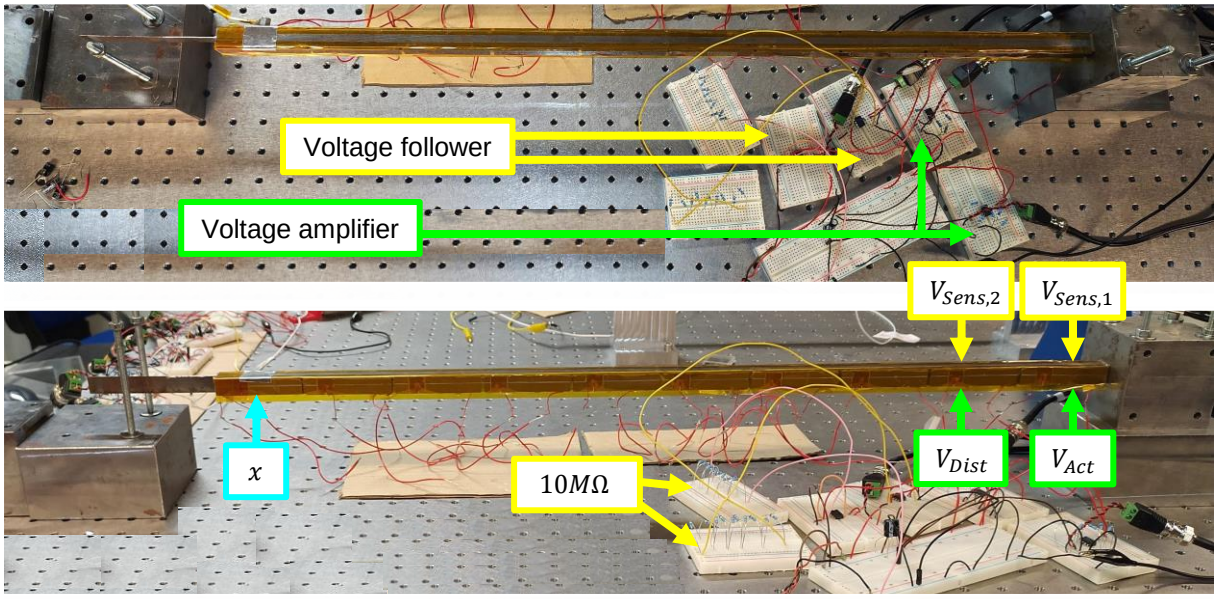

Figure 6.9: Experimental setup.

second, a frequency resolution of 0.2 Hz could be realized. To obtain the plant transfer functions in Figure 6.10, an averaging of the measurements took place over P and R. The figure shows that the FRF is low in magnitude before the first resonance in the

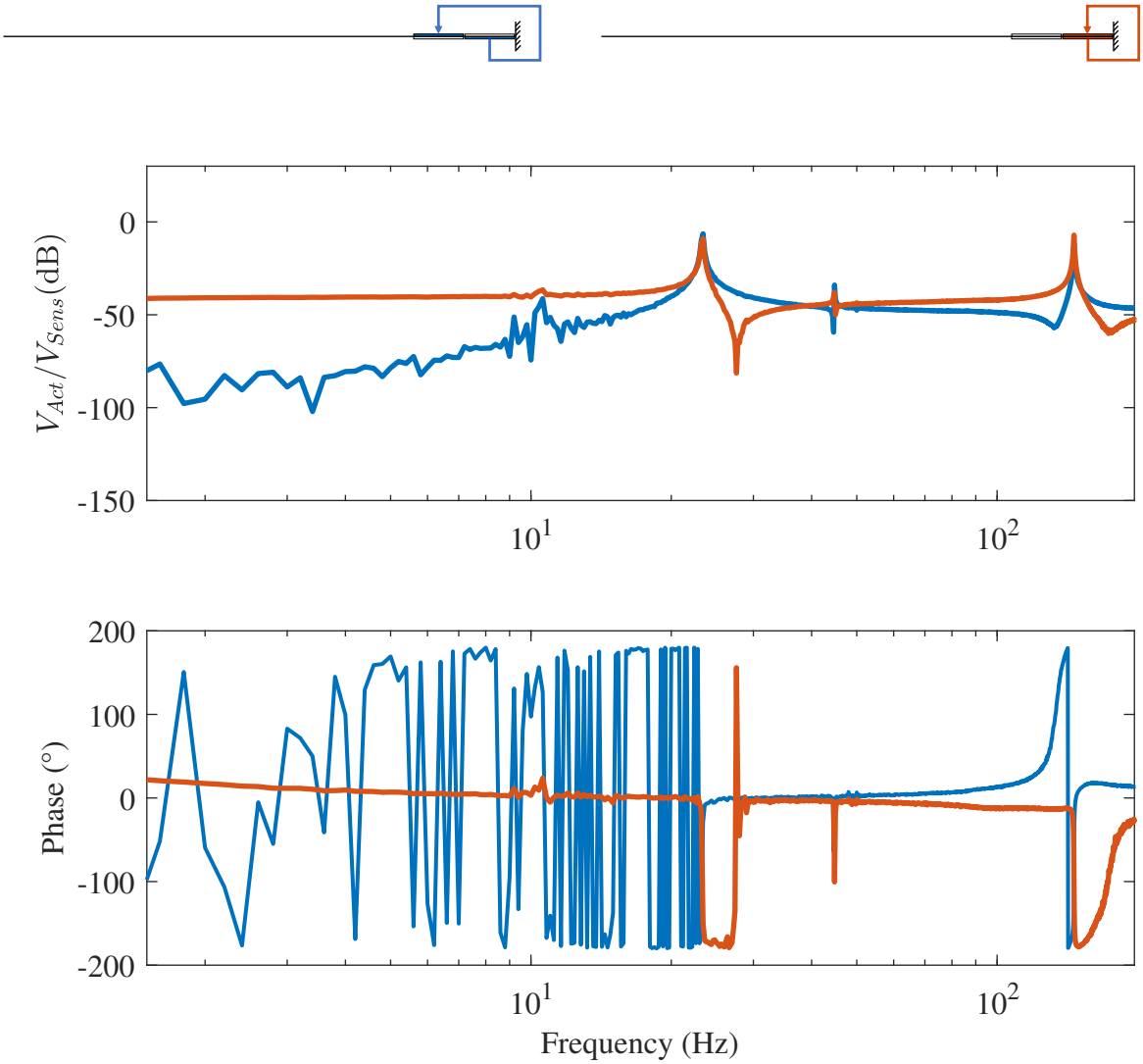

Figure 6.10: FRFs and phase evolutions between the voltage actuator and voltage sensor of the experimental cantilever beam in a collocated (—) and a non-collocated (—) setup.

non-collocated configuration, which is consistent with the numerical results (cf. Figure 6.3). It is also observed that both configurations yielded an alternating pole-zero pattern. The first resonance frequency was found to be 23.2 Hz and was set as a target in the controller. The second and third modes were located at 44.8 Hz and 146 Hz, respectively. Their influence was taken into account in the tuning procedure. Finally, the Matlab functions *tfest* and *tf2ss* were applied to the measured transfer function data in order to create a state-space model. This model served to define the PPF controller parameters.

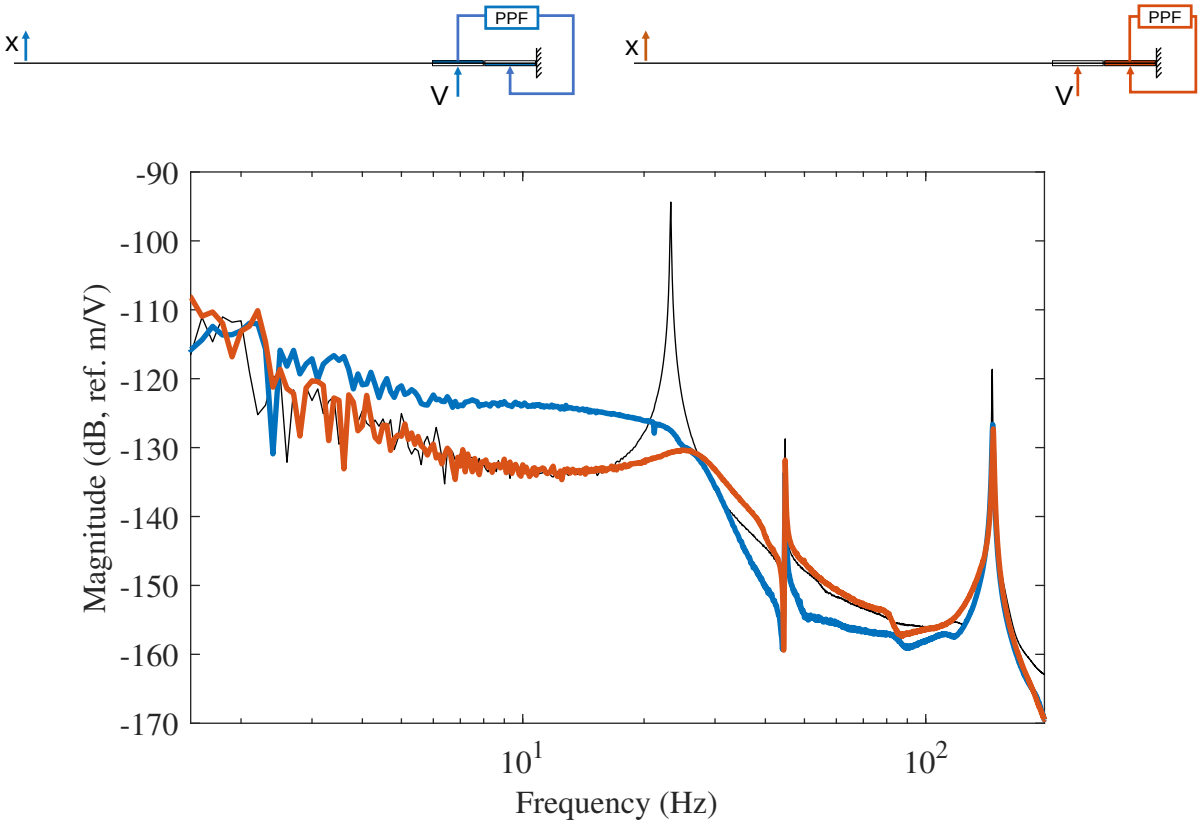

Figure 6.11: FRFs between the voltage actuator and voltage sensor of the experimental cantilever beam for the uncontrolled case (▬) and controlled by a PPF controller accounting for the influence of higher order modes in a collocated (▬) and a non-collocated (▬) setup.

6.4.2 Damping performance

For performance assessment, the receptance functions between the disturbance voltage to the tip displacement in Figure 6.11 were calculated. The excitation signal had an RMS amplitude of $A = 0.5V$ from 1 Hz to 200 Hz, 100000 samples per period, 20 periods and 10 realizations. A sampling rate of 10000 samples per second resulted in a frequency resolution of 0.1 Hz. In the controlled case, the peak amplitude of the first resonance could be reduced by 36 dB and 30 dB in the collocated and non-collocated case, respectively. For the collocated setup, the two expected resonance peaks are not clearly visible, maybe due to the influence of the higher-order modes and the static response. In agreement with the numerical simulations, the static response was (not) strongly increased in the non-collocated (collocated) case. Overall, the performance of the PPF controller tuned according to the H_∞ tuning can be considered as highly satisfactory. A look at the phase margins of the controlled systems, namely $-19.46°$ and $61.03°$ in the collocated and non-collocated cases, respectively, confirms this conclusion. However, when the higher-order modes are not taken into account, the open-loop transfer function shows that the controlled system would be unstable (see Section 6.2). Hence, a practical implementation of the PPF controller would have been impossible.

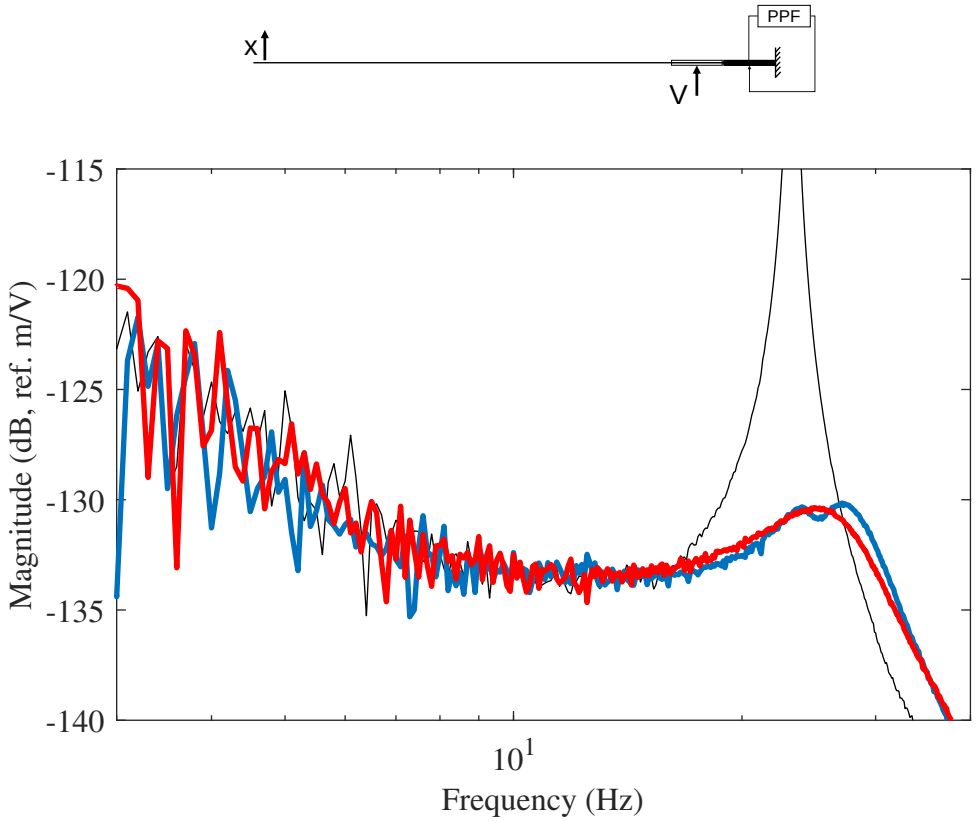

Figure 6.12: FRFs between the disturbance voltage and the tip displacement of the experimental cantilever beam for the uncontrolled case (▬) and controlled by a PPF controller tuned with exact H_∞ rules (▬) and with a fixed-points tuning (▬).

6.4.3 Comparison with the fixed-points method

The comparison is displayed in Figure 6.12. An amplitude reduction of 36.5 dB (exact tuning rule) or 35.80 dB (fixed-points method) could be achieved with both methods. The first method yielded a single resonant peak with higher damping whereas the second method resulted in a FRF with two imbalanced peaks.

6.4.4 Gain variations

Finally, the different FRFs resulting from variations of the controller gain are presented in Figure 6.13. When g varies around the optimal value g_{opt}, the resonance amplitude was more reduced using g_{max} instead of g_{opt}. This observation is not in line with the theoretical developments in Chapter 5 and can be possibly explained by experimental uncertainties, particularly since g_{opt} is very close to g_{max}. For larger gain variations, the best performance could be achieved with g_{opt}. If the gain was chosen significantly lower than g_{opt}, two resonance peaks appeared in the FRF. In this configuration, the static response seemed to absorb the left resonance peak. The more the amplitude of the resonance peak was distinguished from the amplitude of the resonance frequency, the better two resonance peak could evolve.

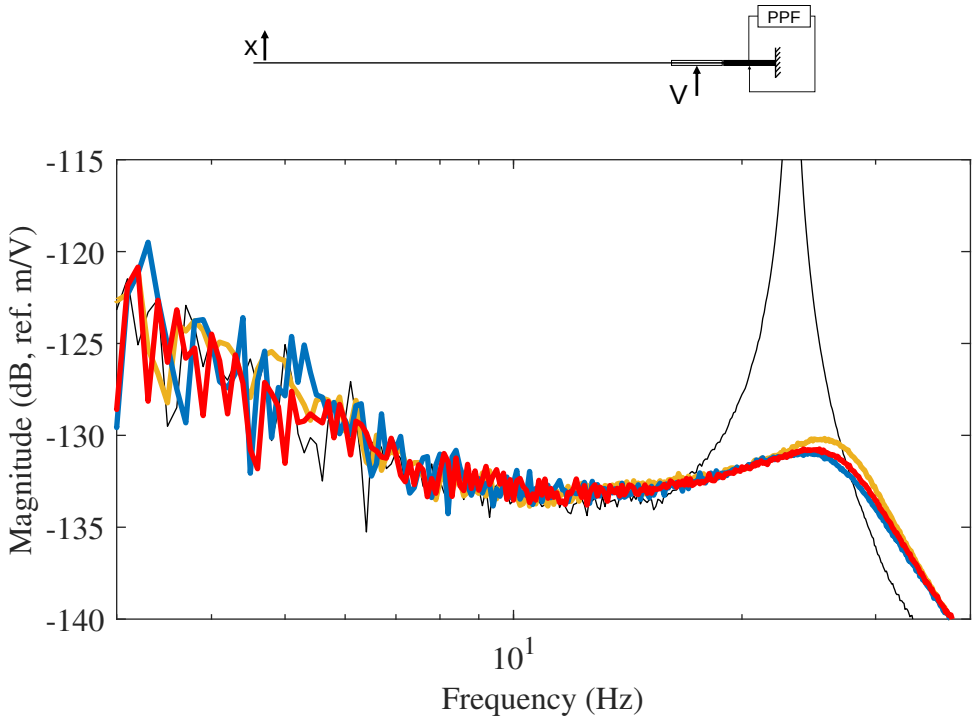

(a) Gain variations of $g = 0.85g_{opt}$ (▬), $g = g_{opt}$ (▬) and $g = 1.046g_{opt} = g_{max}$ (▬).

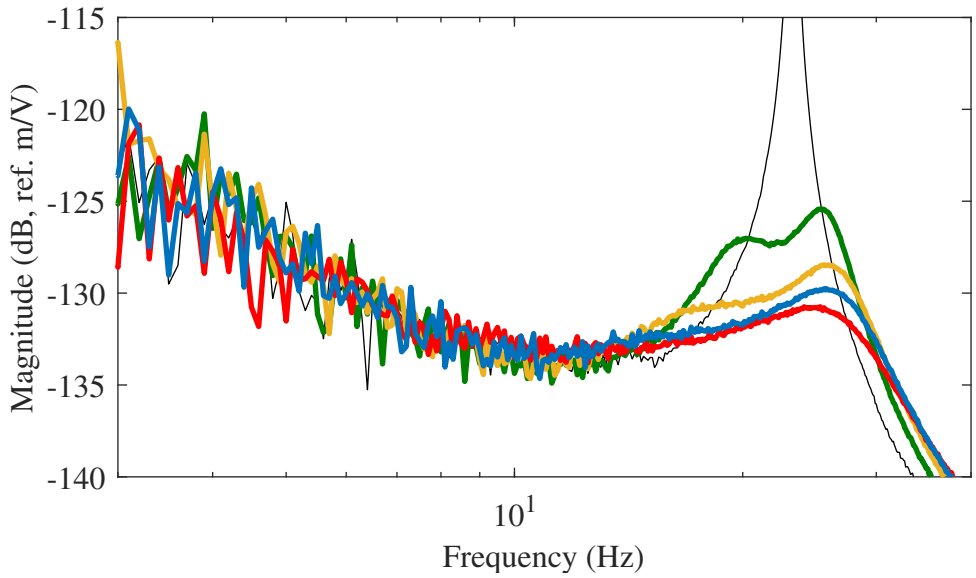

(b) Gain variations of $g = 0.2g_{opt}$ (▬), $g = 0.5g_{opt}$ (▬), $g = 0.75g_{opt}$ (▬) and $g = g_{opt}$ (▬).

Figure 6.13: FRFs between the structural response and the external disturbance voltage of the experimental cantilever beam controlled by a PPF controller with different gain settings in contrast to the uncontrolled response (▬).

6.5 Conclusion

The developments from Chapter 5 were extended to the MDOF case by introducing a correction procedure for the PPF parameters accounting for the influence of out-of-bandwidth modes. Using these corrections, the H_∞ tuning rule was demonstrated using numerical and experimental cantilever beam examples. In the numerical study, different sensor-actuator positions were studied whereas the experimental demonstration was conducted in a collocated setup. The results of both studies were consistent and proved the effectiveness of the controller proposed in this work. We demonstrated that the consideration of the out-of-bandwidth modes is crucial not only for effective damping performance, but also for acceptable phase margins.

Yet, a limitation of the proposed approach is that the controller performance depends on the choice of the transfer function considered; an equal-peak design cannot be enforced for every FRF. An interesting continuation of this work could be the inclusion of lower modes in case a higher mode is targeted or several modes are considered simultaneously in the correction factors.

Conclusions and outlook

This thesis developed multimodal damping strategies for complex mechanical structures based on the use of multiple DVAs. This work also established a bridge between classical shunt damping approaches, traditionally classified as passive, and the field of active control. We provided specific contributions to the following problems with supporting experimental demonstrations:

(a) Efficient vibration mitigation of families of closely-spaced modes.

(b) Attenuation of multiple modes with one shunt circuit.

(c) Robust vibration attenuation that can be adapted to changes in the host structure.

(d) Design of DVAs together with their practical implementation.

(e) Transition from passive to active control approaches from a piezoelectric shunt damping viewpoint.

In Chapter 1, the basic equations of piezoelectric shunt damping were recalled together with the advantages of digital shunts. The chapter presented a DVA circuit design, its practical realization on a PCB as well as the associated technical difficulties. The reader was provided with all the necessary information to interpret the experimental results obtained with these DVAs, addressing point (d). In addition, we introduced a discretization method for the shunt transfer function to be implemented. Its straightforward character makes this method particularly attractive for ensuring closed-loop stability.

Chapter 2 outlined the dynamic characteristics and difficulties that come along with bladed structures and presented solutions for tasks (a) and (b). Two strategies specifically designed for their complex dynamics were presented, namely the isolated mode and the mean shunt strategies. They take advantage of the fact that multiple DVAs are used simultaneously. If one may want to mitigate the vibrations of multiple modes in different mode families, these strategies can then be integrated in a multimodal shunt circuit design.

Practical applications followed to demonstrate these theoretical developments. Chapters 3 and 4 comprise results from extensive experimental campaigns conducted on bladed structures. First, in Chapter 3, a bladed rail served as the structure of interest, exhibiting similar dynamic properties as industrial bladed structures but a significantly smaller number of modes. Chapter 4 presented the results of an experimental campaign on a BluM on which 16 DVAs acted. In both examples, the DVAs tuned according to the developed strategies proved efficient and yielded highly satisfactory damping performances.

In addition, they were also found to be robust to changes in the host structure, including mistuning, meeting the requirement (c). A retuning of the shunt parameters could be conducted easily thanks to the digital realization. In the BluM setup, despite the multitude of DVAs that were used, a compact solution could be provided for the experimental realization.

In Chapter 5, we addressed point (e) by pointing out similarities between RL shunts with an NC and the classical active control approach of a PPF. Tuning rules for passive RL shunts based on an H_∞ optimization of the receptance function were extended to the active control case of an NCRL shunt and then translated to a PPF controller. This could be achieved by comparing their receptance functions, revealing an equivalence between their controller parameters. In that way, the extended H_∞ tuning could be applied to both cases, and their performance was compared by means of an SDOF example. Considering that the PPF controller exhibited significant greater stability margins, it is considered to be the best solution for practical applications.

Finally, the newly-derived H_∞ tuning rule for a PPF controller was applied to numerical and experimental cantilever beams in Chapter 6. To this end, we presented a method to account for the influence of modes of higher frequency than that of the targeted mode. Overall, the tuning rules proved to be efficient.

Outlook

In the first part of this thesis, we conducted a proof of concept study for different damping strategies applied to structures featuring high modal density. Future works could now progress further toward vibration mitigation of structures in operational conditions. In the experimental campaigns, we showed that a retuning of the shunts could be easily achieved thanks to the DVA concept. So far, this retuning was neither achieved automatically nor in real-time. An interesting continuation of this work would thus be an automation of the post-processing procedure to provide self-tuning shunts. This would require frequent updates of the plant transfer function.

Another logical extension of this research could be the consideration of a rotating BluM under a synchronous harmonic excitation, representing the actual excitation these structures are subject to. Exploiting the rotational energy, an electromagnetic induction system could be installed in the drum, using the relative moment between the coils and the rows of rotating magnets to create a variable magnetic flux. In this way, the DVA could operate autonomously from an energy standpoint. It would also be desirable to achieve a DVA design that can be placed completely inside the drum without significantly disturbing the airflow. To achieve this, the control law could be imposed via a micro-controller unit on a powered digital signal processor chip implemented in the drum.

In the second part of this thesis, the performance enhancement of classical RL shunts through the addition of a negative capacitance was discussed. From the experience we gained, we know that the piezo-BluM structure does not feature great electromechanical coupling. A way to gain better control authority could be to use NCRL shunts on the

BluM. However, as outlined in Chapter 5, the NC value is to be chosen as a trade-off between stability margins and performance. Because a PPF controller exhibits significantly greater phase margins for the newly-derived H_∞ tuning rule, it could be interesting to apply this active control approach on the BluM. An adaptation of the setup for this case would be needed so that, e.g., collocated pairs of piezoelectric patches would act on the BluM. We note that this was already realized on a bladed rail in [108] and for the application of an IFF controller on a BluM in [109]. It would also be desirable to extend the method taking out-of-bandwidth modes into account in way that not only higher but also lower modes are considered.

Finally, DVAs represent an attractive damping solution that is not limited to bladed structures, but may also be of interest for vibration attenuation of other industrial applications.

Appendix A

A multi-stage current blocking circuit

The identification procedure to fit a dynamic capacitance is described in the following. We write the following expression that is then to be approximated:

$$\frac{q_s}{V_s} = -\frac{\tilde{B}}{s^2} - \frac{\tilde{G}}{s} - \tilde{C}_p^{\varepsilon}\frac{s^2+\tilde{\omega}_{oc}^2}{s^2+\tilde{\omega}_{sc}^2} = -\frac{\tilde{C}_p^{\varepsilon}s^4 + \tilde{G}s^3 + (\tilde{B}+\tilde{C}_p^{\varepsilon}\tilde{\omega}_{oc}^2)s^2 + \tilde{G}\tilde{\omega}_{sc}^2 s + \tilde{B}\tilde{\omega}_{sc}^2}{s^2(s^2+\tilde{\omega}_{sc}^2)} \ . \quad \text{(A.1)}$$

We seek Equation (A.1) to take the form

$$\frac{q_s}{V_s} \approx \frac{(as^2+bs+c)(s^2+2z_r s+z^2)}{s^2(s^2+2p_r s+p^2)} \ . \quad \text{(A.2)}$$

The identification procedure reads:

1. Considering the actual q_s/V_s and set the pole p that is closest to $j\omega_{oc}$ (of magnitude p and real part p_r) to $\tilde{\omega}_{sc}$.
2. Find the closest zero q_s/V_s (of magnitude z and real part z_r) to this p.
3. The function $f(s) = (s^2(s^2+2p_r s+p^2)/(s^2+2z_r s+z^2)q_s/V_s$. The constants a, b and c are determined by fitting $f(s)$ in a LSE sense to a frequency range that comprises p and z.
4. Equating Equations (A.1) and (A.2) yields the parameters $\tilde{G}$, $\tilde{B}$, $\tilde{\omega}_{oc}$, $\tilde{\omega}_{sc}$ and $\tilde{C}_p^{\varepsilon}$.

Appendix B

Supplementary experimental data from the BluM structure

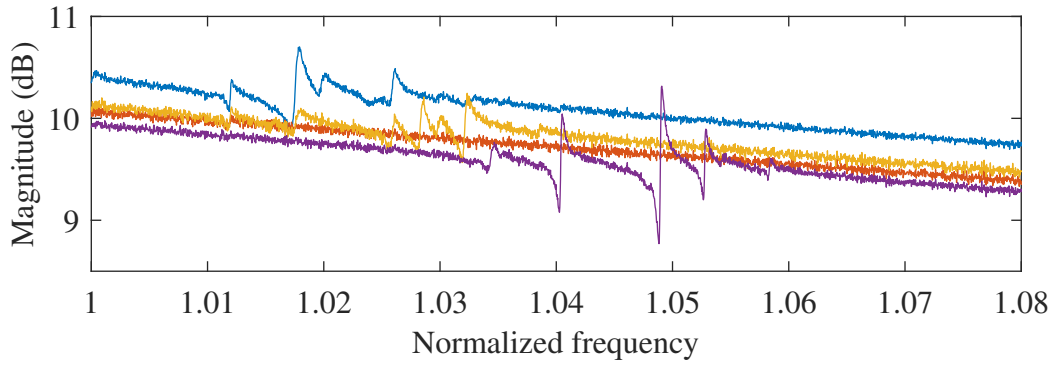

(a) Patch 1 (—), patch 2 (—), patch 3 (—) and patch 4 (—).

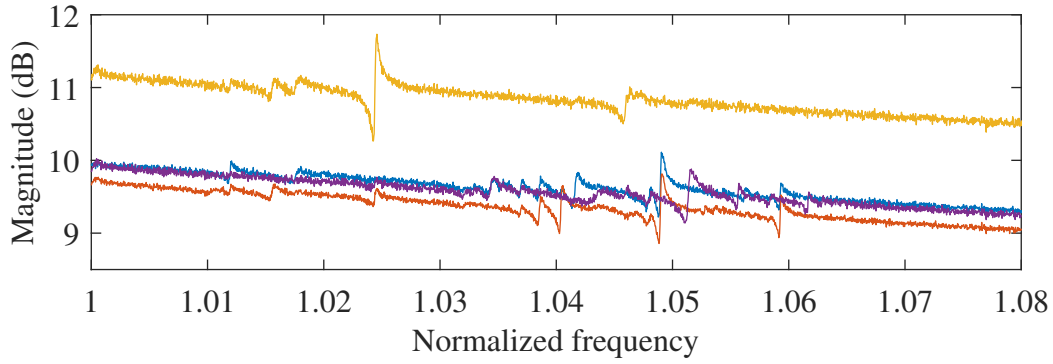

(b) Patch 5 (—), patch 6 (—), patch 7 (—) and patch 9 (—).

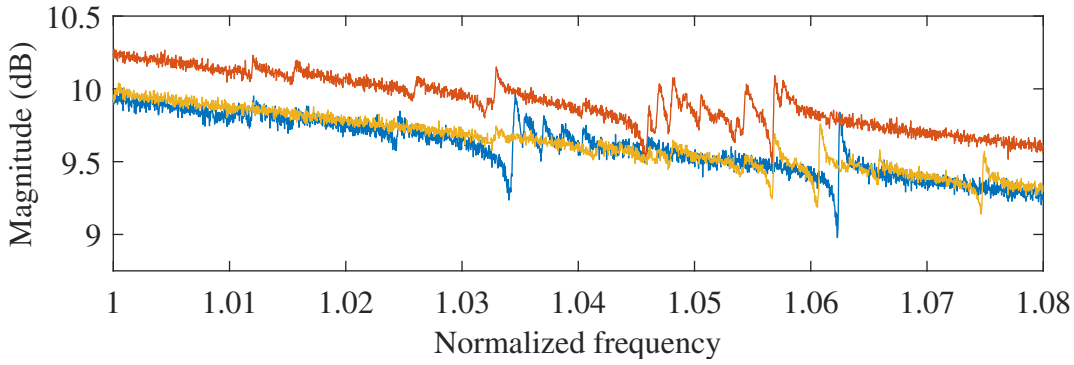

(c) Patch 11 (—), patch 13 (—), patch 15 (—) and patch 17 (—).

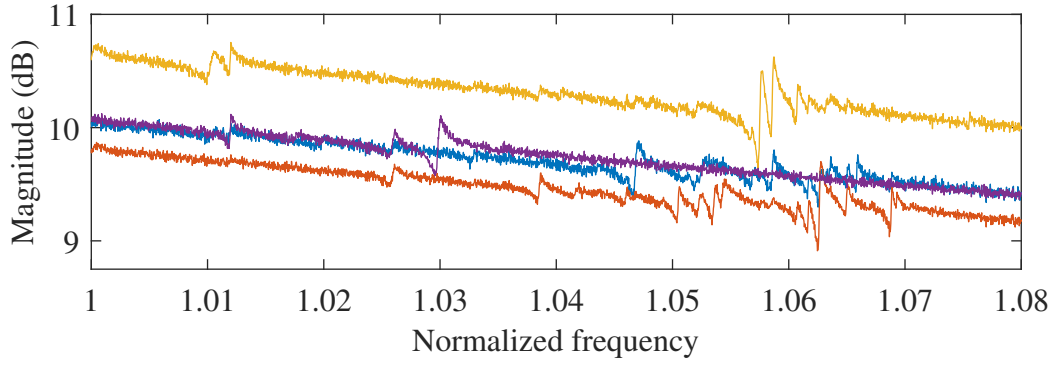

(d) Patch 19 (—), patch 21 (—), patch 23 (—) and patch 25 (—).

Figure B.1: Dynamic impedance measurements of the 16 shunted patches for patch configuration 1.

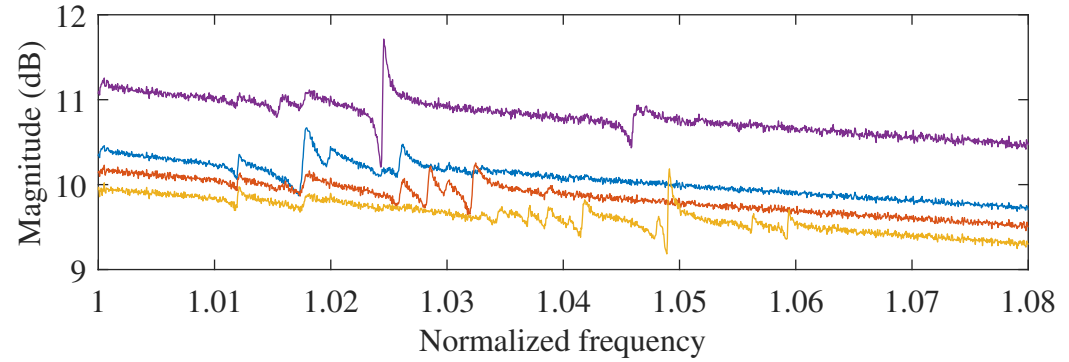

(a) Patch 1 (—), patch 3 (—), patch 5 (—) and patch 7 (—).

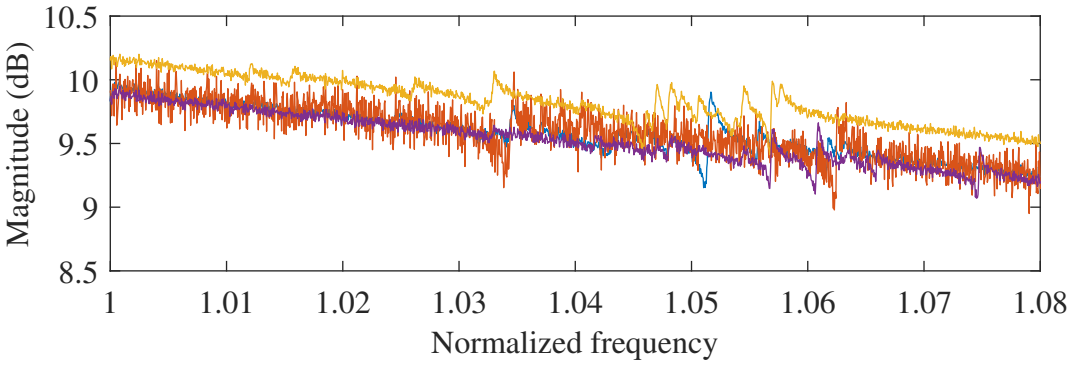

(b) Patch 9 (—), patch 11 (—), patch 13 (—) and patch 14 (—).

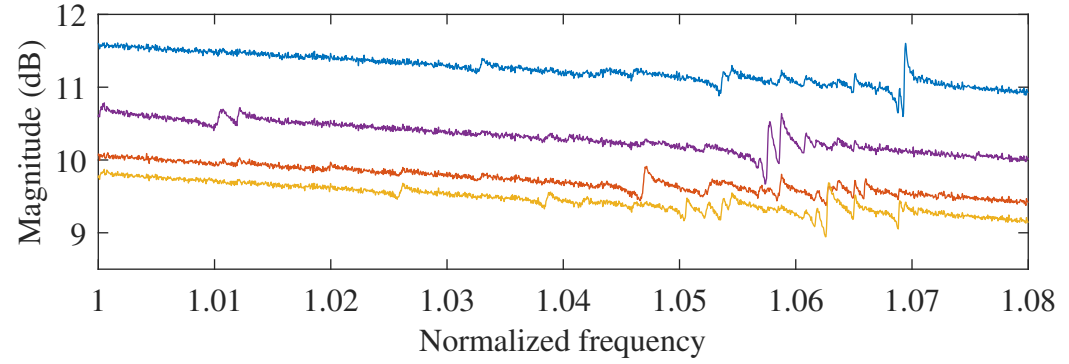

(c) Patch 15 (—), patch 17 (—), patch 19 (—) and patch 21 (—).

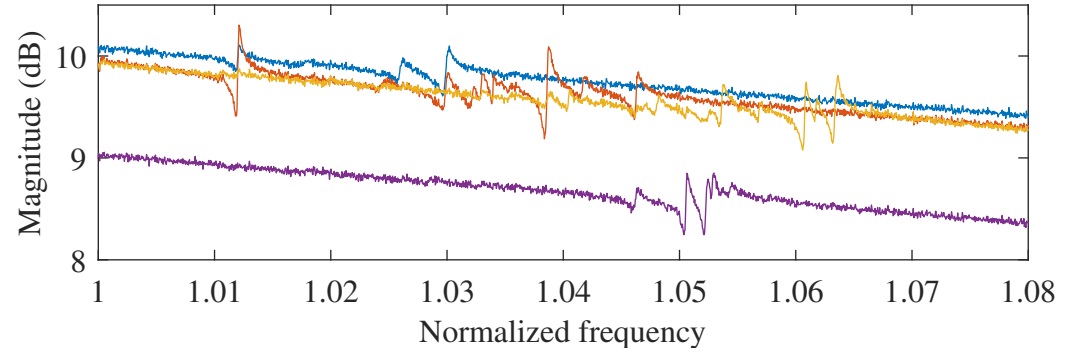

(d) Patch 23 (—), patch 25 (—), patch 27 (—) and patch 28 (—).

Figure B.2: Dynamic impedance measurements of the 16 shunted patches for patch configuration 2.

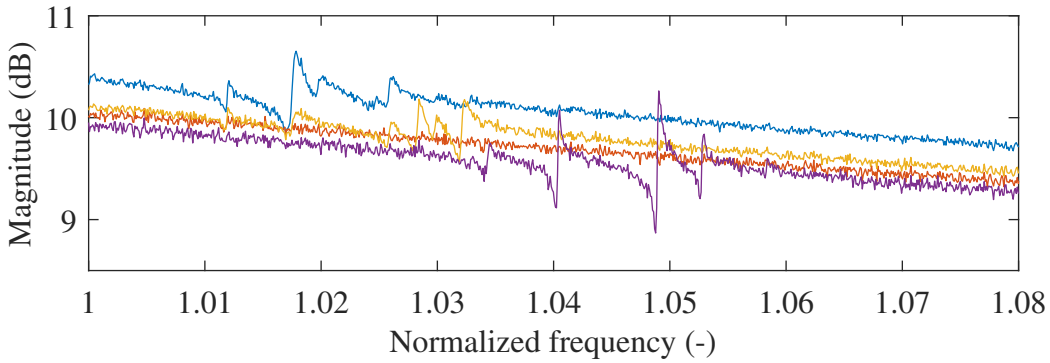

(a) Patch 13 (—), patch 14 (—), patch 15 (—) and patch 16 (—).

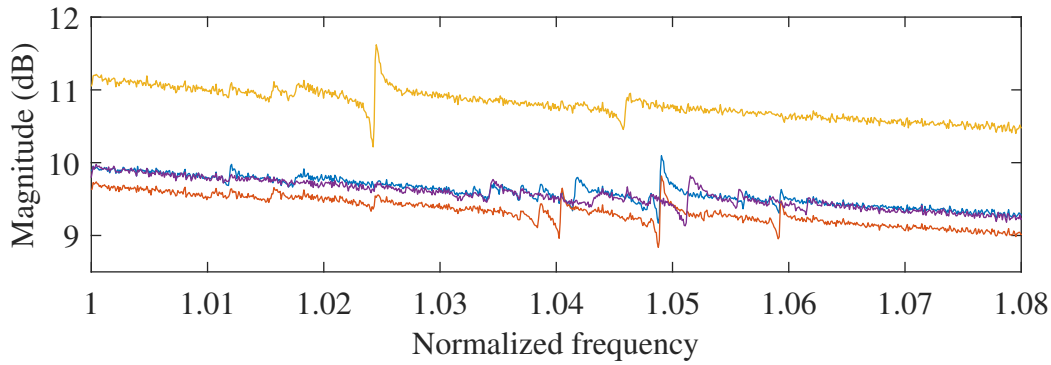

(b) Patch 17 (—), patch 18 (—), patch 19 (—) and patch 20 (—).

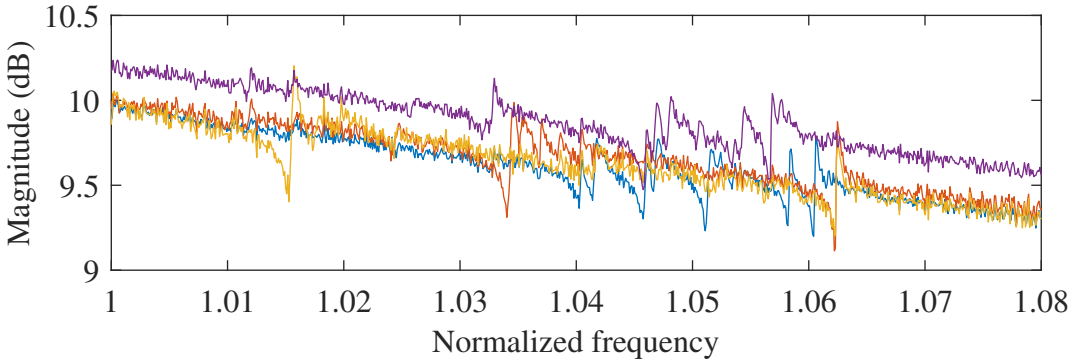

(c) Patch 21 (—), patch 22 (—), patch 23 (—) and patch 24 (—).

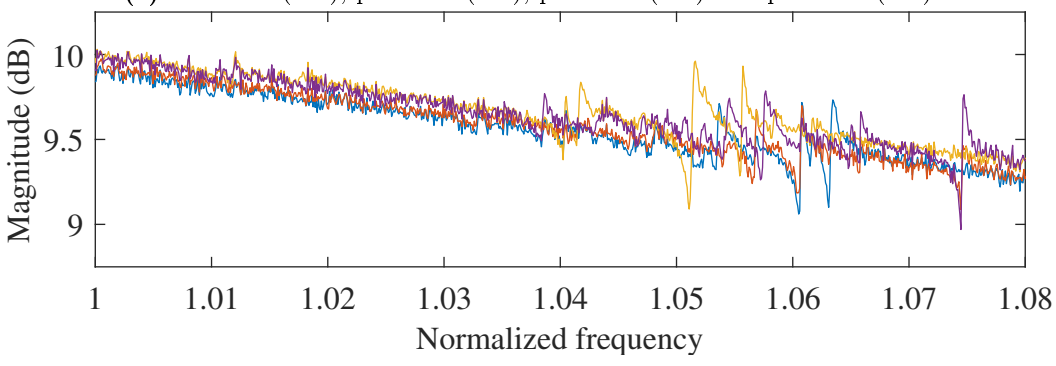

(d) Patch 25 (—), patch 26 (—), patch 27 (—) and patch 28 (—).

Figure B.3: Dynamic impedance measurements of the 16 shunted patches for patch configuration 4.

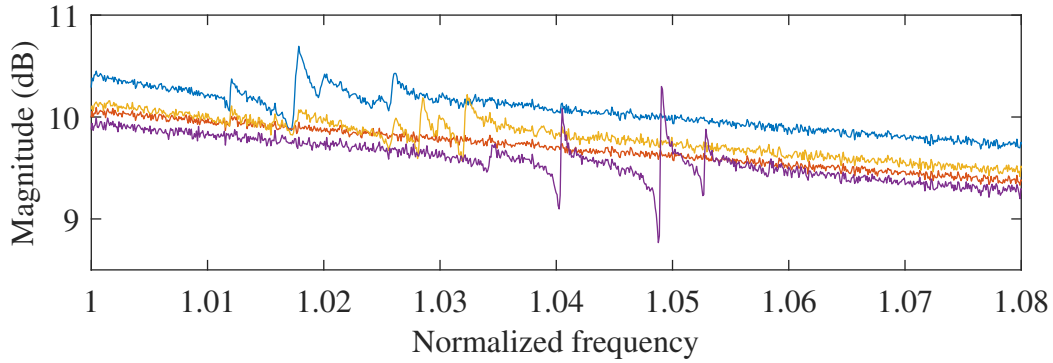

(a) Patch 1 (—), patch 2 (—), patch 3 (—) and patch 4 (—).

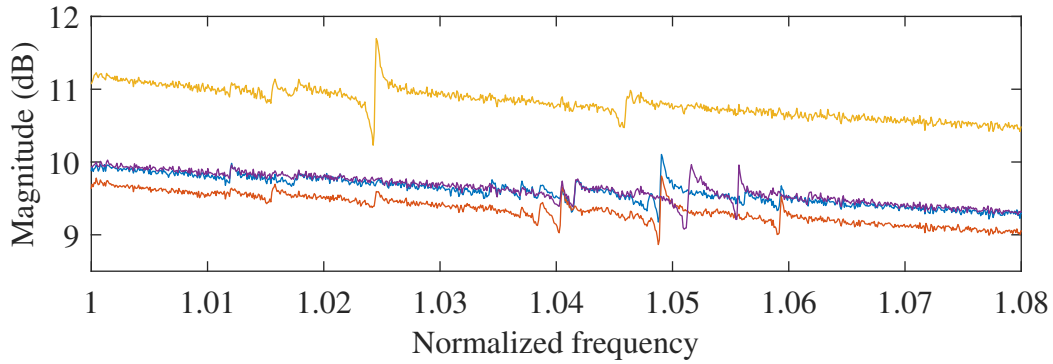

(b) Patch 5 (—), patch 6 (—), patch 7 (—) and patch 8 (—).

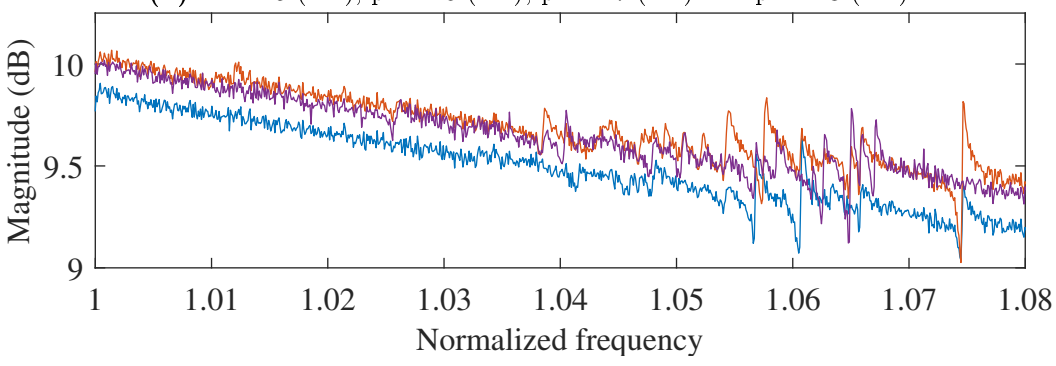

(c) Patch 15 (—), patch 16 (—), patch 17 (—) and patch 18 (—).

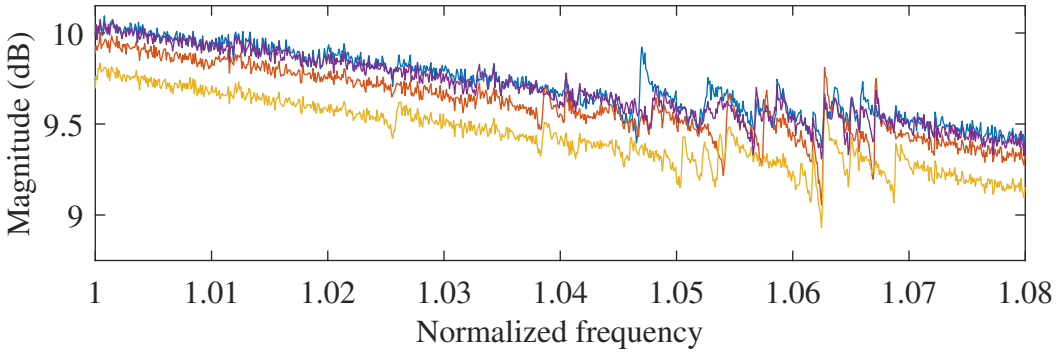

(d) Patch 19 (—), patch 20 (—), patch 21 (—) and patch 22 (—).

Figure B.4: Dynamic impedance measurements of the 16 shunted patches for patch configuration 5.

	EMCF					
Patch number	Conf. 1	Conf. 2	Conf. 3	Conf. 4	Conf. 5	Conf. 3 (Robustness)
1	0.0079	0.0079	0.0062	0.0082	0.0077	0.0090
2	0.0010	0.0060	0.0053	0.0035	0.0028	0.0023
3	0.0060	0.0063	0.0053	0.0060	0.0063	0.0080
4	0.0053	0.0067	0.0047	0.0053	0.0057	0.0076
5	0.0048	0.0060	0.0056	0.0047	0.0051	0.0047
6	0.0052	0.0060	0.0057	0.0054	0.0055	0.0057
7	0.0067	0.0051	0.0056	0.0067	0.0066	0.0066
8	0.0069	0.0055	0.0049	0.0060	0.0080	0.0039
9	0.0056	0.0053	0.0440	0.0042	0.0053	0.0030
10	0.0046	0.0038	0.0063	0.0061	0.0043	0.0066
11	0.0040	0.0055	0.0056	0.0061	0.0057	0.0080
12	0.0051	0.0047	0.0106	0.0051	0.0043	0.0053
13	0.0027	0.0054	0.0049	0.0042	0.0051	0.0053
14	0.0042	0.0057	0.0074	0.0034	0.0057	0.0044
15	0.0045	0.0056	0.0057	0.0043	0.0055	0.0054
16	0.0049	0.0045	0.0042	0.0040	0.0065	0.0054

Table B.1: EMCF for the RL shunts for the isolated mode strategy applied to the different patch configurations 1 - 5 based on Table 4.2. The numbers of the respective modes are related to each configuration individually and are not globally valid (cf. Table 4.1).

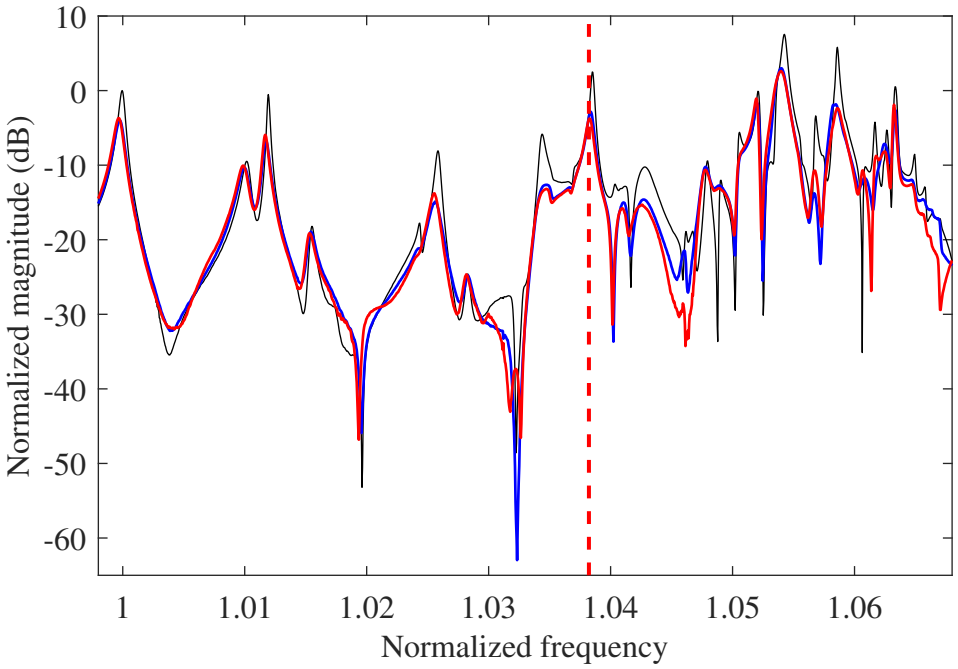

Figure B.5: FRFs from the excitation force to the blade tip in patch configuration 1. Open circuit (—), isolated mode (—) and mean shunt (—). The mean frequency is indicated in (- - -).

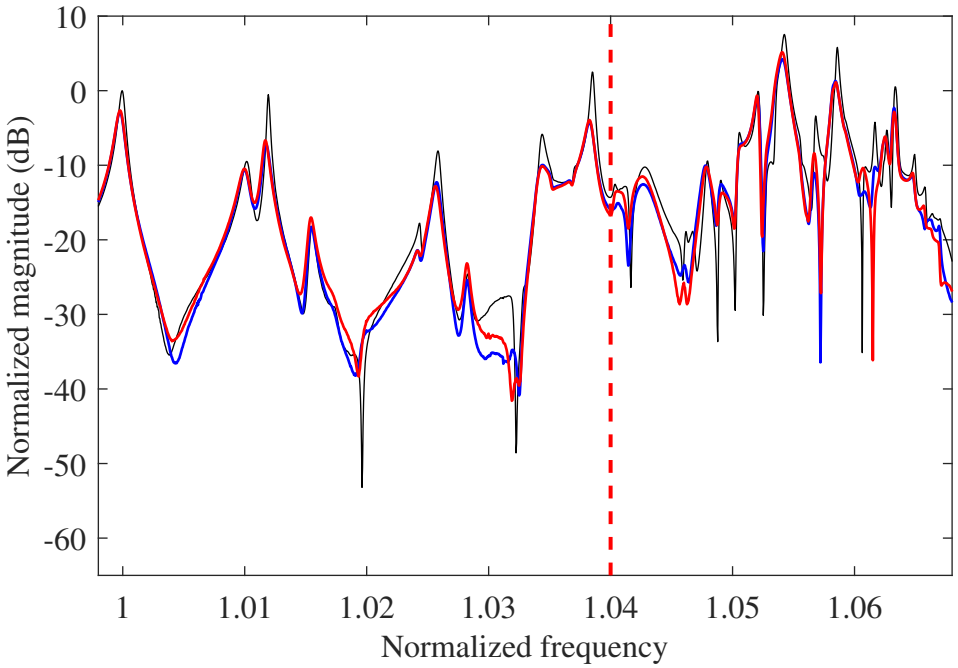

Figure B.6: FRFs from the excitation force to the blade tip in patch configuration 2. Open circuit (▬), isolated mode (▬) and mean shunt (▬). The mean frequency is indicated in (▪ ▪ ▪).

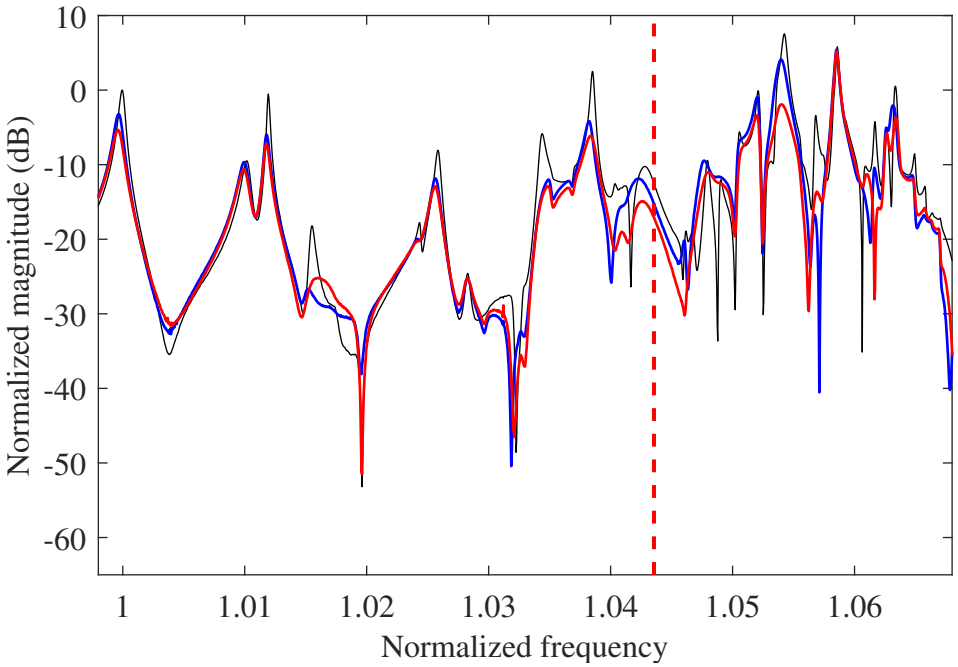

Figure B.7: FRFs from the excitation force to the blade tip in patch configuration 4. Open circuit (▬), isolated mode (▬) and mean shunt (▬). The mean frequency is indicated in (▪ ▪ ▪).

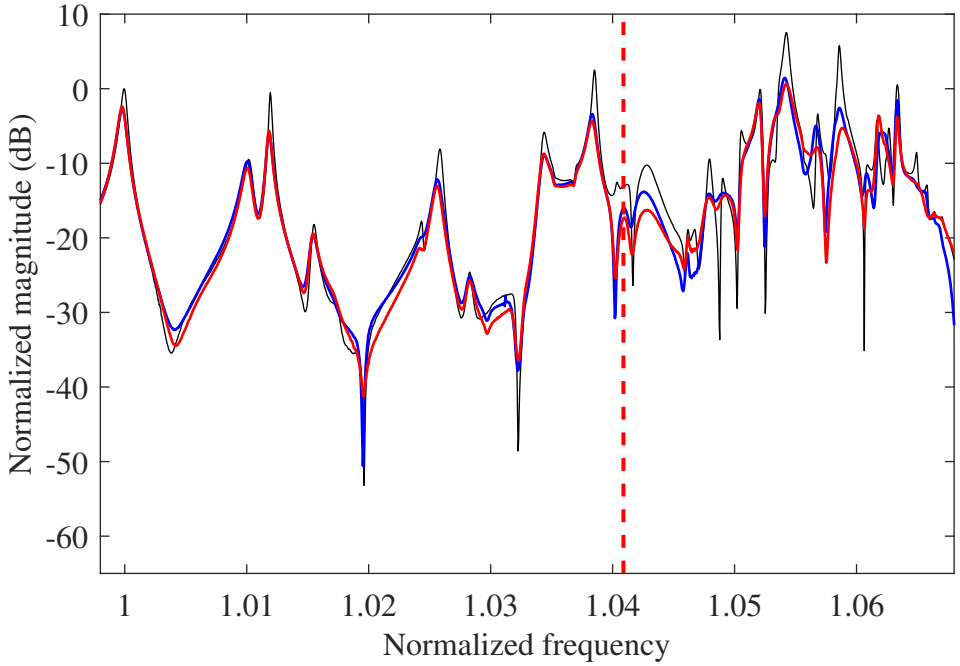

Figure B.8: FRFs from the excitation force to the blade tip in patch configuration 5. Open circuit (—), isolated mode (—) and mean shunt (—). The mean frequency is indicated in (- - -).

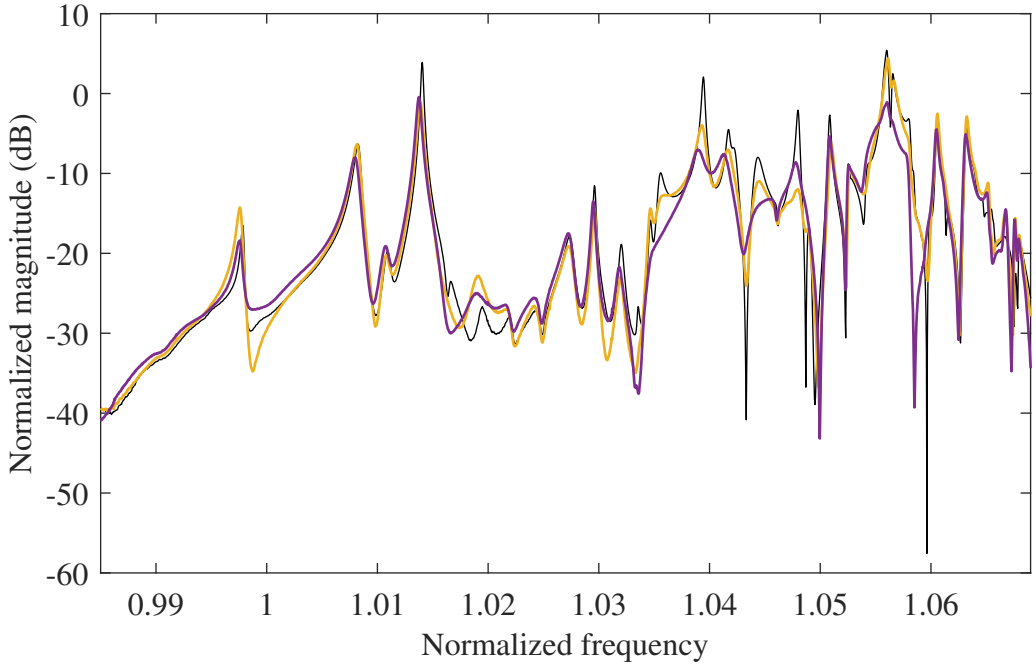

Figure B.9: Open-circuit FRF of the altered system (—) and FRFs of the system controlled by detuned (—) and retuned (—) shunts, both according to the isolated mode strategy.

List of Figures

List of Tables

Bibliography

[1] *Survey completed by True Intelligence for IATA in June 2021, with passengers in 12 markets. Results were fairly consistent and shown here are the average figures across Australia, Canada, the United States, Germany, France, the Netherlands, Spain, Sweden, the United Kingdom, India, Japan and Mexico.*

[2] Statistica. URL: https://www.statista.com/statistics/1185535/transport-carbon-dioxide-emissions-breakdown/.

[3] International Civil Aviation Organization. *Carbon Offsetting and Reduction Scheme for International Aviation (CORSIA).* 2016. URL: https://www.icao.int/environmental-protection/CORSIA/Pages/default.aspx.

[4] Council of the EU. *Council adopts decision on offsetting requirements for air transport emissions (CORSIA).* 2022. URL: https://www.consilium.europa.eu/en/press/press-releases/2022/12/19/council-adopts-decision-on-offsetting-requirements-for-air-transport-emissions-corsia/.

[5] WINGS. *Wallon Innovations for Green Skies https://www.wingspartnership.be/.* URL: https://www.wingspartnership.be/.

[6] European Commission. Directorate General for Research and Innovation. *Fly the Green Deal: Europe's vision for sustainable aviation.* LU: Publications Office, 2022. URL: https://data.europa.eu/doi/10.2777/732726.

[7] Clean Aviation. *Clean Sky 2.* URL: https://www.clean-aviation.eu/clean-sky-2/programme-overview-and-structure.

[8] Aviation Impact Accelerator. URL: https://www.aiazero.org/the-project/.

[9] Air Transport Action Group. *Waypoint 2050.* Tech. rep. 2021. URL: https://aviationbenefits.org/media/167417/w2050_v2021_27sept_full.pdf.

[10] International Energy Agency. *Energy Technology Perspectives 2020.* Tech. rep. 2020. URL: https://iea.blob.core.windows.net/assets/7f8aed40-89af-4348-be19-c8a67df0b9ea/Energy_Technology_Perspectives_2020_PDF.pdf.

[11] E. Drab. "Avec RISE, Safran et GE Aviation misent sur les soufflantes non carénées pour décarboner l'aviation". *Le journal de l'aviation* (2021).

[12] AIRBUS. *ZEROe - Towards the world's first hydrogen-powered commercial aircraft.* URL: https://www.airbus.com/en/innovation/low-carbon-aviation/hydrogen/zeroe.

[13] Heart Aerospace. URL: https://heartaerospace.com/about/.

[14] L. Rouleau, O. De Smet, and J.-F. Deü. "Vibration prediction of rotating composite fan blades comprising viscoelastic damping treatments". *Journal of Sound and Vibration* Vol. 536 (2022), p. 117135. DOI: 10.1016/j.jsv.2022.117135.

[15] D. Laxalde, F. Thouverez, and J.-P. Lombard. "Forced Response Analysis of Integrally Bladed Disks With Friction Ring Dampers". *Journal of Vibration and Acoustics* Vol. 132, no. 1 (2010), p. 011013. DOI: 10.1115/1.4000763.

[16] J. P. Den Hartog. *Mechanical vibrations*. Dover books on engineering. New York: Dover Publications, 1985. ISBN: 978-0-486-64785-2.

[17] J. Ormondroyd and J. P. Den Hartog. "Theory of the dynamic vibration absorber". *Transaction of the ASME* (1928).

[18] R. L. Forward. *Electromechanical transducer-coupled mechanical structure with negative capacitance compensation circuit*. U.S. Patent US4158787A, 1979.

[19] N. W. Hagood and A. von Flotow. "Damping of structural vibrations with piezoelectric materials and passive electrical networks". *Journal of Sound and Vibration* Vol. 146, no. 2 (1991), pp. 243–268. DOI: 10.1016/0022-460X(91)90762-9.

[20] M. J. Balas. "Direct Velocity Feedback Control of Large Space Structures". *Journal of Guidance and Control* Vol. 2, no. 3 (1979), pp. 252–253. DOI: 10.2514/3.55869.

[21] A. Preumont, J.-P. Dufour, and C. Malekian. "Active damping by a local force feedback with piezoelectric actuators". *Journal of Guidance, Control, and Dynamics* Vol. 15, no. 2 (1992), pp. 390–395. DOI: 10.2514/3.20848.

[22] C. J. Goh and T. K. Caughey. "On the stability problem caused by finite actuator dynamics in the collocated control of large space structures". *International Journal of Control* Vol. 41, no. 3 (1985), pp. 787–802. DOI: 10.1080/0020718508961163.

[23] C. Liu, L. Chen, X. Yang, X. Zhang, and Y. Yang. "General Theory of Skyhook Control and its Application to Semi-Active Suspension Control Strategy Design". *IEEE Access* Vol. 7 (2019), pp. 101552–101560. DOI: 10.1109/ACCESS.2019.2930567.

[24] C. Collette, S. Janssens, K. Artoos, and C. Hauviller. "Active vibration isolation of high precision machines". *Diamond Light Source Proceedings* Vol. 1, no. MEDSI-6 (2010), e1. DOI: 10.1017/S2044820110000134.

[25] I. Nishimura, T. Kobori, M. Sakamoto, N. Koshika, K. Sasaki, and S. Ohrui. "Active tuned mass damper". *Smart Materials and Structures* Vol. 1, no. 4 (1992), pp. 306–311. DOI: 10.1088/0964-1726/1/4/005.

[26] A. J. Fleming, S. Behrens, and S. O. R. Moheimani. "Synthetic impedance for implementation of piezoelectric shunt-damping circuits". *Electronics Letters* Vol. 36, no. 18 (2000), p. 1525. DOI: 10.1049/el:20001083.

[27] A. J. Fleming and S. O. R. Moheimani. " Control orientated synthesis of high-performance piezoelectric shunt impedances for structural vibration control". *IEEE Transactions on Control Systems Technology* Vol. 13, no. 1 (2005), pp. 98–112. DOI: 10.1109/TCST.2004.838547.

[28] B. de Marneffe and A. Preumont. "Vibration damping with negative capacitance shunts: theory and experiment". *Smart Materials and Structures* Vol. 17, no. 3 (2008), p. 035015. DOI: 10.1088/0964-1726/17/3/035015.

[29] *CFM56 turbofan aircraft engine Cutaway Drawing.* URL: https://conceptbunny.com/cfm56-turbofan-aircraft-engine/.

[30] G. Raze. "Piezoelectric Digital Vibration Absorbers for Multimodal Vibration Mitigation of Complex Mechanical Structures". Doctoral Thesis. Liège: Université de Liège, 2021. URL: https://orbi.uliege.be/handle/2268/256608.

[31] A. Tacher. "Forced response and stability of mistuned structures subject to the Coriolis effect". Doctoral thesis. Ecole centrale de Lyon, 2022. URL: http://www.theses.fr/2022ECDL0001/document.

[32] B. Mokrani. "Piezoelectric Shunt Damping of Rotationally Periodic Structures". Doctoral thesis. Brussels, Belgium: Universitè Libre de Bruxelles, 2015. URL: https://dipot.ulb.ac.be/dspace/bitstream/2013/209112/4/b6f8b434-eb55-4020-b677-bc8a56ee298b.txt.

[33] G. Kerschen. *Scientific Report 1. WALInnov MAVERIC 1610122, 5 2018.* Technical report. WALInnov MAVERIC 1610122, 2018.

[34] N. Soin, S.C. Anand, and T.H. Shah. "Energy harvesting and storage textiles". *Handbook of Technical Textiles*. Elsevier, 2016, pp. 357–396. ISBN: 978-1-78242-465-9. DOI: 10.1016/B978-1-78242-465-9.00012-4.

[35] *ANSI/IEEE Std 176-1987 - IEEE Standard on Piezoelectricity.* Tech. rep. New York, USA: The Institute of Electrical and Electronics Engineers, Inc, 1987. DOI: 10.1109/IEEESTD.1988.79638. URL: https://ieeexplore.ieee.org/document/26560/.

[36] D. H. Johnson. "Scanning our past origins of the equivalent circuit concept: the current-source equivalent". *Proceedings of the IEEE* Vol. 91, no. 5 (2003), pp. 817–821. DOI: 10.1109/JPROC.2003.811795.

[37] D. H. Johnson. "Origins of the equivalent circuit concept: the voltage-source equivalent". *Proceedings of the IEEE* Vol. 91, no. 4 (2003), pp. 636–640. DOI: 10.1109/JPROC.2003.811716.

[38] J. F. Toftekær, A. Benjeddou, and J. Høgsberg. "General numerical implementation of a new piezoelectric shunt tuning method based on the effective electromechanical coupling coefficient". *Mechanics of Advanced Materials and Structures* Vol. 27, no. 22 (2020), pp. 1908–1922. DOI: 10.1080/15376494.2018.1549297.

[39] M. Berardengo, O. Thomas, C. Giraud-Audine, and S. Manzoni. "Improved resistive shunt by means of negative capacitance: new circuit, performances and multi-mode control". *Smart Materials and Structures* Vol. 25, no. 7 (2016). DOI: 10.1088/0964-1726/25/7/075033.

[40] M. Berardengo. "Innovative vibration control systems based on smart materials for light structures". Doctoral thesis. Milan, Italy: Politecnico di Milano, 2016. URL: https://www.politesi.polimi.it/handle/10589/117763.

[41] R. L. Forward. "Electronic damping of vibrations in optical structures". *Applied Optics* Vol. 18, no. 5 (1979), p. 690. DOI: 10.1364/AO.18.000690.

[42] S. O. R. Moheimani and A. J. Fleming. *Piezoelectric Transducers for Vibration Control and Damping*. Advances in Industrial Control Ser. New York Berlin: Springer, 2006. ISBN: 978-1-84628-332-1.

[43] B. D. O. Anderson and S. Vongpanitlerd. "Network analysis and synthesis - A modern systems theory approach". *Networks* Vol. 4, no. 3 (1974), pp. 283–285. DOI: 10.1002/net.3230040308.

[44] D. L. Edberg, A. S. Bicos, and J. S. Fechter. "On piezoelectric energy conversion for electronic passive damping enhancement". *Proceedings of Damping* (1991), pp. 717–724.

[45] O. Thomas, J. Ducarne, and J.-F. Deü. "Performance of piezoelectric shunts for vibration reduction". *Smart Materials and Structures* Vol. 21, no. 1 (2012), p. 015008. DOI: 10.1088/0964-1726/21/1/015008.

[46] K. Yamada, H. Matsuhisa, H. Utsuno, and K. Sawada. "Optimum tuning of series and parallel LR circuits for passive vibration suppression using piezoelectric elements". *Journal of Sound and Vibration* Vol. 329, no. 24 (2010), pp. 5036–5057. DOI: 10.1016/j.jsv.2010.06.021.

[47] P. Soltani, G. Kerschen, G. Tondreau, and A. Deraemaeker. "Piezoelectric vibration damping using resonant shunt circuits: an exact solution". *Smart Materials and Structures* Vol. 23, no. 12 (2014). DOI: 10.1088/0964-1726/23/12/125014.

[48] T. Ikegame, K. Takagi, and T. Inoue. "Exact Solutions to H_∞ and H_2 Optimizations of Passive Resonant Shunt Circuit for Electromagnetic or Piezoelectric Shunt Damper". *J. Vib. Acoust. Trans. ASME* Vol. 141, no. 3 (2019). DOI: 10.1115/1.4042819.

[49] B. Lossouarn, M. Aucejo, J.-F. Deü, and B. Multon. "Design of inductors with high inductance values for resonant piezoelectric damping". *Sensors and Actuators A: Physical* Vol. 259 (2017), pp. 68–76. DOI: 10.1016/j.sna.2017.03.030.

[50] R. Darleux. "Development of analogous piezoelectric networks for the vibration damping of complex structures". Doctoral thesis. HESAM Université, 2020. URL: https://theses.hal.science/tel-02902755.

[51] T. Funck, A. Muller, and H. Bothe. "Synthetic inductance standards made up of capacitances and gyrators". *2020 Conference on Precision Electromagnetic Measurements (CPEM)*. Denver (Aurora), CO, USA: IEEE, 2020, pp. 1–2. ISBN: 978-1-72815-898-3. DOI: 10.1109/CPEM49742.2020.9191919.

[52] B. D. H. Tellegen. "The gyrator, a new electric network element". *Philips Res. Rept.* Vol. 3 (1948), pp. 81–101.

[53] A. Antoniou. "Realisation of gyrators using operational amplifiers, and their use in RC-active-network synthesis". *Proceedings of the Institution of Electrical Engineers* Vol. 116, no. 11 (1969), p. 1838. DOI: 10.1049/piee.1969.0339.

[54] S. O. R. Moheimani and Behrens S. Fleming A. J. "On the feedback structure of wideband piezoelectric shunt damping systems". *Smart Materials and Structures* Vol. 12, no. 1 (2003), pp. 49–56. DOI: https://doi.org/10.1016/j.jsv.2023.117723.

[55] S. O. R. Moheimani, A. J. Fleming, and S. Behrens. "Dynamics, Stability, and Control of Multivariable Piezoelectric Shunts". *IEEE/ASME Transactions on Mechatronics* Vol. 9, no. 1 (2004), pp. 87–99. DOI: 10.1109/TMECH.2004.823882.

[56] I. Giorgio, A. Culla, and D. Del Vescovo. "Multimode vibration control using several piezoelectric transducers shunted with a multiterminal network". *Archive of Applied Mechanics* Vol. 79, no. 9 (2009), pp. 859–879. DOI: 10.1007/s00419-008-0258-x.

[57] I. Giorgio. "Multimode Collocated Vibration Control with Multiple Piezoelectric Transducers". Doctoral Thesis. Rome: Sapienza Università di Roma, 2008.

[58] G. Rosi, R. Paccapeli, F. Ollivier, and J. Pouget. "Optimization of piezoelectric patch positioning for passive sound radiation control of plates". *Journal of Vibration and Control* Vol. 19, no. 5 (2013), pp. 658–673. DOI: 10.1177/1077546312437236.

[59] G. Rosi. "Control of sound radiation and transmission by means of passive piezoelectric networks : modelling, optimization and experimental implementation". Doctoral Thesis. Rome: Sapienza Università di Roma, 2010.

[60] G. Matten, M. Collet, S. Cogan, and E. Sadoulet-Reboul. "Synthetic Impedance for Adaptive Piezoelectric Metacomposite". *Procedia Technology* Vol. 15 (2014), pp. 84–89. DOI: 10.1016/j.protcy.2014.09.037.

[61] K. Yi, G. Matten, M. Ouisse, E. Sadoulet-Reboul, M. Collet, and G. Chevallier. "Programmable metamaterials with digital synthetic impedance circuits for vibration control". *Smart Materials and Structures* Vol. 29, no. 3 (2020), p. 035005. DOI: 10.1088/1361-665X/ab6693.

[62] L. Dal Bo, H. He, P. Gardonio, Y. Li, and J. Z. Jiang. "Design tool for elementary shunts connected to piezoelectric patches set to control multi-resonant flexural vibrations". *Journal of Sound and Vibration* (2021), p. 116554. DOI: 10.1016/j.jsv.2021.116554.

[63] G. Raze, A. Jadoul, S. Guichaux, V. Broun, and G. Kerschen. "A digital nonlinear piezoelectric tuned vibration absorber". *Smart Materials and Structures* Vol. 29, no. 1 (2020), p. 015007. DOI: 10.1088/1361-665X/ab5176.

[64] G. Raze, J. Dietrich, B. Lossouarn, and G. Kerschen. "Shunts vs networks: tuning and comparison of centralized and decentralized piezoelectric vibration absorbers". *Smart Materials and Structures* Vol. 31, no. 11 (2022), p. 115006. DOI: 10.1088/1361-665X/ac92b0.

[65] G. Raze, J. Dietrich, and G. Kerschen. "Passive control of multiple structural resonances with piezoelectric vibration absorbers". *Journal of Sound and Vibration* Vol. 515 (2021), p. 116490. DOI: 10.1016/j.jsv.2021.116490.

[66] dSPACE GmbH. *MicroLabBox product-brochure - Compact prototyping unit for the laboratory*. 2020. URL: https://www.dspace.com/shared/data/pdf/2020/dSPACE-MicroLabBox_Product-Brochure_2020-01_EN.pdf.

[67] P. Horowitz and W. Hill. *The Art of Electronics*. 3. Cambridge University Press, 2015. ISBN: 978-0-521-37095-0.

[68] A. J. Fleming. "Synthesis and Implementation of Sensor-less Shunt Controllers for Piezoelectric and Electromagnetic Vibration Control". Doctoral thesis. Callaghan, Australia: The University of Newcastle, 2004.

[69] G. F. Franklin, D. J. Powell, and M. L. Workman. *Digital control of dynamic systems*. 3. California: Addison Wesley Longman, 2002. ISBN: 0-201-82054-4.

[70] G. Raze, J. Dietrich, and G. Kerschen. "Onset and stabilization of delay-induced instabilities in piezoelectric digital vibration absorbers". *Journal of Intelligent Material Systems and Structures* Vol. 33, no. 16 (2022). DOI: 10.1177/1045389X211072269.

[71] B. Douglas. *Discretize! Going from continuous to discrete domain*. 2017. URL: https://www.youtube.com/watch?v=rL_1oWrOplk.

[72] D. J. Inman. *Vibration with control*. Hoboken, NJ: Wiley, 2006. ISBN: 978-0-470-01051-8.

[73] H. I. H. Saravanamuttoo, G. Frederick C. Rogers, and H. Cohen. *Gas Turbine Theory*. Pearson Education, 2001. ISBN: 978-0-13-015847-5.

[74] D. L. Thomas. "Dynamics of rotationally periodic structures". *International Journal for Numerical Methods in Engineering* Vol. 14, no. 1 (1979), pp. 81–102. DOI: 10.1002/nme.1620140107.

[75] F. Nyssen. "Numerical Modeling and Experimental Identifcitaion of Mistuned Multi-Stage Bladed Assemblies". Doctoral Thesis. Liège: Université de Liège, 2016. URL: https://orbi.uliege.be/handle/2268/197445.

[76] J. S. Rao. *History of Rotating Machinery Dynamics*. Ed. by Marco Giovanni Ceccarelli. Vol. 20. History of Mechanism and Machine Science. Dordrecht: Springer Netherlands, 2011. ISBN: 978-94-007-1164-8 978-94-007-1165-5. DOI: 10.1007/978-94-007-1165-5.

[77] M. Nikolic, E. P. Petrov, and D. J. Ewins. "Coriolis Forces in Forced Response Analysis of Mistuned Bladed Disks". *Journal of Turbomachinery* Vol. 129, no. 4 (2007), pp. 730–739. DOI: 10.1115/1.2720866.

[78] D. J. Ewins. "The effects of detuning upon the forced vibrations of bladed disks". *Journal of Sound and Vibration* Vol. 9, no. 1 (1969), pp. 65–79. DOI: 10.1016/0022-460X(69)90264-8.

[79] S.-T. Wei and C. Pierre. "Localization phenomena in mistuned assemblies with cyclic symmetry part I: free vibrations". *Journal of Vibration, Acoustics, Stress, and Reliability in Design* Vol. 110, no. 4 (1988), pp. 429–438. DOI: 10.1115/1.3269547.

[80] J. A. Judge, C. Pierre, and S. L. Ceccio. "Experimental Mistuning Identification in Bladed Disks Using a Component-Mode-Based Reduced-Order Model". *AIAA Journal* Vol. 47, no. 5 (2009), pp. 1277–1287. DOI: 10.2514/1.41214.

[81] F. Nyssen and J. C. Golinval. "Identification of mistuning and model updating of an academic blisk based on geometry and vibration measurements". *Mechanical Systems and Signal Processing* Vol. 68-69 (2016), pp. 252–264. DOI: 10.1016/j.ymssp.2015.08.006.

[82] S. T. Kelly, A. Lupini, and B. I. Epureanu. "Data-Driven Approach for Identifying Mistuning in As-Manufactured Blisks". *Journal of Engineering for Gas Turbines and Power* Vol. 144, no. 5 (2022). DOI: 10.1115/1.4052503.

[83] B. Mokrani, R. Bastaits, M. Horodinca, I. Romanescu, I. Burda, R. Viguié, and A. Preumont. "Parallel Piezoelectric Shunt Damping of Rotationally Periodic Structures". *Advances in Materials Science and Engineering* Vol. 2015 (2015), pp. 1–12. DOI: 10.1155/2015/162782.

[84] B. Mokrani, R. Bastaits, R. Viguié, and A. Preumont. "Vibration damping of turbomachinery components with piezoelectric transducers: Theory and Experiment". *PROCEEDINGS OF ISMA2012-USD2012*. Leuven, 2012.

[85] B. Mokrani, R. Bastaits, M. Horodinca, I. Romanescu, I. Burda, R. Vigiué, and A. Preumont. "Passive piezo damping of rotationally periodic structures with application to a bladed drum". *Proceedings of ISMA 2014 including USD 2014*. Leuven, Belgium, 2014. ISBN: 978-90-73802-91-9.

[86] A. Mateo. "On the feasibility of BLISK produced by linear friction welding". *Revista de Metalurgia* Vol. 50, no. 3 (2014), e023. DOI: 10.3989/revmetalm.023.

[87] A. Kermanpur, H. Sepehri Amin, S. Ziaei-Rad, N. Nourbakhshnia, and M. Mosaddeghfar. "Failure analysis of Ti6Al4V gas turbine compressor blades". *Engineering Failure Analysis* Vol. 15, no. 8 (2008), pp. 1052–1064. DOI: 10.1016/j.engfailanal.2007.11.018.

[88] D. Charleux, C. Gibert, F. Thouverez, and J. Dupeux. "Numerical and Experimental Study of Friction Damping Blade Attachments of Rotating Bladed Disks". *International Journal of Rotating Machinery* Vol. 2006 (2006), e71302. DOI: 10.1155/IJRM/2006/71302.

[89] E. P. Petrov and D. J. Ewins. "Advanced Modeling of Underplatform Friction Dampers for Analysis of Bladed Disk Vibration". *Journal of Turbomachinery* Vol. 129, no. 1 (2006), pp. 143–150. DOI: 10.1115/1.2372775.

[90] M. Gola and C. Gastaldi. "Understanding Complexities in Underplatform Damper Mechanics". American Society of Mechanical Engineers Digital Collection, 2014. DOI: 10.1115/GT2014-25240.

[91] D. Laxalde, C. Gibert, and F. Thouverez. "Experimental and Numerical Investigations of Friction Rings Damping of Blisks". American Society of Mechanical Engineers Digital Collection, 2009, pp. 469–479. DOI: 10.1115/GT2008-50862.

[92] M. Krack, L. Salles, and F. Thouverez. "Vibration Prediction of Bladed Disks Coupled by Friction Joints". *Archives of Computational Methods in Engineering* Vol. 24, no. 3 (2017), pp. 589–636. DOI: 10.1007/s11831-016-9183-2.

[93] N. Nguyen. "Blading system and method for controlling structural vibrations". Pat. 6,102,664 (Santa Clara, California). 2000.

[94] E. P. Bowyer and V. V. Krylov. "Damping of flexural vibrations in turbofan blades using the acoustic black hole effect". *Applied Acoustics* Vol. 76 (2014), pp. 359–365. DOI: 10.1016/j.apacoust.2013.09.009.

[95] J. Tang and K. W. Wang. "Vibration Control of Rotationally Periodic Structures Using Passive Piezoelectric Shunt Networks and Active Compensation". *Journal of Vibration and Acoustics* Vol. 121, no. 3 (1999), pp. 379–390. DOI: 10.1115/1.2893991.

[96] H. Yu and K. W. Wang. "Piezoelectric Networks for Vibration Suppression of Mistuned Bladed Disks". *Journal of Vibration and Acoustics* Vol. 129, no. 5 (2007), pp. 559–566. DOI: 10.1115/1.2775511.

[97] H. Yu and K. W. Wang. "Vibration Suppression of Mistuned Coupled-Blade-Disk Systems Using Piezoelectric Circuitry Network". *Volume 1: 21st Biennial Conference on Mechanical Vibration and Noise, Parts A, B, and C*. Las Vegas, Nevada, USA: ASMEDC, 2007, pp. 57–68. ISBN: 978-0-7918-4802-9. DOI: 10.1115/DETC2007-34443.

[98] J. Liu, L. Li, P. Deng, and C. Li. "A Comparative Study on the Dynamic Characteristics of Bladed Disks With Piezoelectric Network and Piezoelectric Shunt Circuit". *Volume 7A: Structures and Dynamics*. Seoul, South Korea: American Society of Mechanical Engineers, 2016. ISBN: 978-0-7918-4983-5. DOI: 10.1115/GT2016-56794.

[99] J. L. Kauffman and G. A. Lesieutre. "Piezoelectric-Based Vibration Reduction of Turbomachinery Bladed Disks via Resonance Frequency Detuning". *AIAA Journal* Vol. 50, no. 5 (2012), pp. 1137–1144. DOI: 10.2514/1.J051344.

[100] B. B. Choi, C. Morrison, and K. Duffy. *An Active Damping at Blade Resonances Using Piezoelectric Transducers*. Technical Report NASA/TM-2008-215212. National Aeronautics and Space Administration, 2008.

[101] B. Choi, K. Duffy, J. L. Kauffman, and N. Kray. "Optimal topology and experimental evaluation of PE materials for actively shunted GE polymer matrix fiber composite blades". Ed. by M. Tomizuka, C.-B. Yun, and J. P. Lynch. San Diego, California, 2012, 83452G. DOI: 10.1117/12.917224.

[102] P. Bisegna and G. Caruso. "Optimization of a passive vibration control scheme acting on a bladed rotor using an homogenized model". *Structural and Multidisciplinary Optimization* Vol. 39, no. 6 (2009), pp. 625–636. DOI: 10.1007/s00158-009-0375-3.

[103] O. Thierry, O. De Smet, and J.F. Deü. "Vibration reduction of a woven composite fan blade by piezoelectric shunted devices". *Journal of Physics: Conference Series* Vol. 744 (2016), p. 012164. DOI: 10.1088/1742-6596/744/1/012164.

[104] S. M. Schwarzendahl, J. Szwedowicz, M. Neubauer, L. Panning, and J. Wallaschek. "On Blade Damping Technology Using Passive Piezoelectric Dampers". *Structures and Dynamics, Parts A and B*. Vol. 7. Copenhagen, Denmark: American Society of Mechanical Engineers, 2012, pp. 1205–1215. ISBN: 978-0-7918-4473-1. DOI: 10.1115/GT2012-68600.

[105] A. Rossi, F. Botta, A. Giovannelli, and N. P. Belfiore. "A novel approach to reduce fan rotor blades stress in case of resonance due to inlet flow distortion by means of piezoelectric actuators". *Journal of Sound and Vibration* Vol. 548 (2023), p. 117552. DOI: 10.1016/j.jsv.2023.117552.

[106] B. Zhou, F. Thouverez, and D. Lenoir. "Vibration Reduction of Mistuned Bladed Disks by Passive Piezoelectric Shunt Damping Techniques". *AIAA Journal* Vol. 52, no. 6 (2014), pp. 1194–1206. DOI: 10.2514/1.J052202.

[107] R. Viguié, D. Verhelst, A. Preumont, and B. Mokrani. "Piezoelectric damper system for an axial turbomachine rotor (US Patent US10125794B2)". Pat. US10125794B2. 2015.

[108] A. Paknejad, R. Jamshidi, S. Pathak, and C. Collette. "Active Vibration Mitigation of Bladed Structures With Piezoelectric Patches by Decentralized Positive Position Feedback Controller". *Journal of Engineering for Gas Turbines and Power* Vol. 145, no. 2 (2023), p. 021003. DOI: 10.1115/1.4056013.

[109] R. Jamshidi. *Active Vibration Mitigation of High Modal Density of BLUM with Piezoelectric Patches, presented at European Nonlinear Oscillations Conference ENOC, Lyon*. Conference presentation. Lyon, 2022.

[110] J. F. Toftekær and J. Høgsberg. "Multi-mode piezoelectric shunt damping with residual mode correction by evaluation of modal charge and voltage". *Journal of Intelligent Material Systems and Structures* Vol. 31, no. 4 (2020), pp. 570–586. DOI: 10.1177/1045389X19891646.

[111] J. Hollkamp. "Multimodal Passive Vibration Suppression with Piezoelectric Materials and Resonant Shunts". *Journal of Intelligent Material Systems and Structures* Vol. 5, no. 1 (1994), pp. 49–57. DOI: 10.1177/1045389X9400500106.

[112] S.-Y. Wu. "Method for multiple-mode shunt damping of structural vibration using a single PZT transducer". *Proceedings Volume 3327, Smart structures and materials 1998: passive damping and isolation*. San Diego, CA, 1998, pp. 159–168. DOI: 10.1117/12.310680.

[113] A. Agneni, M. Del Sorbo, F. Mastroddi, and G. M. Pollo. "Multi-modal damping by shunted piezo-patches: Possible aeroelastic applications". *International Journal of Applied Electromagnetics and Mechanics 24* (2006).

[114] S. Behrens, S. O. R. Moheimani, and A. J. Fleming. "Multiple mode current flowing passive piezoelectric shunt controller". *Journal of Sound and Vibration* Vol. 266, no. 5 (2003), pp. 929–942. DOI: 10.1016/S0022-460X(02)01380-9.

[115] A. L. Goldstein. "Self-Tuning Multimodal Piezoelectric Shunt Damping". *Journal of the Brazilian Society of Mechanical Sciences and Engineering* Vol. 33, no. 4 (2011), pp. 428–436. DOI: 10.1590/S1678-58782011000400006.

[116] A. J. Fleming, S. Behrens, and S. O. R. Moheimani. "Reducing the inductance requirements of piezoelectric shunt damping systems". *Smart Materials and Structures* Vol. 12, no. 1 (2003), pp. 57–64. DOI: 10.1088/0964-1726/12/1/307.

[117] G. Raze, A. Paknejad, G. Zhao, C. Collette, and G. Kerschen. "Multimodal vibration damping using a simplified current blocking shunt circuit". *Journal of Intelligent Material Systems and Structures* Vol. 31, no. 14 (2020), pp. 1731–1747. DOI: 10.1177/1045389X20930103.

[118] S. O. R. Moheimani, A. J. Fleming, and S. Behrens. "On the feedback structure of wideband piezoelectric shunt damping systems". *Smart Materials and Structures* Vol. 12 (2003), pp. 49–56.

[119] A. J. Fleming, S. Behrens, and S. O. R. Moheimani. "Optimization and implementation of multimode piezoelectric shunt damping systems". *IEEE/ASME Transactions on Mechatronics* Vol. 7, no. 1 (2002), pp. 87–94. DOI: 10.1109/3516.990891.

[120] A. Cigada, S. Manzoni, M. Redaelli, and M. Vanali. "Optimization of the current flowing technique aimed at semi-passive multi-modal vibration reduction". *Journal of Vibration and Control* Vol. 18, no. 2 (2012), pp. 298–312. DOI: 10.1177/1077546311407537.

[121] P. Gardonio, M. Zientek, and L. Dal Bo. "Panel with self-tuning shunted piezoelectric patches for broadband flexural vibration control". *Mechanical Systems and Signal Processing* Vol. 134 (2019), p. 106299. DOI: 10.1016/j.ymssp.2019.106299.

[122] M. Berardengo, S. Manzoni, and A.M. Conti. "Multi-mode passive piezoelectric shunt damping by means of matrix inequalities". *Journal of Sound and Vibration* Vol. 405 (2017), pp. 287–305. DOI: 10.1016/j.jsv.2017.06.002.

[123] J. F. Toftekær and J. Høgsberg. "Multi-mode piezoelectric shunt damping with residual mode correction by evaluation of modal charge and voltage". *Journal of Intelligent Material Systems and Structures* Vol. 31, no. 4 (2020), pp. 570–586. DOI: 10.1177/1045389X19891646.

[124] O. Thomas, J.-F. Deü, and J. Ducarne. "Vibrations of an elastic structure with shunted piezoelectric patches: efficient finite element formulation and electromechanical coupling coefficients". *Int. J. Numer. Methods Eng.* Vol. 80, no. 2 (2009), pp. 235–268. DOI: 10.1002/nme.2632.

[125] C. K. Alexander and M. N. O. Sadiku. *Fundamentals of electric circuits*. 5. New York, NY: McGraw-Hill, 2013. ISBN: 978-0-07-338057-5.

[126] A. Paknejad Seyedahmadian. "Passive and Active Strategies for Vibration Control of Lightly Damped Structures". Doctoral Thesis. Université libre de Bruxelles, 2021.

[127] A. Paknejad, G. Raze, G. Zhao, A. Deraemaeker, G. Kerschen, and C. Collette. "Active Damping of Bladed Disk Assemblies". *Proceedings of ICSV27, Annual Congress of International Institute of Acoustics and Vibration (IIAV)*. Prague, 2020.

[128] J. Schoukens, M. Vaes, and R. Pintelon. "Linear System Identification in a Nonlinear Setting: Nonparametric Analysis of the Nonlinear Distortions and Their Impact on the Best Linear Approximation". *IEEE Control Systems* Vol. 36, no. 3 (2016), pp. 38–69. DOI: 10.1109/MCS.2016.2535918.

[129] B. Peeters, H. Van der Auweraer, P. Guillaume, and J. Leuridan. "The PolyMAX Frequency-Domain Method: A New Standard for Modal Parameter Estimation?" *Shock and Vibration* Vol. 11, no. 3-4 (2004), pp. 395–409. DOI: 10.1155/2004/523692.

[130] W. Heylen, S. Lammens, and P. Sas. *Modal analysis theory and testing*. 2. Leuven: Katholieke Univ. Leuven, Departement Werktuigkunde, 2007. ISBN: 978-90-73802-61-2.

[131] P. Soltani, G. Kerschen, G. Tondreau, and A. Deraemaeker. "Tuning of a piezoelectric vibration absorber attached to a damped structure". *Journal of Intelligent Material Systems and Structures* Vol. 28, no. 9 (2017), pp. 1115–1129. DOI: 10.1177/1045389X16666180.

[132] Safran Aero Boosters. URL: https://www.safran-group.com/.

[133] Siemens Digital Industries Software. *NX*. 2023.

[134] S.-T. Wei and C. Pierre. "Localization Phenomena in Mistuned Assemblies with Cyclic Symmetry Part II: Forced Vibrations". *Journal of Vibration and Acoustics* Vol. 110, no. 4 (1988), pp. 439–449. DOI: 10.1115/1.3269548.

[135] D. Bondoux. "Piezodamping: a low-power-consumption technique for semi-active damping of light structures". *Proceedings of the SPIE, Volume 2779*. Lyon, France, 1996, p. 694. DOI: 10.1117/12.237038.

[136] J. Tang and K. W. Wang. "Active-passive hybrid piezoelectric networks for vibration control: comparisons and improvement". *Smart Materials and Structures* Vol. 10, no. (2001) 794–806 (2001).

[137] S. Behrens, A. J. Fleming, and S. O. R. Moheimani. "A broadband controller for shunt piezoelectric damping of structural vibration". *Smart Materials and Structures* Vol. 12, no. 1 (2003). DOI: 10.1088/0964-1726/12/1/303.

[138] M. Neubauer, R. Oleskiewicz, K. Popp, and T. Krzyzynski. "Optimization of damping and absorbing performance of shunted piezo elements utilizing negative capacitance". *Journal of Sound and Vibration* Vol. 298 (2006), pp. 84–107. DOI: 10.1016/j.jsv.2006.04.043.

[139] M. Berardengo, S. Manzoni, O. Thomas, and M. Vanali. "Piezoelectric resonant shunt enhancement by negative capacitances: Optimisation, performance and resonance cancellation". *Journal of Intelligent Material Systems and Structures* Vol. 29, no. 12 (2018), pp. 2581–2606. DOI: 10.1177/1045389X18770874.

[140] M. Berardengo, S. Manzoni, M. Vanali, and R. Bonsignori. "Enhancement of the broadband vibration attenuation of a resistive piezoelectric shunt". *Journal of Intelligent Material Systems and Structures* (2021). DOI: 10.1177/1045389X20988090.

[141] C. Sugino, M. Ruzzene, and A. Erturk. "Digitally Programmable Resonant Elastic Metamaterials". *Physical Review Applied* Vol. 13, no. 6 (2020), p. 061001. DOI: 10.1103/PhysRevApplied.13.061001.

[142] Wolfram Research, Inc. *Mathematica, Version 12.2*. URL: https://www.wolfram.com/wolfram-alpha-notebook-edition.

[143] J. L. Fanson. "An Experimental Investigation of Vibration Suppression in Large Space Structures Using Positive Position Feedback". Doctoral Thesis. California Institute of Technology, 1987. DOI: 10.7907/0SA8-HW86.

[144] J. L. Fanson and T. K. Caughey. "Positive position feedback control for large space structures". *AIAA Journal* Vol. 28, no. 4 (1990). DOI: 10.2514/3.10451.

[145] G. S. Agnes. "Performance of Nonlinear Mechanical, Resonant-Shunted Piezoelectric, and Electronic Vibration Absorbers for Multi-Degree-of-Freedom Structures". Doctoral Thesis. Virginia State University, 1997.

[146] J. J. Dosch, D. J. Inman, and E. Garcia. "A Self-Sensing Piezoelectric Actuator for Collocated Control". *Journal of Intelligent Material Systems and Structures* Vol. 3, no. 1 (1992), pp. 166–185. DOI: 10.1177/1045389X9200300109.

[147] J. J. Dosch, D. J. Leo, and D. J. Inman. "Comparison of vibration control schemes for a smart antenna". *[1992] Proceedings of the 31st IEEE Conference on Decision and Control*. Tucson, AZ, USA: IEEE, 1992, pp. 1815–1820. ISBN: 978-0-7803-0872-5. DOI: 10.1109/CDC.1992.371116.

[148] M. K. Kwak and S.-B. Han. "Application of genetic algorithms to the determination of multiple positive-position feedback controller gains for smart structures". Ed. by Vasundara V. Varadan. San Diego, CA, 1998, pp. 637–648. DOI: 10.1117/12.316341.

[149] J. Enríquez-Zárate, L. Trujillo, G. K. Toledo-Ramírez, Á. J. Ramos-Cirilo, and . Hernández. "Optimization of PPF Control of a Building-like Structure for Vibration Control". *Computación y Sistemas* Vol. 22, no. 2 (2018). DOI: 10.13053/cys-22-2-2945.

[150] V. V. Huertas and V. Roha'-Ilkiv. "Vibration Suppression of a Flexible Structure". *Procedia Engineering* Vol. 48 (2012), pp. 233–241. DOI: 10.1016/j.proeng.2012.09.509.

[151] D. Russell, A. San-Millan, V. Feliu, and S. S. Aphale. "Butterworth Pattern-based Simultaneous Damping and Tracking Controller Designs for Nanopositioning Systems". *Frontiers in Mechanical Engineering* Vol. 2 (2016). DOI: 10.3389/fmech.2016.00002.

[152] A. Paknejad, G. Zhao, M. Osée, A. Deraemaeker, F. Robert, and C. Collette. "A novel design of positive position feedback controller based on maximum damping and H_2 optimization". *Journal of Vibration and Control* Vol. 26, no. 15-16 (2020). DOI: 10.1177/1077546319892755.

[153] J. MacLean, M. Aleyaasin, and S. S. Aphale. "How Far Should Poles Be Placed? Selecting Positive Feedback Controllers for Damping and Tracking Applications: A Complete Characterisation". *Vibration* Vol. 5, no. 4 (2022), pp. 641–658. DOI: 10.3390/vibration5040038.

[154] L. Marinangeli, F. Alijani, and S. Hassan HosseinNia. "Fractional-order positive position feedback compensator for active vibration control of a smart composite plate". *Journal of Sound and Vibration* Vol. 412 (2018), pp. 1–16. DOI: 10.1016/j.jsv.2017.09.009.

[155] W. Niu, B. Li, T. Xin, and W. Wang. "Vibration active control of structure with parameter perturbation using fractional order positive position feedback controller". *Journal of Sound and Vibration* Vol. 430 (2018), pp. 101–114. DOI: 10.1016/j.jsv.2018.05.038.

[156] B. Mokrani. *Active vibration isolation with positive position feedback, Oral presentation at ISMA-USD2022*. Leuven, Belgium, 2022.

[157] G. Zhao, A. Paknejad, G. Raze, A. Deraemaeker, G. Kerschen, and C. Collette. "Nonlinear positive position feedback control for mitigation of nonlinear vibrations". *Mechanical Systems and Signal Processing* Vol. 132 (2019), pp. 457–470. DOI: 10.1016/j.ymssp.2019.07.005.

[158] G. Zhao, A. Paknejad, G. Raze, G. Kerschen, and C. Collette. "H_∞ optimization of positive position feedback control for mitigation of nonlinear vibrations". *Conference Proceedings of ISMA2018 - USD2018*. Leuven, 2018.

[159] S. Krenk and J. Høgsberg. "Equal modal damping design for a family of resonant vibration control formats". *Journal of Vibration and Control* Vol. 19, no. 9 (2013), pp. 1294–1315. DOI: 10.1177/1077546312446796.

[160] R. L. Clark. "Accounting for Out-of-Bandwidth Modes in the Assumed Modes Approach: Implications on Colocated Output Feedback Control". *Journal of Dynamic Systems, Measurement, and Control* Vol. 119, no. 3 (1997), pp. 390–395. DOI: 10.1115/1.2801270.

[161] S. O. R. Moheimani, B.J.G. Vautier, and B. Bhikkaji. "Experimental implementation of extended multivariable PPF control on an active structure". *IEEE Transactions on Control Systems Technology* Vol. 14, no. 3 (2006), pp. 443–455. DOI: 10.1109/TCST.2006.872532.

[162] T. M. P. Silva, C. Hameury, G. Ferrari, P. Balasubramanian, G. Franchini, and M. Amabili. "Particle swarm optimization of a non-collocated MIMO PPF active vibration control of a composite sandwich plate". *Journal of Sound and Vibration* Vol. 555 (2023), p. 117723. DOI: 10.1016/j.jsv.2023.117723.

[163] D. Hoffmeyer and J. Høgsberg. "Damping of coupled bending-torsion beam vibrations by spatially filtered warping position feedback". *Journal of Sound and Vibration* Vol. 477 (2020), p. 115323. DOI: 10.1016/j.jsv.2020.115323.

[164] S. Fenik. "Optimal PPF controller for multimodal vibration mitigation". *Engineering MECHANICS* Vol. 15, no. 3 (2008), p. 153–173.

[165] J. Høgsberg and S. Krenk. "Calibration of piezoelectric RL shunts with explicit residual mode correction". *Journal of Sound and Vibration* Vol. 386 (2017), pp. 65–81. DOI: 10.1016/j.jsv.2016.08.028.

[166] G. Raze, J. Dietrich, and G. Kerschen. "Tuning and performance comparison of multiresonant piezoelectric shunts". *Journal of Intelligent Material Systems and Structures* (2022), p. 1045389X2210880. DOI: 10.1177/1045389X221088031.

[167] A. Preumont. *Vibration Control of Active Structures*. 3. Vol. 179. Solid Mechanics and Its Applications. Dordrecht: Springer Netherlands, 2011. ISBN: 978-94-007-2032-9. DOI: 10.1007/978-94-007-2033-6.

Publications

The complete list of the author's publications is available in the institutional repository ORBI (https://orbi.uliege.be/profile?uid=p226206)

Publications associated with this thesis

Journal articles

J. Dietrich, G. Raze, X. Charles, and G. Kerschen. "Multimodal shunt damping of monolithic bladed drums using multiple digital vibration absorbers". To be submitted to *Journal of Engineering for Gas Turbines and Power*.

J. Dietrich, G. Raze, A. Deraemaeker, C. Collette, and G. Kerschen. "H_∞ tuning rules for positive position feedback controllers: the single-degree-of-freedom case and beyond". Submitted to *Journal of Vibration and Control* (2023).

J. Dietrich, G. Raze, and G. Kerschen. "Multimodal shunt damping of mechanical structures using multiple digital vibration absorbers". *Engineering Research Express* (2022). DOI: 10.1088/2631-8695/ac9fa8

Conference proceedings and presentations

J. Dietrich, G. Raze, C. Collette, A. Deraemaeker, and G. Kerschen. "Resistive-inductive piezoelectric shunts with negative capacitances and positive position feedback - a comparative study". *Proceedings of ISMA2022 including USD2022 International Conference on Noise and Vibration Engineering* Leuven, Belgium: KU Leuven (2022). URL: https://orbi.uliege.be/handle/2268/294927

J. Dietrich, G. Raze, A. Paknejad, A. Deraemaeker, C. Collette, and G. Kerschen. "Vibration mitigation of bladed structures using piezoelectric digital vibration absorbers". *Paper presented at IMAC XL 2022*, Orlando, United States (2022). DOI:10.1007/978-3-031-05405-1-11

Publications in collaborations

Journal articles

L. Zhang, X. Sun, J. Dietrich, G. Kerschen, and L. Cheng. "Enhanced energy transfer and multimodal vibration mitigation in an electromechanical acoustic black hole beam". *Journal of Sound and Vibration* (2023). DOI: 10.1016/j.jsv.2023.117841

G. Raze, J. Dietrich, B. Lossouarn, and G. Kerschen. "Shunts vs networks: tuning and comparison of centralized and decentralized piezoelectric vibration absorbers". *Smart Materials and Structures*, Vol. 31 (11) (2022), p. 15006. DOI:10.1088/1361-665X/ac92b0

G. Raze, J. Dietrich, B. Lossouarn, and G. Kerschen. "Modal-based synthesis of passive electrical networks for multimodal piezoelectric damping".*Mechanical Systems and Signal Processing*, Vol. 176 (2022), p. 109120. DOI:10.1016/j.ymssp.2022.109120

G. Raze, J. Dietrich, and G. Kerschen. "Tuning and performance comparison of multiresonant piezoelectric shunts". *Journal of Intelligent Material Systems and Structures* (2022). DOI:10.1177/1045389x221088031

G. Raze, J. Dietrich, and G. Kerschen. "Onset and stabilization of delay-induced instabilities in piezoelectric digital vibration absorbers". *Journal of Intelligent Material Systems and Structures*, Vol. 33 (16) (2022), pp. 2033-2048. DOI:10.1177/1045389X211072269

G. Raze, J. Dietrich, and G. Kerschen. "Passive control of multiple structural resonances with piezoelectric vibration absorbers". *Journal of Sound and Vibration*, Vol. 515 (2021), p. 116490. DOI:10.1016/j.jsv.2021.116490

Conference proceedings and presentations

L. Zhang, X. Sun, J. Dietrich, G. Kerschen, and L. Cheng. "Enhanced energy transfer and multimodal vibration mitigation in an electromechanical acoustic black hole beam". The 19th Asia Pacific Vibration Conference, Qingdao, China (2021). URL: https://orbi.uliege.be/handle/2268/302386

G. Raze, J. Dietrich, A. Paknejad, B. Lossouarn, G. Zhao, A. Deraemaeker, C. Collette, and G. Kerschen. "Passive control of a periodic structure using a network of periodically-coupled piezoelectric shunt circuits"*Proceedings of ISMA 2020 - International Conference on Noise and Vibration Engineering and USD 2020 - International Conference on Uncertainty in Structural Dynamics*, pp. 145-160. Leuven, Belgium: KU Leuven (2020). URL: https://orbi.uliege.be/handle/2268/252957